Biomimetic Approach to Anti-Fouling Surfaces

Wen Choo Cheong

Submitted in accordance with the requirements for the degree of
Doctor of Philosophy

The University of Leeds
School of Mechanical Engineering

November 2010

The candidate confirms that the work submitted is his/her own and that appropriate credit has been given where reference has been made to the work of others.

Acknowledgements

I owe my deepest gratitude to Professor Anne Neville for granting me the opportunity to work in this project. Her advice, encouragement and patience were most invaluable in the process. I am also grateful to Professor Philip Gaskell for his support throughout.

A special thanks to the FAST team in Heriot Watt University for the financial support and involvement in this project.

This thesis would definitely not have been possible without the love and support from my family.

It is a pleasure to thank my friends and colleagues in the research group for their unequivocal support. Thanks to Violette, Eleftheria, Aurelie, Thibaut, Rob, Abinesh, Laura, John, Nasser, Nasim, I would also like to acknowledge the administrative and technical staff who were always available and helpful. I offer my regards and blessings to all of those who have supported me in any respect during the completion of the project.

Lastly, I would like to thank David R., who was a huge part of my life and a driving force for me to go on in my thesis.

Abstract

Scale formation is recognized as one of the major problems affecting production in the oil and gas sector. There are many approaches to remove and prevent scaling with chemical inhibition, chemical scale removers and mechanical methods being the most prevalent ones. Recently the focus has shifted onto more environmentally friendly inhibitors that are less toxic to the environment, thus the development of green inhibitors. Another way forward is to turn to surface engineering - this is a very popular approach in the control of biofouling but only a few attempts have been made to use it for the purpose of scale inhibition. It is fair to say that there is a potential for more widespread study and exploitation of such systems.

Biomimetics in surface engineering is receiving more attention as nature provides surfaces with a whole range of functionality. In the present work, micro- and nano-structured polymers surfaces with the self-cleaning Lotus and anti-reflective Moth-eye effects have been assessed as potential surfaces able to reduce mineral scale deposition. Calcium carbonate ($CaCO_3$) was deposited onto them and their performance compared with reference stainless steel surfaces. In addition, the anti-scaling performance of three commercially available coatings – DLC, Tech 100 and Tech 23 was also investigated. The surfaces were tested in a rotating cylinder electrode (RCE) under different fluid hydrodynamic conditions i.e. both laminar to turbulent flow.

Last but not least, micro-adhesion tests under water were conducted in an attempt to relate deposition tests to the adhesion properties of a single $CaCO_3$ crystal against a surface as a measure of anti-scaling performance.

Contents

Figures

Tables

Nomenclature

ΔG_s	Surface excess free energy (J)
ΔG_v	Volume excess free energy (J)
ΔG	Overall excess free energy (J)
θ	Contact angle (°)
φ	Nucleation correction factor
γ	Interfacial tension (N/m)
γ^+	Electron acceptor (Lewis acid) parameter ($mJ.m^{-2}$)
γ^-	Electron donor (Lewis base) parameter ($mJ.m^{-2}$)
μ	Absolute viscosity of solution ($kg.m^{-1}\ s^{-1}$)
ρ_s	Solution density ($kg\ m^{-3}$)
η	Viscosity ($kg.m^{-1}s^{-1}$)
A	Nucleation rate constant (s^{-1})
δ_h	Hydrodynamic boundary layer
δ_m	Mass transfer or diffusion boundary layer
A_F	Flat projection of the solid-liquid contact area upon a horizontal plane
τ_{cyl}	Wall shear stress ($kg.m^{-1}s^{-1}$)
A_{sl}	Actual area of rough surface
ω	Angular rotation rate ($rad.s^{-1}$)
D	Diffusivity ($m^2.s^{-1}$)
d_{cyl}	Outer diameter of rotating cylinder electrode (RCE) (cm)
f_1	Roughness factor
FAU	Turbidity unit
F_L	Hydraulic lift force (N)
F_i	Interaction force obtained by adding electrical double layer force and the van der Waal force (N)
F_{net}	Net adhesive force (N)
F	Rotations per minute (RPM)
J	Rate of nucleation (Number of nuclei/ $s.m^3$)

k	Boltzmann constant (1.3805 x 10-23 JK^{-1})
K_{eq}	Chemical equilibrium constant
K_{sp}	Solubility product
l	Length of profile used for the measurement of surface roughness parameters
N	Avogadro number (6.023 x 10^{23} mol^{-1})
r	Roughness factor
R_a	Surface roughness
R_f	Roughness factor
Re	Reynolds number
R	Gas constant (8.314 $J.K^{-1}mol^{-1}$)
r	Radius of nucleus
r_c	Critical radius of nucleus
SR	Saturation ratio
SI	Saturation index
Sc	Schmidt number
S	Degree of entropy (J/K)
t_{ind}	Induction time (s)
u^+	Velocity profile in the viscous sublayer
U_{cyl}	Linear velocity at outer surface of rotating cylinder ($m.s^{-1}$)
U	Internal surface energy (J)
v	Molecular volume (m^3)
W_{ad}	Work of adhesion ($MJ.m^{-2}$)
W_{132}	Theoretical work of adhesion ($mJ.m^{-2}$)

Chapter 1
Introduction

The primary focus of this thesis is the problem of calcium carbonate ($CaCO_3$) scaling formed in the oil and gas industry. The presence of scale layers poses a series of problems such as impedance of heat transfer, increased energy consumption and even unscheduled equipment shutdown or failures. The management of scale is a challenge and the focus is increasingly on environmentally-friendly solutions to control scale. Several aspects relating to $CaCO_3$ scaling on surfaces are studied here: (1) polymers with micro- and nano-structured physical features and some commercial coatings as potential anti-scaling surfaces; (2) the effect of various surface parameters such as roughness and surface energy; (3) micro-adhesion tests between test substrates and $CaCO_3$ crystal plate under water for predicting the scaling tendency of the substrates; (4) the hydrodynamic effects on scale formation on surfaces.

1.1 Oil and gas formation

It is in the sedimentary rock basins that most gas and oil is found and produced. Due to the thickness of the sedimentary rocks, most basins have source rocks that were buried sufficiently deep in the geological past to generate gas and oil. This deep part of the basin where the oil and gas forms is called the *kitchen* or the *oven*. Once the gas and oil is generated, it flows upwards into the overlying rocks (see Figure 1.1). If it intersects a layer of reservoir rock, the gas and oil then migrates through the interconnected pores of the reservoir rock layer up the flanks of the basin where becomes trapped and concentrated.

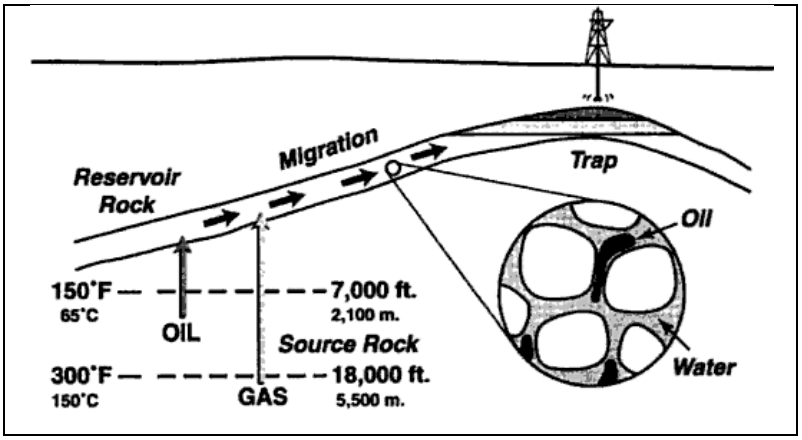

Figure 1.1: Schematic showing generation and migration of gas and oil [1]

Once the natural reservoir drive has been depleted in the oilfield, water flooding and enhanced oil recovery methods can be employed. Water is pumped under pressure down injection wells into the reservoir pushing oil towards producing wells during water flooding (refer to Figure 1.2); alternatively carbon dioxide or steam and fluids, not natural to the reservoir, are pumped down into the reservoir to enhance oil recovery.

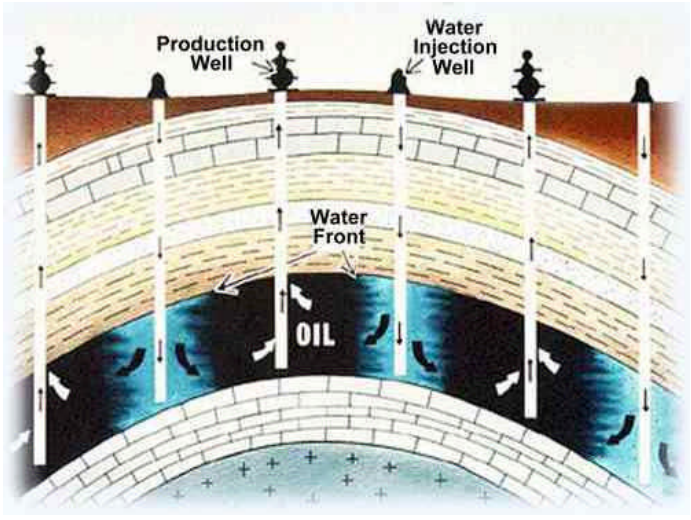

Figure 1.2: Water flooding of a reservoir to enhance oil recovery [1]

Special attention is required to formation damage caused by the adverse reactions encountered during acid stimulation, brine incompatibility in seawater injection for water flooding, precipitation caused by CO_2 and light hydrocarbons near wellbore, and sulphur deposition [2].

1.2 Inorganic scaling

Inorganic scaling is the process of deposition of scales from aqueous solutions of minerals, referred to as brines, when they become supersaturated as a result of the alteration of the state of their thermodynamic and chemical equilibrium [3]. This poses as a significant problem as these deposits cake or build up on the walls of perforations, casings, production tubing, valves, pumps and downhole completion equipment, thereby clogging the wellbore and preventing fluid flow. An example of scale formed in tubing is provided in Figure 1.3. In addition, scale can be deposited all along water paths from injectors through the reservoir to surface equipment.

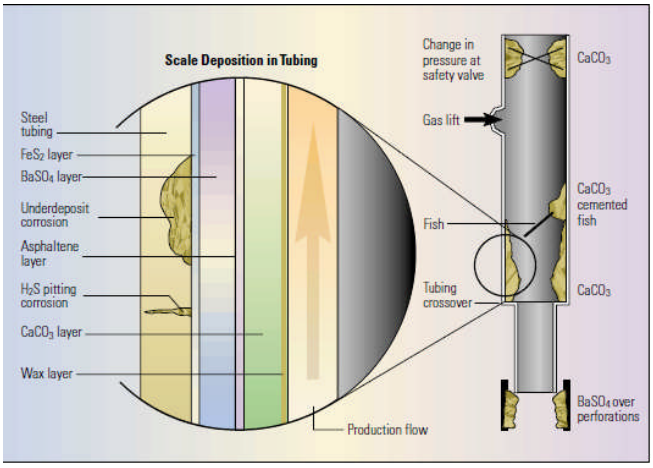

Figure 1.3a

Figure 1.3b

Figure 1.3: (a) Scale formation in tubing [4]; (b) How scale looks in the internal bore of a pipe [4]

1.3 Objectives of the thesis

In the work reported herein, a rotating cylinder electrode (RCE) is used to develop insight into the mechanisms involved in calcium carbonate surface precipitation and deposition. Since inorganic scaling is driven by surface-specific interactions between solids and liquids, understanding their interactions is important at a fundamental level.

The specific objectives of the thesis are :

- To determine which surface properties are important in preventing adhesion of scale so they can be quantified and controlled in a reproducible manner.

- To quantify how surface chemistry, surface roughness and water contact angle measurement relate to the scaling tendency of a surface.

- To determine if micro-adhesion tests conducted in a wet environment between crystal plate and test substrates can provide a reasonable measure of scale adhesion tendency.

- To observe the effects of various hydrodynamic conditions on surface scale deposition.

- To assess the potential practical applications of polymer coatings or novel surfaces in the oil and gas sector.

1.4 Thesis layout

The thesis is laid out as follows.

Chapter 1 gives a brief introduction to oil and gas production process with a focus on the problem of inorganic scaling as well as the objectives of this work.

An extensive literature review is presented in Chapter 2 describing the types of scale found in oil fields along with the theory of crystallization underlying the formation of $CaCO_3$. A review of the various methodologies used to study $CaCO_3$ formation and the parameters influencing the process is given. The chapter also includes a look at some biomimetic surfaces and biomineralization where crystallization can be surface-controlled.

Chapter 3 provides details of the experimental methodology employed and the various analysis techniques utilised in this work.

The experimental results obtained are presented in Chapters 4 and 5. The former is concerned with the substrate effects on $CaCO_3$ scaling tendency; the latter focuses on the hydrodynamic effects on scaling tendency.

Chapter 6 discusses the results presented in this thesis with reference to the current literature; in addition, the practical implications of the findings of the work for the oil and gas industry are discussed.

Conclusions are drawn and recommendations for future work are provided in Chapter 7.

Chapter 2
Background on inorganic scaling and literature review

This chapter gives an overview as to the problems of and remedies for scale formation in the oil and gas sector, encountered during oil production and recovery phase. Inorganic scaling is also present in various other industries such as the dairy sector, desalination plants and in heat exchanger equipment. The various surface parameters that affect scaling such as temperature, pH and impurities are reviewed. Next, an overview of the various surface modifications employed by other industries to tackle the problem of scale is presented. The effects of surface energy, chemistry and physical parameters such as topography on scale formation and on adhesion between surfaces are discussed. In addition, the relationship between hydrodynamic parameters and scaling tendency is explored.

2.1 Scaling in the oil and gas industry

Water injection for flooding and pressure support is a key process in oilfield operations. Formation water in most reservoirs is typically a hypersaline chloride-type fluid that contains alkaline cations such as calcium, strontium, barium and even radium in some cases [5, 6]. Inorganic scaling is a process of deposition of scales from aqueous solutions of minerals, referred to as brines, when they become supersaturated as a result of alteration of the state of their thermodynamic and chemical equilibria [7]. There are many causes of scaling:

- when incompatible fluids are mixed during well development operations such as drilling, completion and acidizing;
- during theproduction of reservoir fluids which causes a decrease of pressure and temperature;

- improved recovery processes include use of water, carbonated water, alkaline water and carbon dioxide and this leads to both incompatible mixing of fluids and also pressure and temperature variations.

Inorganic scaling can occur in the well tubing and near wellbore formations of production and injection wells. Natural scaling occurs mostly in the near production wellbore regions as a result of the liberation of dissolved light gases from the formation brine by high drawdown (pressure difference in well and reservoir) which consequently leads to the loss of CO_2 gas from the brine and promotion of calcium carbonate precipitation [3]. The two main types of scale which are commonly found in the oilfield are carbonate and sulphate scales [8-11]. The deposits are seldom pure calcium sulphate or calcium carbonate but made up of a few inorganic components along with corrosion products, congealed oil, paraffin, silica and other impurities. Table 2.1 lists some of the common scales that can be found in the oilfield environment.

Table 2.1: Some common scales found in oilfields [12].

Name	Chemical formula	Primary variables
Calcium carbonate (Calcite)	$CaCO_3$	Partial pressure of CO_2, temperature, total dissolved salts
Calcium sulfate:		
Gypsum (most common)	$CaSO_4.2H_2O$	Temperature, total dissolved salts, pressure
Hemihydrate	$CaSO_4.1/2H_2O$	
Anhydrate	$CaSO_4$	
Barium sulfate	$BaSO_4$	Temperature, pressure
Strontium sulfate	$SrSO_4$	Total dissolved salts
Iron compounds:		
Ferrous carbonate	$FeCO_3$	Corrosion, dissolved gases, pH
Ferrous sulfide	FeS	
Ferrous hydroxide	$Fe(OH)_2$	

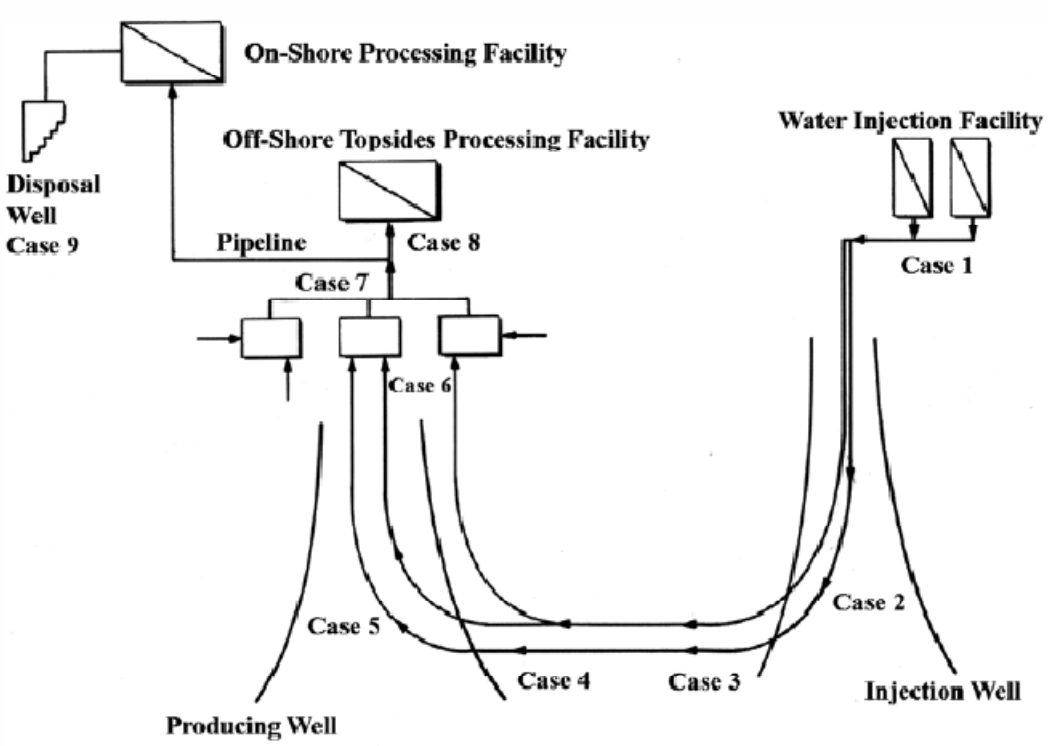

Figure 2.1: : Schematic showing possible locations for scale deposits [5]

Figure 2.1 shows the possible locations of scale deposits throughout the flow paths of water. Scale deposits could take place at [5]:

1. the surface water injection facility where incompatible sources of water are mixed prior to injection;

2. injection wells where the injected water starts to mix with the reservoir formation water;

3. downhole locations in the reservoir where the injected water displaces reservoir formation water;

4. downhole locations in the reservoir where the mixed injected water and formation water are about to reach the range of producing wells;

5. downhole locations in the reservoir where the mixed (injected and formation) waters are within the range of producing wells;

6. the connection of a branched zone where each branch produces different water;

7. the manifold of a producing zone where water is produced from different blocks within the same producing zone;

8. the topside facility where produced fluids are mixed from different production zones to separate oil and gas from produced water, or in pipelines that transport produced fluids to on-shore processing facilities; and if applicable

9. disposal wells where produced water is injected for final disposal.

The waters in oilfield reservoir conditions are generally at thermodynamic equilibrium and these formation waters contain relatively high concentrations of Ca^{2+} in addition to CO_2 concentrations that are higher than surface conditions. Some of this water will be produced along with oil to the surface during production and during this process, the pressure decreases and the dissolved CO_2 is released causing the solution pH to increase. Consequently, the water becomes supersaturated with respect to $CaCO_3$. This scaling can cause deposits in surface equipment, well-bore flow restrictions or even block the near well-bore formation [13]. The equilibrium relationship for calcium carbonate scale formation is given by the reaction

$$\boldsymbol{Ca^{+2} + 2HCO_3^- \leftrightarrow CaCO_{3(s)} + CO_{2(g)} + H_2O.} \qquad \textbf{(2.1)}$$

The chemical equilibrium constant for calcium carbonate is then given by equation (2.2), the braces in the equation indicate activity.

$$K_{eq} = \frac{[CaCO_3][CO_2]}{[Ca^{+2}][HCO_3^-]^2}. \qquad \textbf{(2.2)}$$

By applying Le Chatelier's principle, when CO_2 is liberated and removed by pressure reduction, the CO_2 concentration drops. In order to compensate for this decrease, more $CaCO_3$ will be produced to maintain the K_{eq}. When incompatible fluids are mixed or during enhanced recovery processs, any increase of the dissolved calcium [Ca^{+2}] ion concentration caused by these operations is compensated by calcium carbonate [$CaCO_3$] precipitation following the cause-and-effect of Le Chatelier's principle.

2.2 Various types of fouling

There are various types of fouling – crystallization or precipitation, particulate, chemical reaction, biological and corrosion fouling. The stages of fouling processes can be generalized via Epstein's classification which are initiation, delay or induction period, transport, attachment, removal and aging [14].

An example of inorganic or precipitation fouling was provided in the previous section. Precipitation fouling mainly occurs due to the existence of a supersaturated solution where ionic species in the solution are transferred by diffusion and/or bulk transport to a solid surface followed by crystallization of insoluble species at, and their further attachment to, the surface. In supersaturated solutions, particulate material can be produced if crystallization occurs in the bulk solution or if already deposited material is sheared off by the fluid flow. This can be followed by the transport of these crystals towards the surface and subsequent attachment and growth on the surface [15]. Hence, diffusion is the mechanism of transport and the attachment stage is controlled by Van der Waals forces, electric double layer and Born energies for particulate fouling [16, 17].

Before the onset of inorganic scaling, organic deposits usually form first; these include precipitates that contain wax, asphaltenes, gas hydrates, naphthenic acid salts and mixtures of these chemicals [18].

Likewise, biological fouling also occurs in the majority of aqueous processes. This type of fouling occurs on surfaces immersed in water due to the existence of microorganisms such as at tooth surfaces, a ship's hull, heat exchanger surfaces and membrane surfaces. Generally, the surface will be immediately covered by dissolved chemical compounds that adsorb on the surface and evolve to form a macromolecular film. This is followed by a process of biofouling where the initial film is colonized by microorganisms, algal spores and invertebrate larvae [19]. This process is illustrated in Figure 2.2.

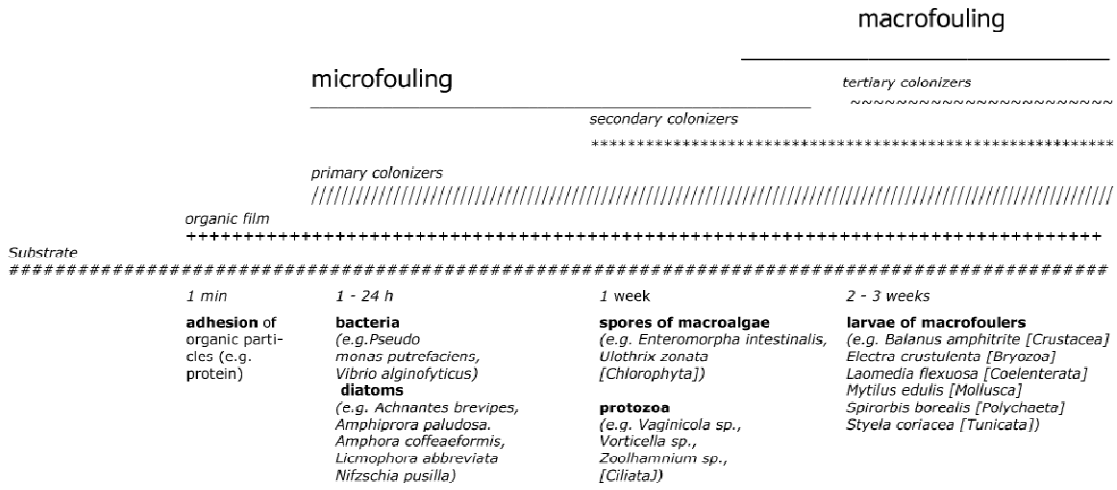

Figure 2.2: An illustration of the process of marine fouling [20]

The initial interaction between bacteria and surfaces may be considered in terms of colloidal behaviour. Adhesion to the surface follows the arrival of bacteria at the surface with the Derjaguin-Landau and Verwey Overbeek (DLVO) theory usually used to describe the initial stages of biofilm formation [21-23]. Colonisation comes next for biological particles where a combination of the microorganisms

embedded in a polymeric matrix of their own making, which is called the extra-cellular polymeric substance (EPS), is formed – this combination is called a biofilm [24].

As can be seen, inorganic scaling is not the only deposition and precipitation problem encountered by the oil and gas sector during production. There are various forms of fouling and they all involve various mechanisms for forming. The present study focuses on the inorganic scaling of calcium carbonate onto surfaces only.

2.3 Biomineralization

Calcium carbonate is an inorganic mineral and scaling occurs at the crystal-surface interface. Gaining deeper insight into the processes occurring at the molecular level could contribute to a better understanding of the formation of these inorganic materials and is therefore of fundamental importance. Hence, it is useful to learn how living organisms possess the ability to control the precipitation of calcium carbonate with respect to nucleation, growth, morphology and polymorphic structure [25]. It is worthwhile looking at biomineralization in biological systems where advanced architectures are created with precise control of size and structure as this is of relevance here since the test substrates used in this work are patterned.

A general definition of biomineralization is: “Biomineralization is many different things to different organisms. It is the formation of spicules in the tissues of coccolithophorids, flowering plants, sponges, alcyonarians, holothurians, and tunicates; the formation of a box to live in for diatoms, foraminifera, radiolarians,

molluscs, annelids, and barnacles; and the formation of an articulated skeleton for echninoderms, arthropods, and vertebrates. It is also sometimes pathologic.” [26]

Many organisms have the ability to selectively deposit one polymorph and not the other, i.e. the formation of crystalline materials in nature is highly regulated. Biological systems such as bones, teeth and mollusc shells have the unique ability to control crystal polymorph, structure, orientation and hierarchical structure of inorganic phases [27]. This is achieved by means of organized assemblies of specialized biological macromolecules, specific additives, small organic molecules and inorganic ions [28]. The most commonly encountered biologically formed polymorphs are calcite and aragonite, which are structurally very similar [29]. The major difference between these two polymorphs is that the carbonate groups in calcite are all in a plane, whereas in aragonite they are slightly staggered and rotated [30]. Figure 2.3 shows the differences in the unit cells of calcite, vaterite and aragonite.

By studying these unique natural surfaces, the approach to artificial crystallization [28] is based on the combination of two concepts – the use of organized organic surfaces patterned with specific initiation domains on a nanoscale to study and orchestrate the crystallization proves that it is possible to achieve a remarkable level of control over various aspects of the crystal nucleation and growth. This includes the precise localization of particles, nucleation density, crystal sizes, morphology, crystallographic orientation, arbitrary shapes, nanostructure, stability and architecture.

Many studies have been carried out on the mechanism involved in biomineralization processes and several new biologically inspired synthetic routes have been designed for control of the formation of the mineral phase [31-33].

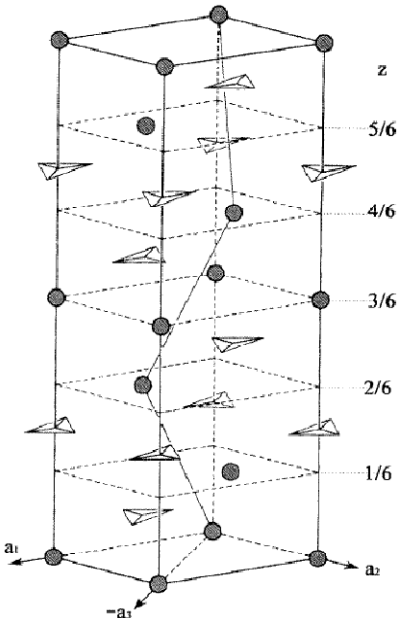

Figure 2.3: Unit cell of calcite

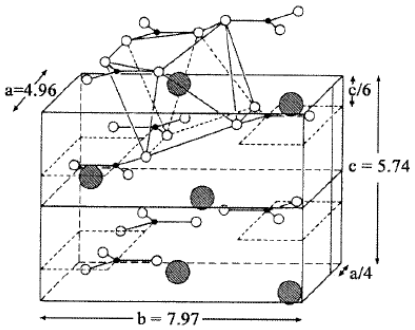

Figure 2.3b: Unit cell of aragonite, with additional CO_3^{2-} groups outside the cell to demonstrate coordination of Ca ion.

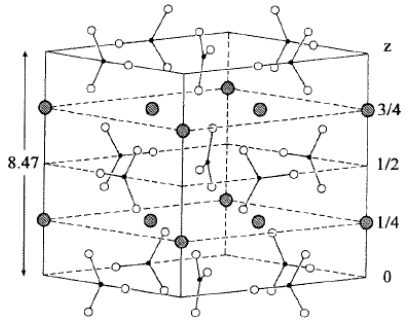

Figure 2.3c: Unit cell of vaterite

Figure 2.3: Schematic diagrams of the unit cells of calcium carbonate polymorphs [30]

Figure 2.4 illustrates the abalone shell which is a composite of calcium carbonate with a few percent of an organic component. The core of the organic template is composed of a few layers of β-chitin confined between “silk-like” glycine- and aniline- rich proteins. The outer surfaces of the template are coated with hydrophilic acidic macromolecules [34].

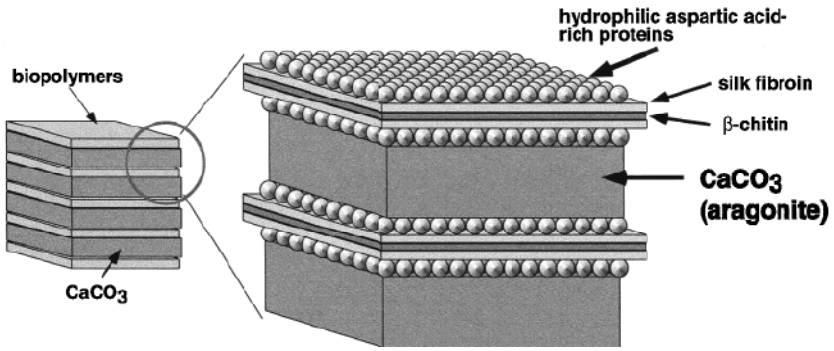

Figure 2.4: Schematic illustration of the nacre of an abalone shell [34]

Biomineralization occurs within specific environments, which implies stimulation of crystal formation at certain interfacial sites and relative inhibition of the process at all other sites [28]. A study [35] recently addressed the question of calcite/aragonite polymorphism using mollusc shells as a starting model. They managed to prove that soluble shell proteins can determine the polymorphs of crystals grown on a substrate of squid chitin and silkworm fibroin. Their experiment also suggests that soluble proteins alone are sufficient to control the crystal phase. The proteins extracted from nacreous layers in mollusc shells induced aragonite formation, while those extracted from the prismatic layer induced calcite formation.

Another study [36] showed that aragonite formation can be induced under a Langmuir monolayer composed of 5-hexadecyloxyisopthalic acid (C_{16}ISA). In addition, self-assembled monolayers of alkylthiols can induce crystallization of the three polymorphs of calcium carbonate at two different temperatures. One such example [28] would be where controlled crystallization is based on engineering the nucleation site and on controlling mass transport to the surface at the micron scale, using micropatterned SAMs of alkanethiols supported on metal films. This method the nanoscale control over many of the nucleation and crystal growth – oriented nucleation, location and density of nucleation, crystal sizes and patterns in one experiment.

All of the above studies show that considerable control can be exerted in vitro over the crystal formation process. This includes control over nucleation and the type of polymorph formed, as well as over crystal growth. The above synthetic systems have highlighted the importance of electrostatic binding, geometric matching and stereochemical correspondence in recognition processes [27].

2.4 Theories of crystal growth

Generally, precipitation takes place in two stages: nucleation and growth. In the initial stage, microscopic nuclei of salt are formed from the crystal building blocks, which grow subsequently to macroscopic crystals, which may undergo secondary processes such as aggregation and secondary nucleation.

Of primary importance is the development of supersaturation which is necessary as it is the driving force for nucleation. This can be attained by increasing the salt concentration above the equilibrium level.

2.4.1 Equilibrium constants, solubility and supersaturation

The solubility of a salt is the mass of the salt dissolved in a known weight (or volume) of fluid [18]. For salts, there are different numbers of charge on the cations and anions, the generalized equation is

$$M_m X_x(s) \leftrightarrow mM^{z+}(aq) + xX^{z-}(aq) \cdot \quad \textbf{(2.3)}$$

Here m is the number of cations with charge z^+, and x is the number of the anions with a charge of z^-.

The equilibrium constant, K_{eq}, for dissolution of salts is of special importance in scaling studies and the general dissolution reaction is expressed as

$$K_{eq} = \frac{\{M^{z+}\}^m \{X^{z-}\}^x}{\{M_m X_x\}}. \quad \textbf{(2.4)}$$

The activity of a pure solid is by definition equal to one, in which case equation (2.4) simplifies to

$$K_{eq} = K_{sp} = \{M^{z+}\}^m \{X^{z-}\}^x, \quad \textbf{(2.5)}$$

where K_{sp} is the equilibrium constant for the dissolution of the salt and called the solubility product. If the salt is dissolving into a dilute solution, then activities of the species are equal to their concentration.

Saturation ratio, SR, for a salt measures the degree of supersaturation. Precipitation can only occur if the SR is greater than 1.0.

$$SR = \frac{\{M^{z+}\}^m \{X^{z-}\}^x}{K_{sp}}, \quad \textbf{(2.6)}$$

$$SI = \log_{10} SR, \quad \textbf{(2.7)}$$

where SI is the supersaturation index.

Hence for calcium carbonate precipitation, equation (2.6) becomes

$$SR = \frac{m_{Ca^{2+}} m_{CO_3^{2-}}}{K_{sp}}, \quad \textbf{(2.8)}$$

where m_i is the molarity of the ion.

Supersaturation can occur under various conditions [37]:

- A solution of normal solubility salts cooled below the solubility temperature.
- A solution of inverse solubility salts heated above the solubility temperature.
- Solutions evaporated beyond the solubility limits of the dissolved species.
- Mixing of different streams leading to supersaturated conditions.
- Change in pH of a process solution.

Accordingly, the driving force for scale to form is the supersaturation ratio (SR) of the solution which affects the induction time, growth and morphology of crystals and rate of nucleation. In thermodynamic terms, three possibilities exist in terms of scale formation from solution [38, 39].

(1) SR < 1: the solution is undersaturated and scale formation is not thermodynamically feasible.
(2) SR = 1: The solution is saturated. The scale formation and dissolution rate in the solution is the same and no scale is formed in the solution.
(3) SR > 1: The solution is supersaturated and scale formation is thermodynamically possible.

Before crystals can develop, there must exist in the solution a number of minute solid bodies, embryos, nuclei or seeds that act as centres of crystallization. Nucleation may occur spontaneously or be induced artificially [40].

Although there is no general agreement on nucleation, primary nucleation occurs in the absence of crystalline or any other type of suspended matter. When new crystals are formed in the neighbourhood of suspended crystallites or particles, secondary nucleation takes place. A supersaturated solution nucleates much more readily, i.e. at a lower supersaturation, when crystals of the solute are

already present or deliberately added. Primary nucleation can be further distinguished into homogeneous and heterogeneous nucleation [41].

2.4.2 Homogeneous nucleation

According to the classical theory of nucleation [18, 38], the free energy changes associated with the process of homogeneous nucleation may be considered as follows: The overall excess free energy, ΔG, between a small solid particle of solute (assumed to be a sphere of radius r for simplicity) and the solute in solution is equal to the sum of the surface excess free energy, ΔG_s, i.e. the excess free energy between the surface of the particle and the bulk of the particle, and the volume excess free energy, ΔG_v, i.e. the excess free energy between a very large particle ($r = \infty$) and the solute in solution. ΔG_s is a positive quantity, the magnitude of which is proportional to r^2. In a supersaturated solution, G_v is a negative quantity proportional to r^3. Thus

$$\Delta G = \Delta G_s + \Delta G_v = 4\pi r^2 \gamma + \frac{4}{3}\pi r^3 \Delta G_v \,. \qquad \textbf{(2.9)}$$

In the free energy change associated with nucleation, there are two competing factors: (a) the transfer of a molecule from a supersaturated solution to the solid phase results in a decrease in free energy per molecule; (b) the surface of the new solid phase has an energy associated with it and this surface energy results in an increase in the free energy per unit surface area of the cluster.

ΔG_v in equation (2.9) is the free energy change of the transformation per unit volume and γ is the interfacial tension, i.e. between the developing crystalline surface and the supersaturated solution in which it is located. The two terms on the right hand side of the equation (2.9) are of opposite signs and depend

differently on r, so the free energy of formation, ΔG, passes through a maximum. This maximum value, ΔG_{crit}, corresponds to the critical nucleus, r_c, and for a spherical cluster is obtained by setting $\frac{d\Delta G}{dr} = 0$.

$$\frac{d\Delta G}{dr} = 8\pi r\gamma + 4\pi r^2 \Delta G_v = 0, \quad \textbf{(2.10)}$$

$$r_c = \frac{-2\gamma}{\Delta G_v}, \quad \textbf{(2.11)}$$

where G_v is a negative quantity.

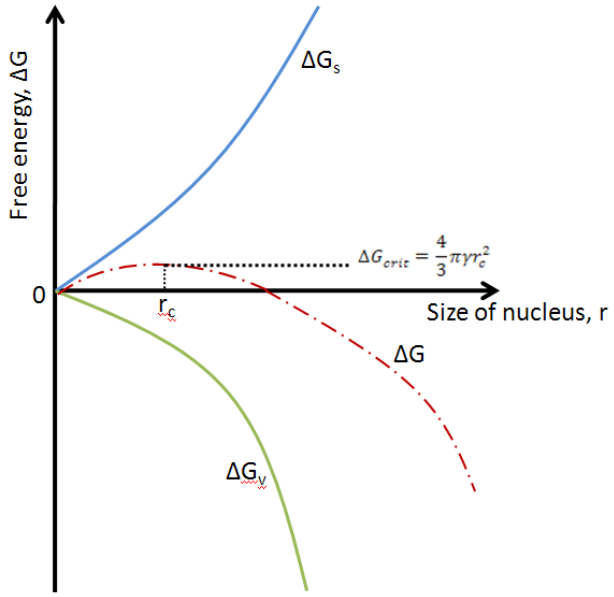

Figure 2.5: Free energy diagram for nucleation and critical radius

From equation (2.9) and equation (2.11),

$$\Delta G_{crit} = \frac{16\pi y^3}{3(\Delta G_v)^2} = \frac{4\pi\gamma r_c^2}{3}. \quad \textbf{(2.12)}$$

The behaviour of a newly created crystalline lattice structure in a supersaturated solution depends on its size; it can either grow or redissolve, but the process it

undergoes should result in a decrease in the free energy of the particle. The critical size, r_c, therefore, represents the minimum size of a stable nucleus. Particles with radii smaller than r_c will dissolve, or evaporate if the particle is a liquid in a supersaturated vapour, because only in this way can the particle achieve a reduction in its free energy. Similarly, particles with radii larger than r_c will continue to grow.

The rate of nucleation, J, e.g. the number of nuclei formed per unit time per unit volume, can be expressed in the form of the Arrhenius reaction velocity equation commonly used for the rate of a thermally activated process:

$$J = Aexp(-\Delta G/kT), \qquad \textbf{(2.13)}$$

where k is the Boltzmann constant, the gas constant per molecule = 1.3805 x 10^{-23} m^2 kg s^{-2} K^{-1} ,

The basic Gibbs-Thomson relationship for a non-electrolyte may be written as

$$\ln SR = \frac{2\gamma v}{kTr_,} \qquad \textbf{(2.14)}$$

where SR is the supersaturation ratio and υ is the molecular volume. This gives

$$-\Delta G_v = \frac{2\gamma}{r} = \frac{kTln\ SR}{v}\cdot \qquad \textbf{(2.15)}$$

Hence from equation (2.12)

$$\Delta G_{crit} = \frac{16\pi\gamma^3 v^2}{3(kTln\,S)^2}, \qquad \textbf{(2.16)}$$

and from equation (2.13),

$$J = A\exp\left[-\frac{16\pi\gamma^3 v^2}{3k^3T^3(\ln S)^2}\right]. \qquad \textbf{(2.17)}$$

2.4.3 Heterogeneous nucleation

The rate of nucleation of a solution can be affected considerably by the presence of mere traces of impurities in the system. An impurity that acts as a nucleation inhibitor in one case may not necessarily be effective in another; indeed it may even act as an accelerator. Crystal growth also tends to initiate on a pre-existing fluid-boundary surface and heterogeneous nucleation sites include surface defects, such as pipe surface roughness, existing scale or perforations in production liners, or even joints and seams in tubing and pipelines.

As the presence of a foreign body can induce nucleation, the overall free energy associated with the formation of a critical nucleus under heterogeneous conditions, $\Delta G'_{crit,}$ must be less than the corresponding free energy change, ΔG_{crit}, associated with homogeneous nucleation, i.e.

$$\Delta G'_{crit} = \varphi\Delta G_{crit}, \qquad \textbf{(2.18)}$$

where the factor φ is less than unity.

It can be seen from equation (2.17) that interfacial tension, γ, is an important factor in the nucleation process.

Figure 2.6 shows the interfacial energy diagram for three phases in contact: two solids and a liquid. γ_{cl} denotes the interfacial tension between the solid crystalline phase, c, and the liquid, *l*; γ_{cs} denotes the interfacial tension between the crystalline solid, c, and the solid surface, s; γ_{sl} denotes the interfacial tension between the solid surface, s, and the liquid, l.

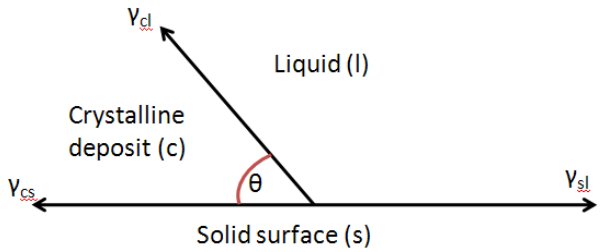

Figure 2.6: Interfacial tension

Resolving these forces yields

$$\cos\theta = \frac{\gamma_{sl} - \gamma_{cs}}{\gamma_{cl}}. \qquad \textbf{(2.19)}$$

The factor φ in equation (2.18) can be expressed as

$$\varphi = \frac{(2 + \cos\theta)(1 - \cos\theta)^2}{4}. \qquad \textbf{(2.20)}$$

In the case of complete non-affinity between the crystalline solid and solid surface (corresponding to that of complete non-wetting in liquid-solid systems):

θ = 180°, cos θ = -1 and φ =1, equation (2.18) gives $\Delta G'_{crit} = \Delta G_{crit}$.

Here the overall free energy of nucleation is the same as that required for homogeneous or spontaneous nucleation.

In the case of partial affinity corresponding to the partial wetting of a solid with a liquid:

$0 < \theta < 180°$, $\varphi < 1$ and equation (2.18) gives $\Delta G'_{crit} < \Delta G_{crit}$.

Nucleation is easier here because the overall excess free energy required is less than that for homogeneous nucleation.

In the case of complete affinity corresponding to complete wetting:

$\theta = 0°$, $\cos\theta = 1$ and $\varphi = 0$ and equation (2.18) gives $\Delta G'_{crit} = 0$

Here the free energy of nucleation is zero, this corresponds to the seeding of a supersaturated solution with crystals of the required crystalline product where no nuclei have to be formed in the solution.

2.4.4 Induction time

Nucleation theories relate the induction time in unseeded experiments (that is the time elapsed from the moment of mixing the reactants until the moment at which the onset of the precipitation can be detected) with both the time to form stable nuclei and the time for their subsequent growth to an observable size [42, 43].

The rate at which scales form is usually described in terms of the induction time (t_{ind}) after a supersaturated condition exists and before the appearance of scale. The induction period has frequently been used as a measure of the nucleation event, making the simplifying assumption that it can be considered to be inversely proportional to the rate of nucleation:

$$t_{ind} \propto J^{-1} . \quad \textbf{(2.21)}$$

The classical nucleation relationship may therefore be written as

$$\log t_{ind} \propto \left[\frac{\gamma^3}{T^3((\log S)^2)}\right], \quad \textbf{(2.22)}$$

which assumes that the nucleation time is much greater than the time required for growth of crystal nuclei to a detectable size.

2.4.5 Ostwald ripening process

Growth rates of small crystals formed at the later stage of fouling are substantially retarded by the presence of large adjacent crystals formed earlier [44, 45]. When two crystals of different size compete for dissolved mineral ions, the larger crystal attract the ions much more efficiently than the smaller crystal and therefore the larger crystal grows at a much faster rate than the smaller one. However, the smaller crystal would eventually grow to the equivalent size of the larger crystal, as the growth rate of the larger crystal would have reached an asymptotic value.

2.4.6 Main types of crystal growth

There are two types of crystal growth [38]. One is based on the existence of an adsorbed layer of solute ions on the crystal face and the subsequent growth is governed by Gibbs-Volmer theory: when units of a crystallizing substance arrive at a crystal face, they are not immediately integrated into the lattice but are free to migrate over the crystal face like a surface diffusion.

The other type of crystal growth is based on the bulk-growth mechanism which can be described by a surface energy theory in that the growth rate of each face of a crystal is not the same because of different surface energies. According to the theory, a crystal growing in a supersaturated medium will grow in a way so as to ensure that the whole crystal has a minimum total surface free energy for a given volume. If the crystal changes to a simple rounded shape, the total surface energy decreases. In practice, a crystal will not always maintain geometric similarity during growth; the smaller, faster growing faces are often limited.

2.5 Methods to study calcium carbonate

The kinetics of $CaCO_3$ nucleation and growth can be studied with a visual glass micromodel which is a 2D transparent flow network and allows us to observe and record the process of crystal nucleation and growth at a steady rate [46]; the setup is shown in Figure 2.7.

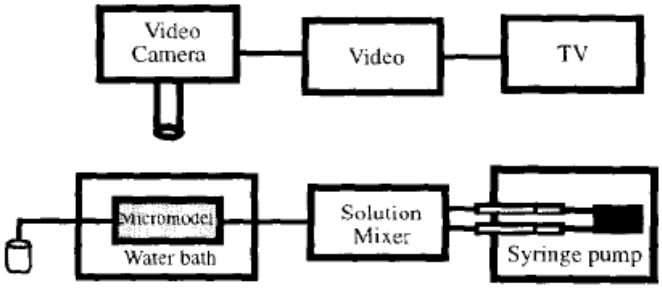

Figure 2.7: Schematic of the glass micromodel experimental system

The time-dependent process of calcium carbonate inception and growth through a transparent heat transfer test section can be observed with the microscopic system presented in Figure 2.8. To study the mechanism of scale formation on a solid surface, a few techniques have been applied mainly based on

the electrochemical approach combined with other techniques such as impedance spectroscopy [47, 48], a rotating disc electrode [49, 50] and a quartz crystal microbalance [51, 52]. Combining these techniques allow the scaling rate, morphology and the thickness of the scale layer to be investigated.

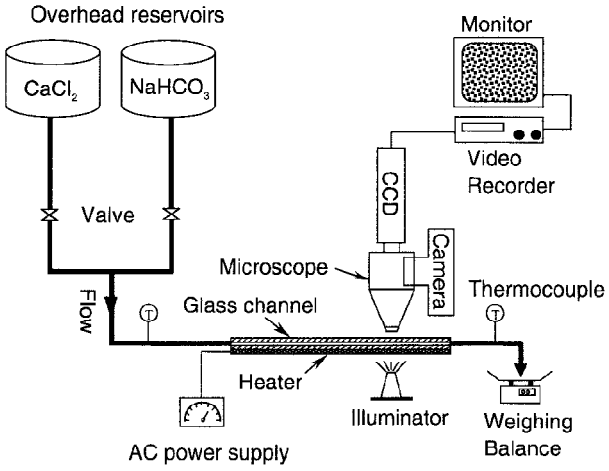

Figure 2.8: Schematic diagram for microscope system used to study fouling layers [44]

An electrochemical quartz crystal microbalance (EQCM) can be used in conjunction with an impinging jet cell to allow a controlled hydrodynamic flow on the electrode surface and by positioning a microscope lens behind the transparent electrode, the nucleation-growth process of calcium carbonate can be observed and analyzed [53]. An experimental setup that includes a number of the techniques mentioned above is shown in Figure 2.9.

Atomic force microscopy (AFM) allows the study of crystal surface features with high resolution [54]. Precipitated phases can be identified by X-ray powder diffraction (XRD) and by infrared spectroscopy (IR) while the morphology of

calcium carbonate can be investigated using a scanning electron microscope (SEM).

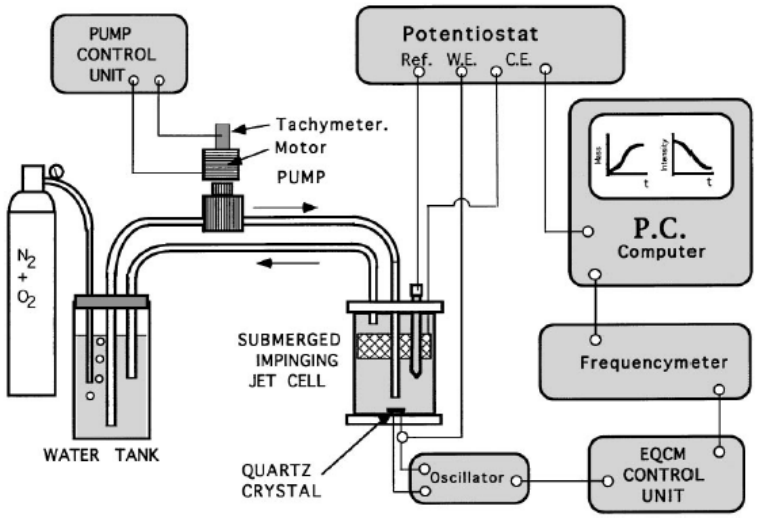

Figure 2.9: Experimental setup including the submerged impinging jet cell, the water supply system, the quartz crystal microbalance with its frequency meter, the electrochemical control and the monitoring by a PC [55]

2.6 Effects of various operating parameters on scale formation

Operating conditions such as solution composition, pH, together with temperature, dissolved and suspended impurities contribute to the crystal habit and particle morphology and polymorphism [56-59].

Inorganic fouling is influenced by the hydrodynamics of the flow, bulk and substratum temperature, suspended particles, the presence of gas bubbles, surface roughness, augmentation and material, and water quality such as pH and CO_2 content. Fouling rate increases with increasing flow velocity due to greater

deposition up to the point where the removal by shear stress will become inhibitive. Increasing temperature both in the bulk and at the surface enhances fouling. The presence of suspended particles can either enhance or inhibit fouling depending upon the type of particulate material: the particulate material can have a scouring effect and reduce fouling or it can act as nucleation sites for crystallization and hence promote fouling. In a mixture of different types of particles, the ones which are more adsorptive than the surface will enhance attachment of other particles once they are attached to the surface. In some cases, deposits formed by particulate fouling might easily be removed.

2.6.1 Effect of temperature

Owing to its inverse temperature-solubility characteristics, calcium carbonate is less soluble at high temperatures, this can be seen from Figure 2.10; the induction time is decreased with an increase in the fluid temperature [60].

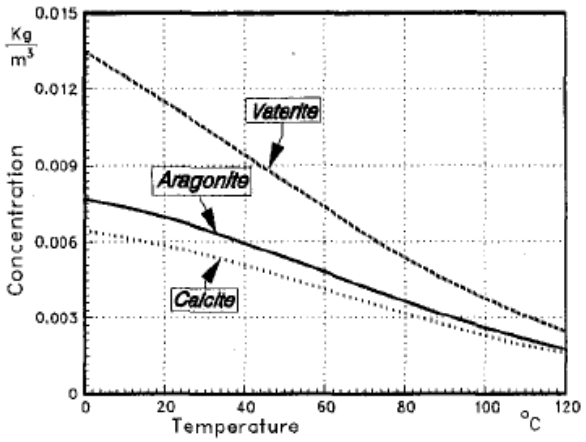

Figure 2.10: Solubility of calcium carbonate in water as a function of temperature [61]

The sulphates of calcium and magnesium pose the most serious complications in oilwell scaling as they are salts with inverse solubility. The higher ambient temperature that characterises the downhole environment promotes the formation of scale deposits of these minerals. Some crystal shapes will agglomerate whereas others will be readily swept away by the fluid. Another possibility is the epitaxial growth of one type of mineral scale forming onto another [40].

2.6.2 Effect of pH

The reactions involved in the precipitation of calcium carbonate are governed by the following equilibria:

$$CO_{2(g)} + H_2O \leftrightarrow H_2CO_3, \quad \textbf{(2.23)}$$

$$H_2CO_3 \leftrightarrow HCO_3^- + H^+, \quad \textbf{(2.24)}$$

$$HCO_3^- \leftrightarrow CO_3^{2-} + H^+, \quad \textbf{(2.25)}$$

$$Ca^{2+} + CO_3^{2-} \leftrightarrow CaCO_3 \cdot \quad \textbf{(2.26)}$$

The above chemical equilibria are strongly influenced by the pH of the solution among other factors such as temperature, ion concentration and flow rate which can shift the equilibrium in the forward or backward direction. This equilibria between CO_3^{2-}, HCO_3^- and H_2CO_3 as a function of pH can be seen in Figure 2.11.

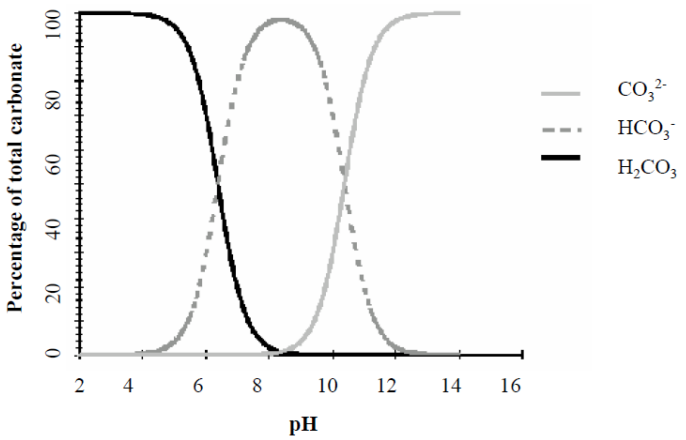

Figure 2.11: Percentage of CO_3^{2-}, HCO_3^- and H_2CO_3 as a function of pH

An increase in pH causes HCO_3^- to decompose and encourages $CaCO_3$ formation. The measurement of pH is essential to understand and follow the kinetics of precipitation because pH decreases along the process. The crystallization produces a progressive local accumulation of protons near the crystal surface, also reflected in the decrease of the pH in the bulk solution. This high concentration of protons can produce a proton attack at sites of the crystal surface [62, 63].

Supersaturation can also be controlled by initial pH conditions [62] or by changing the concentration of calcium while maintaining the pH and total carbonate constants [64]. According to classical nucleation theory, both nucleation and crystal growth rates depend on the solution supersaturation. The rate constants for nucleation and crystal growth are K_J and K_G, respectively, and they do not depend on supersaturation. These constants for calcium carbonate may be calculated according to the analysis of the kinetic data presented by Van der Leeden [65] and Verdoes et al. [64]. The higher the pH the higher the supersaturation [66].

Cheng et al. [67] found that the influence of the initial pH levels of the solution were slight at low pH levels (pH 9) but at higher initial pH levels of 12, the $CaCO_3$ particles formed were irregular aggregates. The loss of morphology control at high pH levels was attributed to the high supersaturation levels of the initial solution. The size of the primary particles also decreased with a rise in pH and is due to the increase in nucleation rate of the primary particles. Although pH levels affected the morphologies, the study also found that all particles consisted of calcite crystals when X-ray diffraction (XRD) was performed [67, 68].

Generally, the pH values of the can be lowered by acid dosing to reduce scale formation, however, this can lead to corrosion problems. Figure 2.12 shows the effect of pH on both calcium sulphate scale and corrosion on a mild steel surface, scale was present at pH values greater than 7 and corrosion increases with a decrease in pH.

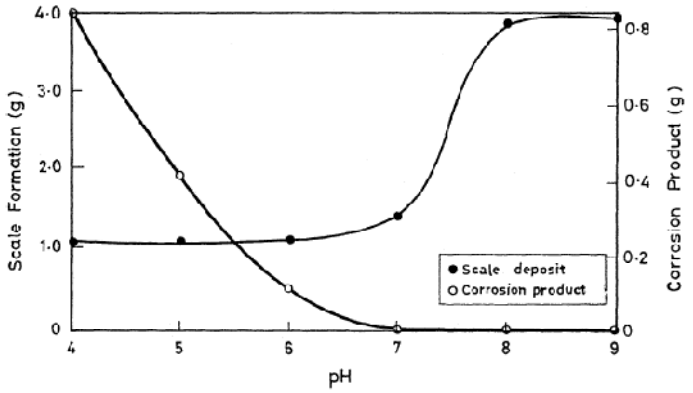

Figure 2.12: : Effect of pH on calcium sulphate scale and corrosion [60]

Monitoring the partial pressure of carbon dioxide is important in managing the behaviour of scaling waters. This is because when spontaneous scaling occurs, the pH rises at the same time by loss of the initial free CO_2 and of the one produced by the hydrogen carbonate ions decomposition [69]. Likewise, an increase in the carbon dioxide partial pressure would cause an increase in the total

carbonate content of solution which is distributed between the chemical species of H_2CO_3, HCO_3 and CO_3 (see Figure 2.11). The degree of supersaturation is proportional to the total carbonate content of the water and the rate of precipitation increases with a rise in supersaturation. Consequently, one of the main causes of calcium carbonate deposition is an increase in the pH of the solution after carbon dioxide evolution [70].

2.6.3 Effect of impurities and water composition

Polymorphism, morphology and structural properties of calcium carbonate can be controlled by the use of specific additives, macromolecules, small organic molecules and inorganic ions [31, 32, 71]. Ionic additives affect crystal nucleation and can also adsorb onto the crystal surface, often inducing the formation of aggregates [72, 73]. Either by inhibiting growth sites of nuclei and thus preventing their growth, or by adsorption on the crystal surface and altering its double-layer surroundings; an increase in the concentration of ionic additive increases the tendency to form aggregates.

Impurities such as Mg^{2+}, Ni^{2+}, Co^{2+}, Fe^{3+}, Zn^{2+} and Cu^{2+} encourage aragonite formation, whereas Mn^{2+}, Cd^{2+}, Ca^{2+}, Sr^{2+}, Pb^{2+} and Ba^{2+} favour calcite. In general, impurities with a small ionic radius and a higher hydration energy than that of Ca^{2+} result in aragonite formation [74]. Among the inorganic components, Mg^{2+} has the strongest influence on $CaCO_3$ precipitation, often favouring the formation of aragonite over calcite. From aqueous solutions containing [Mg]/[Ca] ratios, variously given as 2, 2.5 or 4, calcite is not obtainable by precipitation [75-77]. Mg^{2+} also inhibits the transformation of vaterite and aragonite into calcite [56, 77, 78]. Spontaneous precipitation of calcium carbonates from artificial seawater which contains significant amount of Mg^{2+} always results in the formation of aragonite even if the solution is inoculated with vaterite or calcite [79].

Under certain thermodynamic conditions, magnesium can also act as an effective inhibitor of nucleation and/or crystal growth because of the possible preferential adsorption of strongly hydrated magnesium ions onto the growing calcite surfaces, or by the enhancement of the calcite solubility caused by incorporation of magnesium into the calcite structure. The role of magnesium as a promoter of aragonite formation is closely related to its ability to inhibit calcite nucleation. When the conditions are such that the formation of calcite nuclei is significantly reduced, the nucleation of the less stable polymorph, aragonite, can take place [80]. Figure 2.13 illustrates the effect of Mg^{2+} on vaterite crystals' formation. The chord length of vaterite decreases and the crystals' surface becomes rougher with an increase in Mg^{2+} concentration in solution [81].

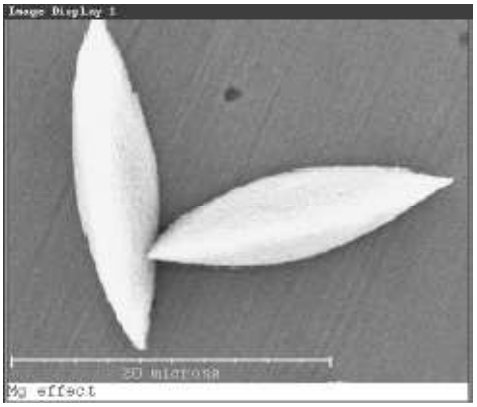

Figure 2.13a: 0 ppm Mg^{2+}

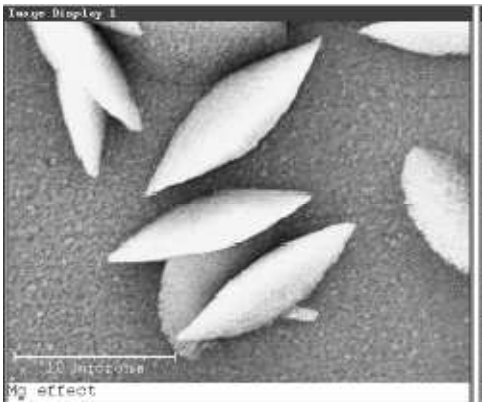

Figure 2.13b: 200ppm Mg^{2+}

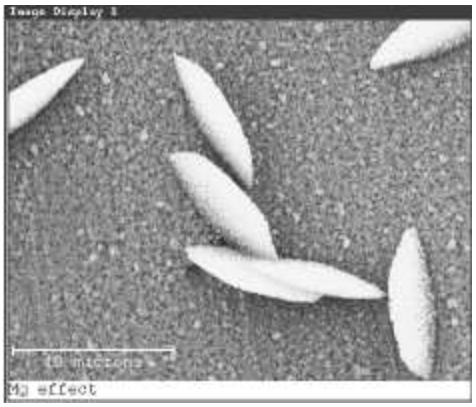

Figure 2.13c: 400ppm Mg^{2+}

Figure 2.13d: 600ppm Mg^{2+}

Figure 2.13: Microscopy of vaterite formed under various Mg^{2+} concentration [81]

When either Mg^{2+} or SO_4^{2-} ions are present in solution, they encourage the formation of spherical calcite crystals, while sulphate ions alone also cause the formation of spherical calcite aggregates [82, 83]. The calcite lattice is most significantly distorted by the presence of SO_4^{2-}, while Cl^- and NO_3^- have a minor impact [80]. Figure 2.14 gives some examples of the effect that combinations of highly concentrated additives have on the formation of calcium carbonate precipitating from solution.

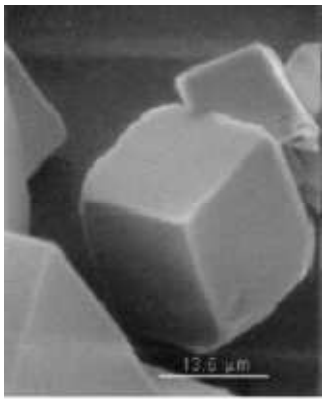

Figure 2.14a

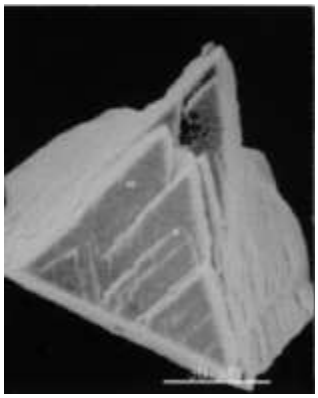

Figure 2.14b

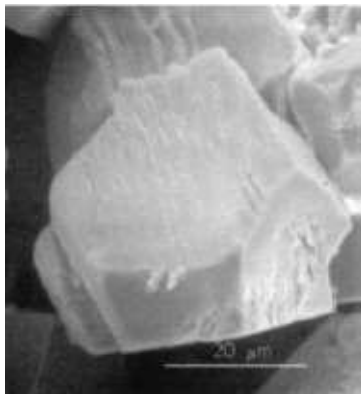

Figure 2.14c

Figure 2.14: (a) Calcite rhombohedron precipitated at $[Ca^{2+}]=[CO_3^{2-}]=50mM$, (b) Modified rhombohedron with Mg^{2+} present, (c) Modified rhombohedron with SO_4^{2-} present [83]. When calcite was grown in the absence of any additives, the standard rhombohedral morphology of calcite was observed, but when either Mg^{2+} or SO_4^{2-} was present in solution, modified rhombohedral crystals were formed.

The nucleation process is also found to be strongly influenced by the hardness of the solution or Ca^{2+} concentration [68]. In this study, the number of calcite crystals drastically increased from a concentration of 120 to one of 200mg L^{-1} Ca^{2+} concentration. In addition, the growth rate of vaterite and calcite crystals on the surface was not influenced by the Ca^{2+} concentration. Other factors being equal, calcite scaling was also found to be more rampant in calcium rich waters than in calcium poor waters in another study [70]. In calcium poor waters, any small activity of precipitation would greatly decrease the supersaturation degree by the depletion of calcium from the solution.

The presence of particles in the process solution can be considered analogous to the introduction of seeds in a crystallisation process. These particles need not be made up of the crystallising material but should have similar crystallographic properties like atomic arrangement and lattice spacing [84]. Depending on the turbulence of the system, some of the particles would be able to settle in the regions where the conditions are not conducive to crystallisation. In a heat exchanger system, the calcium sulphate deposit coverage was found to be 4-5 times higher with particles present [37, 85]. Calcium carbonate fouling was significantly augmented in the presence of low concentration of fine aragonite particles [86]. Nevertheless, in another study on the fouling in heat exchangers, micron-sized particles have been found to be effective in mitigating crystallisation fouling substantially by lowering the deposition rate and by increasing the removal rate [87].

2.6.4 Effect of gas bubbles

In downhole conditions, the gas is flashing from the liquid phase, including CO_2 and this causes a local increase in the pH of the solution, so the concentration of CO_3^{2-} ions in the solution also increases. A study [46] has found that when the gas phase is present, the calcite saturation index required for spontaneous nucleation was lower than the critical value. Most calcium carbonate nuclei were found downstream of the gas bubbles whereas no nucleation occurred under the same conditions when there were no gas bubbles present.

The presence of gas bubbles on a surface due to boiling conditions or the release of CO_2 from the supersaturated water would enhance scaling [15, 88]. A typical supersaturated solution contains aqueous CO vapour (carbonic acid) generated by the chemical reaction of dissolved calcium and bicarbonate ions.

The release of CO_2 from supersaturated water involves a heterogeneous reaction between vapour and liquid phases due to the effect of CO_2 partial pressure. The CO_2 partial pressure falls off rapidly at the interface region of the liquid phase as shown in Figure 2.15. The release of CO_2 results in a sharp increase in pH, accelerating or promoting nucleation in the liquid region of the interface. Once a small bubble is attached on a heat transfer surface, scale crystals are significantly deposited around the bubble. The phase interface between gas and water might have played an essential role in forming nucleation seeds and subsequent growth of scale crystals. The axial flow around the bubble carries the nucleation seeds to the area downstream of the bubble.

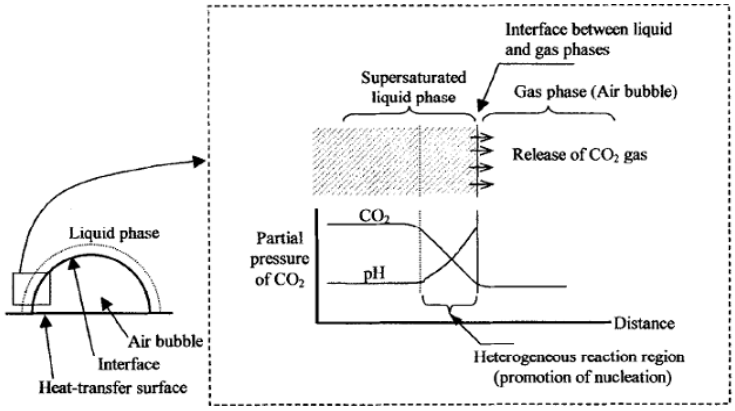

Figure 2.15: Illustration of an accelerated nucleation region at the interface between gas and supersaturated liquid phase [88]

Similar to the study undertaken by Dawe and Zhang [46], most calcium carbonate nuclei appear downstream of gas bubbles whereas no nucleation occurs under the same conditions when there are no gas bubbles present. There are two reasons for the generation of nucleation sites: local pH increase in water around a gas bubble and the onset of nucleation as nucleation catalysis. When a gas phase

was present, the calcite saturation index required for spontaneous nucleation is lower than the critical value for the case without the gas phase.

In general, it is believed that when bubbles form on a heat transfer surface, the solution becomes supersaturated at the gas/liquid/solid interface and deposits form. If the foulant is an inverse soluble salt, the deposit will remain on the heat transfer surface; however, if the foulant is very soluble, it will redissolve as the bubble leaves [89].

2.6.5 Effect of oxygen concentration

The nucleation rate of calcium carbonate increases with oxygen concentration [55]. At a low 5% oxygen concentration, vaterite crystals are seen but with a different morphology than that of the vaterite spherulites obtained at a higher oxygen concentration of 20%. At an oxygen concentration greater than 50%, only calcite was observed.

2.6.6 Hydrodynamic effects on fouling

2.6.6.1 Films and boundary layers

When a fluid flows past a solid surface there is a thin region near the solid-liquid interface where the velocity becomes reduced owing to the influence of the surface. This region, called the ‘hydrodynamic boundary layer’ δ_h, may be partially turbulent or entirely laminar in nature.

A fully developed turbulent flow consists of a turbulent core where the mean velocity is essentially constant, and a boundary layer near the solid/fluid interface. This is illustrated in Figure 2.16. Most of the changes in fluid stress, turbulence, mass transfer and fluid interaction with the wall take place within this boundary layer. The diffusion boundary layer is significantly thinner than the viscous region of the hydrodynamic boundary layer, generally by a factor of ~100 [90]. The mechanism of fouling on heat transfer surfaces can be controlled by either molecular diffusion within this film or by chemical reaction at the surface, or by both mechanisms.

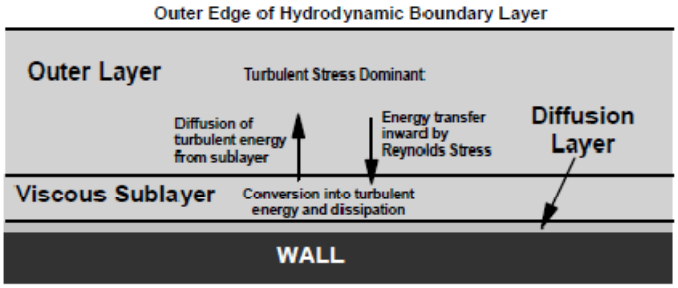

Figure 2.16: General structure of the turbulent boundary layer [90]

For mass transfer processes another boundary layer may be defined which is the mass transfer or diffusion boundary layer, δ_m. This is a thinner region close to the interface across which, in the case of a laminar hydrodynamic boundary layer around the crystal, mass transfer proceeds by molecular diffusion [38]. Under these conditions, the relative magnitudes of the two boundary layers may be estimated from $\frac{\delta_h}{\delta_m} \approx Sc^{1/3}$ where $Sc = \eta/\rho_s D$ is the dimensionless Schmidt number, η = viscosity, ρ_s = solution density and D = diffusivity.

2.6.7 Fluid velocity

At a heat transfer surface, it is found that the fluid velocity increases inhibition effect and in the absence of inhibitor, increases the fouling tendency which shows that the diffusion of foulant ions affects scaling behaviour. At higher fluid velocity, there will be more inhibitor molecules or ions as well as foulant ions diffusing onto the growing $CaCO_3$ surface [54].

In another study carried out using an electrochemical quartz crystal microbalance with impinging jet, it was found that the local pH increased with the flow rate but was not proportional to the reduction current of oxygen thus suggesting that the true parameter allowing the deposition rate to be quantified is the interfacial pH [53]. In desalination plants, high velocities are recommended to reduce calcium sulphate scale formation due to the high shear stress generated [60].

Flow velocity is usually considered to affect fouling in two different ways. Firstly, higher velocities assist in the transportation of ions to the wall and crystallisation at the wall. Secondly, the removal rate is increased with increased velocities because of higher shear rate at the liquid-solid interface if the hydrodynamic interactions are greater than the adhesive bond between the particle and the substrate [91, 92]. However, the rate of particle removal is dependent on the size and frequency of turbulence bursts. Accordingly, the turbulence bursts generate a quasi-steady updraft over a particle, and the particle will be removed when the lift force overcomes the adhesion force [93].

A study of calcium carbonate fouling on heat transfer surfaces in cooling water systems found that the induction period increases with decreasing initial

surface temperature and fluid velocity [94]. An increase in the surface temperature leads to a corresponding increase in the supersaturation near the heated surface as well as an increase in the reaction rate constant. Both the surface temperature and the fluid velocity have interactional effects on the induction period where an increase in fluid velocity leads to a reduction in induction period while a decrease in surface temperature results in an increase in induction period because of more foulant ions diffusing to the surface. During the induction period, the adhesion strength is weak between nuclei and surface, for low energy surfaces, and the nuclei can be easily removed by a high hydrodynamic force. However, during the post-induction period, the heated surface is already covered with a fouling layer and the adhesion strength is stronger. In this case, the detachment of scale under high hydrodynamic force is not as easy as during the induction period. Moreover, another study has found that $CaCO_3$ scale is more compact and more strongly adhering onto stainless steel specimens while $CaSO_4$ scale is comparatively loosely adhering to the surface owing to its fluffly and loose adherence nature; thus flow velocities that can shear off $CaSO_4$ scales may not necessarily be able to shear off $CaCO_3$ scales under the same conditions [95].

Najibi et al. [96] (Figure 2.17) performed many experiments on calcium sulphate and on calcium carbonate scale deposition during sub-cooled flow boiling in a vertical annulus and found that for the range of flow velocity investigated, an almost linear increase in fouling resistance with time was observed, except during the initial period of the experiments. In addition, the deposition rate was found to be controlled by different mechanisms, depending on flow velocity and surface temperature [96].

High flow velocities can reduce deposition [39, 85, 92] while in other cases they accelerate fouling [94, 97]. Falling scale rates with increasing velocity are commonly found where particulate fouling dominates or where deposits are fragile

and vice versa. Fouling is controlled by molecular diffusion through the sub-layer, by chemical reaction at the heat transfer surface or by both mechanisms. If the fouling process is not mass transfer controlled, the deposition rate should be independent of the flow velocity as long as the surface temperature remains constant. Helalizadeh et al. [98] found that at lower fluid velocities, the fouling process is diffusion controlled while with increasing fluid velocity the mechanism changes to reaction controlled - this is illustrated in Figure 2.18 [98]. The mass transfer boundary layer is thicker at lower velocities therefore fouling is affected by molecular diffusion compared to a thinner boundary layer when the fluid velocity is increased and the mass transfer across the boundary layer no longer affects the fouling rate, giving control to surface chemical reaction.

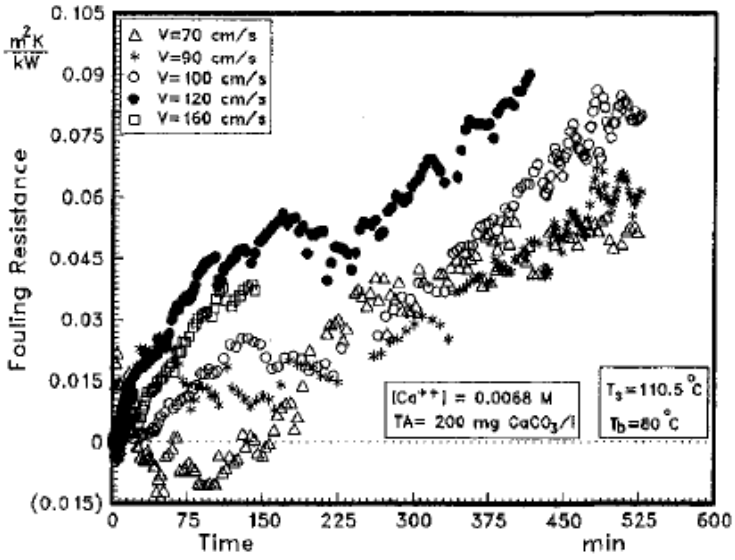

Figure 2.17: Fouling rate on heat transfer surfaces as a function of flow velocity [96]

In another study [85], calcium carbonate scaling showed a pronounced dependence of velocity on rate of scale growth as shown in the log-log plot of Figure 2.19. In the fouling of heat exchangers, the process is considered to be subdivided into two major influences which are (i) the crystallization that depends on the amount of nuclei and growth is the key factor for lower fluid velocities and (ii) with increasing Reynolds number or turbulence, the interaction between surface

and fouling layer becomes more important where adhesion can be considered the key factor [99].

The effect of increasing the Reynolds number on the deposition rate of calcium sulphate on stainless steel surfaces is shown in Figure 2.20. It can be seen that the deposition rate increases linearly in a logarithmic graph with the increasing Reynolds number both for polished as well as pre-scaled samples. According to Levich analysis, the mass transfer coefficient is proportional to the square root of Reynolds number [100]; hence since the gradients of the slopes in Figure 2.20b are close to the theoretical value of 0.5, the results obtained here show that the process was diffusion controlled. A linear trend is observed but in industrial solutions, the deposition may result in non-linear behaviour.

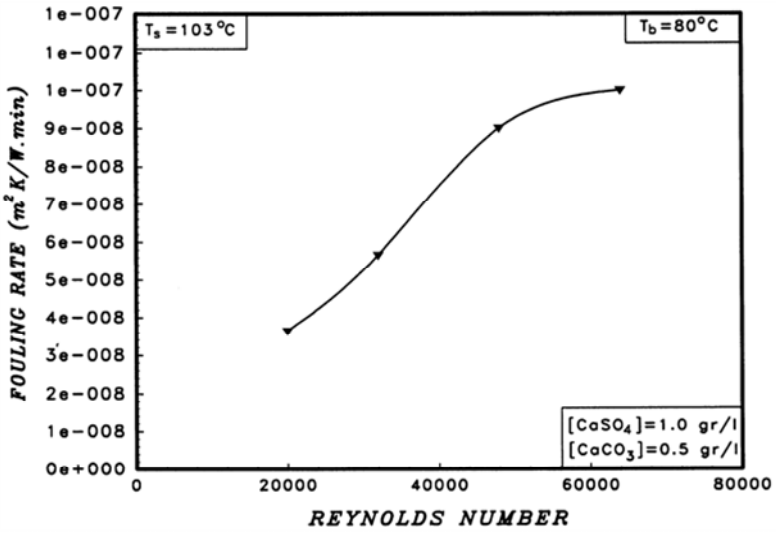

Figure 2.18: Fouling rate as a function of Reynolds number [98]

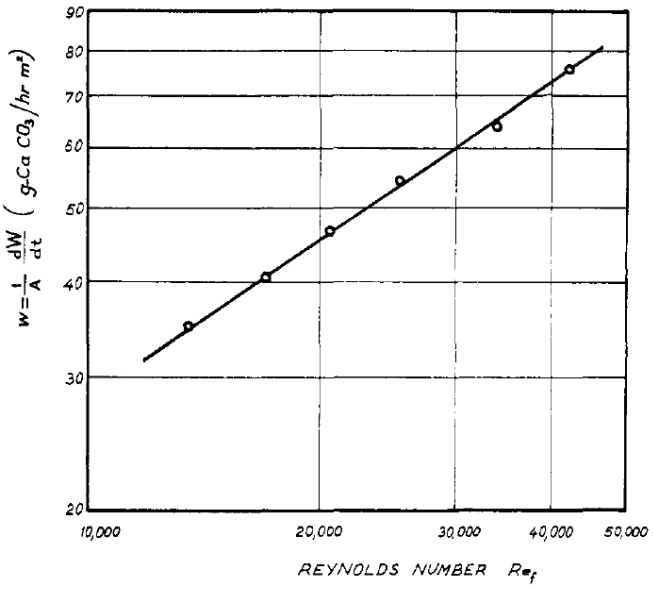

Figure 2.19: Effect of Reynolds number on rate of growth [101]

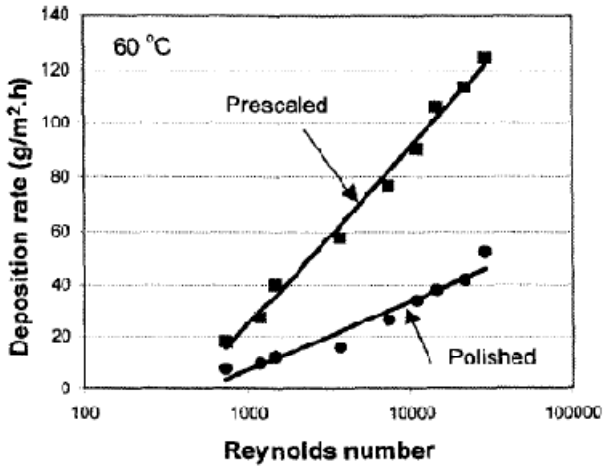

Figure 2.20a

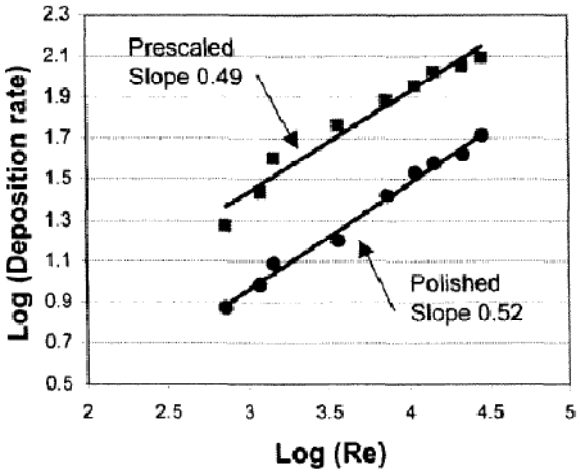

Figure 2.20b

Figure 2.20: Deposition rate of calcium sulphate as a function of Reynolds number [102]

Solution hydrodynamics play a significant role in the scale deposition process, thus it should be included in any scale prediction model or water treatment program for scale control and inhibition.

2.7 Polymorphism of calcium carbonate

Thermodynamically metastable phases are produced in most precipitation systems and these phases – amorphous, hydrates or polymorphs – manifest themselves as a difference in solubility at certain conditions [103]. This complies with Ostwald's Law of Stages where the least stable phase would have highest solubility and would therefore be the first to precipitate and subsequently transform to the more stable phase. There are two possible ways of transformation of the unstable into the stable phase: (1) the solid state transition which is the internal rearrangement of the crystal lattice; (2) the solution mediated transformation which is the dissolution of the unstable phase and the nucleation and growth of the stable modification.

Depending on conditions such as pH, temperature and ion concentrations, calcium carbonate can crystallize generally into three different crystal forms (in decreasing solubility order) - mainly vaterite (hexagonal), aragonite (orthorhombic) and calcite (hexagonal) of which examples of their general forms are shown in Figure 2.21.

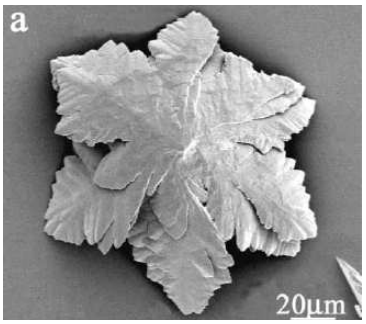

Figure 2.21a: Leaf-like vaterite [104]

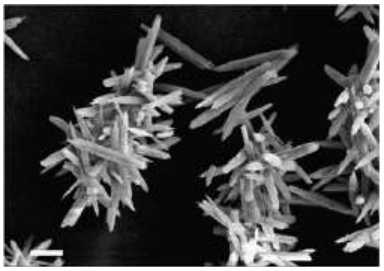

Figure 2.21b: Needle-like aragonite [105]

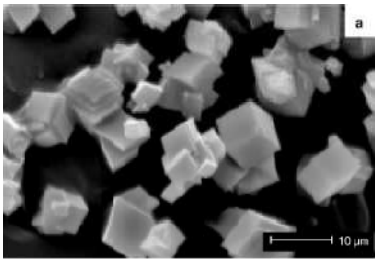

Figure 2.21c: Orthorhombic calcite [80]

Figure 2.21: 3 polymorphs of calcium carbonate

Besides the hydrated salts, calcium carbonate may be found in its anhydrous forms as vaterite, aragonite (of the orthorhombic system) and calcite (of the hexagonal system) in order of decreasing solubility and increasing thermodynamic stability [106]. Supersaturation is a key factor contributing to the stabilization of the polymorphic phases of calcium carbonate [66, 107]. Calcite is the most thermodynamically stable and vaterite the least stable form of the three polymorphic forms of $CaCO_3$. Calcite can be formed from the transformation of aragonite or vaterite in the absence of inhibitors [108, 109]. Vaterite has been found to be the initial phase formed in many $CaCO_3$ supersaturated solutions and then gradually transforms to calcite or aragonite [110].

Several studies on the transformation of the unstable phases (vaterite and aragonite) to the stable phase (calcite) have been reported. Generally, most authors have attributed the transformation to the dissolution of the metastable phase and the growth of the stable phase [111]. However, Bischoff [112] proposed that the nucleation and growth of the growing polymorph occurred on the surface of the disappearing polymorph.

In addition, Ogino et al. [111] reported that the amorphous calcium carbonate phase precipitated from supersaturated solution transforms to metastable polymorphs with aragonite at high temperatures and vaterite at low temperatures by recrystallization. Due to its instability, vaterite irreversibly transforms into more stable forms of aragonite or calcite [103, 113], however, there are some [114] who consider that vaterite is a precursor in every calcium carbonate precipitation.

High temperature (higher than 50°C) and pressure usually favour the formation of dendritic aragonite which has a tendency to agglomerate into rosette particle morphology. Vaterite and dendritic aragonite is the preferred morphology at high supersaturation [56, 115, 116]. On the other hand, calcite nucleates as a rhombohedron in mild supersaturation and moderate temperature such as room temperature [57, 58, 106, 117]. The growth rate is a function of the supersaturation ratio and the number of growth sites on the crystal surface.

Calcite is also believed to be the principal mineral to develop at high salinity and low saturation index (slightly above the critical saturation index) [46]. Furthermore, calcite was preferentially formed each time that a fast nucleation was promoted whatever the experimental parameter varied [55].

2.8 Methods to remove and prevent scale in the oil and gas industry

Most types of scale can be removed using chemical, mechanical, or a combination of both, methods. The method employed has to be non-damaging to the wellbore, tubing or formation environment and effective at preventing scale

formation. In addition, the physical accessibility of equipment and possibility of physical dismantling some downhole equipment has to be accounted for. Furthermore, dismantling the affected equipments can be expensive and would incur a loss of production [4, 18].

In tubes, the strength and texture of scales vary from delicate, brittle whiskers or crystals with high microporosity, to rock-like, low-permeability, low-porosity layers. Scale commonly occurs as a mixture of similar, compatible compounds and seldom as single-mineral phases.

2.8.1 Mechanical removal

Explosives like string shots were one of the earliest scale removal method used to rattle pipes and break off brittle scale [4]. However, such high energy impact loads often damage the walls of tubes and cement structure.

When the scale layer is too thick and non-porous for effective chemical treatment, techniques used for drilling rocks and milling steel are used. Another abrasive/erosive cleaning approach is hydroblasting – such tools may use multiple jet orifices or an indexed jetting head to achieve full wellbore coverage [4, 118]. These tools can be used in conjunction with chemical washes to attack soluble deposits. This type of water jetting is more effective in removing soft scale such as halite than hard scale like barium sulphate and calcite. To improve the ability to cut through scale, a small concentration of solids, 1 to 5% in weight, can be added. Abrasive sand is commonly added and has been found to be very efficient in removing calcium carbonate scale. However, using abrasives like sand and sterling glass beads can erode or perforate the steel tubing. Alternatively, softer abrasives like sodium bicarbonate can be used.

Most mechanical removal methods have a limited range of applicability therefore selecting the correct method depends on the well and the type of scale deposit.

2.8.2 Chemical removal techniques

Chemical dissolution of inorganic scale is usually the first and the lowest cost approach especially when the scaled area is not readily accessible and mechanical removal methods are ineffective [119]. Carbonate minerals are highly soluble in hydrochloric acid while hard sulphate scale has a low acid solubility. In the formation matrix, it can be treated with strong chelating agents; these are compounds that break up acid-resistant scale by isolating and locking up the scale metallic ions within their closed ring-like structure. The efficiency of the chemical technique depends on how well the chemical reagents are able to gain access to the scale surface. In order to affect complete dissolution in a practical time period, the solvent must destroy the crystal structure and stabilize the anions as well as the cations in the solution.

Even though hydrochloric acid is commonly the first choice for dissolving calcium carbonate scale, the acid solutions of scale by-products are good initiators for re-precipitation of scale deposits. Chemicals such as Ethylenediamenetetraacetic acid (EDTA) that dissolve and chelate calcium carbonate can disrupt this re-precipitation cycle but are more costly and slower reacting than hydrochloric acid. EDTA and its variations are also capable of removing noncarbonated scale [120]. Figure 2.22 shows the chemical structures of several commercially used chelating agents.

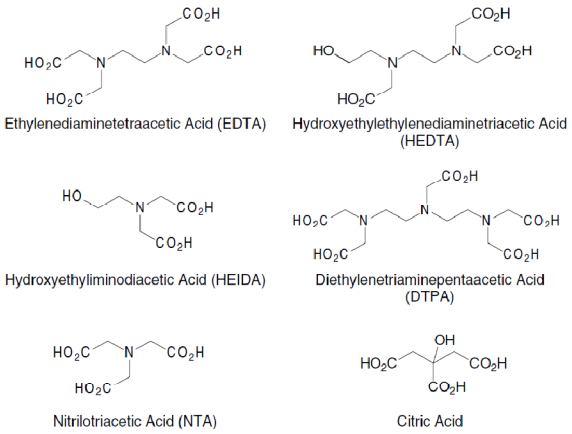

Figure 2.22: Chemical structures of some chelating agents [120]

2.8.3 Inhibition of inorganic scale formation

Inhibition techniques range from basic dilution methods to the more sophisticated and cost-effective methods of threshold scale inhibitors. The threshold effect refers to the ability of organic chemicals at sub-stoichiometric levels to prevent or delay scale formation [121]. For halite precipitation in high salinity wells, dilution is usually carried out to reduce the saturation in the wellbore by continuously delivering fresh water to the sandface and is the easiest way to prevent scaling in production tubing.

There is a whole range of threshold scale inhibitors that basically adsorb onto critical sites on the forming scale crystals and therefore block formation of larger crystals before they contribute to scaling [122]. Such inhibitors effectively inhibit scale formation at concentrations of the order of 1000 times less than a balanced stoichiometric ratio thus considerably reducing the cost. Dispersant-type

chemicals act by preventing any crystals from agglomerating into large clusters and then settling onto surfaces [123].

Most scale inhibitors are phosphate and polymeric compounds: inorganic polyphosphates, organic phosphate esters, organic phosphonates, organic aminophosphates and organic polymers. The inhibitors currently used are phosphonates (PH), phosphino-polycarboxylate acid (PPCA) polymers, polyvinyl sulfonic acid (PVS) and sulfonated polyacylate copolymer (Vs-Co). These inhibitors minimize scale deposition through a combination of crystal dispersion and scale stabilization [124]. Some of the common inhibitors' chemical structures are presented in Figure 2.23.

PPCA is an excellent $CaCO_3$ inhibitor but it cannot remain in solution at high pH or in waters with high calcium. Similarly, some extracts from vegetation and fruit are fairly effective scale inhibitors but not effective corrosion inhibitors [125].

Recently, the focus has shifted more toward environmentally friendly polymer inhibitors. Biodegradable polymers have even been found to be 10 times more effective in delaying the formation of scale such as polyacrylates (PA) [126]. Materials extracted from nature such as polyamino acids and alginates are increasingly being looked at and while amino acids cannot perform as well as synthetic polymers on a weight basis, they are as effective as phosphonates on a molar basis [127].

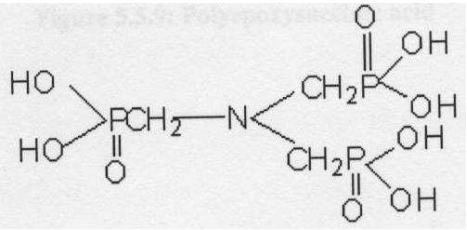

Figure 2.23a: ATMP-Amino tri (methylene-phosphonic) acid [128]

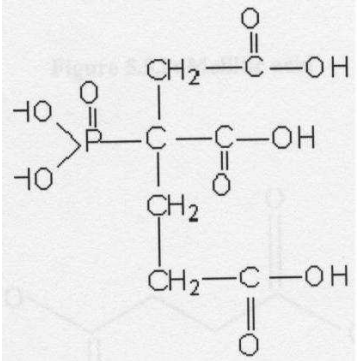

Figure 2.23b: PBTC -2-Phosphonobutane-1,2,4-tricarboxylic acid [129]

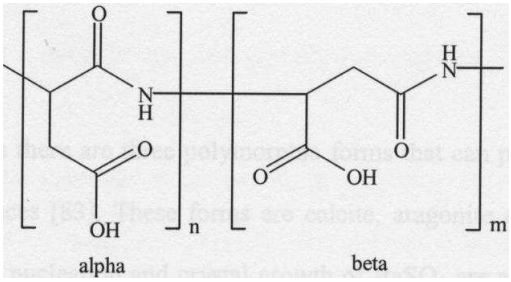

Figure 2.23c: Poly-alpha, beta-D,L-aspartate [130]

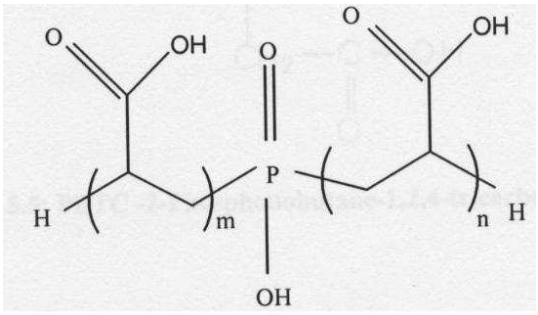

Figure 2.23d: PPCA [131]

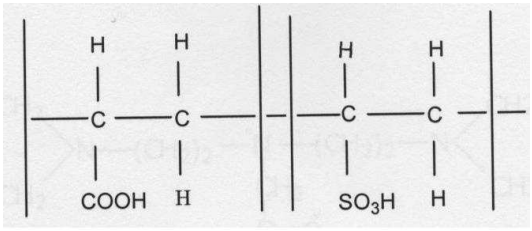

Figure 2.23e: PAA-PVS [132]

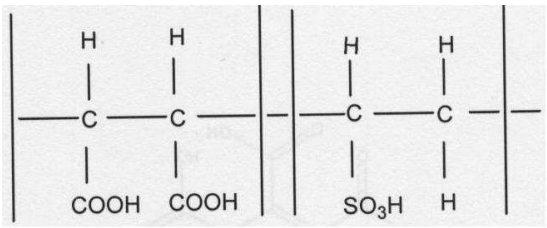

Figure 2.23f: PMA-PVS [133]

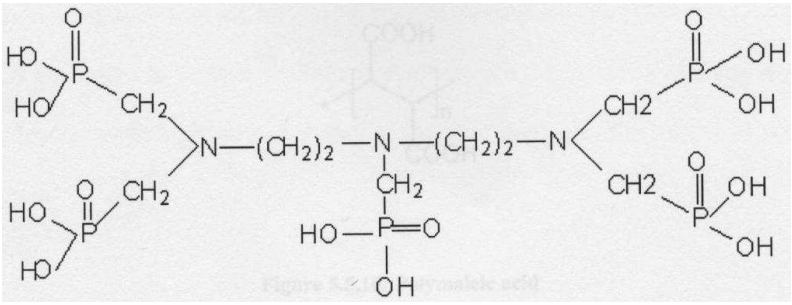

Figure 2.23g: DETPMP-Diethylenetriamine penta methylenephosphonic acid [134]

Figure 2.23: The chemical structures of main inhibitors

Novel polymeric scale inhibitors that possess exceptional scale-control activity with enhanced adsorption properties have been developed and can be stable up to at least 200°C and are effective against $BaSO_4$ and $CaCO_3$ scales [135]. This was observed by incorporating novel “end-cap” technology and the availability of new, patented 1 phosphorous-based monomer species, such as vinylidene diphosphonic acid (VDPA), see Figure 2.24.

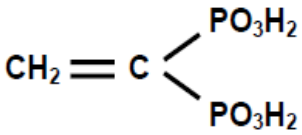

Figure 2.24: Vinylidene diphosphonic acid (VDPA) [135]

Removing one of the ions that causes scale formation is an alternate method that has been carried out. Sulphate can be removed from the injected seawater used for oilfield waterflood operations by a nanofiltration process [136]. Flow assurance was improved because of the elimination of scaling and well souring caused by the conversion of the sulphate to hydrogen sulphide by thermophilic sulphate-reducing bacteria. Sulphate stripping also has been found to be useful in reservoirs with high calcium levels in which calcium anhydrite scaling problems were expected and in a high salinity reservoir where halite scaling would occur. Moreover, since reservoir development has become more complex involving horizontal and multilateral wells, deep offshore subsea wells, sulphate removal is deemed as an extremely cost-effective means to stop scale formation [7].

Nevertheless, regardless of the technique utilised to remove or prevent scale formation, the cost and operation of the system from the initial injection of seawater to the anticipated loss from deferred production have to be analyzed before the actual implementation. Until now, there are many approaches to

remove and prevent scaling with chemical inhibition, chemical scale removers and mechanical methods being the most prevalent ones. Surface modification offers a great potential for controlling scale deposition and in particular can have a profound effect on the initial stages of scale formation. This type of modification can still lose its effect once scale forms on the surface, hence a combination of different approaches such as chemical inhibition with scale control at surfaces can be an interesting alternative to inhibit scaling [18].

Before looking at scale control at a surface, various surface properties such as adhesion, surface roughness, wettability, surface energy and surface chemistry that affects scale deposition on substrates are introduced. Subsequently, a brief overview of surface modifications adapted by various industries for reducing and preventing scale is given.

2.9 Effect of nature of substrate

The driving force for the inorganic scaling of surfaces are surface-specific interactions between solids and liquids, therefore understanding the fundamentals of these interactions is important. Competing interactions between an inorganic foulant, a solid surface and a medium can promote or prevent adhesion. These interactions are also influenced by the properties of the solid substrate such as its surface energy, surface roughness and chemical heterogeneity.

Assuming turbulent flow, the radial temperature profile in a pipe may be represented schematically as shown in Figure 2.25. The scale-liquid interface will be at a temperature T_s, which is higher than the temperature of the bulk liquid T_b. As long as the equilibrium $CaCO_3$ solubility, C^*, at the scale surface temperature,

T_S, is exceeded, an over-all concentration difference ($C-C^*$) will activate the chemical and physical processes leading to the growth of the scale layer [101].

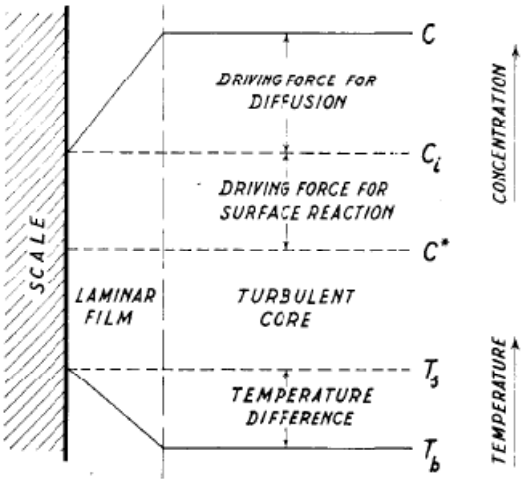

Figure 2.25: Radial temperature and concentration profiles [101]

Different substrates made out of different materials behave differently when exposed to fouling; one such example can be seen in Figure 2.26 where the surfaces are exposed to untreated lake water. This shows the importance of the proper material choice and form of application. Generally the adhesion, morphology and the tenacity to deposit at a surface depends on two classes of parameters: physicochemical variables and surface variables – see Table 2.2.

Table 2.2: Two classes of parameters affecting the nature of the deposit to a surface

Physicochemical variables	Surface variables
Related to the solution from which the deposit is formed – Chemical composition, supersaturation level, temperature and flow field.	Related to the substrate material on which the deposit is attached – Nucleation, adhesion process and crystal growth mechanisms.

It is important to identify and quantify the complex effect that the above parameters have on the fouling mechanisms.

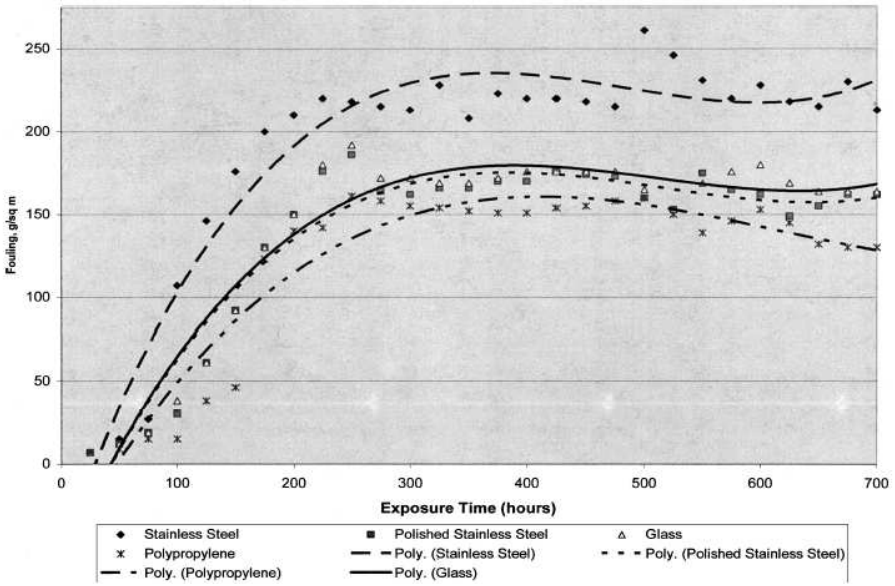

Figure 2.26: A fouling rate comparison of various heat transfer surfaces [137]

2.9.1 Surface Roughness and Wettability

Keysar et al. [138] studied the effect of surface roughness on calcite deposit formation on mild steel and found that the adhesion strength of the fouling layer on the metal surface to be strongly influenced by the degree of surface roughness. It was also observed that the tensile stress required to break away the scaling layer from a rough surface was several times greater than for a smooth surface [138], see Figure 2.27. This concurs with another study of rough and smooth steel surfaces, where rough surfaces were found to have higher fouling tendency when compared with smooth ones [60]. This increase in scaling tendency may be due to the increased contact area for a rough surface thus promoting a stronger adhesion to the surfaces. On a rough surface, it has also been proposed that valleys provide a shelter against removal by shear stress and hills act as nucleation sites [139].

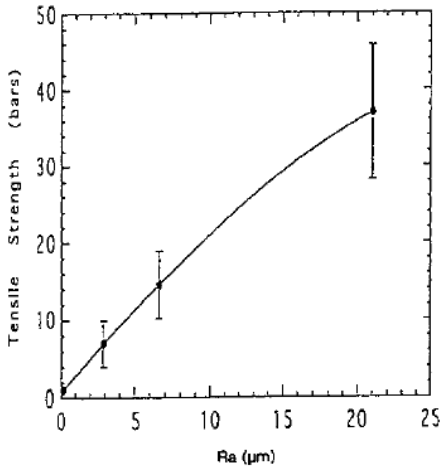

Figure 2.27: Effect of surface roughness (R_a) on calcite layer adhesion strength

Wettability is one of the most important properties associated with a solid surface and is governed by surface chemical composition and the roughness of the solid surfaces. This property is usually measured by means of contact angle measurement. Wettability [140] also gives an indication of the surface energy of the solid surface.

In terms of contact angle between the gas-liquid and solid-liquid interfaces, the wettability of an ideal flat solid is depicted by the Young's equation,

$$\cos\theta = \frac{\gamma_s - \gamma_{sl}}{\gamma_l} \quad , \qquad \textbf{(2.27)}$$

where γ_{sl}, γ_s and γ_l represent the interfacial tensions of the solid-liquid, solid-gas and liquid-gas interfaces respectively. Θ (º) is indicated in Figure 2.28.

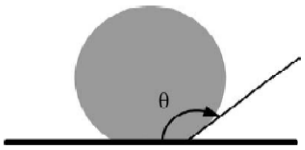

Figure 2.28: Schematic of the definition of contact angle at a solid surface [141]

The interfacial tensions γ_{sl} and γ_s are intrinsic properties that can be controlled by chemical modification. Surfaces can be rendered superhydrophobic when they are micro-textured which is due to air trapped in the structure that gives the droplet a composite surface made of solid and air on which it is resting. A comparison between a droplet on a flat and micro-textured surface is shown in Figure 2.29.

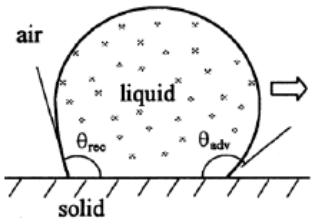

Figure 2.29a: Contact angle on a flat surface

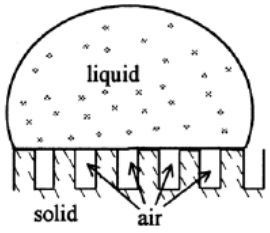

Figure 2.29b: Contact angle on rough surface giving rise to composite interface

Figure 2.29: Contact angle measurement on flat and rough surface [142]

Wetting can be classified into two regimes: Wenzel and Cassie-Baxter. According to the Wenzel equation, the liquid fills up the grooves on the rough surface and the generalized Young's equation were to obtain the apparent contact angle θ_a is

$$\cos\theta_a = r\cos\theta, \tag{2.28}$$

where r is termed the roughness factor and can be found by

$$r = \frac{A_{sl}}{A_F}. \tag{2.29}$$

A_F is the flat projection of the solid-liquid contact area upon a horizontal plane and A_{sl} is the actual area of the rough surface. θ is indicated as the angle in Figure 2.28.

The effect of roughness results in the improvement of wetting for θ<90º but enhances the hydrophobicity for θ>90º, this is illustrated in Figure 2.30. For a very rough surface, a composite interface may form with air pockets trapped in the cavities of the surface (Figure 2.29b). The composite interface consists of the solid-liquid contact area, and therefore decreases adhesion of liquid to solid. For fractional flat geometrical areas of the solid-liquid interface under the droplet, f_1, the apparent contact angle becomes

$$\cos\theta_a = f_1(1 + cos\theta_1) - 1. \tag{2.30}$$

Figure 2.31 demonstrates the effect that surface roughness has on the wettability of water droplets. The water makes the highest contact angle on the higher density micro-structured surface, Figure 2.31c, and the lowest on the flat surface, Figure 2.31a.

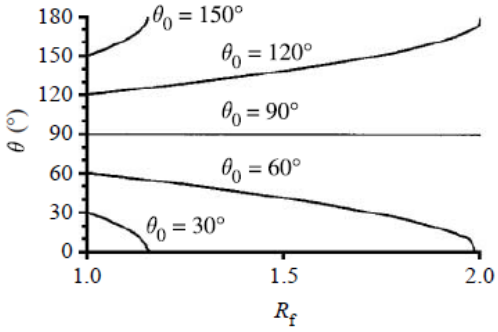

Figure 2.30: Contact angle (θ) for a rough surface as a function of the roughness factor (R_f) for various contact angles of the smooth surface [143]

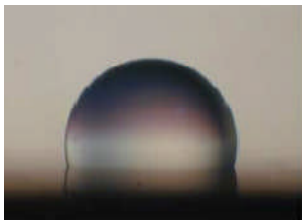

Figure 2.31a: Flat surface

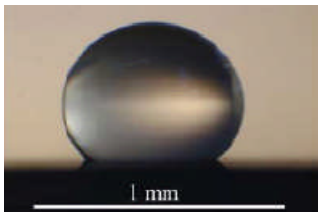

Figure 2.31b: Micro-structured surface

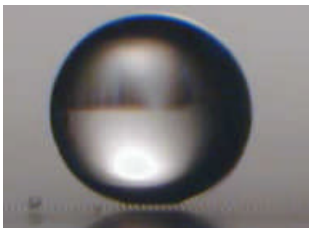

Figure 2.31c: Higher density micro-structured surface

Figure 2.31: Water droplets on surfaces [141]

A study of the effect of stainless steel surface roughness on the contact angle found that the contact angle decreased by increasing the surface roughness and that the calcium sulphate deposit fouling rate at constant bulk concentration increased with decreasing contact angle, this is shown in Figure 2.32. An increase in contact angle is usually associated with a lower surface energy which would result in lower adhesion forces that allows scale to be more easily sheared off by fluid flow or is less feasible to adhere to. The main reason for this is that the nucleation correction factor φ (equation (2.31)) is a function of the contact angle as

proposed by Volmer [144]. As the contact angle decreases, the correction factor reduces causing a drop in the critical free energy as described by equation (2.32). The nucleation rate is directly proportional to the critical free energy as shown by equation (2.33).

$$\varphi = \frac{(2+\cos\theta)(1-\cos\theta)^2}{4}, \quad \textbf{(2.31)}$$

$$\Delta G_{crit}^{het} = \varphi \Delta G_{crit}^{hom}, \quad \textbf{(2.32)}$$

$$J^{het} = Cexp\left(-\frac{\Delta G_{crit}^{het}}{k_b T}\right). \quad \textbf{(2.33)}$$

Enhanced nucleation is more readily apparent on roughness peaks rather than on roughness troughs. This might be attributed to a mass transfer effect; growth on convex points are expected to have mass transfer rates higher than the rates at concave points due to differences in the diffusional boundary layer thickness [138].

One way to produce smoother metal surface conditions is by electropolishing where the metal surface is immersed in an electrolytic solution and acts as an anode. The metallic surface (anode) is surrounded with cathodes, and direct current (DC) is applied to the set-up. Appropriate process parameters such as the composition of the electrolytic solution, current, temperature and treatment time are chosen in order to achieve the erosion of the surface. The erosion occurs preferentially at the peaks and burrs of the surface profile. The chemicals used for this process are usually highly concentrated acids such as perchloric acid, sulphuric acid and chromic acid [145].

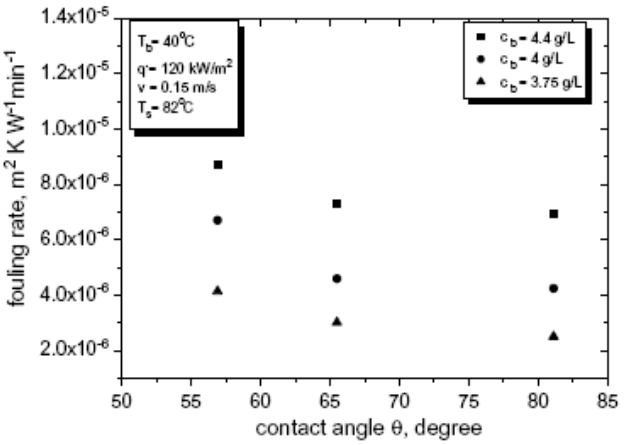

Figure 2.32: Effect of contact angle and fouling rate for stainless steel at various concentrations [146]

According to the Young-Duprè equation [147], the work of adhesion can be expressed as

$$w_{ad} = \gamma_{sl}(1 + \cos\theta_Y), \qquad \textbf{(2.34)}$$

where γ_{sl} is the surface tension of water on the solid surface and $cos\theta_Y$ refers to the contact angle hysteresis which is the difference between the advancing and receding angle. Hydrophobic surfaces that have low adhesion characteristics usually possess low contact angle hysteresis.

Once a thin layer of scale is formed, any subsequent crystal growth on it is accelerated because of the readily available abundant nucleation sites as compared to a polished surface. In addition, the scaled surface becomes sufficiently rough with larger surface area that enhances a deposition process compared to a bare surface [102].

Surface roughness has also been found to influence the induction time. Förster and Bohnet showed that a minimum induction time exists on very rough stainless steel surfaces. Similar trends were observed for other surface materials but not with identical surface roughness [148].

In addition to surface energy, other surface properties, including coating morphology or roughness, and surface charge have significant influence on scale formation and its microstructure. Most real surfaces have roughness on many different length scales, ranging from the macro to the molecular. Normally, each unit area of substrates has a finite number of nucleation active sites and the probability of nucleation depends on the number of free sites. Surface material such as adsorptivity, charge and corrosiveness are surface properties that affect scaling. On the other hand, if the surface presents a microroughness, the minimal number of contact points may reduce the possibility of adhesion since it reduces the contact area between the bodies [149-152]. Surfaces may possess roughness on several length scales, but due to the short range of the van der Waals interaction, roughness at the nanoscale ultimately determines the strength of adhesion [153].

2.9.2 Surface Energy

The surface free energy of a solid or liquid can be considered to be the work required in forming a unit area of a surface. When a new interface is formed, surface molecules attain equilibrium almost immediately due to their mobility. In the case of ion implantation and carbo-nitriding and oxidizing, ions of different material are implanted into the surface layer of a substrate like stainless steel. This decreases the internal surface energy, U^S, but also increases the degree of entropy in the surface S^S. According to the thermodynamic definition of surface energy, given in equation (2.35), this gives a reduced surface energy, γ^S.

$$\gamma^S = U^S - T.S^S \quad \textbf{(2.35)}$$

It has been shown that fouling adhesion is lower and induction times are prolonged in systems that have low surface energies [154-157]. Surface energy on metal surfaces can be reduced with ion implantation whereby elements with weak metal properties e.g. F, C,H, Si, etc are implanted onto metal surfaces causing the number of free electrons on the surface to decrease. In the experiment carried out by Müller-Steinhagen and Zhao [156], the calcium sulphate scale on an implanted stainless steel surface compared to a bare one was comparably more loose and porous which can be broken and washed away more easily [158]. Roques and Girou [74] measured periods of supersaturated $CaCO_3$ solutions held in cells of different materials and found that the induction periods were lowest for polished stainless steel and highest for poly vinyl chloride (PVC) which had the lowest surface energy [74].

There are various ways to lower surface energy, this can be done by ion-sputtered diamond-like carbon [155], self-assembled monolayers (SAMS) [159], electroless plating surfaces [160] and ion implantation [154].

Diamond-like carbon, also called amorphous carbon hydrogen (a-C:H), is a very common coating to enhance wear resistrance and hardness [99]. In the pyramid of diamond, graphite, and polymer, the surface characteristics of a-C:H coatings can have different rates of polymer, diamond or graphite interactions, this can be seen in Figure 2.33.

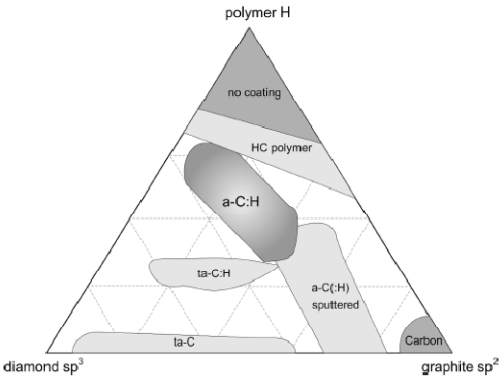

Figure 2.33: Types of carbon based coatings [99]

The increase of silicon inside the coating can lower the surface energy from 40 mN/m (DLC) to 36 mN/m (Si-DLC with 15at% Si) and subsequently to 34 mN/m (SICAN with 33at% Si). Meanwhile, a combination of silicon and oxygen inside the DLC coating can further decrease the surface energy to 21 mN/m (SICON®). Diamond-like carbon coatings with their chemical inertness, high wear and corrosion resistance, good thermal conductivity and adhesion to metal substrate have been successfully applied in many industries. Fluorinated DLC coatings with an optimal surface energy have also been found to significantly reduce scale adhesion [161].

Figure 2.34a and Figure 2.34b show the difference in the calcium sulphate deposit between a F and H implanted heater rods and an untreated heater rod for heating surfaces and equipment. The untreated rod has a thick deposit whereas the ion implanted rod is almost deposit-free.

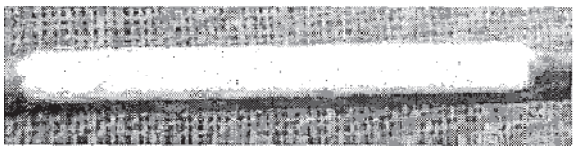

Figure 2.34a

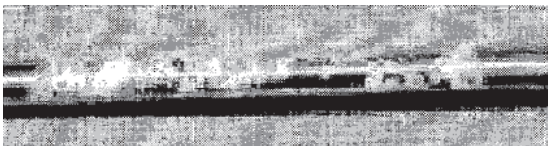

Figure 2.34b

Figure 2.34: Deposit on (a) bare and (b) treated surfaces [162]

Fluoropolymers like polytetrafluoroethylene (PTFE) exhibit a very high melting point and low surface energy – 18.6mN/m, consequently NI-P-PTFE composite films possess high stability and low surface energy [163, 164]. PTFE also possesses excellent non-stick and antifouling properties [165]. A graded electroless Ni-Cu-PTFE composite coating applied on heat transfer surfaces has also been found to inhibit the formation of $CaSO_4$ scale significantly due to its non-stick and corrosion resistant properties [166, 167]. Electroless nickel has shown that it is excellent at protecting parts from corrosion and/or wear. By co-depositing materials such as silicon carbides, ceramics, diamonds and fluoropolymers like PTFE, the scope of electroless nickel can be further increased [168].

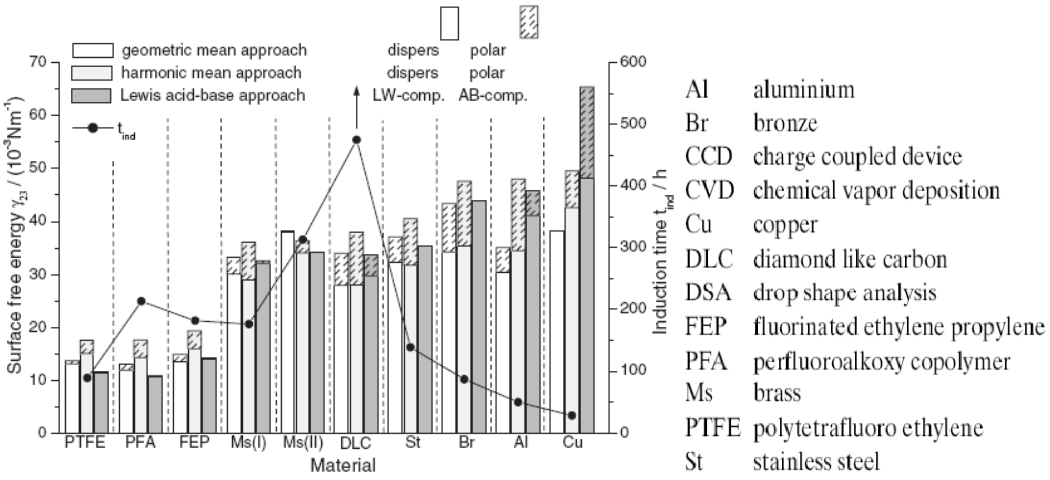

Figure 2.35: Different surfaces with various surface energies along with the induction time [169]

There is no correlation between surface energy and induction time as can be seen in Figure 2.35. Surfaces possessing almost the same surface energy may have various ranges of performance. Nonetheless, both studies found that coated surfaces showed less fouling tendency relative to uncoated surfaces. This is significant as the modified surfaces influence the initial crystallization steps and subsequently lead to different growth behaviour of the overlaying crystals.

On the other hand, there have been studies [155, 170, 171] that negate a direct correlation between surface energy and fouling tendency with respect to induction time, while most of the authors associate a decrease of roughness with an increase of the induction time.

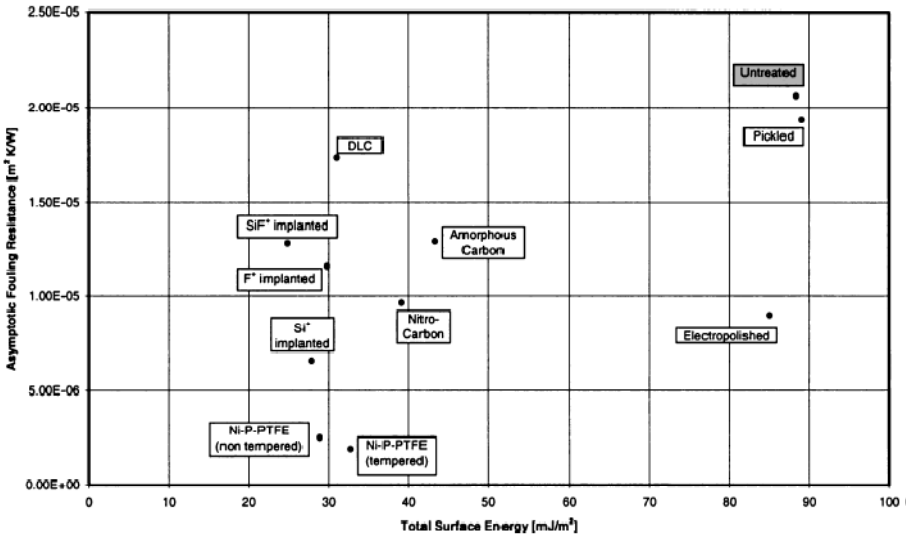

Figure 2.36: Variation of asymptotic fouling resistance with surface energy [171]

Figure 2.36 shows the fouling resistances plotted against the surface energies of various treated heat exchanger plates; there seem to be no obvious correlation between fouling resistance and surface energy. The SiF^+ implanted surface has the lowest surface energy but does not show a great reduction in fouling resistance. Hence surface energy alone is insufficient to describe the fouling behaviour observed.

2.9.3 Surface Chemistry

Studying foulant-surface interactions in the early stages of fouling can provide a useful insight into the initial bonding mechanisms during deposition. One such study [172] found that compositional analysis of clean stainless steel, DLC and Dylyn® surfaces may be used to predict the nature of bonding that occurs during deposition of whey protein in dairy fouling.

The surface chemistry of stainless steel is determined by its oxide layer and when it is exposed to solution surface hydroxides are formed. Therefore interactions with a stainless steel surface is a polar type. On the other hand, DLC surfaces are characterized by C-C and C=C bonding with little amounts of O while Dylyn® surfaces are also DLC coatings with the presence of Si which gives rise to Si-O bonds. For DLC, the bonding would be non-polar in nature and can be non-polar or polar for Dylyn® surfaces. Wide scans of the fouled surfaces showed the main components of C, N and O where N is solely due to the deposit; the results suggested that the deposition mechanisms on Si-doped DLC are different from stainless steel and normal DLC. In addition, it was found that N-C=O, C-N and C-OH bonds were more active in the deposit-surface interface.

In a study to develop better control of calcined hydroxyapatite nanocrystal coatings on biomedical materials, it was found that interfacial interactions between hydroxyapatite nanocrystal coatings and polymer or metal substrates are affected by coating topography such as morphology, surface density and orientation of the HAp nanocrystals [173]. In addition, rod-like HAp nanocrystals adsorbed preferentially onto anionic COOH-modified substrates compared with cationic NH_2 or hydrophobic CH_3-modified substrates. On the other hand, spherical nanocrystals, which had no clear surface plane, adsorbed onto NH_2- and COOH-modified substrates. The adhesion strength between crystal and substrate was

influenced not only by the nature of the functional groups on the substrate but also by the matching of surface roughness between the nanocrystals and the substrate.

2.9.4 Adhesion

Scale adhesion can be described as the molecular attraction that holds the surfaces of two dissimilar substances together [152, 174, 175]. There are many mechanisms that hold surfaces together and these include: mechanical interlocking, adsorption, chemical, electrostatic, diffusion, pressure sensitive and weak boundary layers. Similarly, scale from the bulk precipitate may be attracted to the surface and adhere to it or start nucleating from the surface itself. No distinction has previously been made relating to the adhesion strength of scale as a function of how it originated on the surface. This thesis is primarily concerned with scale that forms on the surface from a nucleation and growth process at the surface.

Real surfaces are rough on an atomic scale and intimate contact occurs only where the asperities on one surface touch the other. It is in these regions that the adhesional and tribological action takes place [176]. Consequently, the strength of the adhesion of small particles on rough surfaces is mainly determined by the geometrical effects of the surface-particle system.

When the particulate material that adheres to the surface is less than 1μm, the net interaction between particulates in a liquid medium and the surface can be described by the classical Derjaguin-Landau-Verwey-Overbeek (DLVO) theory – van der Waals attraction and electrostatic double-layer repulsion. In addition to DLVO forces, there are other types of interactions that play important roles such as hydrophobic interactions in polar media, ion bridging and steric interactions in the

presence of polymers. In biofouling, the adhesion of microorganisms are strongly dependent on their external appendages [152].

In the absence of chemical bonds between particles and the surface, and for systems possessing like sign potentials, the detachment process is diffusion controlled. The rate of entrainment depends essentially on the difference in the magnitude of the potential well at short separations and the maximum of the repulsion barrier [177].

Scale deposition behaviour on metal substrates and on modified metal surfaces can be characterised by six transport mechanisms [178]: (i) Particle motion due to electrostatic forces; (ii) Deposition owing to gravity forces (sedimentation); (iii) Deposition caused by shear dispersion and shear forces; (iv) Brownian diffusion; (v) Transport owing to inertial forces; (vi) Eddy diffusion.

Eddy diffusion will come into play in the turbulent regime where it can keep particles in suspension, especially smaller ones. Electrostatic effects will only have a significant effect on particle transfer when immediately adjacent to the surface where they might contribute to the creation of an energy barrier to deposition. Gravity will play an important part when in horizontal pipes and surface equipment as it causes the deposits to settle at the base forming sludge. In addition, the crystals will also deposit due to gravity when velocities are low and crystals are large.

At the surface, a number of short-range interactions occur which can create an energy barrier to deposition. Such an energy barrier will either produce a

deposition rate lower than that expected from the rate of particle transport to the surface or prevent deposition entirely due to a sufficiently high energy barrier.

In an attempt to relate the theoretical works of adhesion and scaling rate, no correlation could be found when all materials were placed on a single plot [179]. However, it was determined that the theoretical work of adhesion between calcite and a series of materials was found to be influenced by surface topography or their polar surface free energies or both, depending on the physical and chemical homogeneity of the surface. For scaling tests carried out on stainless steel that were modified to increase their roughness, roughness-induced interaction was the dominant factor that controlled the rate of calcium carbonate scaling for these materials. For non-metal and metal surfaces with average roughness, R_a, values below 100nm, calcite adhesion was determined by the polar contribution of the free energies. Analysis of material properties showed the γ^- component had the greatest effect on scaling rate, while γ^+ values had no effect, where γ^- is the electron donor (Lewis base) parameter and γ^+ is the electron acceptor (Lewis acid). It was also found that wettability dictated the thermodynamic work of adhesion that may also control the rate of calcium carbonate scaling. Among the materials compared, amorphous carbon coatings from the non-metals and polished stainless steel from the metal group were the least adhesive according to contact angle measurements. It is believed that materials with low adhesion require a balance between good water wetting behaviour and long-term film stability following exposure to aggressive liquids such as naturally hardened water.

Many studies have shown that surface roughness affects adhesion and friction forces [180-183]. Moreover, a surface roughness of just a few nanometers is sufficient to remove the adhesion between clean and (elastically) hard solid surfaces [184]. In this work, a test was devised to measure the adhesion force between an aragonite surface and different substrates as a means of establishing

whether there is any scope for predicting the tendency for scaling using a relatively quick screening method.

Figure 2.37 shows the adhesive forces for the various structures shown in Figure 2.38, measured using a 15μm radius borosilicate tip.

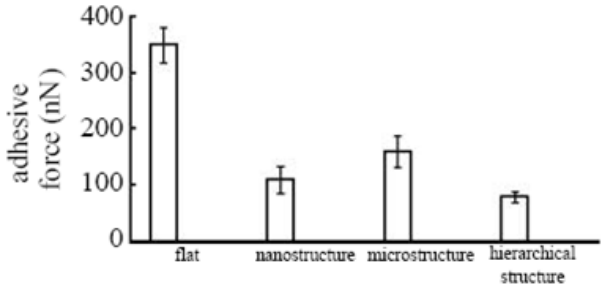

Figure 2.37: Adhesive forces for various structures [181]. The adhesive force for surfaces with hierarchical structures was found to be the lowest among those examined.

In another similar study [185], surface nano-patterning with Ni nanodot arrays (Figure 2.39a) was investigated for adhesion and friction reduction of contacting interfaces. The study showed that between a 100μm radius diamond tip and ordered Ni nanodot patterning, the adhesion forces and coefficients of friction were reduced up to 92% and 83% respectively in comparison to smooth silicon surfaces. The influence of surfaces with hierarchical structures on wettability and adhesion forces has been examined at by Bhushan *et al.* [143]. They found that the adhesion force of the hierarchical surface structure was lower than that of both micro- and nanostructured surfaces because the contact between the tip and the surface was lower as a result of the contact area being reduced.

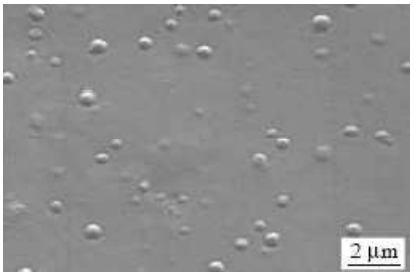

Figure 2.38a: Flat surface

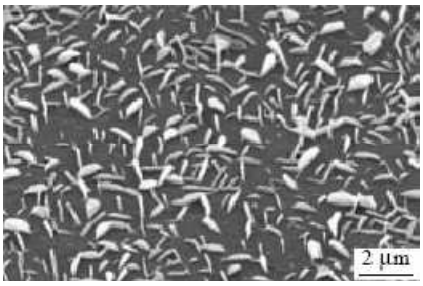

Figure 2.38b: Nano-structures

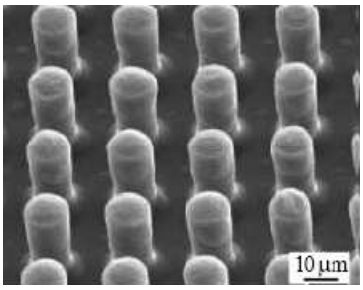

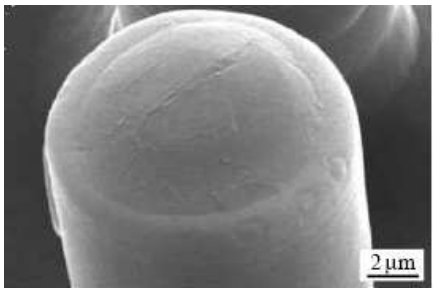

Figure 2.38c: Micro-structured surface

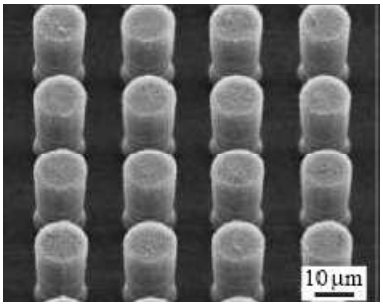

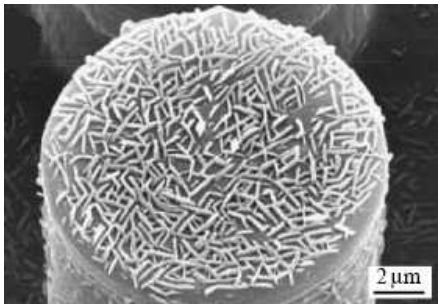

Figure 2.38d: Hierarchical structured surface

Figure 2.38: SEM micrographs of flat, micro- and nano-structured surfaces [181].

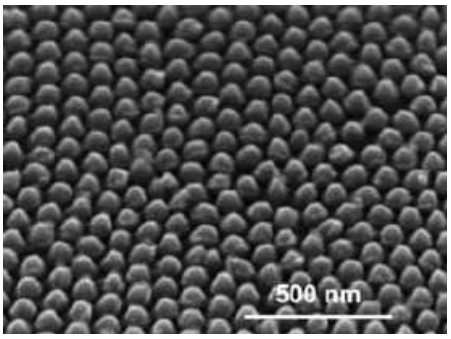

Figure 2.39a: SEM of the Ni nanodot-patterned surface

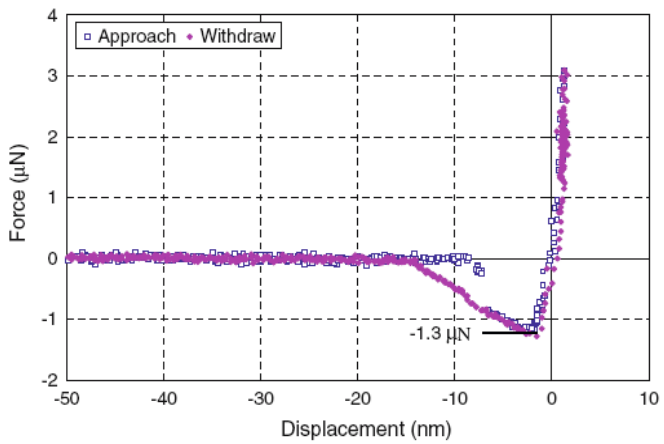

Figure 2.39b: Force-distance curves for nanodot patterned surface

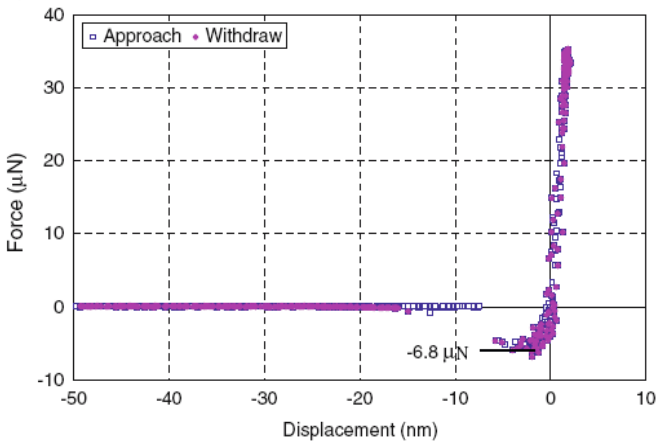

Figure 2.39c: Force-distance curves for a smooth Si(100) surface

Figure 2.39: Comparison of adhesion forces between Ni nanodot-patterned surface and smooth silicon surface [185]

The Si(100) surface (Figure 2.39c) had an adhesion force of 6.8μN compared to an adhesion force of 1.3μN (Figure 2.39b) for the nanodot patterned surface. The pull-off force is proportional to the effective radius of the contacting partners and the surface area in contact which explains the difference in adhesion.

This above mentioned study is of interest as the polymer substrates used here in this work have similar micro- and nano- structured characteristics (Figure 2.40) and carrying out adhesion tests could give a reasonable measure on how surface topography and roughness affect the deposition of calcium carbonate from solution.

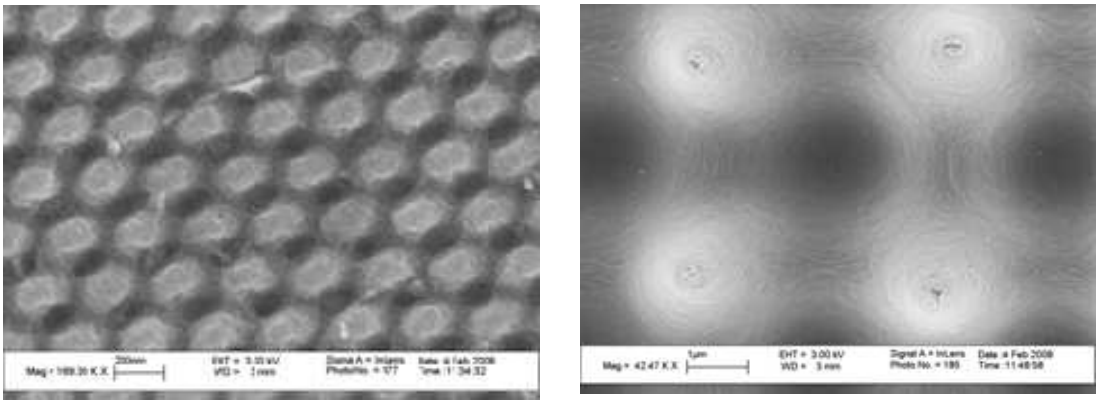

Fig. 6a: Polymer with nanostructures

Fig. 6b: Polymer with microstructures

Figure 2.40: SEM images of two polymers used in this work

Another type of surface is one coated with vertically aligned carbon nanotubes – a nanotubes forest can act as an effective non-stick workbench for the manipulation of micro-objects and fibre/wires with one or more dimensions in the nano-range (see Figure 2.41) [186]. This type of surface exhibits very low static and dynamic friction, the small contact area between objects and the nanotubes forest results in a low adhesion force. It was found that the adhesion of micron-

sized latex beads and organic nanofibres are extremely small for the carbon nanotubes forest compared to other surfaces such as gold, DLC thin films and even Teflon! Although no deposition of crystalline deposit tests were carried out on the nanotubes, it can be seen that when a surface possesses a certain level of structure and roughness, it can affect adhesion to a large extent.

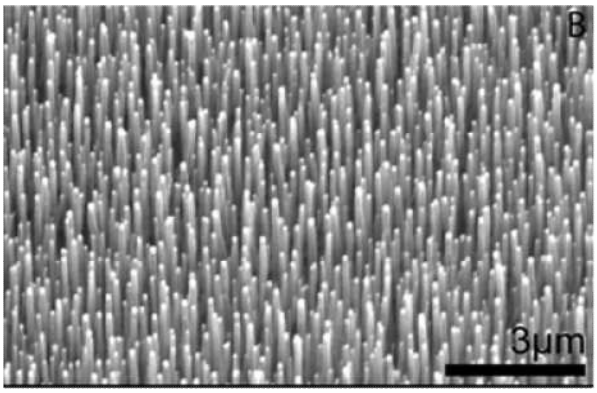

Figure 2.41: SEM micrograph of a typical carbon nanotubes forest [186]

2.10 Scale control at surfaces

2.10.1 A look at other industries

Surface fouling deteriorates the performance of various equipment such as evaporators, condensers and reverse osmosis membranes, which are used in desalination and power generation plants [15]. Inorganic fouling is present in water purification, wastewater treatment, desalination, power generation and chemical plants while biological fouling is present in the majority of aqueous processes. Precipitation fouling occurs if the ionic species in the solution are transferred by diffusion and/or bulk transport to the solid surface followed by crystallization of insoluble species at, and their further attachment, to the surface [14].

The mechanism of deposition for both precipitation and particulate fouling is diffusion. For precipitation it is the diffusion of ions while for particulate fouling, it is the diffusion of colloidal particulate matter to the surface. The attachment stage is controlled by the precipitation rate for precipitation fouling and by Van der Waals forces, electric double layer and Born energies for particulate fouling [15].

The oil and gas sector is not the only one facing the problem of scaling, other industries such as geothermal plants, desalination plants, heat exchanger and cooling water systems and even in the marine industry are also affected. The influence of the nature and surface state of the substrate plays a major role as scaling is usually initiated by heterogeneous nucleation.

Industrial crystallization processes, especially cooling crystallization processes often suffer from fouling or scaling. High levels of supersaturation near metal surfaces are generally considered as the main cause for scaling which mainly takes place in the heat exchanging parts of crystallizers resulting in decreasing overall heat transfer coefficients and decreasing production rates. A second consequence is the increase of pressure drop over the heat exchanger caused by narrowing of tubes which can ultimately lead to blockage [187].

The deterioration of heat transfer performance due to fouling is the prime cause for higher energy consumption and inefficiency in many industrial heat exchangers such as those in power plants, refineries, food and dairy industries. For heat transfer surfaces, the typical deposit is calcium sulphate. In geothermal turbines, the most common deposits on the blading system are silica and calcium carbonate [188]. Deposition not only reduces the lifespan but also decreases output efficiency and capacity. Similarly in geothermal plants, extensive scale

deposits in pipelines and pumps would interrupt operations and cause severe problems [189].

Fouling of nanofiltration membranes used in water quality control applications such as drinking water, wastewater, and industrial applications are often inevitable. Dissolved organic matter is the most prevalent foulant in natural and waste waters and the physicochemical characteristics of the foulant such as charge and molecular conformation, directly control the rate of foulant accumulation and the properties of the fouling layer. For natural organic matter (NOM), solution chemistry also controls the charge and conformation of NOM macromolecules and thus the structure and hydraulic resistance of the foulant deposit layer. Divalent cations, such as Ca^{2+}, may react with organic molecules to form metal-NOM complexes, resulting in a highly compacted fouling layer [183, 190-192].

The outermost parts of most natural surfaces consist of hydrophobic substances, including various lipids, proteins and polysaccharides. A surface that is immersed in the marine environment will be immediately covered by dissolved chemical compounds that adsorb on the surface and evolve to a macromolecular film. The films formed by these substances strongly influences bacterial accumulation. This is then followed by a process of biofouling where the macromolecular film on the surface is colonized by microorganisms, algal spores and invertebrate larvae [193].

2.10.2 Surface modifications employed by various industries to reduce fouling

Another type of surface that has also been proven to inhibit the adhesion of crystallization fouling compared to uncoated copper, stainless steel and carbon steel surfaces is a Ni-P deposited surface, refer to Figure 2.42 [194]. However, it should be emphasized that the minimal adhesion of crystalline deposits may not necessarily correspond to a minimal value of surface free energy.

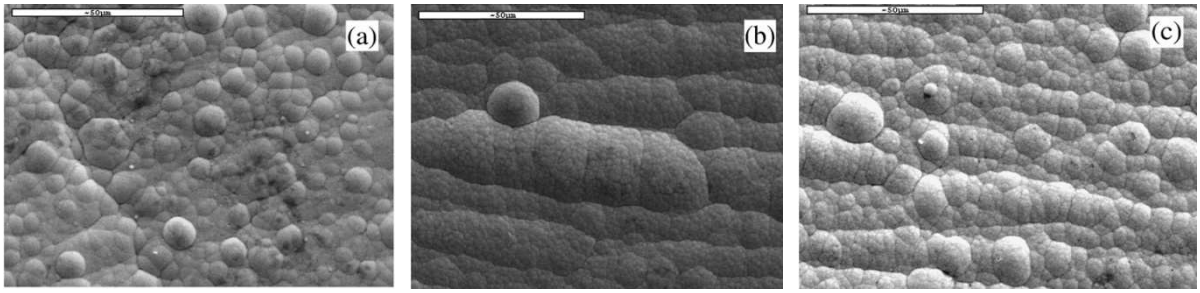

Figure 2.42a Figure 2.42b Figure 2.42c

Figure 2.42: SEM image of Ni-P deposited surface with less amorphous to more nanocrystalline surface from left to right. This type of Ni-P deposited surface was used in heat transfer surfaces in heat exchangers. It was found that less fouling occurred on an amorphous surface than a more nanocrystalline surface which corresponded to an increased trend of fouling adhesion with increase of solid surface energy [194].

Likewise, with Zhao et al. [195] who reported that the lowest adhesion of $CaSO_4$ corresponded to a range of surface energy [195]. As seen in Figure 2.43, there is a window of surface energy (20-25mN/m) where the amount of deposit was found to be low.

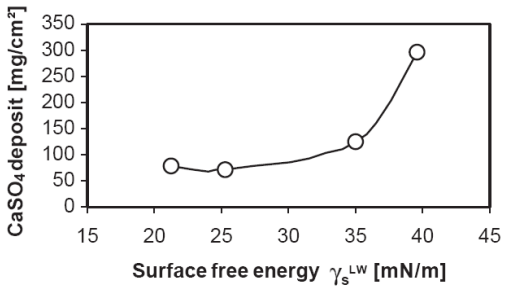

Figure 2.43: Range of surface energy vs. $CaSO_4$ deposit [167]

The above data (Figure 2.43) was obtained from depositing calcium sulphate onto Ni-Cu-P-PTFE composite coatings on stainless steel surfaces. When the surface free energy was approximately 26-30mN/m, the adhesion of $CaSO_4$ was minimal. The amount of deposit was also found to be greater at a lower surface energy of 20mN/m.

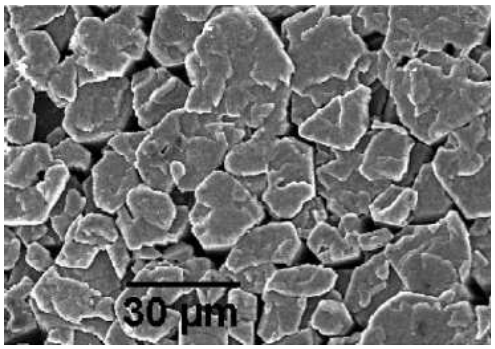

Figure 2.44a: Deposit on stainless steel surface

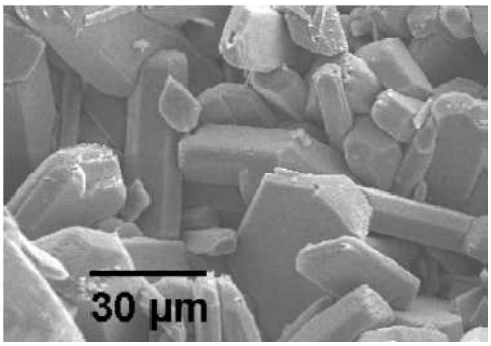

Figure 2.44b: Deposit formed on Ni-Cu-P-PTFE coated surface

Figure 2.44: Difference in $CaSO_4$ deposit formed on bare and coated steel surface [167]. The stainless steel surface here has a higher surface energy of 39.62 mN/m while the coated surface has a surface energy of 26 mN/m.

Figure 2.44 shows that the microstructure of the $CaSO_4$ deposit formed on the stainless steel surface has a packed structure compared to the loose and porous crystal structure on the Ni-Cu-P-PTFE coated surface.

Table 2.3 provides a summary of some of the surface modifications adopted by the marine industry, in heat exchanger and cooling water systems, in geothermal plants and in desalination plants to combat the problem of fouling.

Many attempts have been made to reduce fouling by coating surfaces with PTFE due to its non-stick property. However, the poor thermal conductivity, poor abrasion resistance and poor adhesion to metal substrate of PTFE coatings currently inhibit their commercial use [156].

Coatings have to possess good thermal conductivity, protection of the steel tube against corrosion and oxidation, anti-fouling characteristics and resistance to abrasive wear in order to withstand a harsh environment. In the heat exchanger tubes of geothermal power plants operating at 160°C-200°C, their carbon steel internal surfaces were lined with high-temperature performance poly(phenylenesulfide) (PPS)-based coating systems to inhibit corrosion and fouling by calcium silicate and silica scales [196, 197]; their performance can be seen in Figure 2.45.

Table 2.3: Summary of coatings used in various industries

Marine biofouling	**Heat exchanger surfaces/Cooling water systems/Geothermal plants**	**Membrane filtration/Desalination**
Organic fouling e.g. proteins, bacteria, barnacles, cells, spores, larvae etc.	Inorganic/Organic fouling e.g. calcium sulphate, calcium carbonate, microbes, calcium silicate, silica scales etc.	Organic/Inorganic fouling e.g. mixture of $CaCO_3$ and $Ca(OH)_2$, extracellular polymeric substances and soluble microbial products, magnesium hydroxide etc.
• Ethylene glycol-based surfaces[198] • SAMs with variable composition of hydroxyl- and methyl- terminated alkanethiols (with increasing hydrophobicity)[199] • SAMs made of PEG terminated moieties[200] • Surface topography also plays a role in mechanical defense against macrofouling on a larger scale, hindered by surface structures in the form of spicules[201] and corrugated surfaces[202-204] like the figure shown below[205]. 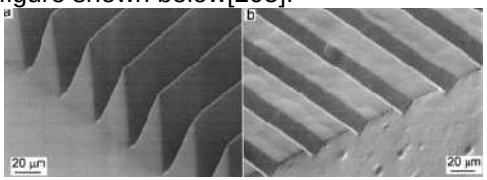 • Adhesion strength related to the number of attachment points of the marine organism on the surface[206]. •	• Ion implantation e.g. F, Si and H[158]. • Ion sputtering with DLC, TaC and TaC-F[158]. • Self-assembled monolayers (SAMs) are ultrathin, well-defined, ordered organic films formed on a solid surface by adsorption of amphiphillic organic molecules from solution, exposing hydrophobic groups to the atmosphere. They possess low surface energy and protect metals against corrosion[94]. One example is copper modified heat transfer surface with Cu-DSA (copper-docosanoic acid) self assembled monolayer film[159]. • Stainless steel surfaces coated with fluorinated diamond-like carbon (DLC) films to minimize scale formation[167]. • Ni-P deposited onto low carbon steel surfaces by electroless plating technique[194]. • Ni-Cu-P-PTFE composite coatings coated onto stainless steel surfaces[167]. • Lining carbon steel surfaces with poly(phenylenesulfide) (PPS)[196, 197]. • Stainless steel surfaces coated with TiN to minimise fouling against calcium phosphate[215].	• Hydrophilic polymers of polycation and polyanion are grafted onto membrane surfaces[216]. • Increasing membrane hydrophilicity through membrane modification e.g. NH_3 and CO_2 plasma treatments of polypropylene hollow fibres[217, 218]. • Addition of TiO_2 nanoparticles to the casting solution and a precoat of TiO_2 allowed the preparation of 2 types of TiO_2-immobilized ultrafiltration membranes(entrapped and deposited) also used in membrane reactor systems[219, 220]. • Membranes precoated with ferric hydroxide flocs[221]. • Polytetrafluoroethylene (PTFE) membranes coated with polyvinyl alcohol(PVA)[222]. • Several simple, lightly cross-linked quaternary phosphonium- and ammonium-based polymer coatings were found to effectively resist the non-specific adsorption of proteins (i.e., bovine serum albumin (BSA) and fibrinogen (Fg)) from aqueous solution under both static exposure and dynamic membrane fouling conditions. In some cases, their protein-

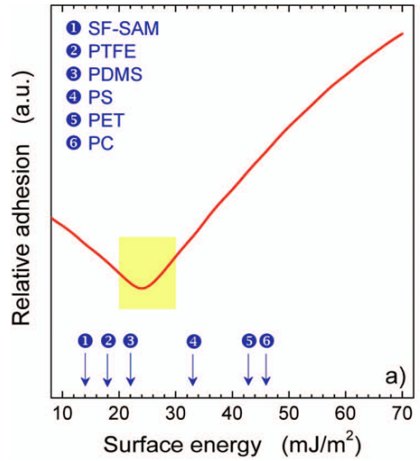 The graph above[207] shows surface energies of typical organic layers and polymers: semifluorinated SAM (SFSAM), poly(tetrafluoro ethylene) (PTFE), poly(dimethyl siloxane) (PDMS), polystyrene (PS), poly(ethylene terephthalate) (PET), and polycarbonate (PC). The yellow area denotes the approximate region of minimal bioadhesion. • Polymeric networks comprising of hyperbranched fluropolymers (HPFP) and poly(ethylene glycol) (PEG), these networks comprised both compositional and topographical structures[208, 209]. • Amphiphilic surfaces[210-213] • Use of silicone fouling release coatings in protecting ships[214].	• The graph above shows when the surface energy was approximately 26-30mN/m, the adhesion of $CaSO_4$ was minimal.	resistance performance is comparable to, or even better than, cross-linked poly(ethylene glycol) (i.e., PEG)-based polymers, which are considered benchmark protein-resistant coating materials[223]. • Epoxy polymers containing phosphorylcholine (PC) groups were prepared by the copolymerization of glycidyl methacrylate and 2-methacryloyloxyethyl phosphorylcholine (MPC), and used as a coating material for an oxygen sensing membrane, in order to protect it against bio-fouling by microorganisms[224].

In the oil and gas industry, the most commonly applied coating and surface modifications are:

- liquid coating comprised of two-part epoxy and polyurethane (PTFE)) [225],
- glass reinforced epoxy (GRE) [226],
- chromium plating, vapour deposition and ion sputtering [227] and
- shape memory polymer that are cross-linked polyethylene pipe produced by mixing peroxide with a polyethylene powder [228].

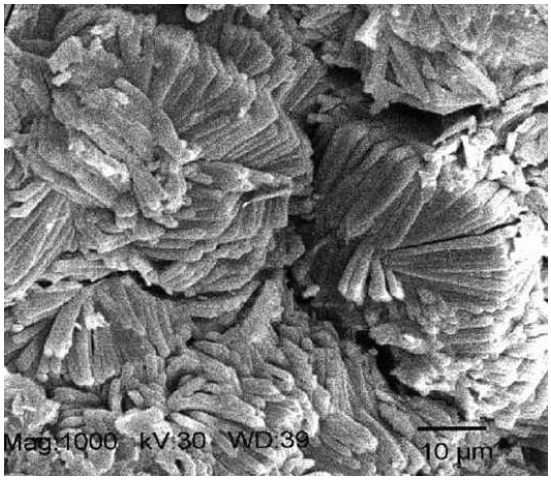

Figure 2.45a: Without coating

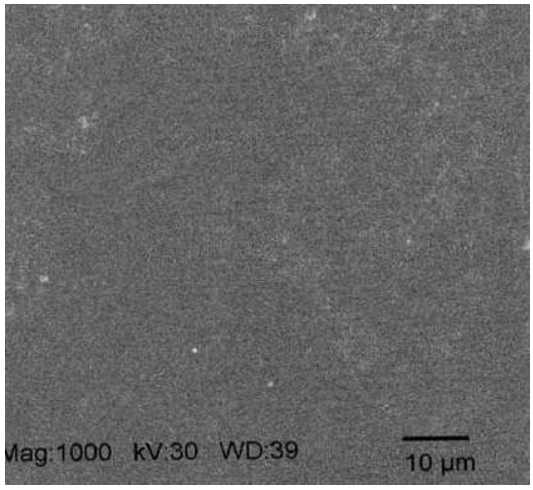

Figure 2.45b: With coating

Figure 2.45: Anti-fouling performance for surfaces with and without coating - neglibible scale formed on the coated surface. This system included the PPS containing polytetrafluoroethylene (PTFE) as an anti-oxidant additive, silicon carbide (SiC) as a thermally conductive filler and aluminium oxide-rich calcium aluminate (ACA) as an abrasive wear resistant filler [196, 197].

Modifying the surfaces slowed the rate of scale deposition and created surfaces unsusceptible to reactions with scales. The main reason for this was due to the segregation of anti-oxidant, hydrophobic PTFE top surface layer above a PPS layer in the coating. Any scale accumulated could be removed by hydroblasting at very low pressures.

In the dairy industry, the mineral deposit encountered is calcium phosphate which is a main mineral component from milk deposits. To emphasize the influence of the surface energy, different stainless steel based surfaces were coated with TiN with a wide range of surface energy values, but similar roughness and qualitative chemical compositions [215]. It was found that the deposition process of calcium phosphate on TiN sputtered stainless steel surfaces, under the laminar flow regime, was found to be characterized by: (1) an increasing relationship between the amounts of deposit formed at 44°C and 70°C with the γ^- value of the surface energy of the different TiN surfaces; (2) a surface reaction coefficient for deposition directly caused by ions that decreases as the γ^- value of the surface increases, meaning that lower energy surfaces are more prone to ion-controlled reaction than the higher energy ones; (3) a particle adhesion coefficient that increases with the γ^- value of the surfaces, meaning that higher energy surfaces are more prone to particle adhesion than the lower energy ones; (4) a prevailing effect of the ion surface reaction in the initial stages and of the particle deposition at longer term. Additionally, the residual deposit mass after cleaning generally increased with the γ^- value of the surface. (Note that γ^- here refers to the electron donor component of the surface energy of a surface; γ^- being the most often used parameter to characterize solid surface.)

Zettler *et al*. [171] applied various surface treatment technologies to heat exchanger plates and ranked their fouling resistance against calcium sulphate. The applied surface treatment technologies for the heat exchanger plates are ion beam implantation, ion sputtering, carbo-nitriding & oxidizing, and Ni-P-PTFE coating. They found that in general, reduced surface energy levels lead to less deposit formed but again, no straightforward correlation could be found. In addition, polished surface had less deposit than roughened surfaces. H^+ implanted plates and DLC-sputtered surfaces did not inhibit fouling to the extent expected from their surface energies.

This complies with other research which found that implantation of the stainless steel heat transfer surface with Si, F and H reduced calcium sulphate scale formation significantly, with the surface implanted with fluorine having the best anti fouling behaviour [162]. This is because when elements with weak metal properties are implanted onto a metal surface, the free electrons on the metal surface and hence its surface energy will be reduced and the probability of scale sticking onto the surface is lowered.

Surfaces act as a catalyst to promote deposit formation directly from the ions that arrive to the surface or attract particles from the bulk to adhere directly onto the surface. Surface properties (roughness, surface composition/chemistry and surface energy) affect the initial adhesion but in the longer term, this distinguishing effect fades out once scale builds up on top of the existing scale layer. However, the surface properties may cause the scale to grow to be more loose and porous and allow easier removal of the deposit.

Not only lattice matching, but also crystal morphology must be important factors to determine the morphology on the surface. Vaterite is spherulite composed of radial crystals and in a study of calcium carbonate onto flat gold surface [229], the shape of vaterite grown on the surface was leaf-like and not spherical or hemispherical which shows that vaterite was unfavourable to be grown on the flat gold surface.

Different types of substrates also exhibit a different tendency to scale. Gold was found to scale faster than bronze and stainless steel when subjected to calcium carbonate scaling. Some of the substrates were also observed to have a delay in scaling due to oxide removal from the substrates [230]. Furthermore, the material of construction such as stainless steel and aluminium influenced only the induction periods, which were longer for the aluminium specimens but the rates of deposition were not significantly different.

Pretreatment of substrates with inhibitor, such as diphosphonates, may cause an increase in induction times and retard the rate of deposition as well [189].

Using an experimental procedure based on the electrocrystallization of calcium carbonate, the growth of calcium carbonate was investigated on several metallic substrates such as soft steel, stainless steel and copper [231]. The results indicated that the nature of the substrate acts on the number of nucleation sites with copper having the most, followed by soft steel and then stainless steel. This could be due to the difference in the degree of supersaturation at the solid-liquid interface. Insulating materials such as Teflon® (polytetrafluoroethylene, PTFE), PVC (polyvinyl choloride) and Plexiglas® (polymethylmethacrylate) were exposed to scaling and the scaling susceptibility of PTFE was found to be about ten times lower than that for other plastic materials [232].

2.11 Surfaces inspired by nature

Functional surfaces with biomimetic texture are becoming increasingly popular because of their great advantages in applications. An example of fabrication of surfaces based on those surfaces of leaves can be seen in Figure 2.46.

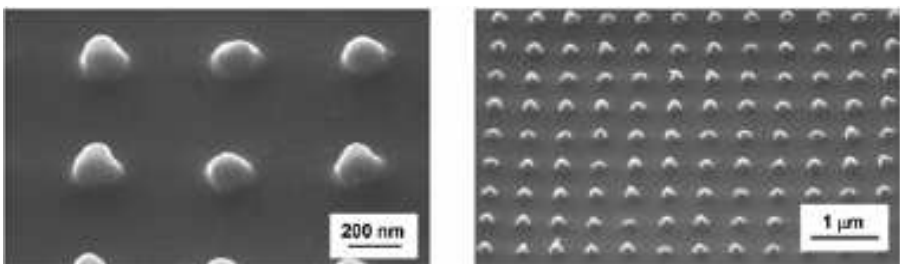

Figure 2.46a: Nanopattern of PMMA low aspect ratio surface

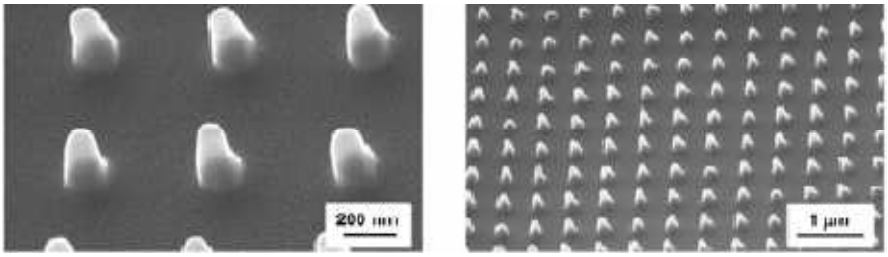

Figure 2.46b: Nanopattern of PMMA high aspect ratio surface

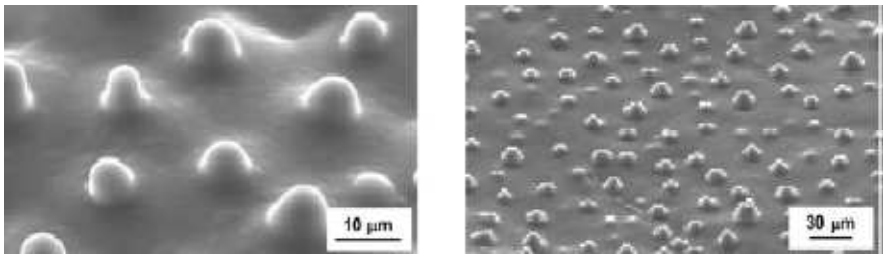

Figure 2.46c: Micropatterned polymer surface of Lotus pattern

Figure 2.46: SEM micrographs of micro- and nano-patterned polymer surfaces [233]

Poly(methylmethacrylate) PMMA polymer was used to fabricate the three types of surface pattern shown in Figure 2.46, low aspect ratio asperities (1:1 height-to-diameter ratio), high aspect ratio asperities (3:1 height-to-diameter ratio), and lotus pattern (replica from the lotus leaf) [233].

Scale control at surfaces may be addressed by surface engineering options. In biofouling, there have been enormous efforts to reduce deposition of marine biological species on surfaces by some really sophisticated surface engineering systems which can release anti-fouling agents at a controlled rate, and decrease the surface roughness and various other mechanisms [19, 234-237]. In scaling, there have been a few attempts at using surface engineering to control scale deposition, except in the desalination industry. Nevertheless, it is fair to say that there is potential for more widespread study and exploitation of potential systems.

Nature provides many extremely interesting surface microstructures and in this thesis, surfaces having the lotus effect structure and the moth-eye antireflective structure are looked at to explore their effectiveness in lowering or preventing scaling tendency.

2.11.1 Lotus effect – Self-cleaning surfaces

The cuticles and waxes of plants play an important role in the cellular structuring and surface wettability by either folding of the cuticle or by forming three dimensional wax crystals on the plant surface [238]. Figure 2.47 is schematic survey of the most significant functions of the plant boundary layer that possesses a hydrophobic micro-structured surface. The list of main functions are (A) Transport barrier: limitation of uncontrolled water loss/leaching from interior and foliar uptake; (B) surface wettability; (C) anti-adhesive, self-cleaning properties; reduction of contamination, pathogen attack and reduction of attachment/locomotion of insects; (D) signalling: cues for host-pathogen/insect recognition and epidermal cell development; (E) optical properties: protection against harmful radiation; (F) mechanical properties: resistance against mechanical stress and maintenance of physiological integrity; (G) reduction of surface temperature by increasing turbulent air flow over the boundary air layer.

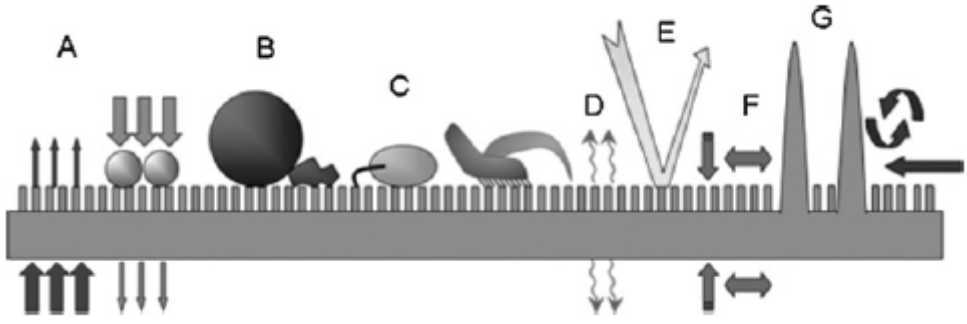

Figure 2.47: Most prominent functions of a plant boundary layer on a hydrophobic micro-structured surface [238]

The lotus leaf exhibits the well-known superhydrophobic behaviour if water drops of macroscopic sizes are placed on the surface. These water drops roll off the surface readily, giving rise to a self-cleaning lotus effect. Other plants that force water to form droplets which roll off at the slightest inclination are cabbage, kohlrabi, nasturtium, beech, oak and gingko, to name just a few [239].

Figure 2.48: SEM micrographs of the Lotus leaf surface at three magnifications [240]

Lotus leaves are a combination of low surface energy species and a peculiar topographic feature based on dual-size roughness: micro-scale mound-like structures protruding from the leaf's surface and nano-scale hair-like structures covering the leaf's surface, this can be seen in Figure 2.48. Water droplets as well as dirt particles only lie on the tips of these rough surfaces and can be easily removed by rain [241].

Rough superhydrophobic surfaces have considerably higher water contact angles because air is enclosed between the surface structures and the contact area between the surface structures and the contact area between water and surface is drastically reduced [242]. Air bubbles are entrapped into micro- and nano-sized pores at the solid surface giving rise to a mixture of solid-liquid and solid-gas interfaces. The extent of contact between a liquid and a rough surface depends on the details of the surface topography [243]; this is illustrated in Figure 2.49.

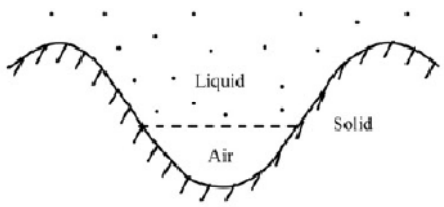

Figure 2.49: Formation of composite liquid-air interface [233]

The extent of solid-gas interface is also proportional to the degree of hydrophobicity of the material. The key is the design of surfaces that can effectively keep the air in place and the amount of air bubbles that are attracted to the hydrophobic surface depends on surface roughness. The rougher the surface, a larger percentage of solid-gas interface will be created. Loss of superhydrophobicity occurs in many way. One being the air may be dissolved in water after a long period of submersion [244].

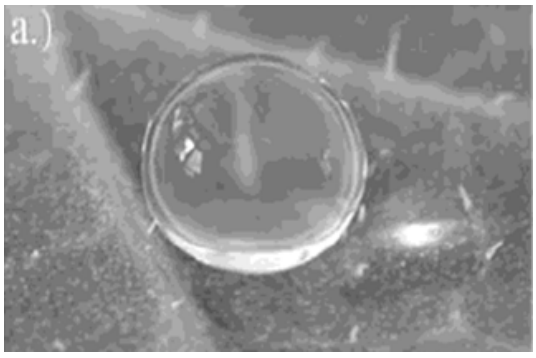

Figure 2.50a: A water droplet (1mm diameter) on an Indian Cress leaf

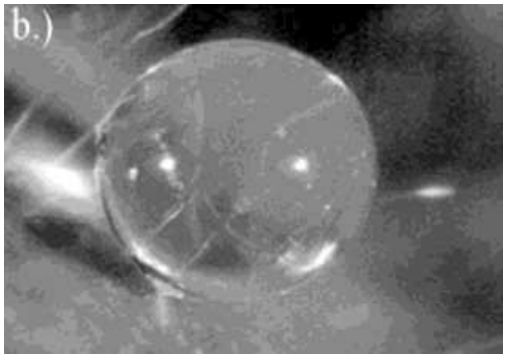

Figure 2.50b: A water droplet on a Lady's Mantle leaf

Figure 2.50: High water contact angles on superhydrophobic leaf surfaces [245]

A surface with roughness-induced superhydrophobic properties should satisfy the following requirements [246]:

- Asperities must have high aspect ratio to provide high surface area.
- Sharp edges should be avoided, to prevent pinning of the triple line.
- Asperities should be tightly packed in to minimize the distance between them and avoid destabilization of the composite interface.

- Asperities should be small compared to typical droplet size.
- In the case of a hydrophilic surface, a hydrophobic film must be applied in order to have initial θ>90°.

All the above requirements are satisfied by biological water-repellent surfaces e.g. leaves. They have tightly packed hemispherically topped papillae with high aspect ratios and a wax coating. Nevertheless, the self-cleaning effect can fail at times when strong water adhesion occurs if the leaf surface loses its nano-scale hair-like structures and when water condenses onto the leaf's surface. Small water droplets can be trapped in the nano-scale hairy regions on the leaf surface and these drops gradually grow or connect to form larger drops. The trapping of water in the hairy region is also possible if the surface of the hairy structures is not intrinsically hydrophobic [247].

There are various applications for superhydrophobic and self-cleaning surfaces such as self-cleaning windows, windshields, exterior paints for buildings and navigation of ships, utensils, roof tiles, textiles, solar panels and applications requiring antifouling and a reduction in drag in fluid flow, e.g. in micro/nanochannels [143].

2.11.2 Moth eye effect

The ability of nanostructured optical surfaces to not reflect light is termed the moth eye effect. For nocturnal insects like moths, this effect would allow them to be less vulnerable to predators as they do not reflect the moonlight [248]. Since the moth flies in the night, it has large eyes and the laws of physics show that 4% of the light incident on the moth's eye will be reflected [249].

The antireflection property is achieved by continuously increasing the refractive index of the optical medium. The little protuberances upon the cornea surface increase the refractive index. These protuberances are very small microtrichia that are approximately 200nm in diameter. In other words, the features on the moth eye surfaces are tapered and this fraction gradually increases from the surrounding medium to the substrate, effectively blurring the interface and thereby reducing reflection across a relatively broad spectral range with reflection increasing at long wavelengths (when the interface thickness is small compared to the wavelength) and at short wavelengths (when structures are no longer subwavelength and are diffractive) [250]. For an increase in transmission and reduced reflection, a continuous matching of the refraction index at the boundary of the adjacent materials (cornea and air) is required. If the periodicity of the surface pattern is smaller than the light wavelength, the light is not reflected [251].

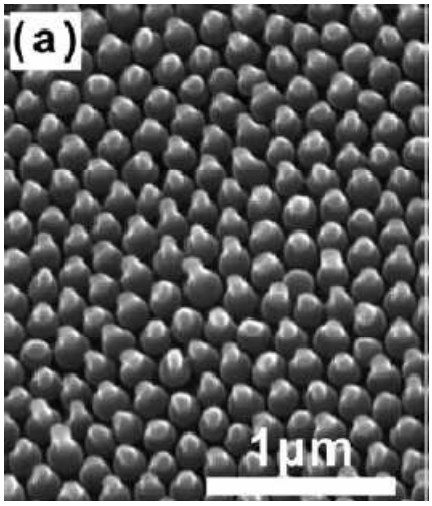

Figure 2.51a: Subwavelength features found on the wings of the moth species *Cryptotympana Aquila*

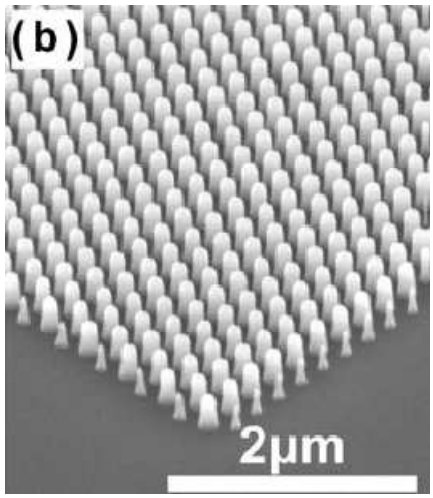

Figure 2.51b: A biomimetic silicon moth-eye surface

Figure 2.51: SEM images of moth eye antireflective surfaces [250]

For protuberances with 220nm depth and the same spacing which are typical values for the moth eye, a very low reflectance is expected for the wavelengths between 440 and 550nm [252]. Since the purpose is to make the structures significantly below the wavelength of light, the typical moth eye has a

period and depth of 200-250nm. It is possible to also create transparent surfaces using the moth eye effect [253]. The moth eye effect involves surface roughness; therefore, it can be combined with the lotus effect, so that self-cleaning non-reflective glass can be obtained. Owing to the recent development in nanophotonics and plasmonics physics, it is now possible to manipulate light at the nanoscale using arrays of nanoparticles [254].

Chapter 3
Methodology

A combination of methods and techniques have been employed to study the formation and characterization of the various surfaces and of calcium carbonate scale formation. They are described in this chapter.

3.1 Reagents

The scaling solutions investigated were based on the properties of typical scaling solutions found in a west Texas oilfield, provided by Baker Petrolite. Brine 1 (containing calcium ions) and Brine 2 (containing bicarbonate ions) were prepared separately by weighing the appropriate quantity of salts of analytical grade and mixing with distilled water, their composition is reported in Table 3.1 and Table 3.2.

Table 3.1: Brine compositions

	Brine 1 (mg/L)	Brine 2 (mg/L)
NaCl	15,367	15,367
CaCl2.6H20	15,743	-
NaHCO3	-	6,046

Table 3.2: Ion composition

	Brine 1 (mg/L)	Brine 2 (mg/L)
Na+	6045	7700
Cl-	14417.4	9322
Ca++	2880.2	0
HCO3-	0	4391.4

$CaCO_3$ was precipitated spontaneously by mixing 500 ml of brine 1 (containing calcium ions) and 500 ml of brine 2 (containing bicarbonate ions) at time, t=0 minute. Before mixing, the two brine solutions were heated up to 70°C and buffered to pH of 6.8 by bubbling CO_2 gas at 100cm^3/min for 20 minutes. The pH of the experiment was kept constant at 6.8 throughout with the addition of NaOH when required. The supersaturation index was calculated with Multiscale and found to be SI=2.33 which would give severe scaling conditions.

After each test, the sample is rinsed with distilled water and dried with compressed air. In order to obtain the scaling tendency, the samples were weighed before and after an experiment with a mass balance (OHAUS Analytical+) having a resolution of 0.01mg.

3.2 Substrates for deposition

Functional surfaces with biomimetic texture are becoming increasingly popular because of their great advantages in applications. This study looks to surface engineering to control scale deposition and polymers with the lotus effect or self-cleaning property and the moth-eye or anti-reflective property are studied. In addition, the scaling tendency of some commercial coatings on stainless steel are also assessed.

3.2.1 Polymer nanostructured surfaces used

All polymer samples were supplied by MacDermid using MacDermid Autotype's PNR process (Precision Nano Replication) which on a roll-to-roll basis presses a sheet of nickel containing the required nanostructure into a coating of a UV-curable material on polyester. Once in contact, UV light is shone through the polyester, curing the material which is then released from the

nickel sheet. This gives faithful replication of nano-scaled high aspect-ratio structures such as the motheye structures used in these tests. Special treatments are provided to ensure that the UV-curing material has high adhesion to the polyester film.

In these tests, the following range of UV-curable materials was used.

MS A typical UV-curable acrylate system

MF MS polymer + fluoro-molecules for lower surface energy

MN MS polymer system containing silica nanoparticles

MSi A UV curable silicone system with lower surface energy

MD A 1.4x deeper/wider structure than the polymer MN formulation

LS A 10x deeper/wider structure than the polymer MS formulation.

Different polymer surfaces and a reference stainless steel sample were used as the substrates onto which $CaCO_3$ scale was deposited. Each polymer sample was wrapped around a stainless steel rotating cylinder electrode that was then rotated at various speeds for an hour. These polymer surfaces were selected because of their unique nanostructured surfaces with varying surface chemistry. Polymer LS exhibited the lotus-effect or self-cleaning property while the rest of the polymers exhibited the motheye effect which are anti-reflective surfaces. A great portion of current research and development is directed towards multifunctional surfaces with properties like scratch resistance, antireflectivity, water and oil repellency, ease of cleaning, low thermal absorption; any combination of these are of great interest. Thus, it is worthwhile to examine these biomimetic surfaces to see if they are inherently anti-scaling as their structures, according to Chapter 2, might suggest. SEM images of the bare polymers and stainless steel surface that was used as a reference can be seen in Figures 3.3 to 3.9.

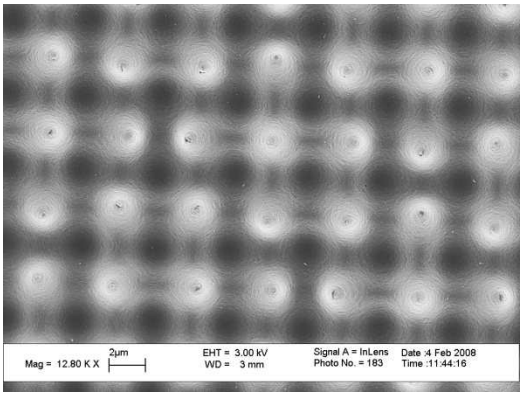

Figure 3.1a

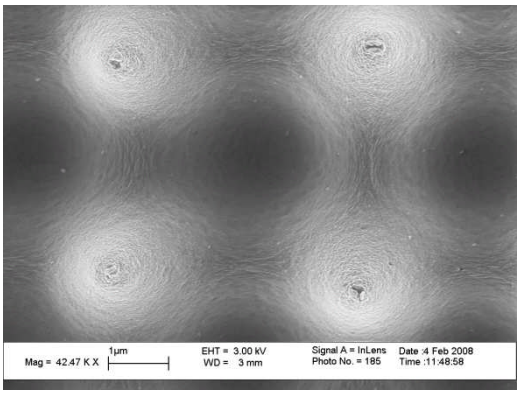

Figure 3.1b

Figure 3.1: SEM image of Polymer LS (top view) - Micro-mounds are approximately 3µm apart

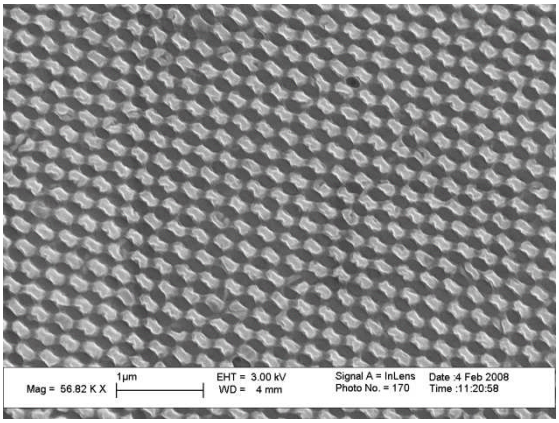

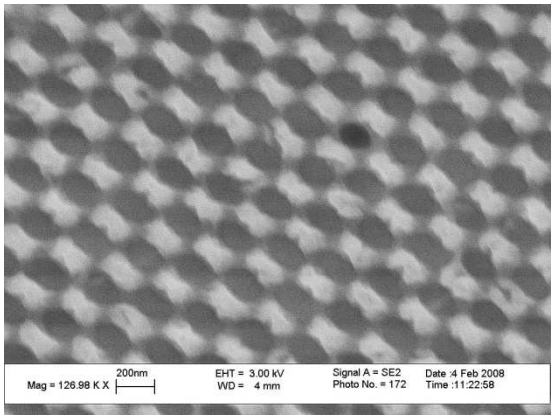

Figure 3.2: SEM image of Polymer MF (top view) – Nanostructures are 250nm apart and regularly patterned

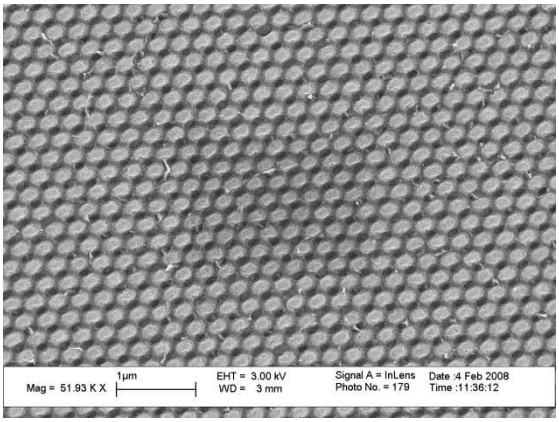

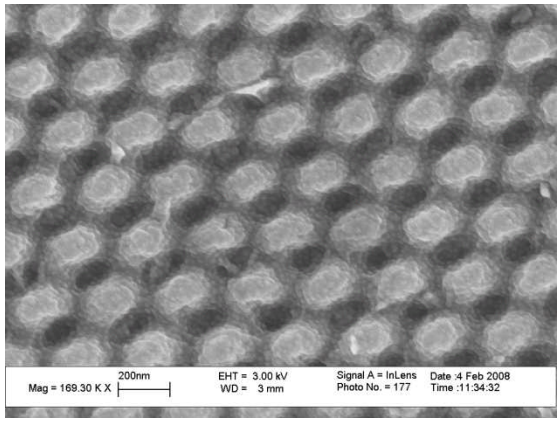

Figure 3.3: SEM image of Polymer MN (top view) - Nanostructures are 250nm apart and regularly patterned. The nanostructures are also covered by nano-silica bumps to render the surface with hierarchical surface roughness.

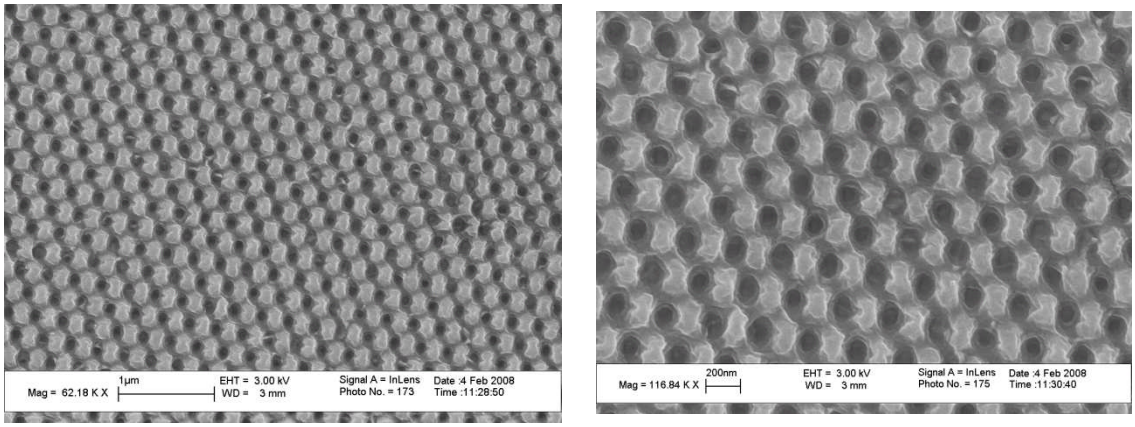

Figure 3.4: SEM image of Polymer MS (top view) - Nanostructures are 250nm apart and regularly patterned.

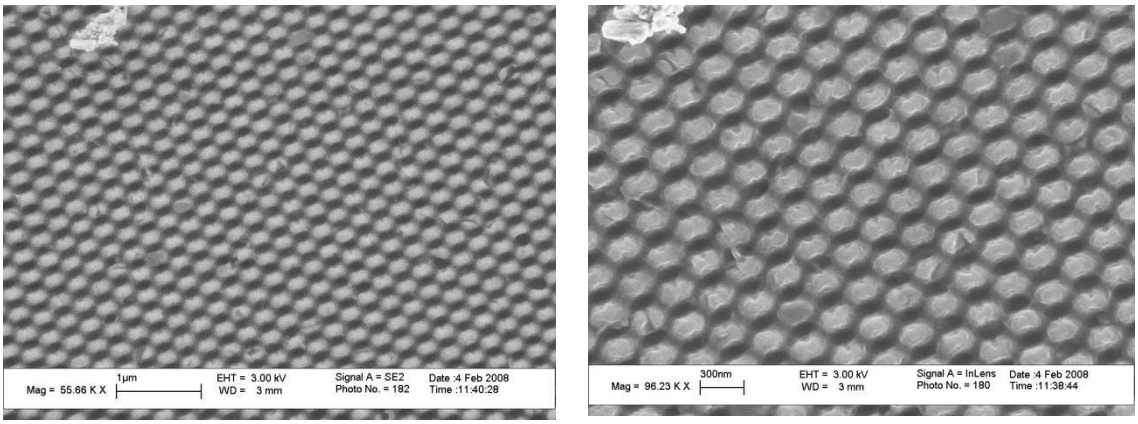

Figure 3.5: SEM image of Polymer MSi (top view) - Nanostructures are 250nm apart and regularly patterned.

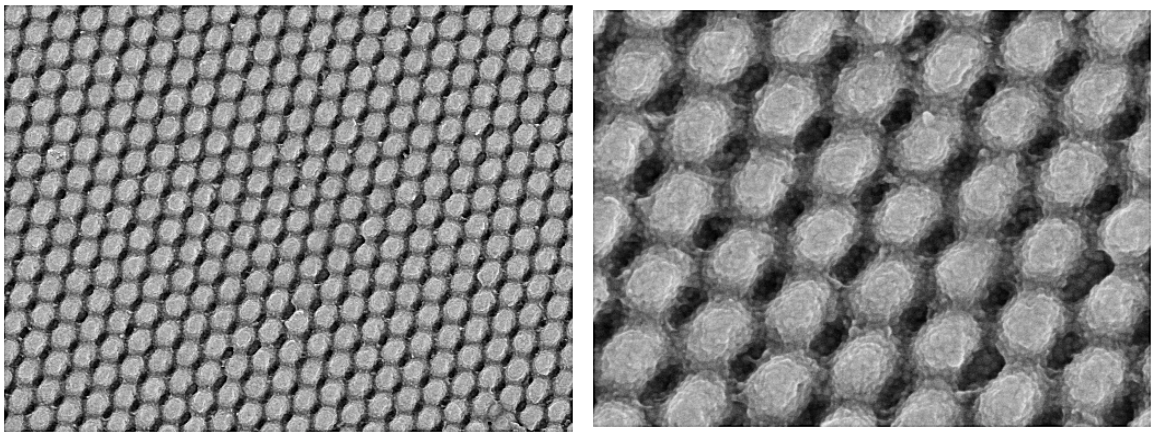

Figure 3.6: SEM image of Polymer MD (top view) – Nanostructures are 350nm apart and 350nm deep.

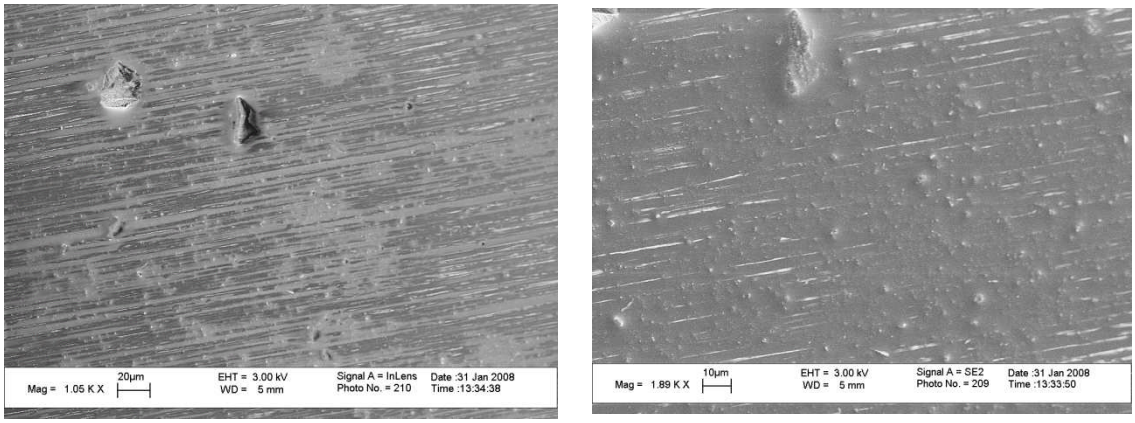

Figure 3.7: SEM image of Stainless steel (top view) – Bare surface used as a reference.

Cross section of some of the polymers can be seen with SEM, shown in Figure 3.8.

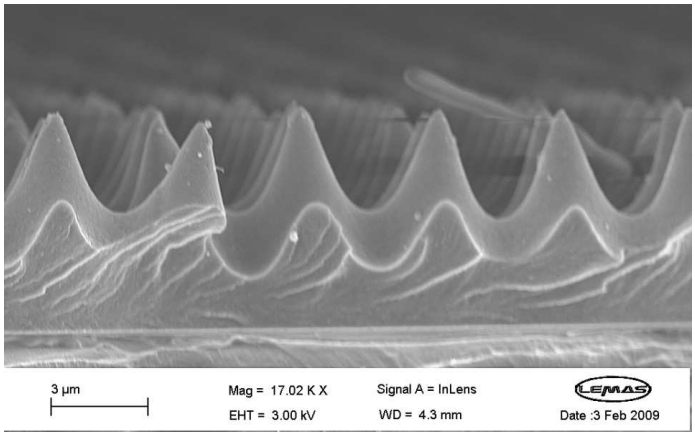

Figure 3.8a: Cross section of polymer LS

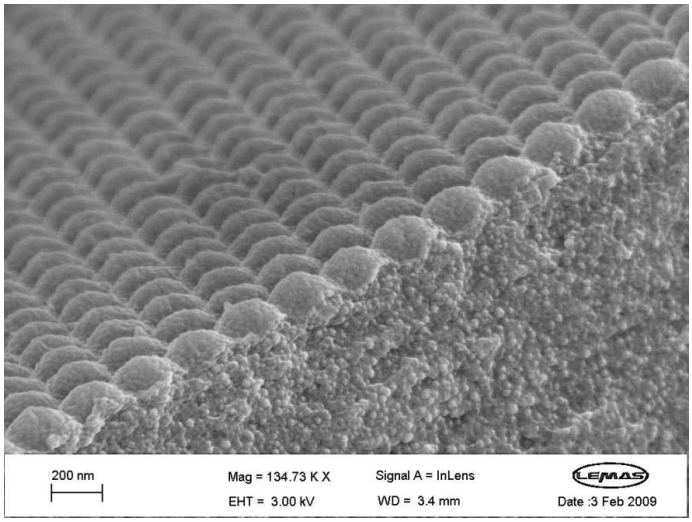

Figure 3.8b: Cross section of polymer MN

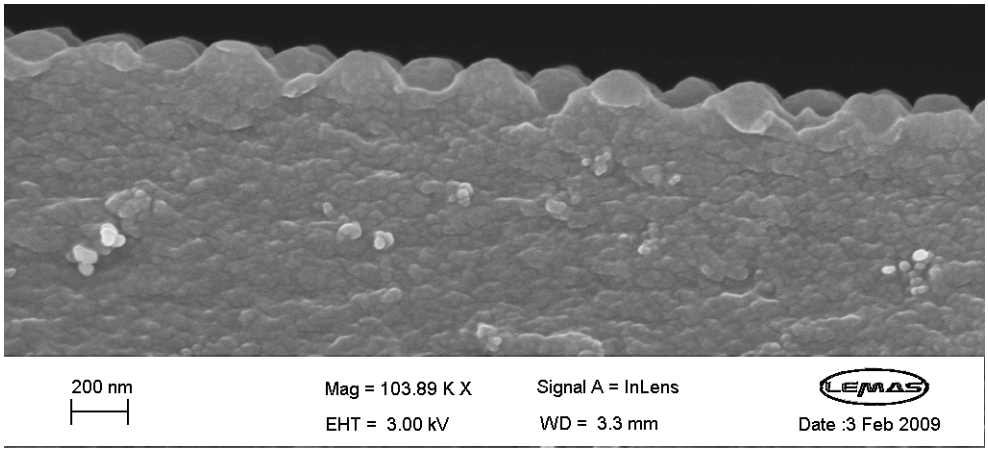

Figure 3.8c: Cross section of polymer MSi

Figure 3.8: SEM image of the cross-sections of various polymers

The contact angle of water on each of these substrates and their measured surface roughness are given in Table 3.3.

Table 3.3: Water contact angle and surface roughness of test substrates

Substrate	Contact angle (º)	Measured surface roughness (nm)
Stainless steel	84º	84º
Polymer MSi	107º	107º
Polymer MS	65º	65º
Polymer MN	77º	77º
Polymer MF	127º	127º
Polymer MD	89º	89º
Polymer LS	107º	107º
DLC	69°	69°
Tech 100	114°	114°
Tech 23	103°	103°

3.2.1.1 Surface chemistry of the polymers

All systems are a UV-cross-linked acrylate system with varying functional groups to alter the surface energy. An acrylate is CH_2=CHCOOR where R can be a simple group such as methyl (making this methyl acrylate and the polymer polymethylacrylate) or a perfluoroalkane or a siliocone or a complex group such as a substituted polyol, so there are multiple CH_2=CHCOO- groups on the same R.

3.2.2 Coatings used in this study

Three new commercially available coatings were introduced in addition to the polymers studied before; they are stainless steel samples coated with DLC, TECH 100 and TECH 23. The DLC coatings were performed by Oerlikon Balzers Coating UK Limited. The coating properties of DLC are given in Table 3.4.

Table 3.4: DLC coating properties

Coating Material	a-C:H
Microhardness	>2000
Friction Coefficient Against Steel (dry)	0.1-0.2
Max. Service Temperature	350

BALINIT® DLC is suitable for the most extreme wear conditions and high relative speeds, even when running dry. The coating gives excellent protection against abrasion, tribo-oxidation and adhesion. The coating permits surface pressures that, under normal conditions, would lead at once to scuffing and cold welding. Friction losses are reduced to a minimum. The good corrosion resistance protects the substrate from destructive attack. The coatings are

approximately 0.5μm – 3μm thick; SEM images of them are shown in Figure 3.9.

The Tech 100 PEEK™ and Tech 23 coatings were produced by Bodycote Metallurgical Coatings Ltd. TECH 23 is a composite ceramic material made up of individual chromium oxide (Cr_2O_3) ceramic particles which are sub-micron in size and consist of mixtures of selected ceramic materials bonded together and to the substrate. Tech 23 is an almost totally dense (>97%) ceramic coating and has no open porosity. Tech 23 processing completely seals off open porosity, making the part impervious to most chemical attack. In addition, Tech 23 is resistant to thermal cycling/shock and can withstand 30% $CaCl_2$, 90% H_2SO_4. The thickness of the coating ranges from 50.8μm – 101.6μm. SEM images of Tech 23 coating are displayed in Figure 3.10.

Tech 100 PEEK™ polymer coating is a linear, aromatic and semi-crystalline thermoplastic. It is a high performance material with non-stick properties and improved mechanical performance up to 260ºC continuous use in demanding corrosion and temperature environments. It also possesses electrical resistance, chemical resistance, dimensional stability and low permeability/moisture adsorption. Furthermore, it displays low moisture absorption and excellent hydrolysis resistance. SEM images of the Tech 100 coating can be seen in Figure 3.11.

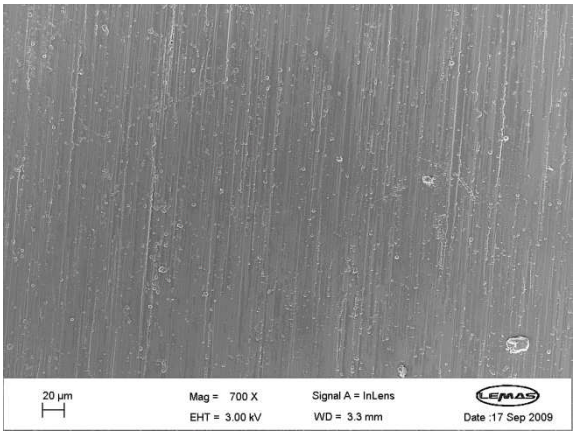

Figure 3.9a

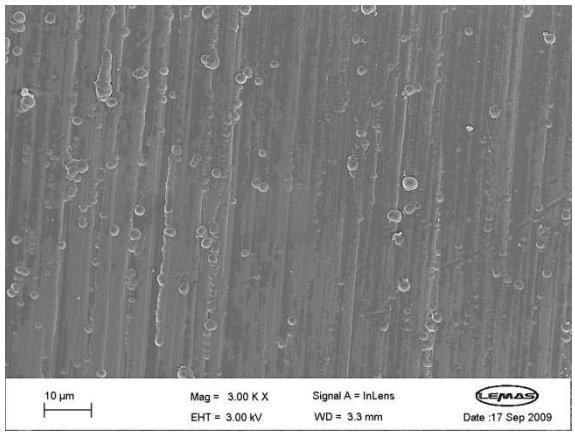

Figure 3.9b

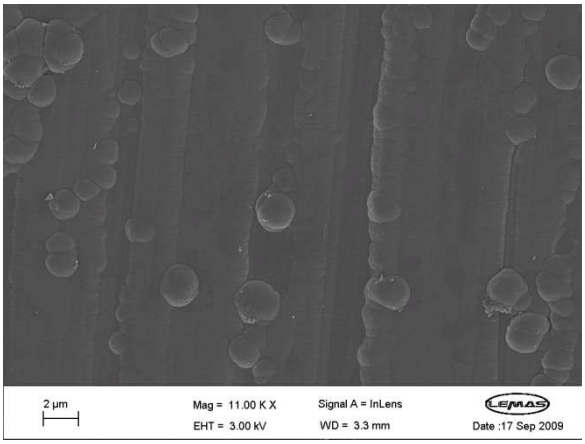

Figure 3.9c

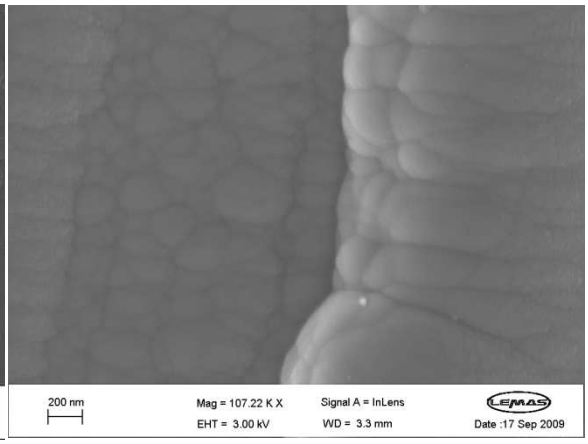

Figure 3.9d

Figure 3.9: SEM images of DLC coated stainless steel surface at different magnifications.

The DLC coating is characterised by having parallel grooves that following closer inspection are littered with nanobumps while the Tech 23 coating does not seem to have a uniform layer and exhibits a high surface roughness.

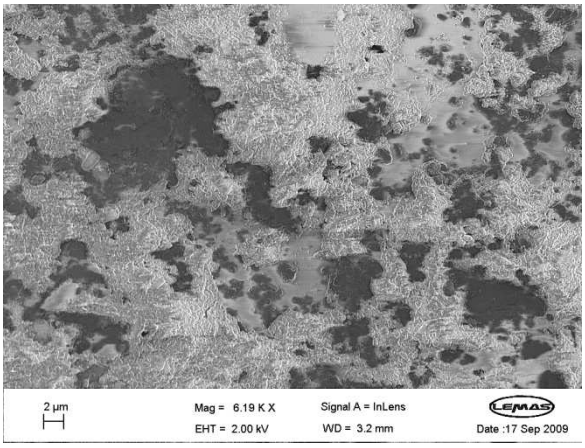

Figure 3.10a

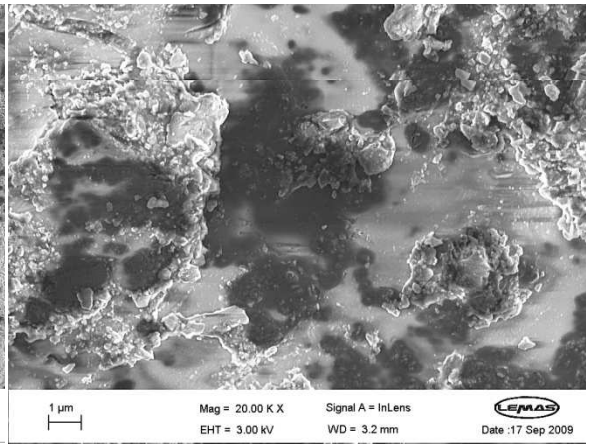

Figure 3.10b

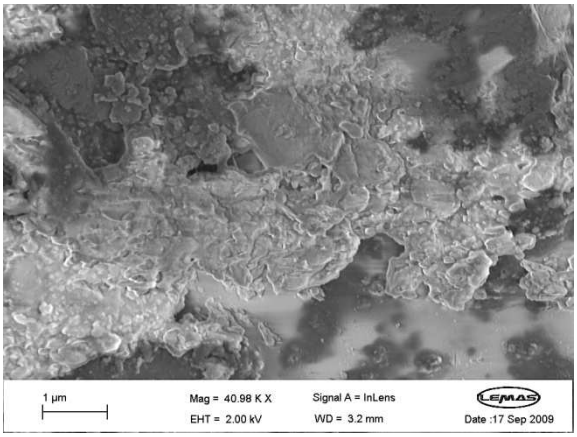

Figure 3.10c

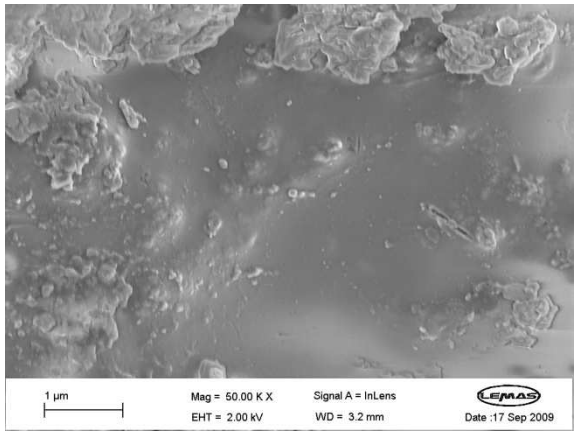

Figure 3.10d

Figure 3.10: SEM images of Tech 23 coated stainless steel surface at different magnifications.

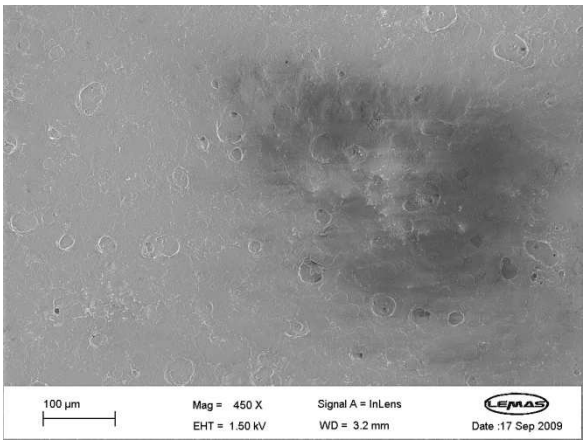

Figure 3.11a

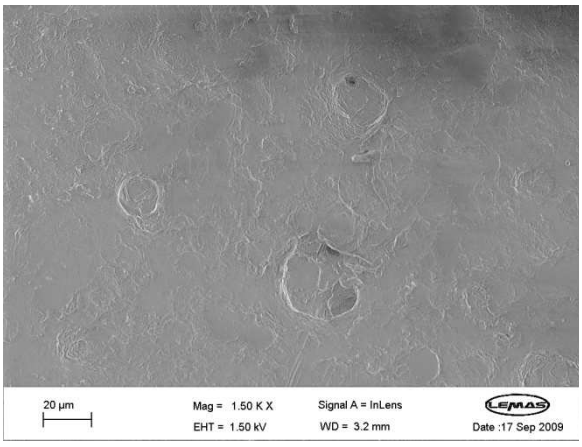

Figure 3.11b

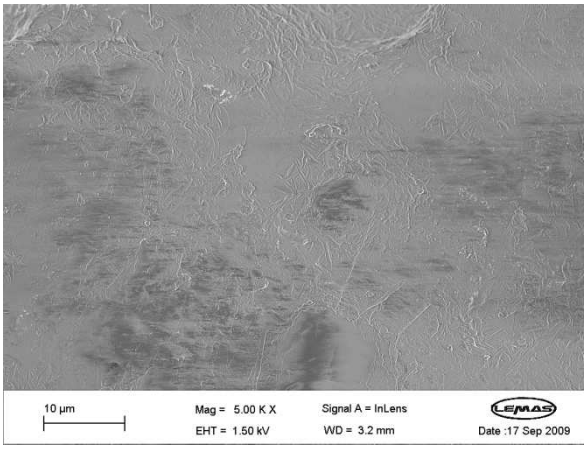

Figure 3.11c

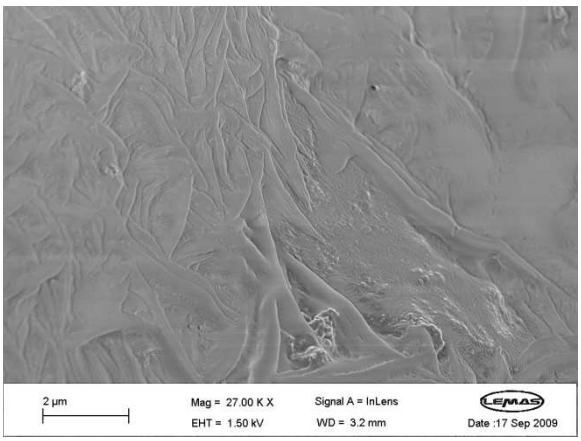

Figure 3.11d

Figure 3.11: SEM images of Tech 100 coated stainless steel surface at different magnfications

The Tech 100 coating can be seen to contain little black pores especially at lower magnifications (Figure 3.11a and Figure 3.11b), while up close, it does seem to look thermoplastic as it is a liquid dispersion coating.

3.3 Aragonite crystal plates for adhesion testing

In addition to the test substrates used in the calcium carbonate deposition studies, flat aragonite crystal plates were required in the adhesion tests and these were manufactured by PI-KEM Ltd. Each crystal plate was 10mm by 10mm, with a polished and rough side. SEM images of the crystal plates are given in Figure 3.12 and Figure 3.13.

The roughness (R_a) of the polished side of the aragonite crystal plate was found to be 18.7nm while the roughness (R_a) of the rough aragonite surface had a value of 565nm. The smooth side of the crystal plate is also observed to have a few dents into the surface.

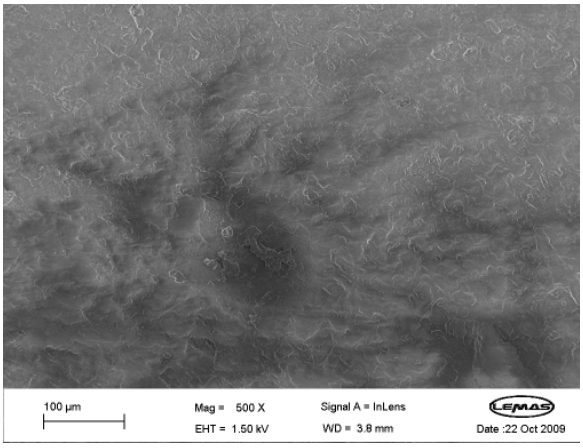

Figure 3.12a

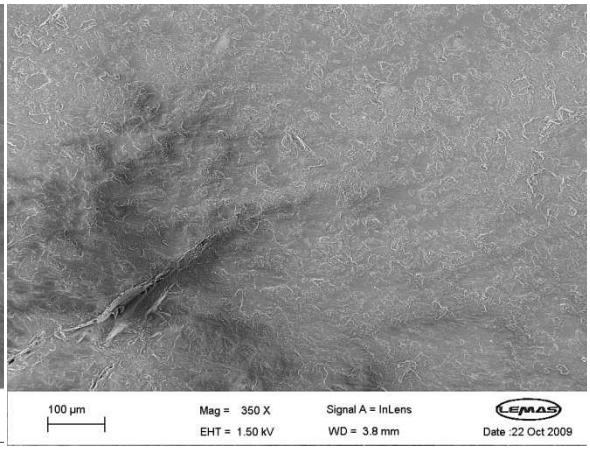

Figure 3.12b

Figure 3.12: SEM images of the rough aragonite surface of crystal plate

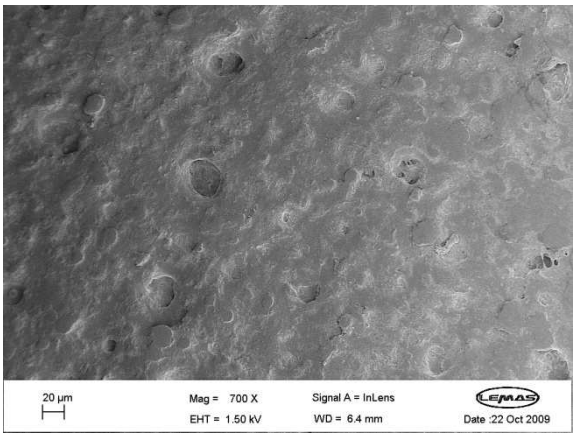

Figure 3.13a

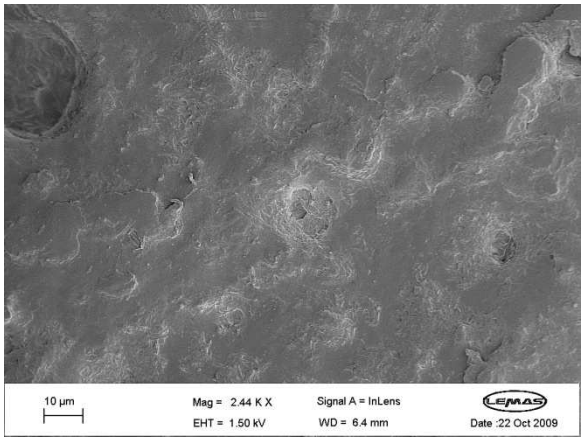

Figure 3.13b

Figure 3.13: SEM images of the smooth aragonite surface of crystal plate

3.4 Rotating cylinder electrode (RCE)

Corrosion and scaling processes can accelerate significantly under extreme environmental conditions such as high temperature, high pressure and turbulent fluid flow. These conditions have to be replicated in the lab and such flow loop systems often require complex plumbing, maintenance, and calibration to move fluid past a metal sample. The need for this type of large-scale lab equipment can be avoided by moving the metal sample with respect to

the fluid instead; a convenient instrument for doing this is the rotating cylinder electrode (RCE).

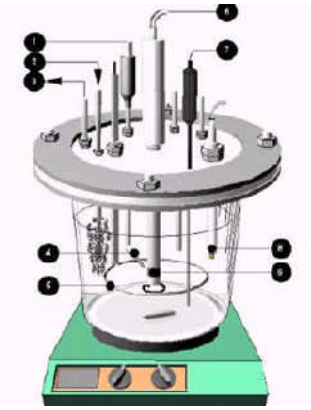

Figure 3.14a: 1L vessel thermostated to 70°C

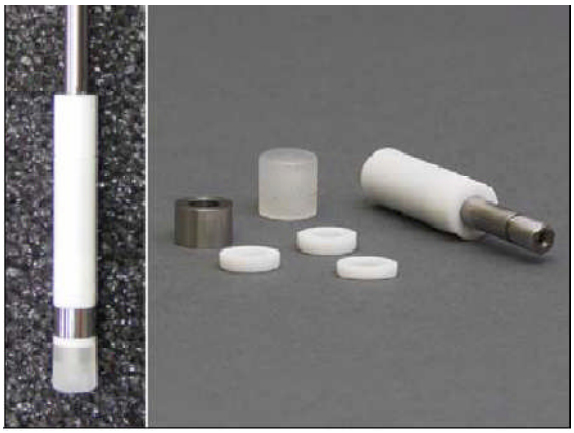

Figure 3.14b: RCE tip; metal sample is coated or wrapped with test polymers then immersed and rotated in 1L vessel

Figure 3.14c: Variable rotational speed of the RCE

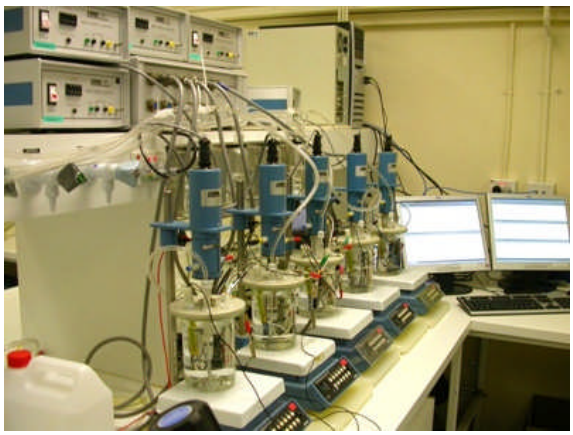

Figure 3.14d: Experimental setup

Figure 3.14: Diagram and pictures of the rotating cylinder electrode (RCE) and its components

This apparatus consists of an electrode rotator and a control unit (see Figure 3.14c) that enables the rotation rate of a vertically oriented shaft to be adjusted. A special tip capable of holding a cylindrical shaped metal sample is mounted at the lower end of the shaft. The tip is made primarily from chemically inert and electrically insulating materials such as Teflon, but buried within the tip is a metal shank which provides mechanical stability and also electrical contact with the metal cylinder sample (see Figure 3.14b).

Hydrodynamic conditions generated by the RCE can be turbulent even at low rotation rates which makes the RCE an ideal probe for studying scaling processes under low velocity but turbulent conditions. The hydrodynamic conditions adjacent to the metal sample can be adjusted by tuning the rotation rate up or down. It is possible to adjust the rotation rate so that the lab fluid flow conditions match those found in the field. Once this is done, the corrosion or scaling process can be monitored by classic mass loss methods or by electrochemical methods.

At very slow rotation rates, the solution near a rotating cylinder flows with a regular and smooth motion called laminar flow. As the rotation rate increases, the flow becomes more complex. While the layer of solution in direct contact with the cylinder continues to cling to the surface, the shear stress between this layer and layers further from the cylinder begins to spin off vortices. At this point, there is a transition from laminar to turbulent flow, and as the rotation rate increases, the vortices themselves spawn further vortices.

The transition from laminar to turbulent flow is characterized using the Reynolds number (Re) representing the ratio of inertial forces to viscous forces. For a rotating cylinder electrode with outer diameter, d_{cyl} (cm), the Reynolds number is

$$Re = U_{cyl} d_{cyl} \rho / \mu, \quad \textbf{(3.1)}$$

where ρ is the solution density (g cm^{-3}) and μ is the absolute viscosity of the solution (g cm^{-1} s^{-1}). The linear velocity, U_{cyl} (cm s^{-1}), at the outer surface of the cylinder is given by

$$U_{cyl} = \pi d_{cyl} F / 60, \quad \textbf{(3.2)}$$

where the rate can either be expressed as the angular rotation rate, ω (rad s^{-1}) or as F (RPM).

The transition from laminar to turbulent flow occurs at a relatively small rotation rate (30rpm), making the RCE an ideal tool for studying turbulent flow at low velocity which is exactly the condition frequently found in pipeline infrastructures [255, 256]. Higher turbulent velocities are also easily accessible at higher rotation rates. For all but the very slowest rotation rates, the turbulent condition is the norm. Rotation rates between 5 and 2000 RPM correspond to a range of Reynolds numbers spanning several orders of magnitude (see Table 3.5).

Table 3.5: Hydrodynamic computations for a typical RCE electrode in water

Rotation rate, F (RPM)	Surface velocity U_{cyl} (cm/sec)	Reynolds number, Re
5	0.31	42
50	3.14	422
500	31.4	4219
2000	125.7	16876

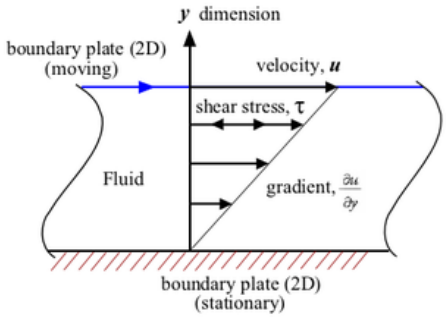

Figure 3.15: Schematic diagram for wall shear stress

The turbulent flow at the RCE induces a wall shear stress on the surface of the cylinder (see Figure 3.15). The wall shear stress, τ_{cyl}, for a typical RCE tip can be calculated from Eisenberg equation

$$\tau_{cyl} = 0.0791 \rho Re^{0.3} U_{cyl}^2 \cdot \quad \textbf{(3.3)}$$

Table 3.6: Hydrodynamic conditions in this study

	10 rpm	900 rpm	1800 rpm
Re	64	5800	11600
τ (g. cm^{-1}s^{-1})	0.0092	19.36	63
Viscous layer (μm)	6536	103.5	59.7
Diffusion boundary layer (μm)	65.4	1.04	0.6

In this study, a MUST (Modular Universal Surface Tester) was used to measure the adhesion between various test substrates and an aragonite plate. Aragonite was chosen as it was found to be dominant in the deposition studies carried out earlier.

3.5 Modular Universal Surface Tester

No one to-date had looked at the adhesion of single crystals. Yet, there is a lot of debate regarding deposition versus adhesion., The MUST tester has the capability to be able to measure relatively small forces in the milli-Newton (mN) range.

Adhesion tests were carried out using a MUST (Modular Universal Surface Tester) rig manufactured by Falex Tribology.

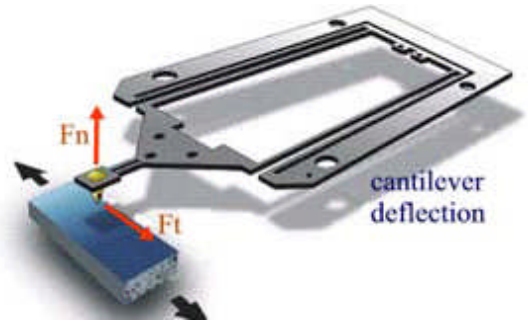

Figure 3.16a: Force transducer

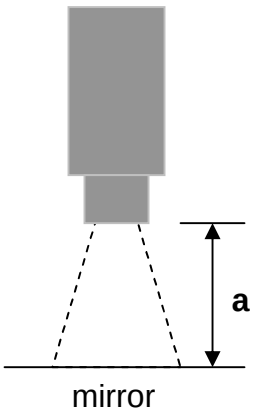

Figure 3.16b: Fibre Optic Sensor (FOS)

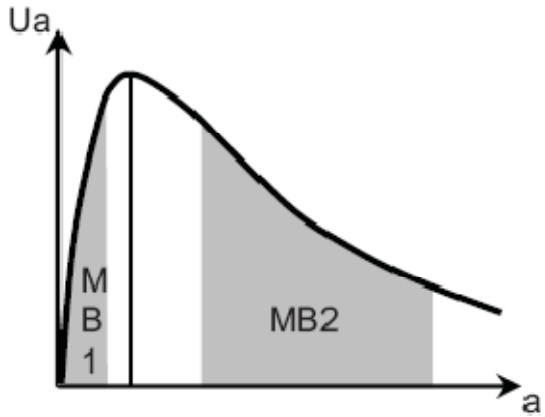

Figure 3.16c: Measurement characteristic of FOS

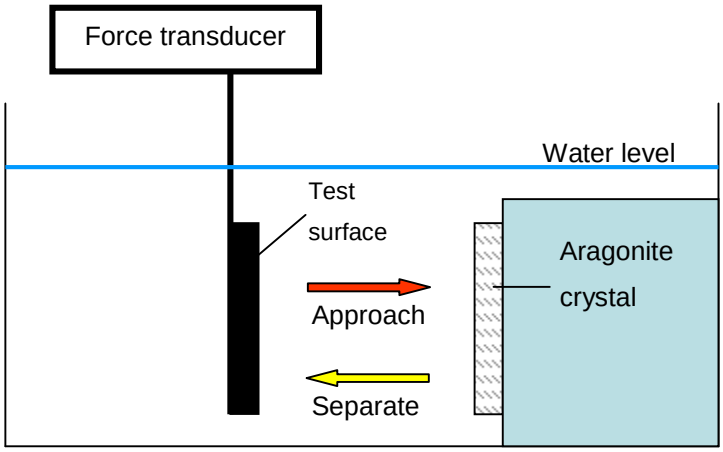

Figure 3.16d: Experimental Setup

Figure 3.16: Mechanism of the MUST and experimental setup

The force transducer (Figure 3.16a) is a cantilever based on a parallel spring system fixed in a mechanical carrier. Measurement of the deflection of the force transducer and the positioning of the drives is accomplished by the use of fibre optic sensors (FOS) see in Figure 3.16b. The FOS tip is made up of joined glass fibres and has an optical flat finish; light is radiated from the end to be reflected back from a micro mirror that is attached to the moving part of the cantilever. This reflected light is then received and converted by opto-electronic transducers to electrical signals.

The sensing rate characteristic Ua = f(a) is based on the optical behaviour and the photometric distance law which allows the sensor to be operating in two measuring ranges (Figure 3.16c). The first measuring range, MB1, is a near range indicating a strong rise of the characteristic when there is a relatively small change in distance. The second measuring range, MB2, is a far range indicating a larger measuring range and the characteristic rise is smaller.

In the experimental setup shown in Figure 3.16d, an indentation cycle consists of the test substrate being brought into contact with the crystal surface and then separated from it. Each indentation cycle generates a force-distance curve for the forces acting on the substrate-crystal interface; a typical curve obtained is shown in Figure 3.17.

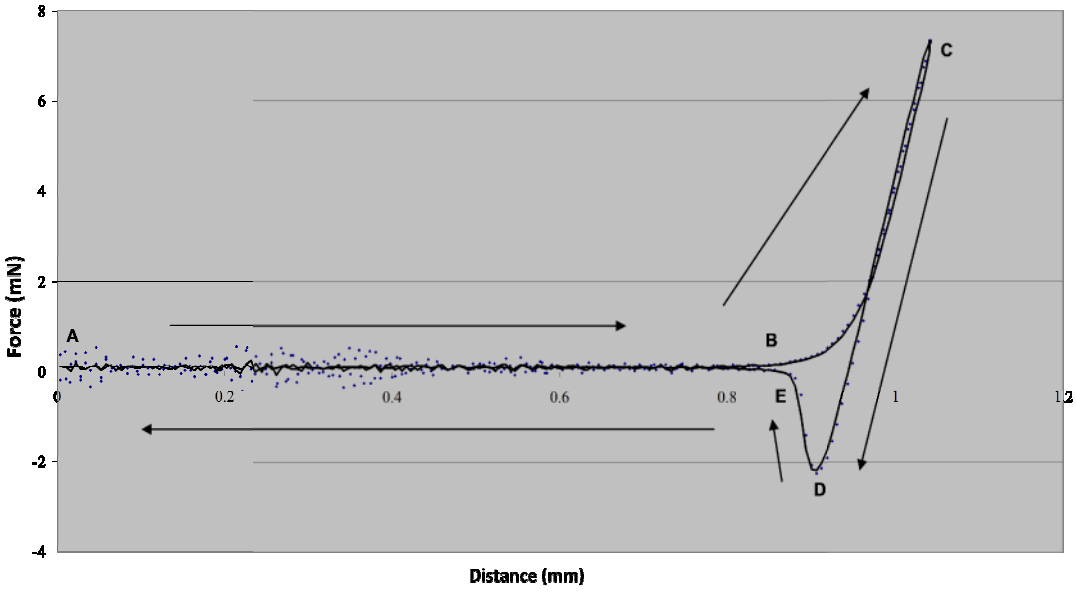

Figure 3.17: Typical force-distance curve for an indentation cycle

The indentation test starts at point A as the test substrate approaches the aragonite crystal surface. At point B, contact between the surfaces occurs and the test substrate continues to be pushed onto the aragonite crystal at an uniform rate until the pre-defined loading force is reached at point C. The slope BC is dependent on the spring constant within the cantilever and the elastic modulus of the crystal. After reaching the pre-defined load, the surfaces are separated; however, the test substrate stays in contact even as the force acting upon it turns negative which indicates an adhesive force at the interface whose maximum value is at point D. As the adhesive force is overcome the separating force returns to zero as indicated by point E. The slope DE indicates a gradual separation.

The aim of this test is to assess whether the scaling tendency can be predicted by measuring the adhesion between a calcium carbonate crystal plate and the test substrates under water.

3.6 Surface profiler for surface roughness measurement

The surface of every material has some form of texture which varies according to its structure and the way it had been manufactured. These surfaces can be broken down into three main categories: surface roughness, waviness and form. In order to predict the behaviour of these materials it is necessary to quantify these surface characteristics. R_a is the universally recognised parameter of roughness. It is the arithmetic mean of the absolute departures of the roughness profile from the mean line,

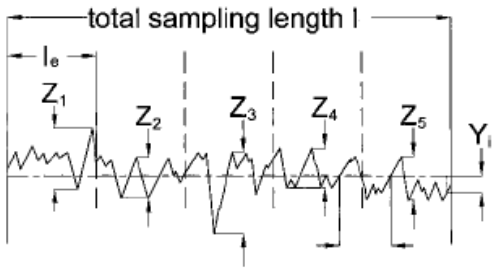

Figure 3.18: Evaluation of the surface roughness profile

$$R_a = \frac{1}{l}\int_0^l |z(x)|dx \qquad \textbf{(3.4)}$$

From Figure 3.18, the assessment length l is defined as the length of profile used for the measurement of surface roughness parameters, five consecutive sampling lengths are taken as standard.

Surface roughness (R_a) was measured by a Taylor Hobson surface profiler (Figure 3.19) which is based on a laser interferometric transducer. A computer controlled stylus passes over the test substrate's surface and data is simultaneously used to generate an output graph displaying the profile of the scanned surface.

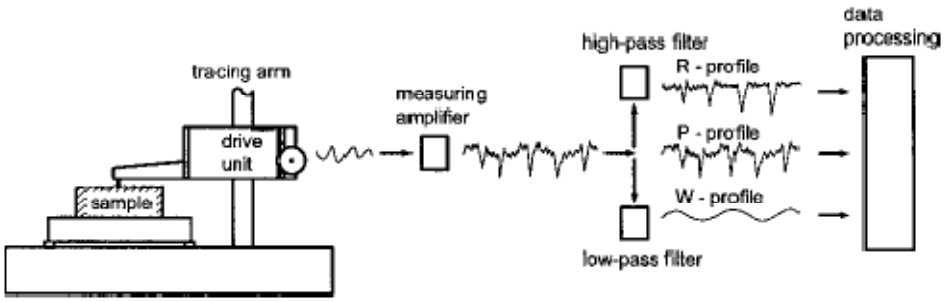

Figure 3.19: Measurement of surface roughness with a surface profiler [169]

3.7 Contact angle measurement

Wettability is one of the most important properties associated with a solid surface and is governed by a surface's chemical composition and roughness. This property is usually measured in terms of contact angle. Wettability also gives an indication of the surface energy of a solid surface [140].

In terms of the contact angle between the gas-liquid and solid-liquid interfaces, the wettability of an ideal flat solid is depicted by Young's equation,

$$\cos\theta_1 = \frac{\gamma_s - \gamma_{sl}}{\gamma_l}, \qquad \textbf{(3.5)}$$

where γ_{sl}, γ_s and γ_l represent the interfacial tensions of the solid-liquid, solid-gas and liquid-gas interfaces respectively.

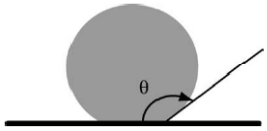

Figure 3.20: Definition of the contact angle formed at a solid surface [141]

The static contact angle, a measure of surface hydrophobicity, was measured using the sessile drop method with a contact angle goniometer and water droplets of deionized water. Droplets of about 3-5µL in volume were gently deposited on the substrate using a micro-syringe. The average water contact angle value was determined by measuring at three different positions of the same sample and their images were captured with a camera and input into software that measures the contact angle. Typical results obtained is shown in Figure 3.22 for polymer MN and stainless steel. It can be seen that stainless steel has more affinity for water compared to polymer MN.

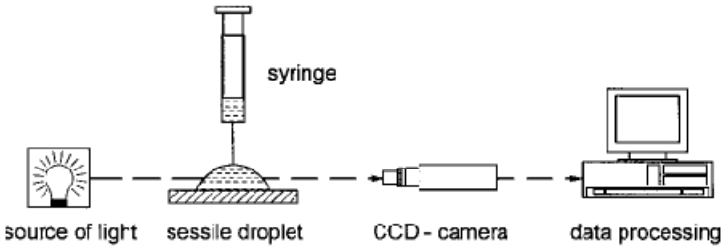

Figure 3.21: Sessile drop method to measure water contact angle with the aid of a contact angle goniometer [169]

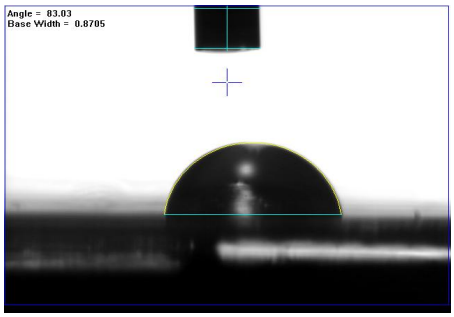

Figure 3.22a: Polymer MN

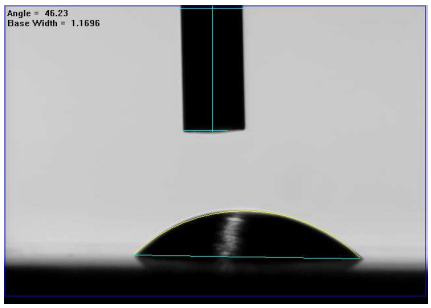

Figure 3.22b: Stainless steel

Figure 3.22: Typical results for water contact angle measurement for a water droplet placed on (a) a polymer and on (b) a stainless steel surface. Both materials are used in this work.

3.8 Scanning electron microscopy (SEM)

The LEO 1530 Gemini FEGSEM (Scanning electron microscope) with a Oxford Instruments 350 EDX system was used to analyze the scale coverage and scale morphology after performing experiments. This instrument possesses high resolution, low kV, secondary electron imaging plus EBSD/EDX capabilities. The stainless steel, polymers and coated steel surfaces had to be coated with a layer of conductive material, in this case it was sputter coated with Pt/Pd (platinum) of 3nm thickness. The coating also improves contrast in addition to increasing its conductivity.

3.9 Turbidity meter

Turbidity as a measure of the relative clarity of a sample is a qualitative characteristic which is imparted by solids obstructing the transmittance of light through the sample. Thus, it is not a direct measure of suspended particles in a sample but, instead, a measure of the scattering effect such particles have on light [257].

A Hach DR/890 Colorimeter was used to measure the turbidity of the scaling solution once brine 1 and 2 were mixed. Turbidity in this study was used to measure the cloudiness or haziness in the solution caused by the precipitation of calcium carbonate and is measured in Formazin Turbidity Unit (FTU). The colorimeter acts by measuring the attenuation or reduction of light as it passes through the sample column of water, in this case the reference used was distilled water.

In order to determine whether the calcium carbonate crystals are growing from the surface instead of settling from the bulk solution, the substrates are

immersed into the scaling solution 15 minutes after the brines are mixed – when the bulk solution has completely precipitated. Turbidity measurements from the start to end of a typical test are presented in Figure 3.23.

The higher the concentration of suspended particles, the higher the scattering and absorbance of light, and hence the higher the turbidity value of the water sample. The induction time for this study can be considered to be negligible due to the high supersaturation index of SI ~ 3.5.

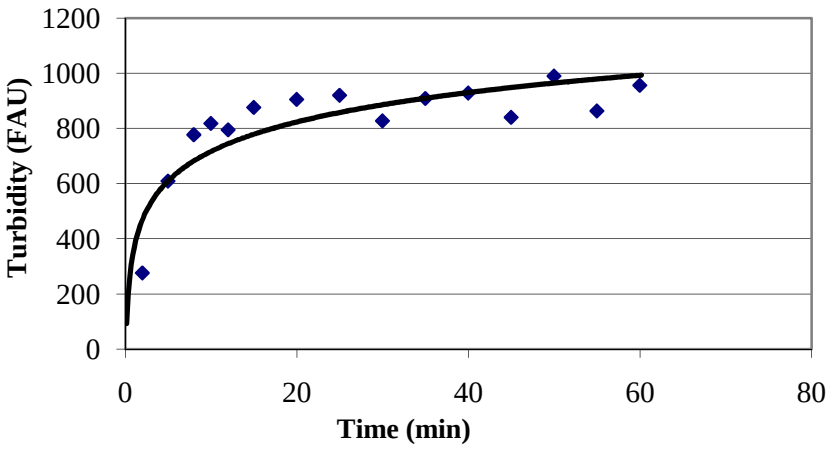

Figure 3.23: Turbidity graph of scale forming solution in this study. After 15 minutes after mixing of brines 1 and 2, the bulk precipitation eventually reaches a plateau.

The typical turbidity graph expected from a medium supersaturated solution is presented in Figure 3.24. In region 1, the solution is clear initially and the rate of nucleation is low. However, as nuclei form and grow into macroscopic crystals, the turbidity starts to increase, this is indicated by region 2. The tangent of the curve in region 2 will give an intersection with the time axis and this indicates the induction time which is a composite of the time required for critical nuclei formation and their growth to a detectable size. In region 3, the curve has reached a plateau indicating no further crystal formation [42, 258].

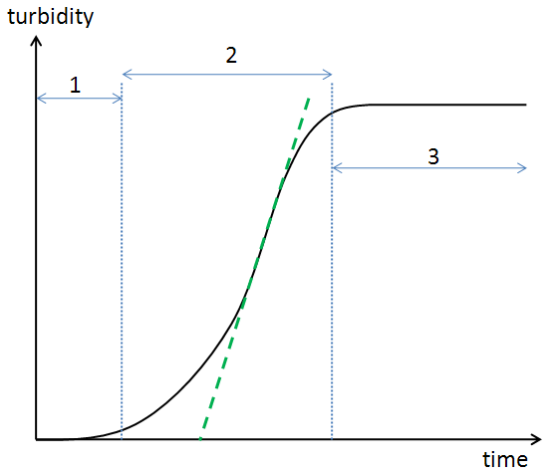

Figure 3.24: Typical turbidity graph

3.10 Inductively Coupled Plasma – Atomic Emission Spectroscopy (ICP-AES)

The analysis of calcium ion concentration was undertaken using ICP-AES in order to determine the supersaturation index of the scaling solution over time. ICP-AES is a multi-element analysis technique that dissociates a sample into its constituent atoms and ions, causing them to emit light at a characteristic wavelength by exciting them to a higher energy level. This is usually achieved by argon that acts as an inductively coupled plasma source. A monochromator separates the specific wavelengths of interest, and a detector measures the intensity of the emitted light. This data is subsequently used to calculate the concentration of that particular element.

In this work, inductively coupled plasma (ICP) mass spectrometry is used to determine the change in calcium concentration and hence the supersaturation index change of the scale forming solution with the aid of Multiscale . The supersaturation index can be calculated by changing the input of Ca^{2+} and HCO_3^- concentration in the Multiscale software. The results of the calculation can be seen in Figure 3.25.

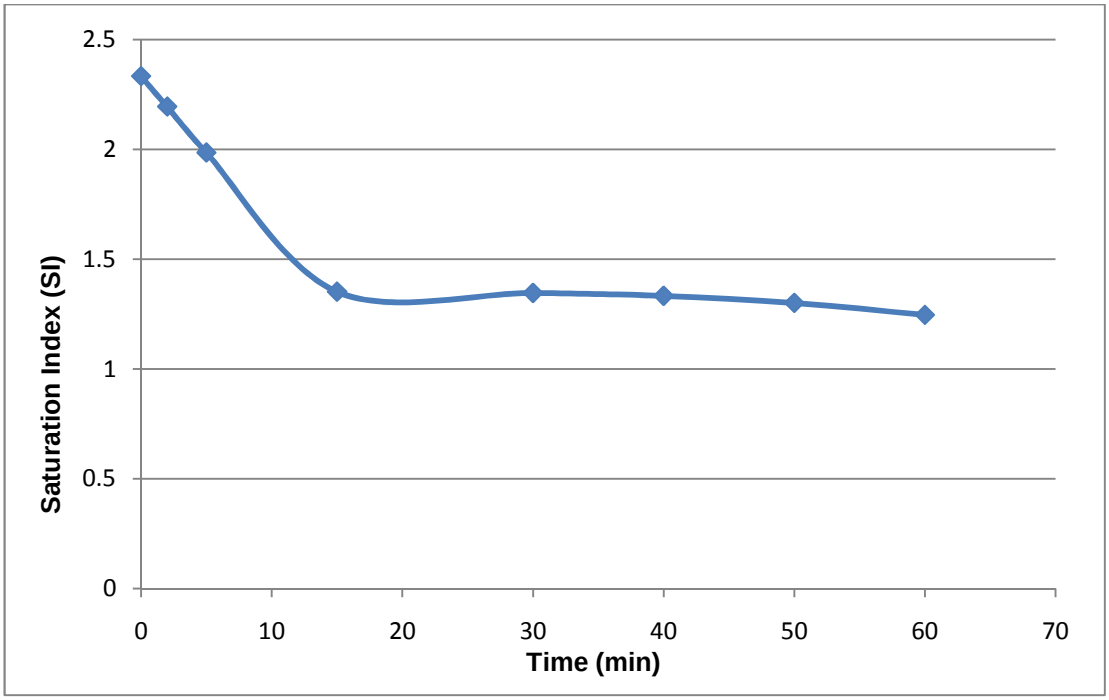

Figure 3.25: Change of supersaturation index (SI) of scale forming solution with time

From Figure 3.25, it can be seen that after the samples were inserted (15 minutes) the supersaturation index remained constant at SI=1.3. Interesting enough, the SI does not fall to equilibrium of 1. Samples were weighed before and after to obtain scaling tendency and crystal morphology was observed with SEM.

3.11 Characterization of precipitate from bulk solution

In order to determine the mass and morphology of the bulk precipitate, the scale forming solution was filtered with a 0.2µm filter and weighed after 48 hours to ensure complete evaporation of water. The crystals were then analyzed under a SEM to determine the surface coverage, crystal phase and their dimensions. .

The average mass of the precipitate was found to be 50.3mg and the observed dominant calcium carbonate phase was found to be aragonite with little calcite, as expected from a high supersaturated solution at 70°C. A SEM image of the bulk precipitate (Figure 3.26) clearly shows needle-like aragonite of average length of 10µm and a few orthorhombic calcite crystals of approximately 1µm.

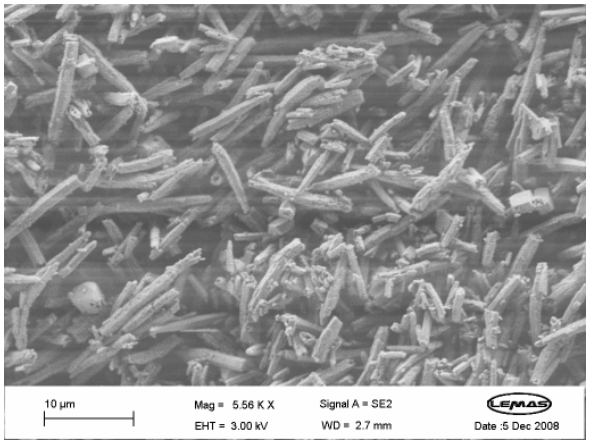

Figure 3.26: SEM image of bulk precipitate with mainly needle-like aragonite approximately 10µm in length; very little calcite can be observed.

This is a significant finding, as will be seen later, where the dominant calcium carbonate crystal phase is calcite on some surfaces while other surfaces had mainly aragonite which indicates that crystals were nucleating and subsequently growing on the surface itself instead of settling from the bulk solution. There is no size difference between the bulk precipitate and the crystals observed growing on the test surfaces.

Chapter 4
Substrate Effect on Surface Adhesion of Calcium Carbonate

In this chapter, the results of calcium carbonate deposition tests on polymers and commercially available coatings with stainless steel (SS316L) as a reference surface are reported. The amount of scaling was recorded in terms of mass gain at various time intervals (5 minutes, 15 minutes, 30 minutes, 45 minutes, 1 hour). The change in polymorph, surface coverage and density were observed with SEM (Scanning Electron Microscope). These various substrates were also exposed to scaling before and after bulk precipitation had occurred to determine the scaling mechanism – deposition onto the substrate from the bulk solution or nucleation and subsequent growth on the surface. In addition, a micro-adhesion test was developed in an attempt to relate deposition tests to the adhesion properties of a single calcium carbonate crystal against a surface, as a measurement of anti-scaling performance.

Scaling is driven by surface-specific interactions between solids and liquids, thus understanding their interactions is important at a fundamental level. The challenge is to determine what surface properties are important in preventing the nucleation and growth of scale so they can be quantified and controlled in a reproducible manner. The determination of calcium carbonate scaling rate and an estimation of the growth rate of scale formed in pipelines is a useful indicator for the lifetime of pipelines and inhibitor squeeze treatment frequency in the oil/gas sector, especially in the operation of downhole valves and other mechanical devices where just a little scaling can prevent the device from operating.

In an analogous way to corrosion, it would be beneficial, for a certain set of conditions, to be able to determine the scale growth rate as a thickness growth rate per unit time. To date, this has not been done in relation to scaling yet is widely used in prediction of corrosion rates.

4.1 Surface deposition of calcium carbonate onto various substrates

4.1.1 1 hr surface deposition tests

The polymers used in this study have varying surface structures at the nano- and micro- scale along with various surface chemistries. This serves as a platform in the fundamental understanding of how surface topography and chemistry affect adhesion and deposition of calcium carbonate scale and aids in optimizing other surfaces with materials that are more resilient to the high temperatures, pressures and the corrosive environment existing in actual oil fields. Furthermore, such surfaces can be introduced onto the surfaces of essential equipment such as electrical submersible pumps (ESPs), safety control valves and gas-lift mandrels where scaling can lead to electrical and mechanical failures. Currently it is appreciated that coatings are not used to their full potential for scale control.

The deposition tests in all cases gave a measurable weight gain due to the calcium carbonate crystals adhering to or growing from the surface. The brine was also precipitating in the bulk solution for the one hour and so during the test the supersaturation index would be decreasing but still remains supersaturated even after an hour, as SI is still above 0 (see Figure 3.25). The induction time for the bulk precipitation was very short (less than 1 minute).

Figure 4.1 displays the results of the 1 hour deposition tests. It can be seen that the coatings (DLC, Tech 100 and Tech 23) had the least scaling tendency compared to the polymer surfaces, while stainless steel had the highest scaling tendency. The coated stainless steel surfaces exhibited much better anti-scaling properties with Tech 100 having performed the best after an hour.

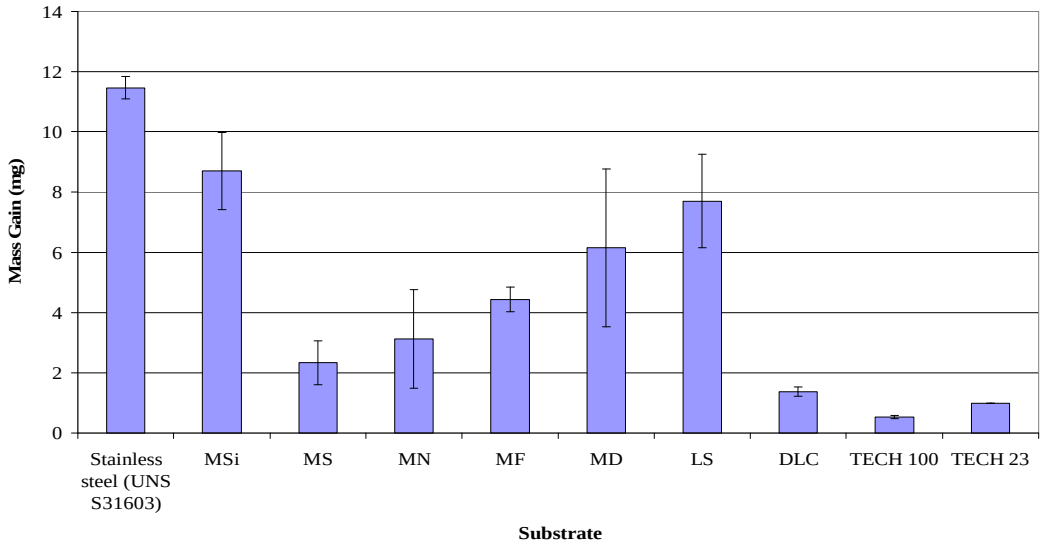

Figure 4.1: Results of 1hr deposition tests to assess the scaling tendency of each test surface.

The weight gain can be translated into a more useful indicator to show the rate of scaling per year onto the respective substrates, these rates are shown in Table 4.1. The rates are obtained by assuming the density of calcite to be 2.71g.cm^{-3} and aragonite to be 2.93g.cm^{-3}, in addition to being a fully dense layer [61].

Until only recently has there been more focus on studies of surface scaling, whereas studies of bulk precipitation processes have always been the main focus despite scaling problems always arising from the deposition of scale onto tubular or equipment surfaces. Just as corrosion rates being widely used for prediction of corrosion, these surface growth rates can be a good indication of the lifetimes of the pipes before they get blocked and the effectiveness of any scale removal methods employed.

Table 4.1: Rate of scaling (cm/year) on the various substrates per year (assuming a fully dense layer is formed)

Substrate	Rate of scaling/year (cm/year)
SS	9.02
Polymer MSi	6.84
Polymer MS	1.84
Polymer MN	2.46
Polymer MF	3.49
Polymer MD	4.84
Polymer LS	6.06
DLC coating	1.08
Tech 100	0.45
Tech 23 coating	0.85

4.1.1.1 SEM Images following 1 hr scale deposition

Figure 4.2 shows the scale formation and surface coverage on the test surfaces after the 1 hour test period. Aragonite formation is expected from this high supersaturated brine at 70°C although there are some calcite crystals that can be seen amongst the aragonite [56, 115, 116]. Stainless steel (Figure 4.2a) is seen to be most densely covered by calcium carbonate crystals. Although the polymers perform better than stainless steel with less mass gain, there seems to be a wide variety of performance amongst the polymer surfaces. The polymers MS and MN (Figure 4.2b and Figure 4.2g) have the most free and visible original surface regions left after the tests, while the remainder of the polymers are covered with crystals but as can be observed the crystal layers are less dense relative to the layer formed on stainless steel. Consequently, the tendency for the deposition of crystals onto existing crystals is what seems to be measured at the end of the tests as any potential benefits offered from the polymers has been lost once they become covered with scale.

The benefits observed in the case of some of the polymer surfaces may be lost within a short period of time but the important point is to understand what controls this initial deposition onto the polymer surface that differs from

deposition onto stainless steel surface. This will be further explored in the discussion chapter.

Similarly, the coatings (DLC, Tech 23 and Tech 100) all have patches of original surface visible after the test and are not as densely populated with scale compared with the polymers (except polymers MN and MS) and the steel surface. After one hour, DLC was observed to have little or no calcite at all, as can be observed from Figure 4.2h. By comparison, the Tech 23 and Tech 100 surfaces were seen to promote the growth of calcite more than aragonite which is interesting as all the surfaces were exposed to the same scale forming solution under the same conditions. This can be seen more clearly in Figure 4.7 which shows higher magnification of the scale deposition at the surfaces.

From Figure 4.2g, it can be seen that calcite crystals are growing on the vaterite crystals which may be attributed to the total concentration of calcium and carbonate ions in the vicinity of the vaterite crystals [229]. The crystals in this work are identified on the basis of characteristic morphologies [259]; calcite displayed planar rhombohedral faces while the vaterite particles were polycrystalline and aragonite were needle-like and had high aspect ratios [260]. It is well recognised that calcite is the most thermodynamically stable form of $CaCO_3$ and aragonite is the metastable form. During the induction period, the growing rate of $CaCO_3$ is lower which encourages the formation of the thermodynamically stable form. Now during the post-induction period, the growing rate of $CaCO_3$ is higher and it is favourable for the metastable phase to form. As a result, the two types of crystals forms are formed owing to different growing rates between the induction and the post-induction periods [94].

The morphology of the crystals can have important effects on the properties of the scale layer; for example, needle-like shaped aragonite crystals produce porous and fragile layers [155, 261]. Normally a fast or instantaneous nucleation leads to calcite whereas slow or progressive nucleation leads preferentially to vaterite form. The nature of the surface would have to account

for these differences. To date, there has been little or no work that addresses the role of the substrate in determining the morphology of the scale.

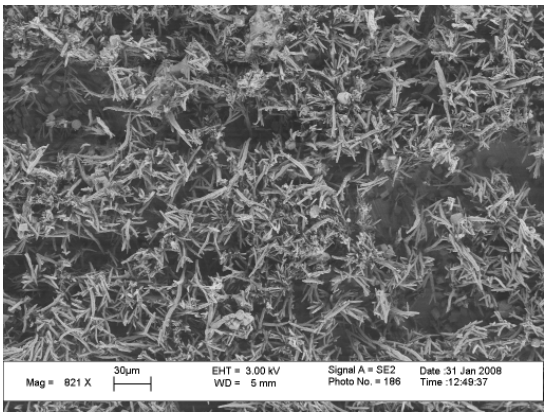

Figure 4.2a: Stainless steel

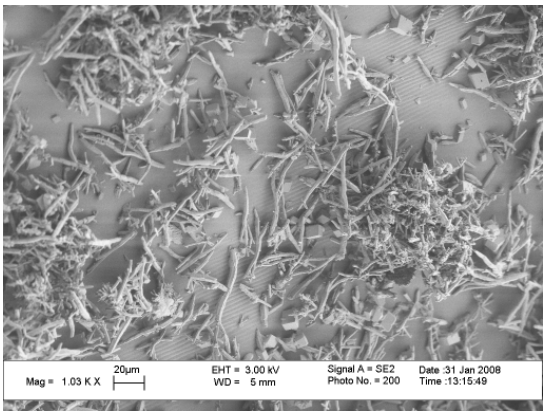

Figure 4.2b: Polymer MN

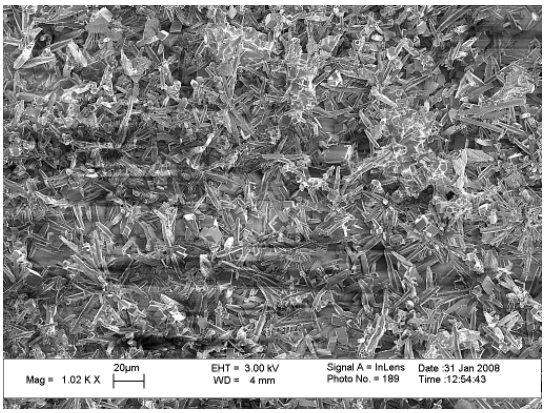

Figure 4.2c: Polymer MD

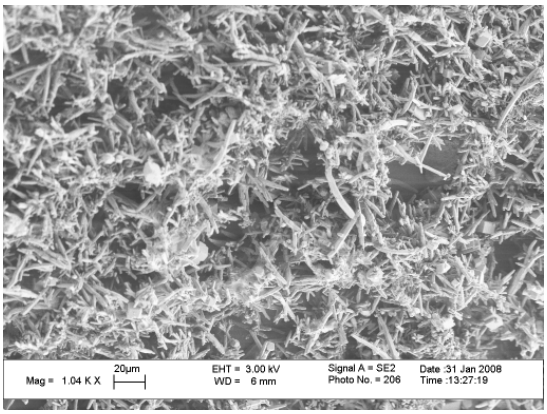

Figure 4.2d: Polymer MSi

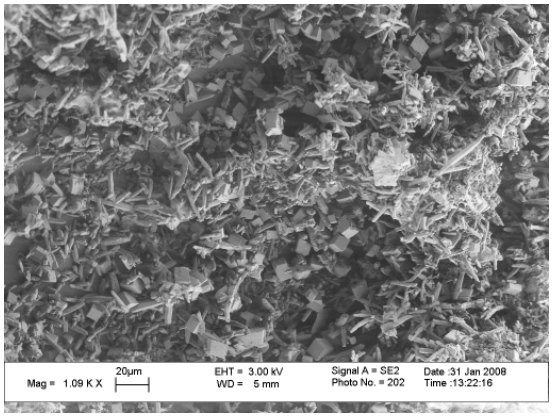

Figure 4.2e: Polymer MF

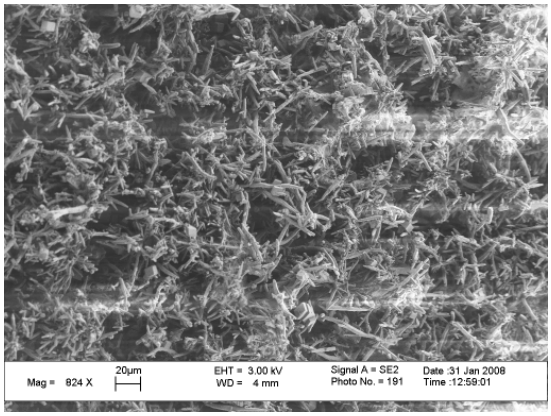

Figure 4.2f: Polymer LS

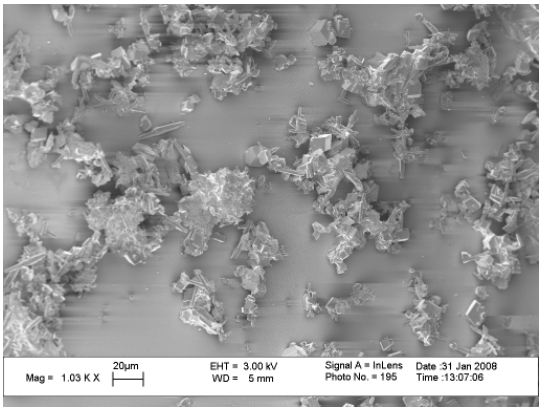

Figure 4.2g: Polymer MS

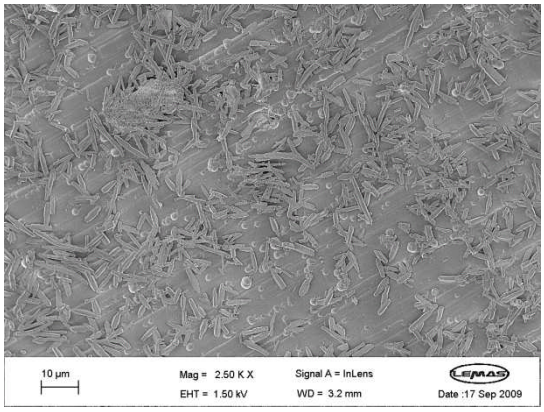

Figure 4.2h: DLC

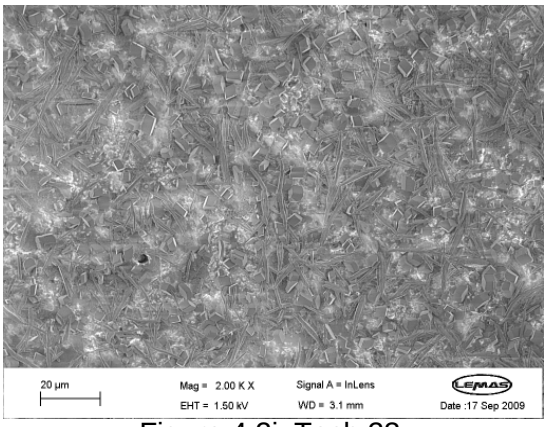

Figure 4.2i: Tech 23

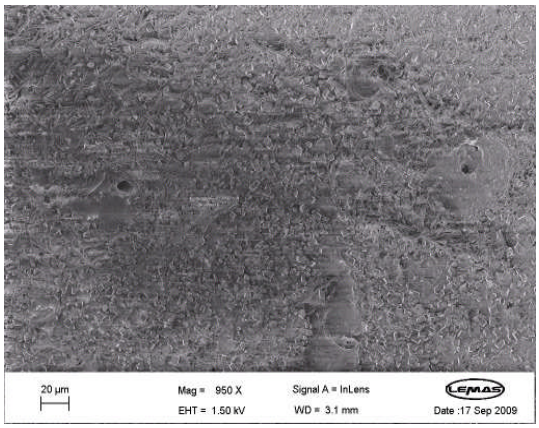

Figure 4.2j: Tech 100

Figure 4.2: Scale formation on various substrates after the 1 hour deposition test

The SEM images (Figure 4.2 and 4.11) seem to show that the upper surface scale layer for almost all surfaces except for the Tech 23 and Tech 100 coatings (Figure 4.2i-j) appears to be needle-like aragonite, which may originate from either the heterogeneous nucleation and growth from the top aragonite itself as the energy required for growth is lower [99] or deposition from the bulk solution which comprises mainly of aragonite crystals. There is also evidence of vaterite on the surface of polymer MS (Figure 4.2g). It is not clear what the underlying layer is. Studying the early stages of deposition would allow us to understand the early scale formed and the crystal phase transformations – such information is presented later.

The effect of surface roughness on scaling tendency can be seen in Figure 4.5. Figure 4.3 presents the surface roughness parameters (R_a, R_z and R_q) measured, while Figure 4.4 shows the surface roughness of the polymers only in higher detail as their values are comparably lower than the rest of the test surfaces. Tech 100 coating is considered the roughest among the surfaces including the polymers while polymer LS is the roughest amongst the polymers.

In this study, the rougher surfaces seem to have less scale (Figure 4.5) which is against the general trend of what has been published. It can be observed that Tech 100 was the roughest yet experienced the least scaling of all the surface and in reference to stainless steel which had the highest scaling tendency. Figure 4.6 shows the correlation between the polymer surface roughness and mass gained from scale. Most polymer surfaces except for polymer LS have similar surface roughness but exhibit various scaling tendency and even though polymer LS was the roughest amongst the polymers, it did not have the highest scale on the surface.

Nevertheless, it is important to note that the roughness regime in this work has to be considered and the surfaces are all essentially “smooth” compared to the roughness results of others, as will be discussed in detail later. The performance of the polymers are further expanded Figure 4.6 to assess for a trend. A higher magnification providing a closer look at the crystal distribution and morphology is then presented in Figure 4.7.

Ideally to analyse the controlling factors for deposition, it would be best to have a scenario where $CaCO_3$ crystals are depositing onto the polymer only (Polymer – $CaCO_3$) but there is clearly deposition onto the polymer and then onto $CaCO_3$ (Polymer – $CaCO_3$ – $CaCO_3$) in the present study.

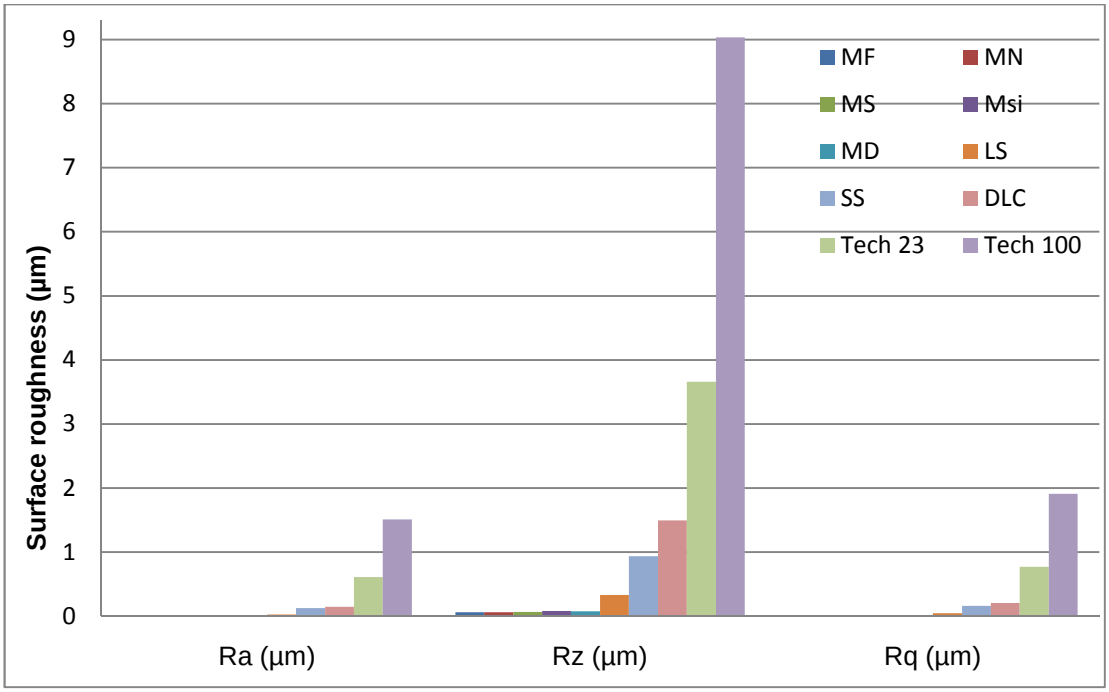

Figure 4.3: Surface roughness for all the substrates used in this work, presented in the form of R_a, R_z and R_q (µm). The surface roughness of the polymers will be shown more clearly in Figure 4.4.

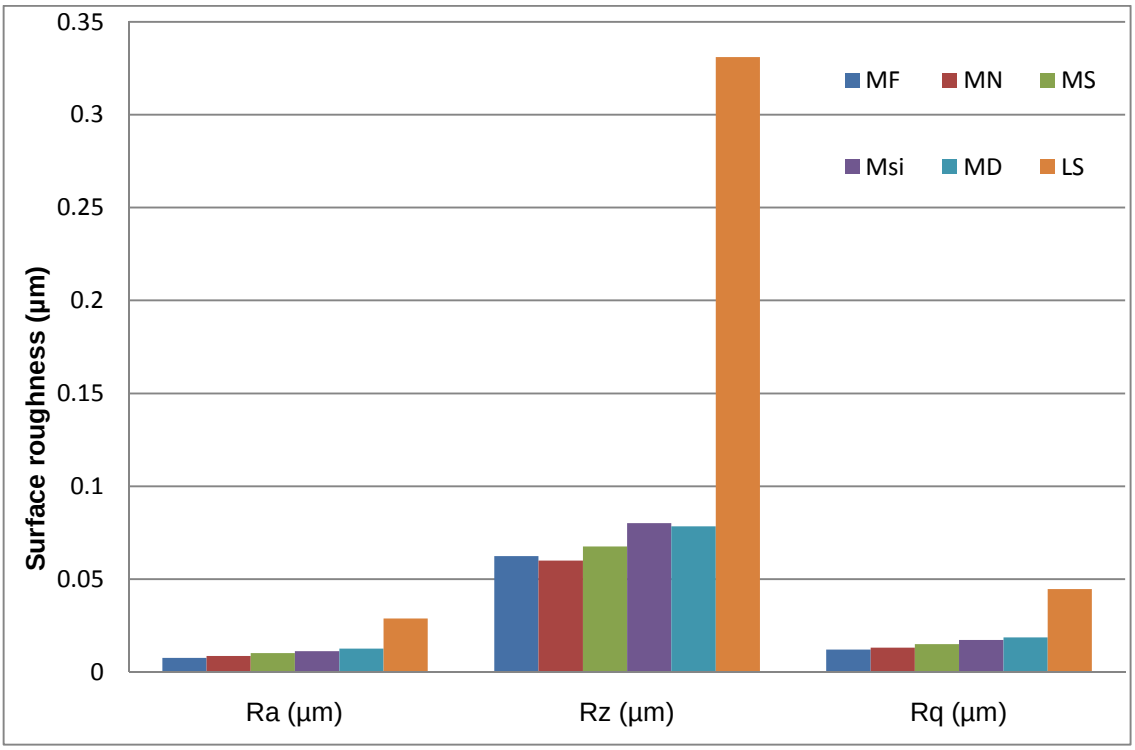

Figure 4.4: Surface roughness measured for the polymers in the surface parameters of R_a, R_z and R_q.

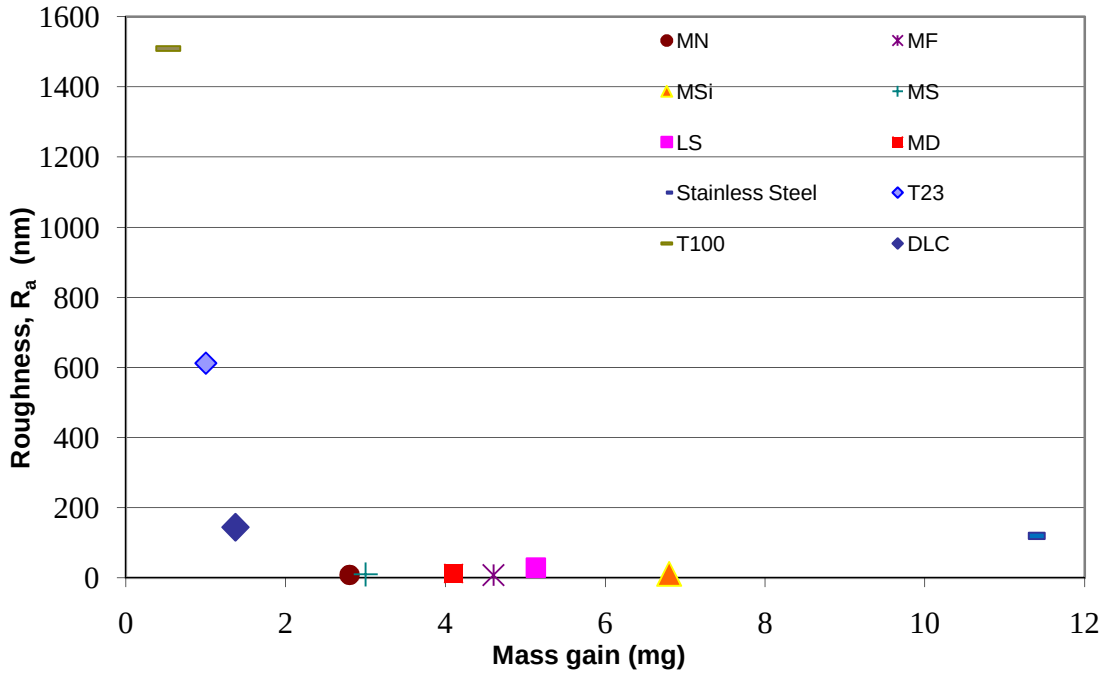

Figure 4.5: Mass gain (mg) vs. Roughness, R_a (nm) – A general trend where the scaling tendency increases with a decrease in surface roughness can be seen. The coatings are the least scaled surfaces, followed by the polymers and finally the stainless steel reference surfaces.

From Figure 4.8a-c, it can be observed that all the crystals are very much larger than the structural features of the surfaces themselves which reduces the number of contact points between these crystals and the surface asperities. All the crystals are at least 40-400 times larger than the width of the polymers' asperities and they "sit" on the tip of these asperities.

Generally, a fewer number of contact points between surfaces would lead to a reduction in adhesion force between them. In this case, the surfaces involved are the crystal itself and the substrate. This is explored further in a later section to assess the effects of surface roughness and topography on adhesion. In addition, a smaller number of adhered points should allow easier removal of crystals by hydrodynamic shear forces when the fluid velocity closest at the surface is high, especially in turbulent pipe flows which generate higher shear stresses at the walls. However, in the case where the crystals are not just 'sitting' on the asperities but are interlocked into the polymer structure, particle

removal was not evident even with increasing shear stresses which is evident in this thesis . Hydrodynamic effects on scale formation at surfaces are explored in Chapter 5.

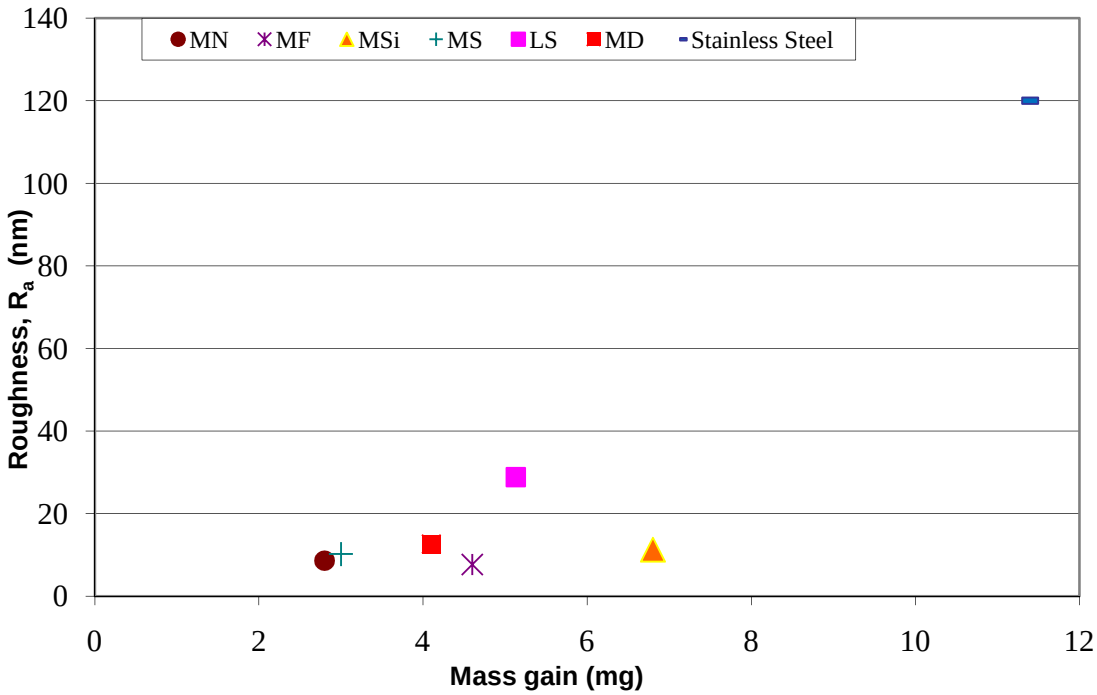

Figure 4.6: Mass gain (mg) vs. Roughness (nm) – Polymer LS is the roughest amongst the polymers but did not display the highest scaling tendency. The other polymers displayed a range of scaling tendency even though they possessed relatively similar theoretical surface roughness. Stainless steel is the roughest and had the most amount of scale.

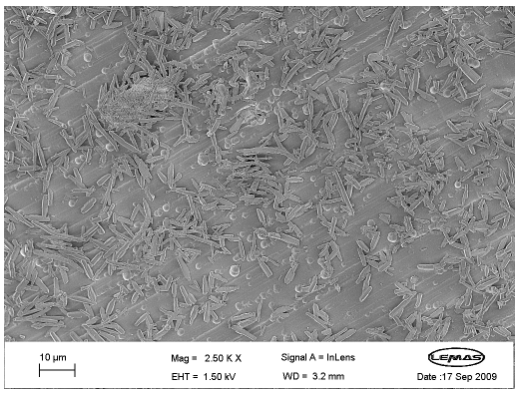

Figure 4.7a: Higher magnification of DLC substrates shows the presence of mainly aragonite

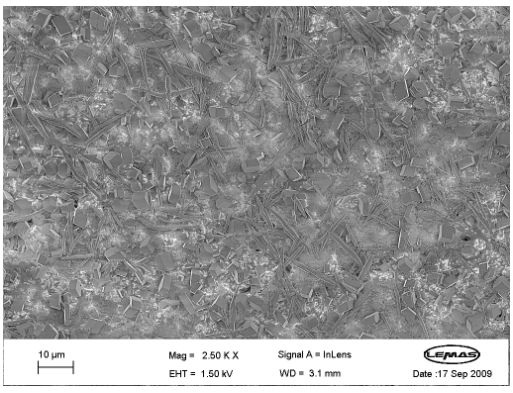

Figure 4.7b: More calcite than aragonite on Tech 23 surface

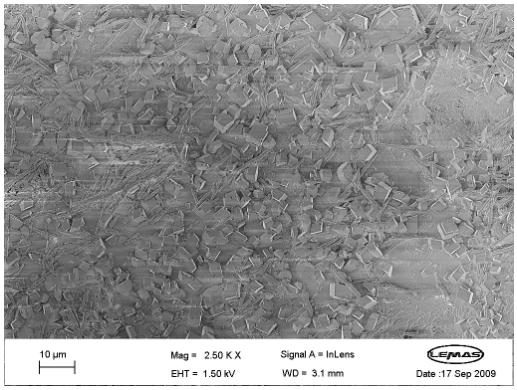

Figure 4.7c: More calcite than aragonite on Tech 100 surface

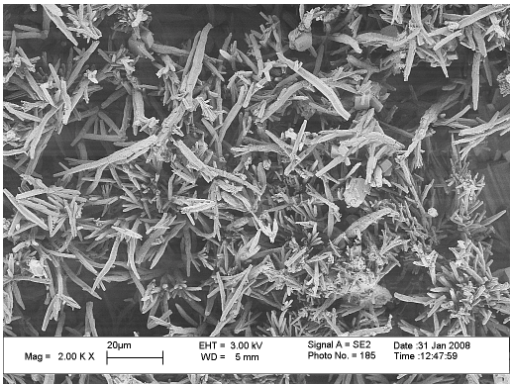

Figure 4.7d: Aragonite crystals dominates on stainless steel surface

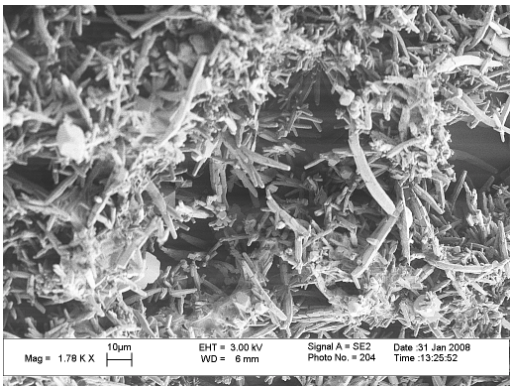

Figure 4.7e: Aragonite crystals dominate on polymer MSi surface

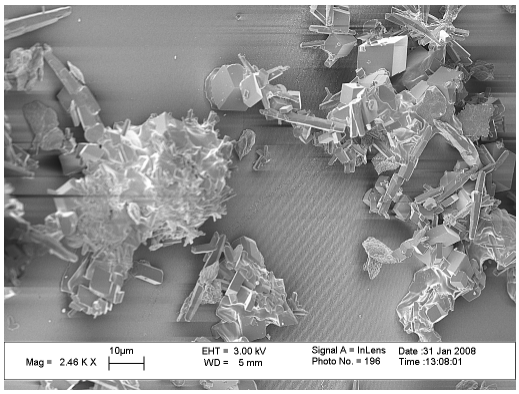

Figure 4.7f: Conglomerates of calcite and aragonite on polymer MS

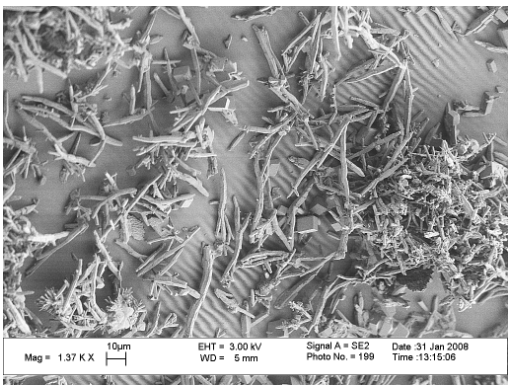

Figure 4.7g: More aragonite crystals than calcite on polymer MN

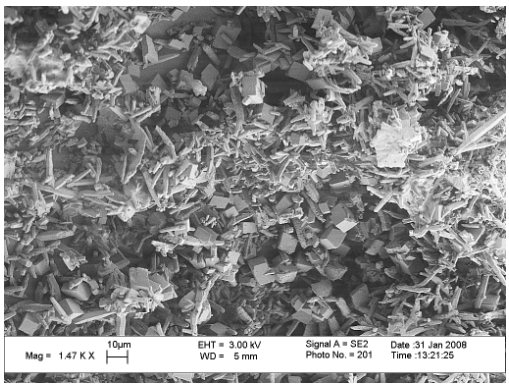

Figure 4.7h: Calcite on the bottom with aragonite stretching on top layer for polymer MF

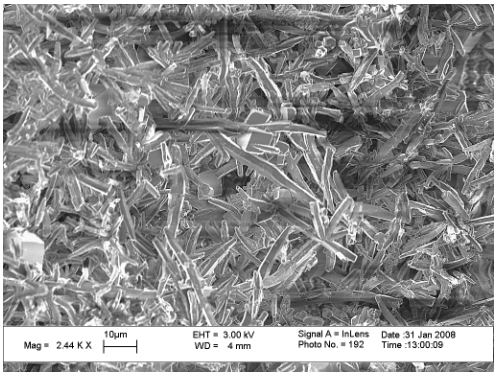

Figure 4.7i: Aragonite is dominant on polymer LS

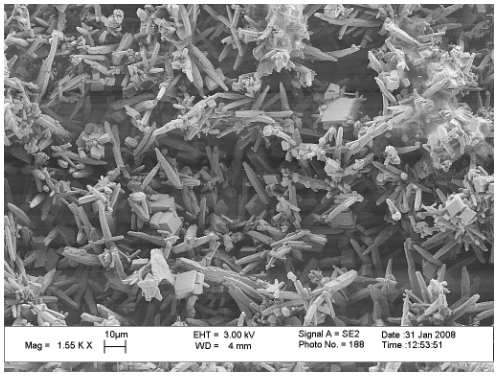

Figure 4.7j: Aragonite is dominant on polymer MD

Figure 4.7: Different crystal morphology on various substrates

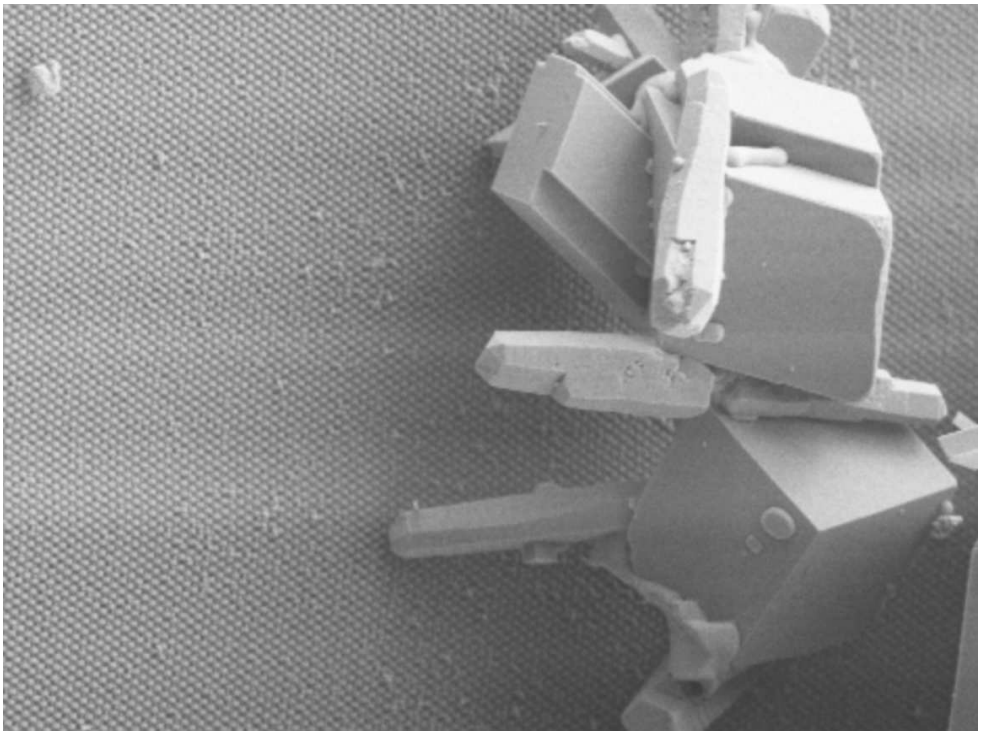

Figure 4.8a: Polymer MS – Conglomerate of calcite and aragonite can be seen.

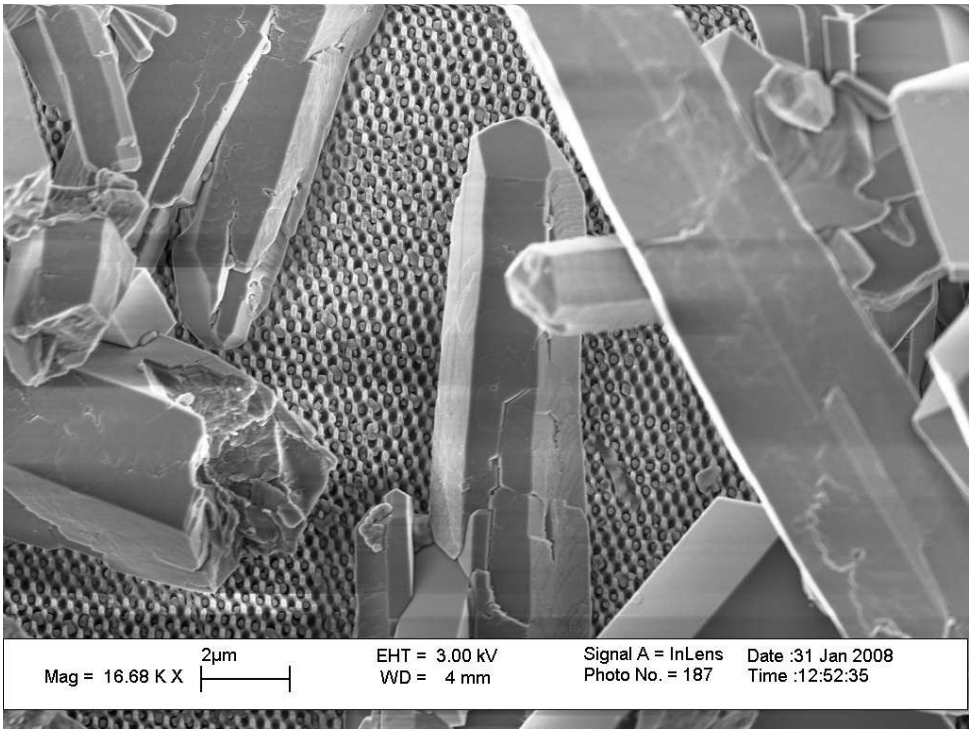

Figure 4.8b: Calcium carbonate deposition on polymer MD

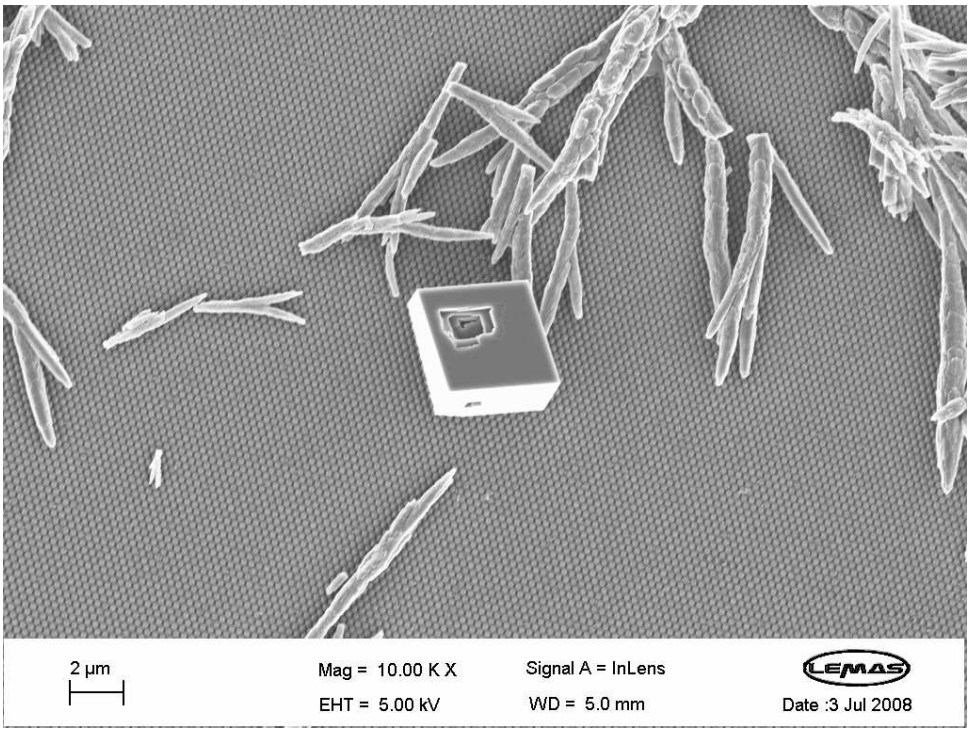

Figure 4.8c: Calcium carbonate deposition on polymer MN

Figure 4.8: Higher magnification of crystal deposition on structured polymer surfaces

4.1.2 Deposition at earlier time intervals

The polymers with the least and highest scaling tendency, polymers MN and polymer MSi respectively, together with stainless steel and the coated surfaces were selected for deposition studies at time intervals less than an hour. Deposition was investigated after 5 minutes, 15 minutes, 30 minutes and 45 minutes. This enabled the observation of the early formation of the scale that is deposited and to assess the performance of the polymer and coated surfaces and how they compare with stainless steel as a reference substrate.

The experimental methodology was the same as used in the 1 hour deposition tests, only the duration of the test varied. The results obtained are shown in Figure 4.9.

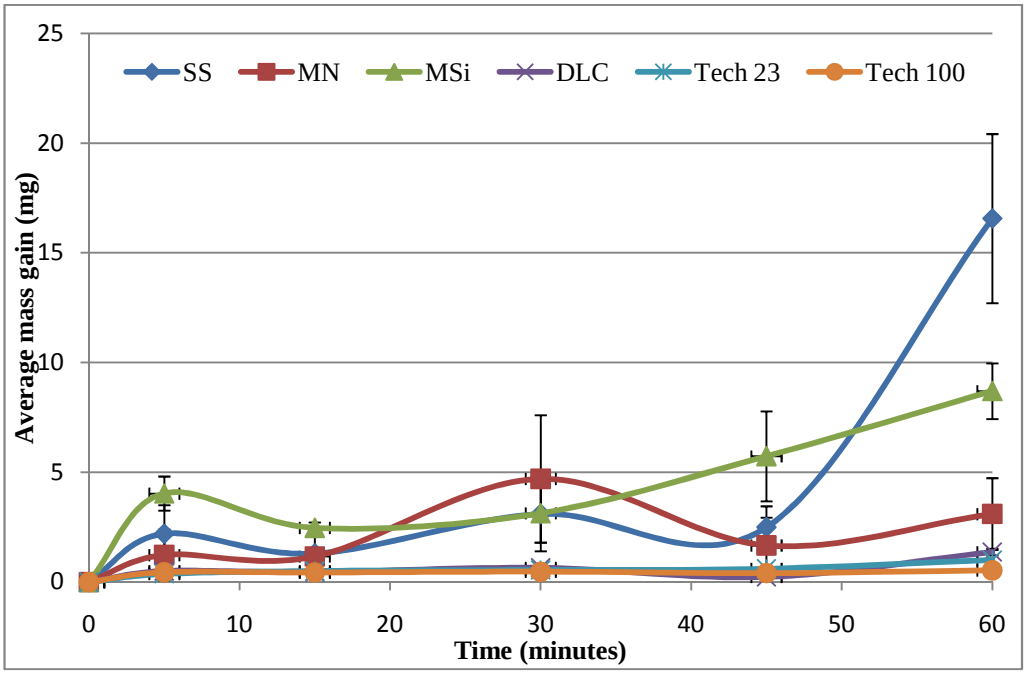

Figure 4.9: Deposition measured as the average mass gain at various time intervals

At time intervals less than an hour, there is no distinct difference between deposition onto the polymer or steel surfaces; however at the 30 minute interval

the steel can be seen to perform better. It is only after an hour that a distinct difference in deposition emerges. The threshold time period for deposition or precipitation on the steel surface to accelerate seems to be approximately an hour whereas the polymer surfaces seem to have the effect of delaying such a sudden increase.

All of the substrates show a general increase in deposition with time except for the coatings (DLC, Tech 23 and Tech 100) where their mass gains are insignificant compared to the other surfaces. A closer look at the variation in their mass gain for these coatings is presented in Figure 4.10. Comparing the mass gains at 5 minute and 1 hour intervals, polymers MN and MSi exhibit a two- to three times mass increase relative to almost a six-times mass increase in the case of stainless steel. The variation in deposition increase at the substrates may be attributed to scale forming and being sheared away by hydrodynamic forces during the deposition tests. SEM images of the deposition at various time intervals are displayed in Figure 4.11-Figure 4.14.

Looking at the above figures, the morphology and coverage of the initial or underlying scale that forms on the surface can be seen. Some of the surfaces have signs of vaterite spherulites with lateral extensions (Figure 4.11bii, Figure 4.11fii, Figure 4.13aii) and they are either transformed into the more stable calcite and aragonite eventually or are covered by layers of scale thereafter for tests carried out at longer time intervals.

So far, the needle-like crystals all tend to grow up to a length of 10µm in length and the calcite crystals of 2µm in dimensions. The ultimate size of the particles is dependent on the reagent concentrations [259]. The local concentrations of ions at the surfaces results in local concentrations equivalent to those in the bulk solution immediately after the reagent solutions are mixed; once precipitation occurs, the availability of ions in the vicinity of the crystals are depleted. Hence, the further growth of the crystals are then limited by diffusion of ions from the bulk solution.

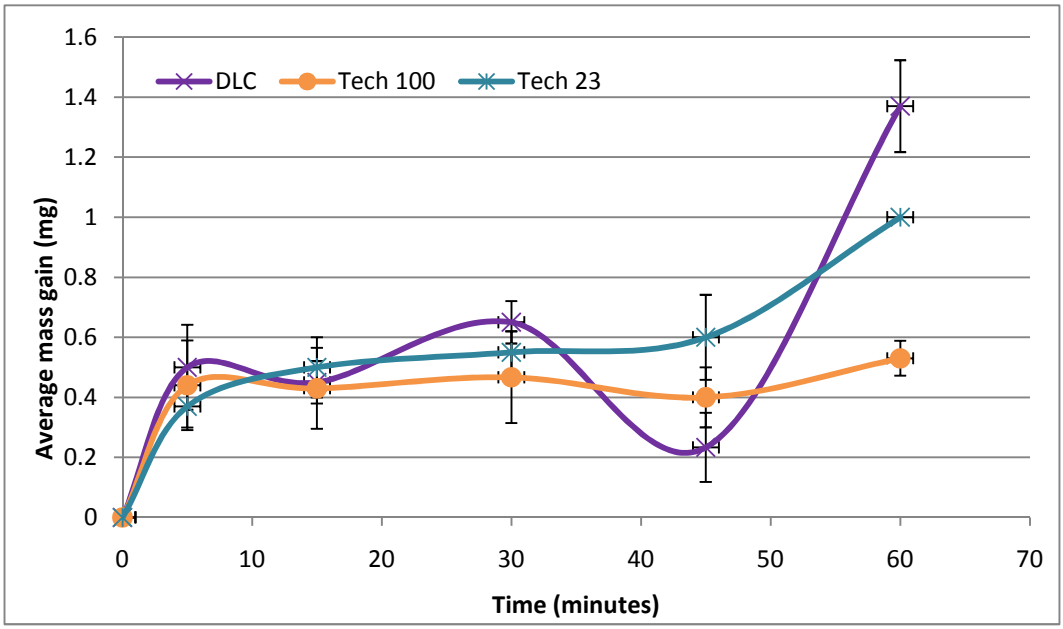

Figure 4.10: Deposition at various time intervals for coatings

Bulk scaling commences immediately as the two incompatible brines are mixed due to the high supersaturation i.e. high thermodynamic driving force. The rate at which the bulk precipitates is much faster than the rate of surface deposition which is driven by diffusion of ions and hydrodynamic forces [262]. Since particles appear after the shortest exposure time of 5 minutes, the induction time for scale formation must be less than 5 minutes for all materials. While some areas of the particles seen on the surfaces appeared to be of single crystal type and showed planar surfaces, other areas were clearly polycrystalline. It can be observed also that there are more apricot shaped calcium carbonate (vaterite) observed on the DLC coating (Figure 4.11f). Another interesting phenomenon is that the crystals on polymer MSi (Figure 4.11bi, Figure 4.12b and Figure 4.13b) displayed irregular morphologies and showed a tendency to clump together and this behaviour persists for tests carried out at other time intervals too; the formation of metastable phases during spontaneous precipitation from highly supersaturated solution is quite common [80]. The preference of polymorphs formation for calcium carbonate is mainly determined by the precipitation condition, such as pH, temperature and supersaturation [263, 264]. In addition, all the needlie-like crystals that

precipitated on the surfaces were mostly mis-shapen cylinders that frequently exhibited crystalline faces.

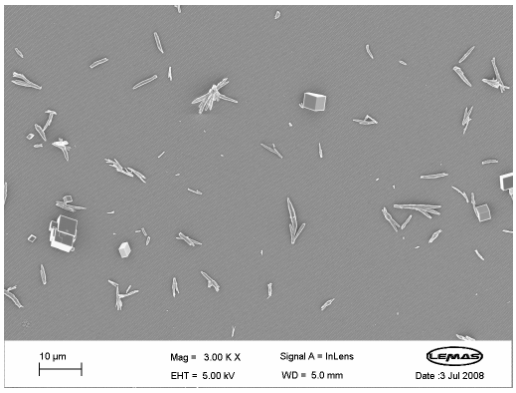

Figure 4.11ai: 5 minute deposition test for polymer MN

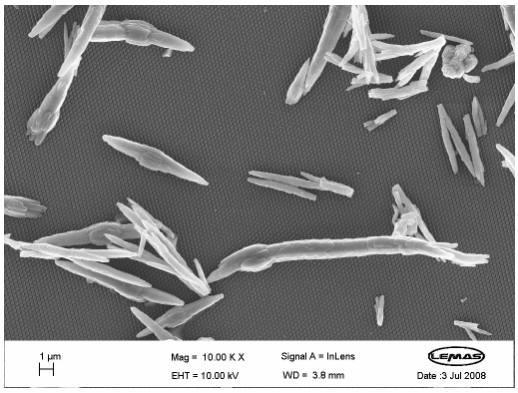

Figure 4.11aii: Highner magnification of crystals on polymer MN

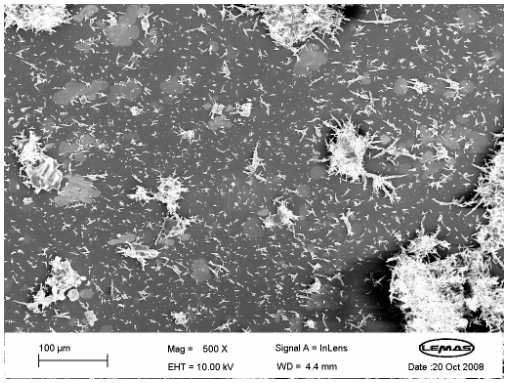

Figure 4.11bi: 5 minute deposition test for polymer MSi

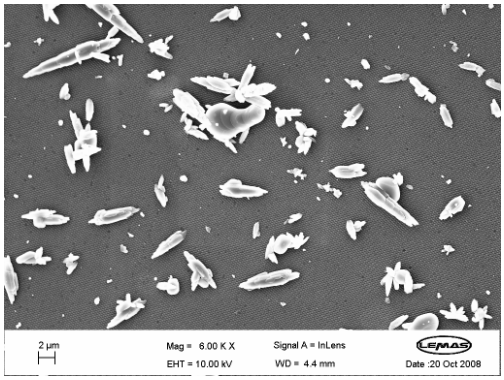

Figure 4.11bii: Higher magnification of crystals on polymer MSi

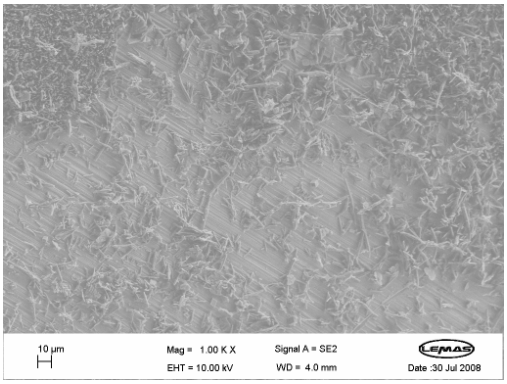

Figure 4.11c: 5 minute deposition test for stainless steel

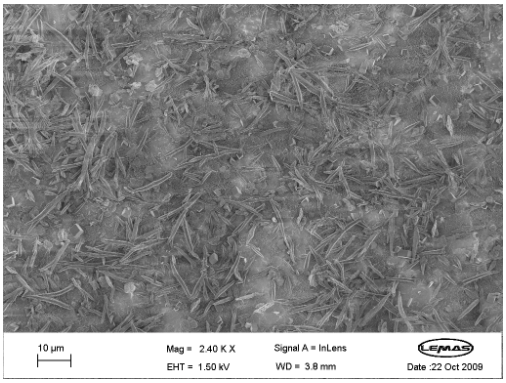

Figure 4.11d: 5 min deposition test for Tech 23

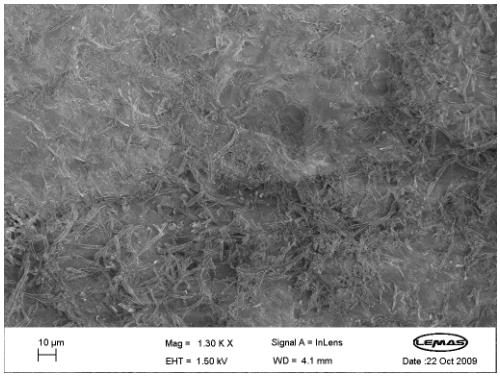

Figure 4.11ei: 5 minute deposition test for Tech 100

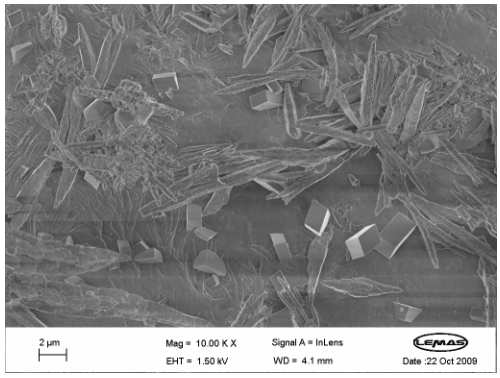

Figure 4.11eii: Higher magnification of crystals on Tech 100

Figure 4.11fi: 5 minute deposition test for DLC

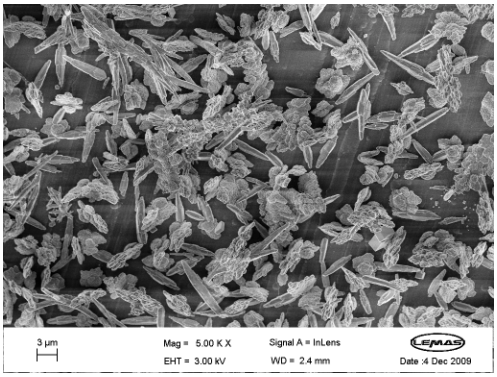

Figure 4.11fii: Higher magnfication for crystals on DLC

Figure 4.11: SEM Images of 5 min deposition tests

The bare Tech 100 coated surface is observed to have tiny pores of 10µm in diameter or more visible on the surface which when exposed to scaling crystals appear to grow around these holes (Figure 4.12e). However, with higher magnification, Figure 4.13e, calcite crystals that are of 2µm in dimension are observed to be lying in the pore itself. The crystals may have been deposited from the bulk solution and in the case of the crystals growing from the surface, the planar faces are parallel thus demonstrating that the particle is a single crystal and therefore it must have formed from a single nucleation site.

The stainless steel surfaces used in the study are rough and have distinct parallel corrugations due to the manufacturing process, the surface grooves do not seem to affect the way the crystals are oriented on the surface. After being immersed from 15 minutes to half an hour, the surface was already

peppered with little crystals as the underlying layer and the needle-like crystals occasionally extended upwards (Figure 4.11c, Figure 4.12c and Figure 4.13c)

In Figure 4.13di which shows the crystal surface coverage on the Tech 23 coating after 30 minutes, it can be seen that there is still a large area of unscaled surface on the Tech 23 coating after 30 minutes have elapsed. Likewise, the crystals on the polymers MN and MSi do not cover the surface homogeneously. Notably for polymer MN, vaterite crystals can still be seen after 15 and 30 minutes (Figure 4.12aii and Figure 4.13aii). Meanwhile, the crystals on polymer MSi are misshapen and intergrow up to 20-30µm in dimensions and there are some smaller needle-like whiskers appearing to be aragonite that are incorporated into the bigger crystals.

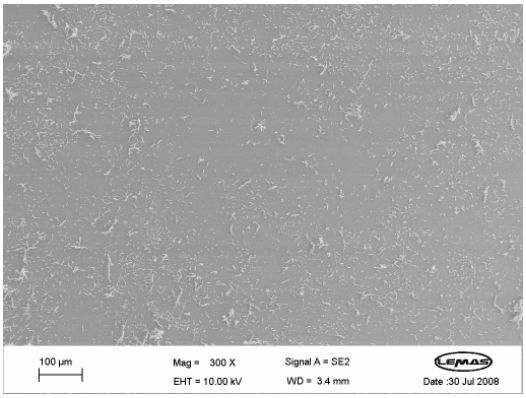

Figure 4.12ai: 15 min deposition test on polymer MN

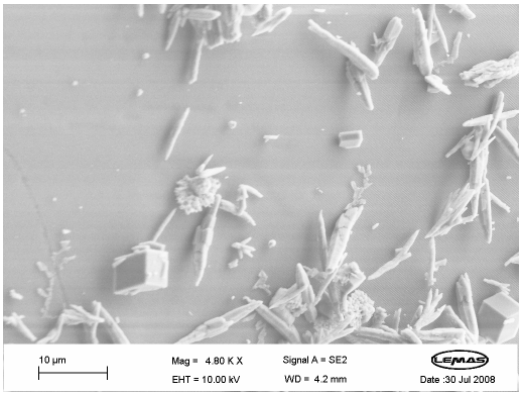

Figure 4.12aii: Higher magnification of crystals on polymer MN

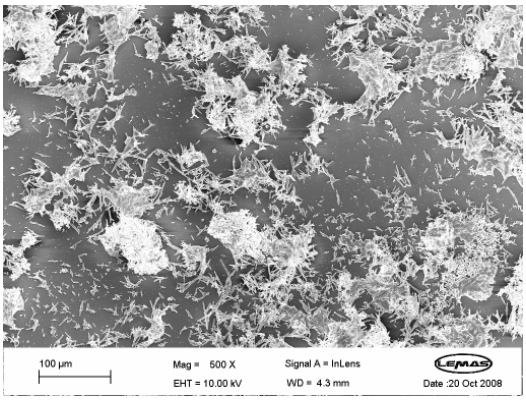

Figure 4.12bi: 15 min deposition test on polymer MSi

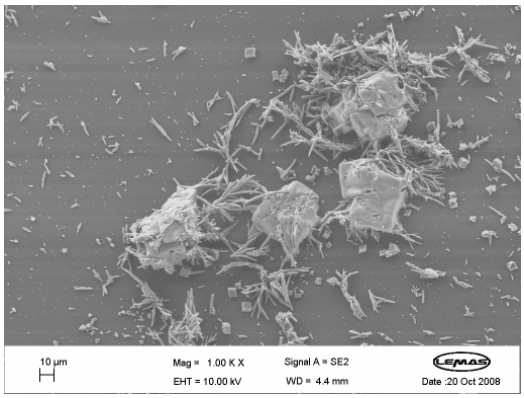

Figure 4.12bii: Higher magnification of crystals on polymer MSi

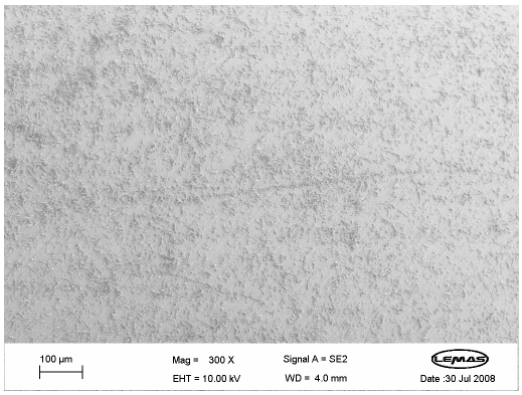

Figure 4.12ci: 15 min deposition test on stainless steel

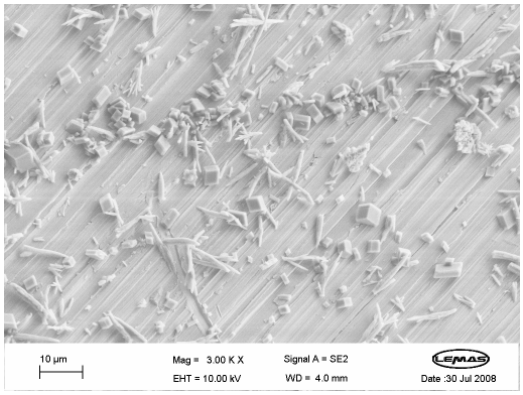

Figure 4.12cii: Higher magnification of crystals on stainless steel

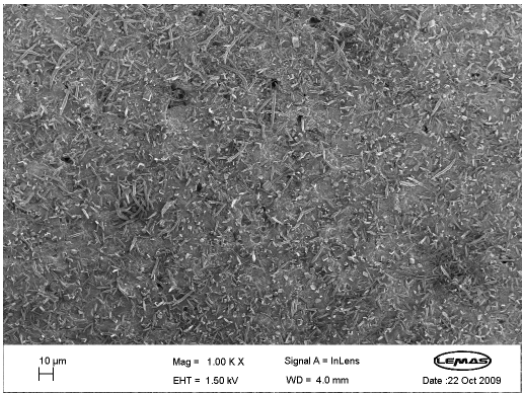

Figure 4.12d: 15 min deposition test on Tech 23

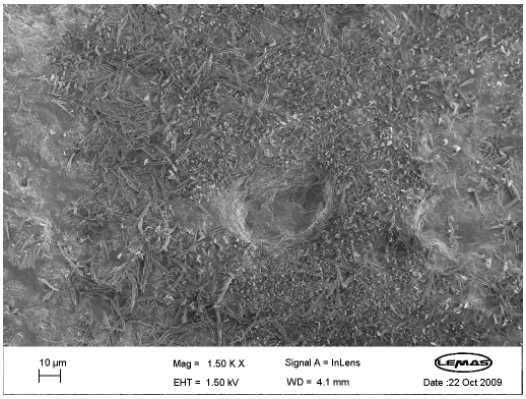

Figure 4.12ei: 15 min deposition test on Tech 100

Figure 4.12eii: Higher magnification of crystals on Tech 100

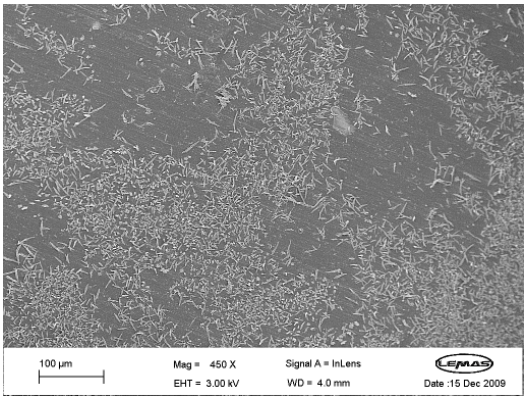

Figure 4.12fi: 15 min deposition test on DLC

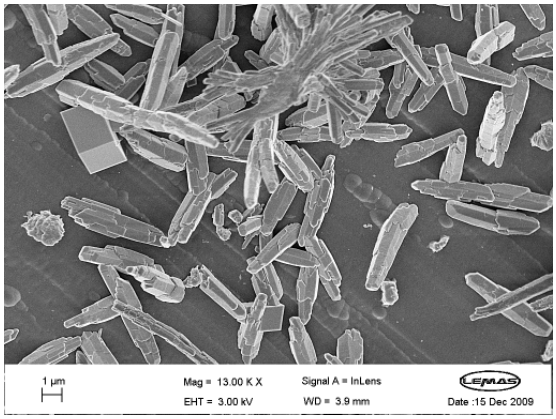

Figure 4.12fii: Higher magnification of crystals on DLC

Figure 4.12: SEM images of 15 minutes deposition tests. For all substrates, the original surface is still visible.

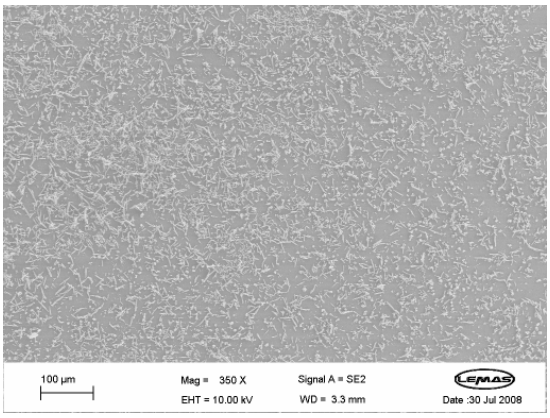

Figure 4.13ai: 30 min deposition test on polymer MN

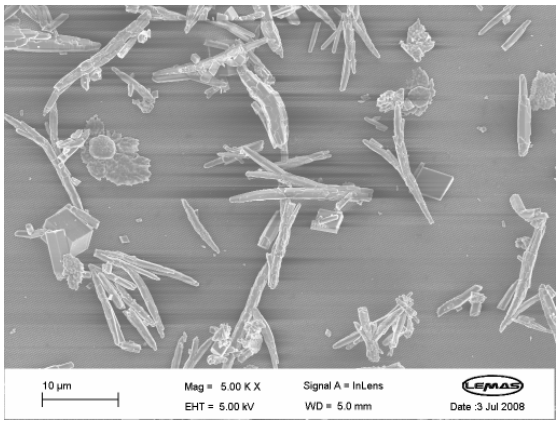

Figure 4.13aii) Higher magnifcation of crystals on polymer MN – vaterite crystals are present

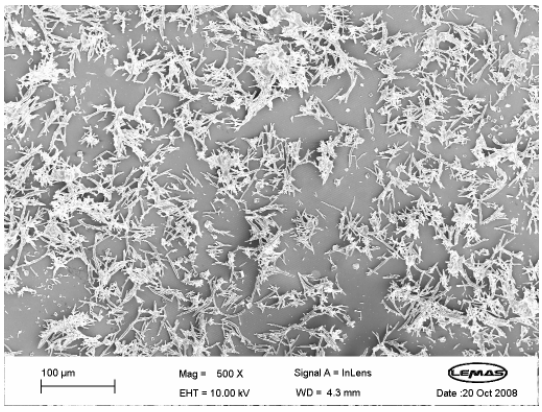

Figure 4.13b: 30 min deposition test on polymer MSi

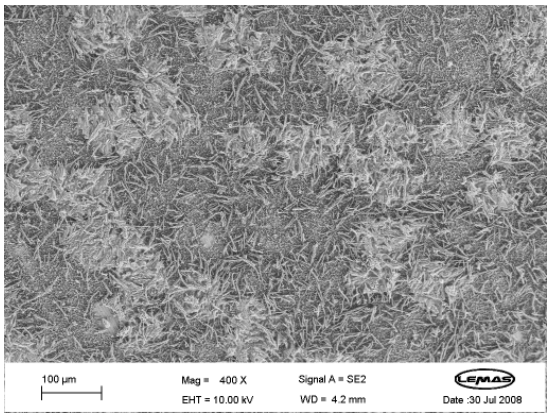

Figure 4.13c: 30 min deposition test on stainless steel

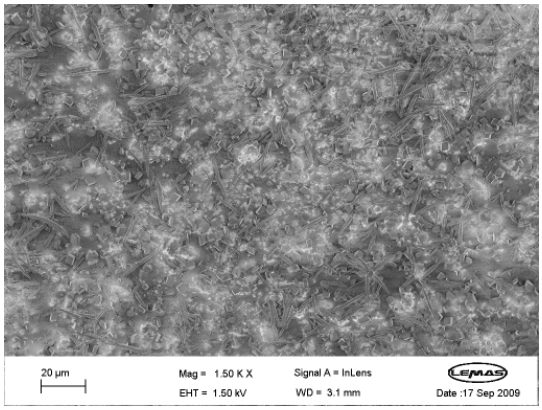

Figure 4.13di: 30 min deposition test on Tech 23

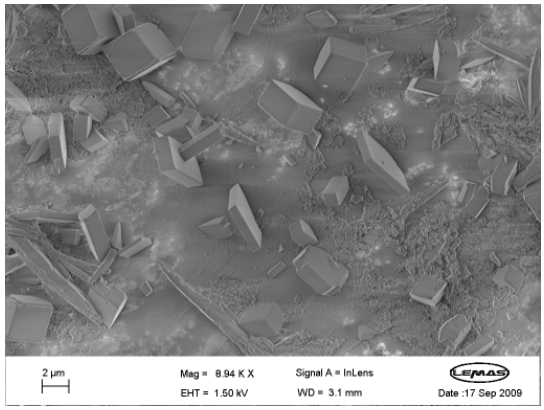

Figure 4.13dii: Higher magnification of crystals on Tech 23

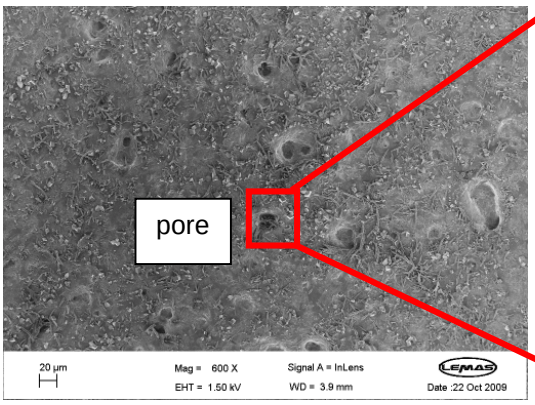

Figure 4.13ei: 30 min deposition on Tech 100

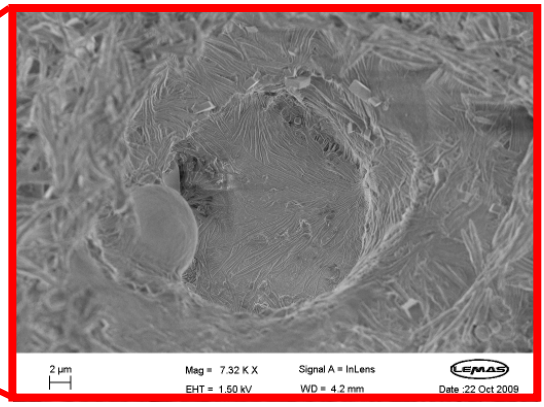

Figure 4.13eii: Little crystals grow inside the surface pores, crystals' tendency were to grow around the pores.

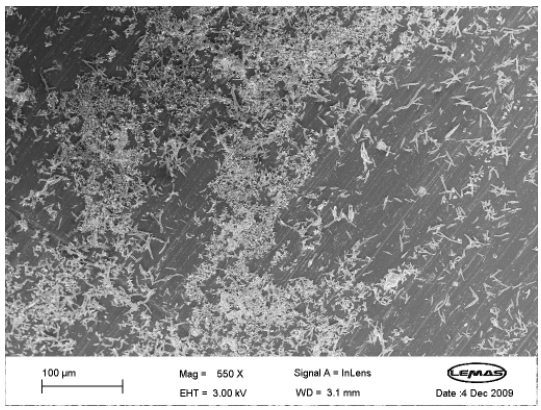

Figure 4.13fi: 30 min deposition test on DLC

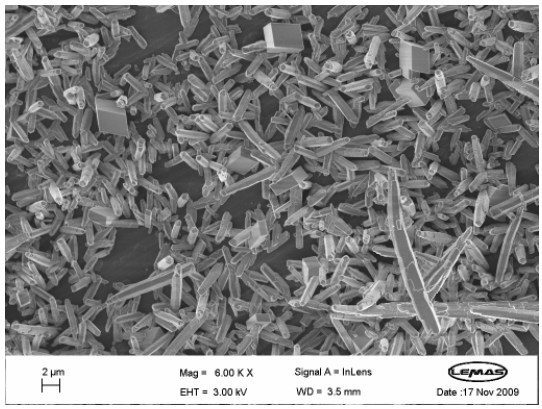

Figure 4.13fii: Higher magnification of crystals on DLC

Figure 4.13: SEM images of 30 min deposition tests

The scale deposited on the polymers is more loosely scattered and less dense relative to that on stainless steel. Once a thin layer of scale is formed, the scaled surface will have a higher surface roughness which promotes the

deposition process compared to a bare surface which has a lesser surface area. The turbulent mixing of the scaling solution may also promote scale formation where the scale forming species are adsorbed onto the surface which subsequently adhere to and are deposited on the substrate. In addition, it provides the activation energy required for the nucleation and growth of crystals.

Random growth of subsequent crystals emanating from already deposited existing crystals can be seen more clearly on the stainless steel surfaces and polymer MSi surfaces, whereas the same is less apparent on polymer MN surfaces. These crystals are growing at preferential nucleation sites readily available on the previously deposited scale layer.

Although polymer MSi is observed to have a densely packed scale similar to stainless steel after an hour, it is still more porous as bits of the polymer surface are visible. On the other hand, polymer MN performed the best with little scaling and with comparably less piling of crystals on top of each other even after an hour. The scale on polymer MN is randomly scattered and there is quite a huge visible area of polymer surface remaining at each time. This behaviour could be due to the polymer MN's surface having silica nanoparticles on top of its egg-boxed surface structures (Figure 4.15) which renders its surface as having a dual-scale roughness, thus contributing to its low adhesion of scale which can be easily removed by shear forces in a turbulent flow.

In addition, the needle-like crystals on the DLC coating seem to be shorter and rounder compared to the aragonite crystals on other surfaces where they seem to be longer and intertwined.

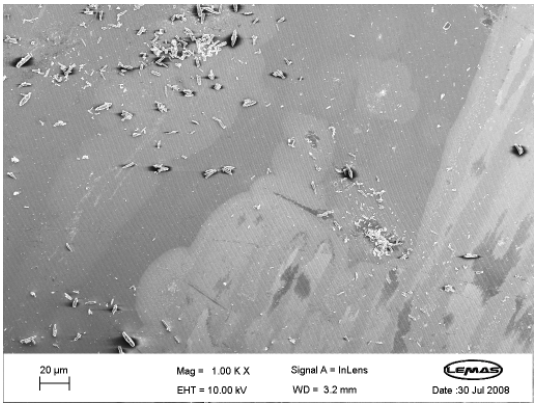

Figure 4.14a: 45 min deposition test on polymer MN

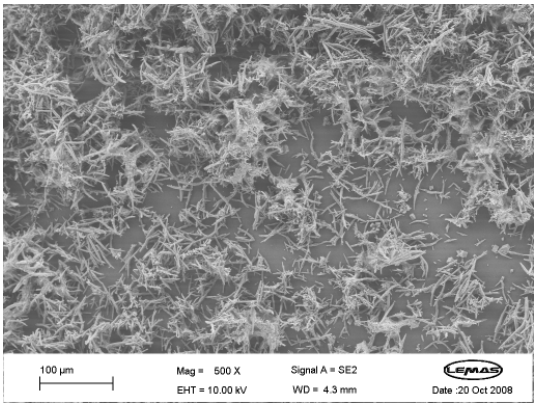

Figure 4.14bi: 45 min deposition test on polymer MSi

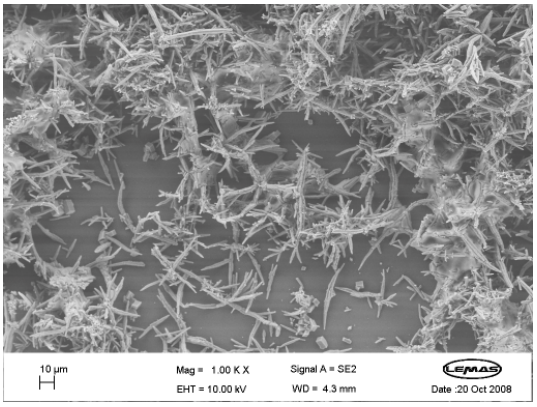

Figure 4.14bii: Higher magnfication of crystals on polymer MSi

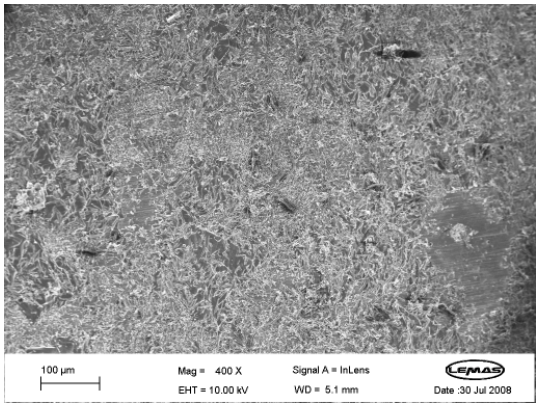

Figure 4.14c: 45 min deposition test on stainless steel

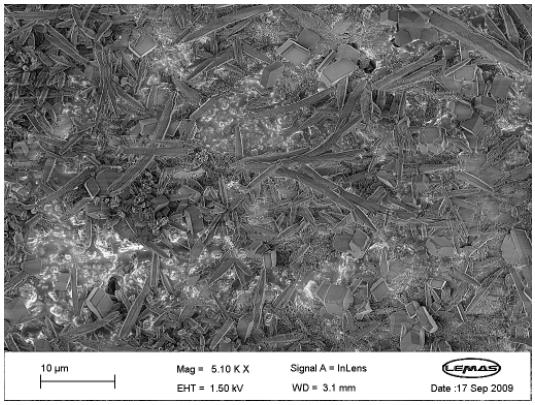

Figure 4.14d: 45 min deposition test on Tech 23

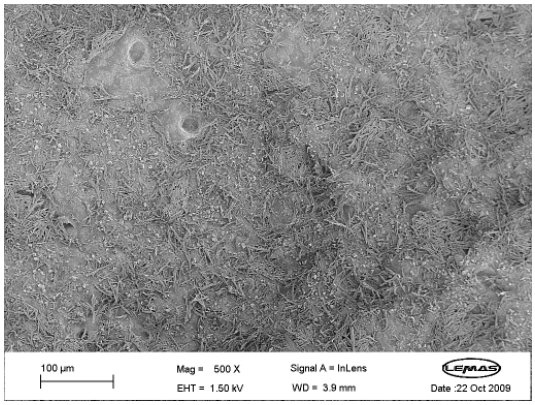

Figure 4.14e: 45 min deposition test on Tech 100

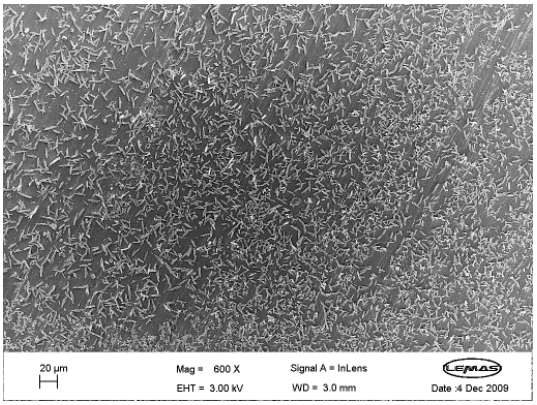

Figure 4.14fi: 45 min deposition test on DLC

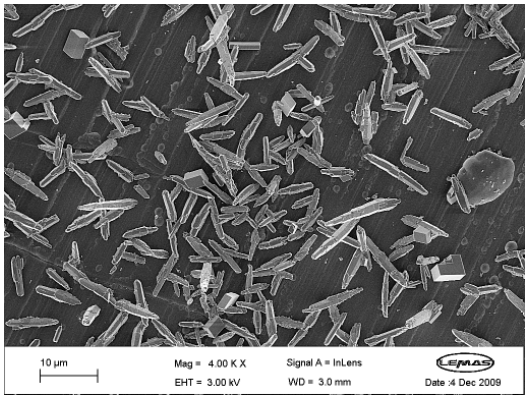

Figure 4.14fii: Higher magnification of crystals on DLC

Figure 4.14: SEM images for 45 min deposition tests

Most natural scaling processes start by heterogeneous nucleation with many isolated and unconnected crystals forming on the substrates [265]. In the early stages of the scaling process, only a small area of the test substrates was found to be covered with deposits. With time, the deposits started to build up and form on top of each other as well as on the uncovered surface. This gives rise to an appreciable increase in the number of crystal growth sites available.

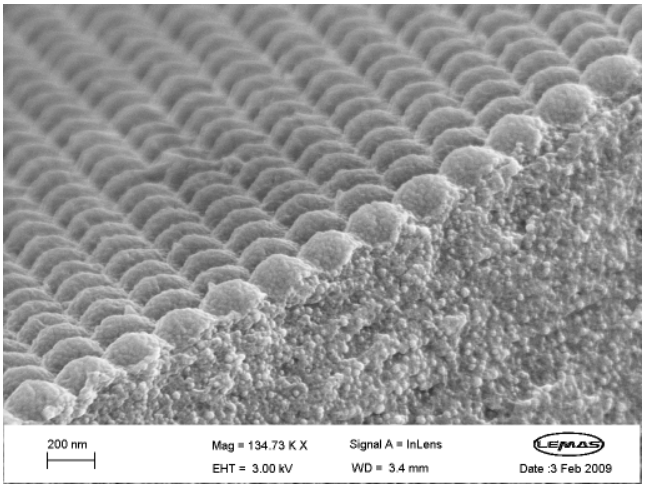

MN with silica nanoparticles on top of its microstructures to give it a hierarchical roughness

Figure 4.15: Egg box structure of polymer MN with silica nanobumps

4.2 Immersion of substrates after bulk precipitation is complete

One of the key questions that arises in studies of surface scaling is the nature of the formation of the scale on the surface. More specifically, whether the scale nucleates and grows on the surface or whether it settles on and adheres to the surface after having been formed in the bulk solution. To address this issue in the thesis some tests were done, as reported below, to assess the deposition on the surface once precipitation in the bulk solution had occurred and reached a steady state.

Here the surfaces were immersed 15 minutes after the brines were mixed at which time the crystals would have fully precipitated in the bulk solution. This was determined by a turbidity test and ICP tests confirmed that the supersaturation index was still greater than 0 indicating the solution to be still supersaturated, as shown in Figure 4.16. The aim is to see if scale grows from the surface instead of settling from the bulk precipitation when the solution is still supersaturated.

Deposition formed on the metal surface and precipitation formed in the bulk solution; being two different processes, each has its own mechanisms and kinetics [39, 229]. The precipitation of calcium carbonate in the bulk solution has been widely studied. However in recent years, focus has been shifted more onto the relationship between precipitation and scale deposition or adhesion on solid surfaces [39, 229, 266-268]. Nevertheless, uncertainties in the shape of the nucleus as well as the interfacial energies make predicting the heterogeneous nucleation rates on different surfaces a challenge [269].

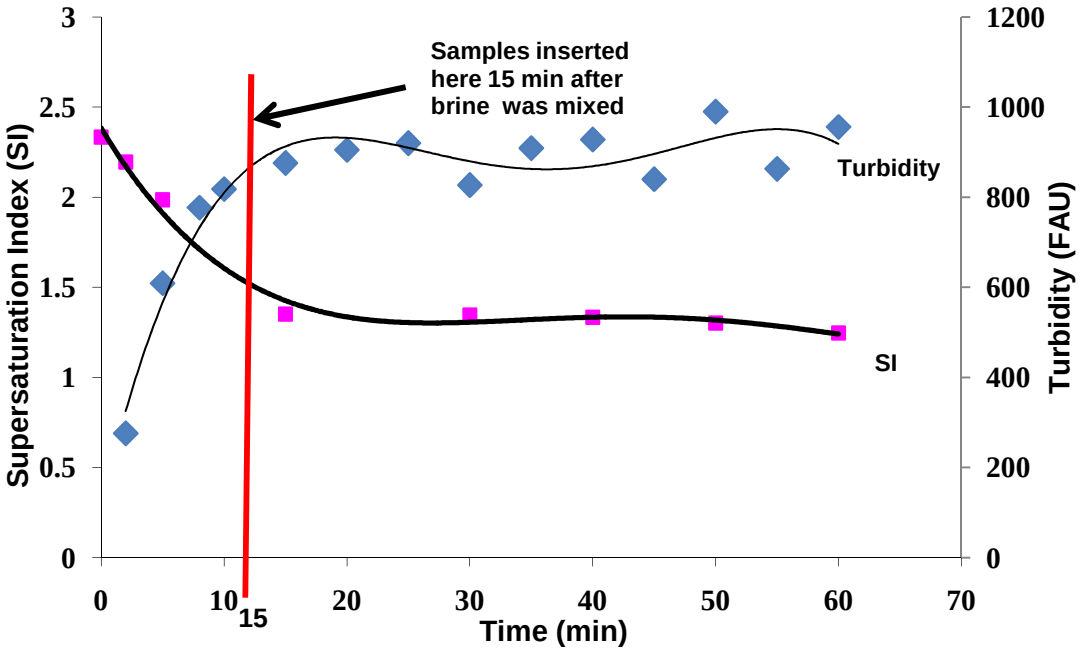

Figure 4.16: All test surfaces were inserted 15 min after brine mixing

The substrates were immersed in the scaling solution for 5 minutes and for an hour and weight measurements indicated negligible mass gain ranging from 0.1-0.2mg for all substrates. Corresponding SEM images are shown in Figure 4.17 and Figure 4.18.

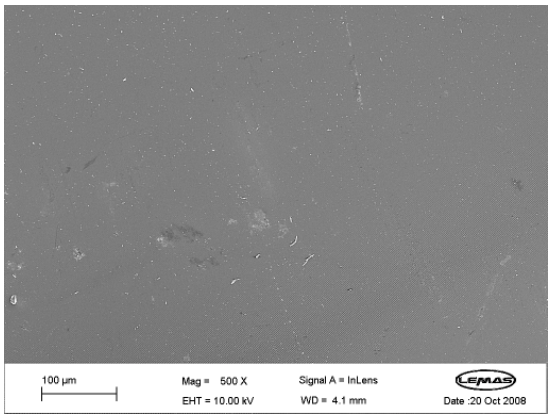

Figure 4.17ai: Polymer MN after 5 minutes

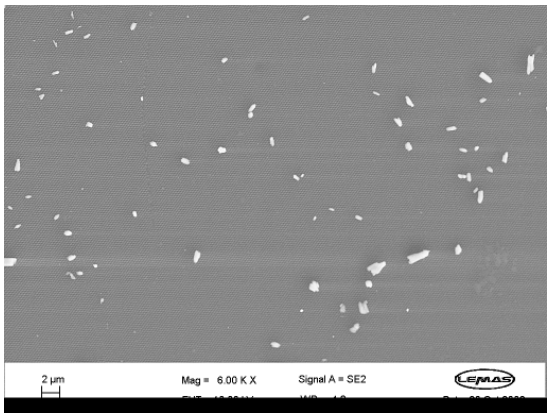

Figure 4.17aii: 1-2µm crystals on polymer MN after 5 minutes

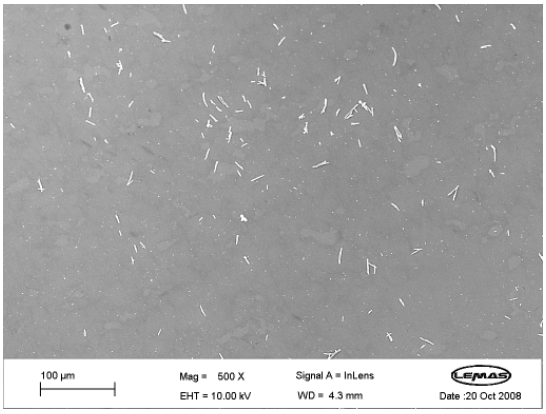

Figure 4.17bi: Polymer MSi after 5 minutes

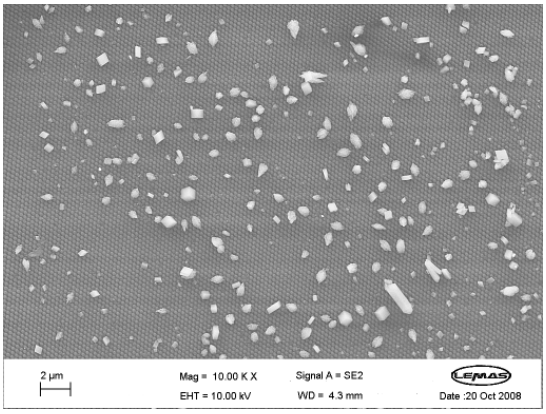

Figure 4.17bii: Higher magnification of crystals on polymer MSi

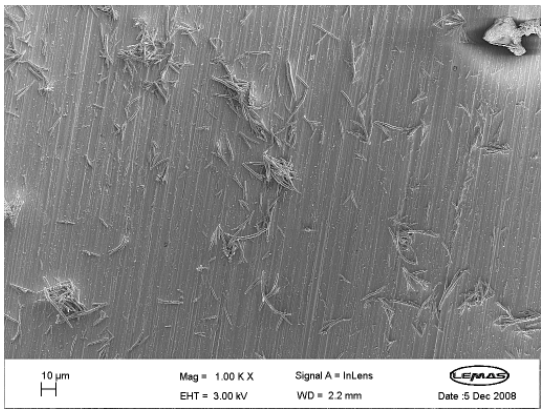

Figure 4.17ci: Stainless steel after 5 minutes

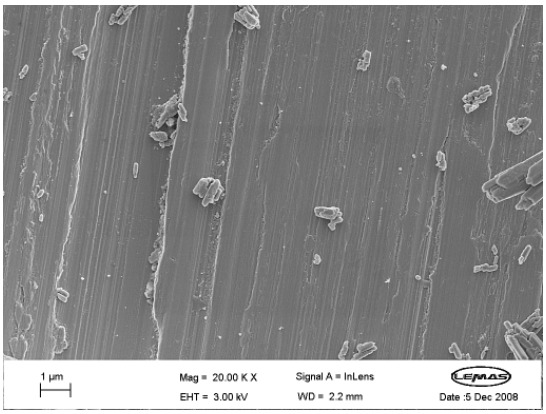

Figure 4.17cii: Smaller crystals were present on steel surface in addition to aragonite crystals

Figure 4.17: SEM images of samples after 5 min

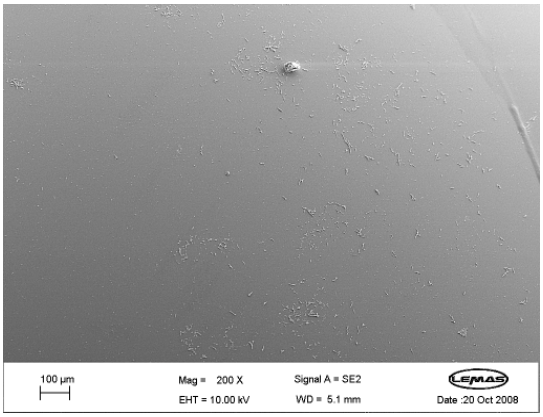

Figure 4.18ai: Polymer MN after an hour

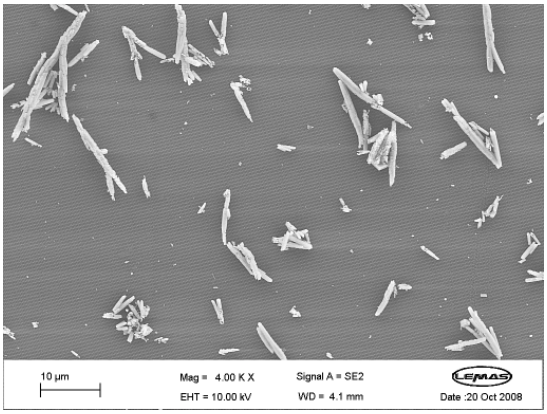

Figure 4.18aii: Higher magnification of crystals on polymer MN

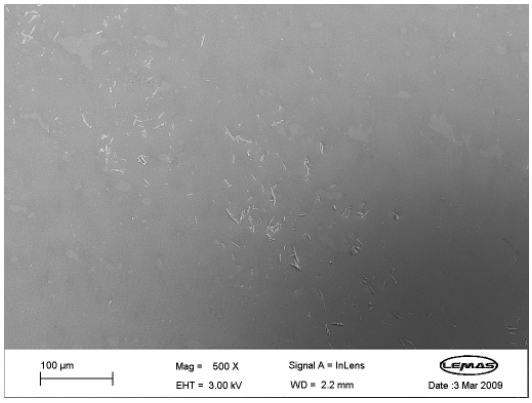

Figure 4.18bi: Polymer MSi after an hour

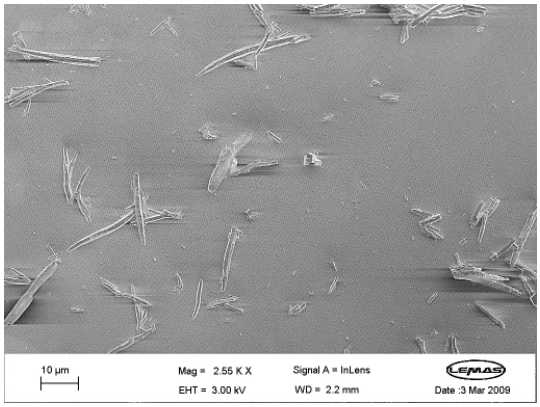

Figure 4.18bii: Higher magnification of crystals on polymer MSi

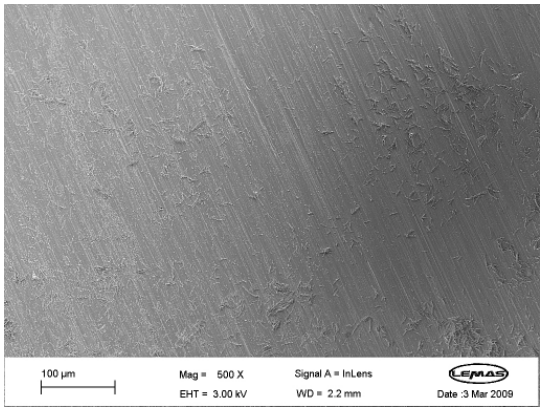

Figure 4.18ci: Stainless steel after an hour

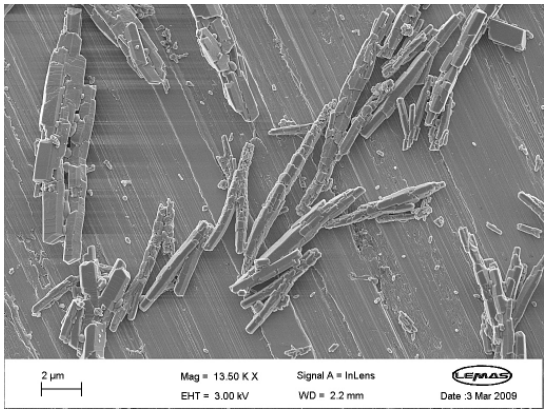

Figure 4.18cii: Higher magnification of crystals on stainless steel

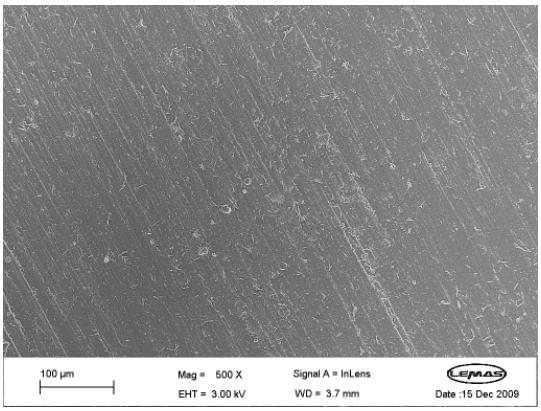

Figure 4.18di: DLC after an hour

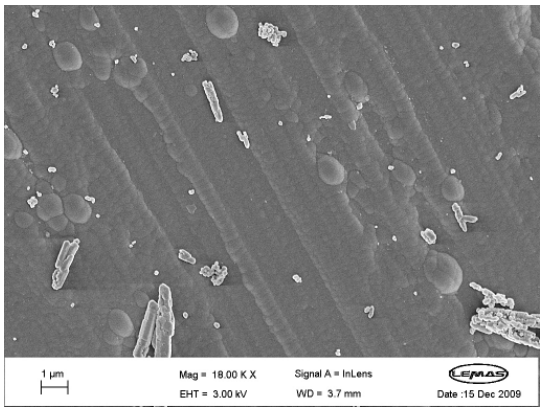

Figure 4.18dii: Higher magnification of crystals on DLC

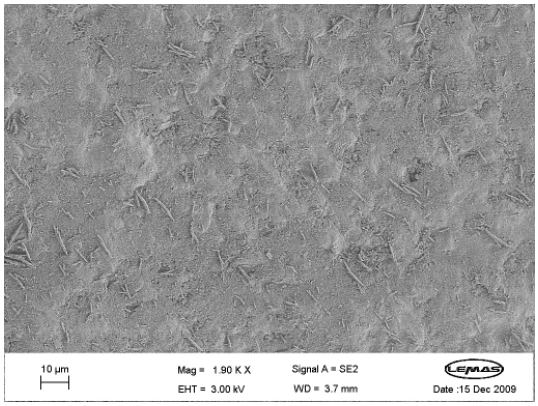

Figure 4.18ei: Tech 23 after an hour

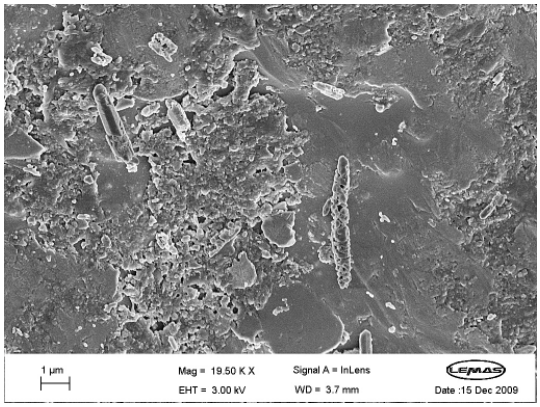

Figure 4.18eii: Higher magnification of crystals on Tech 23

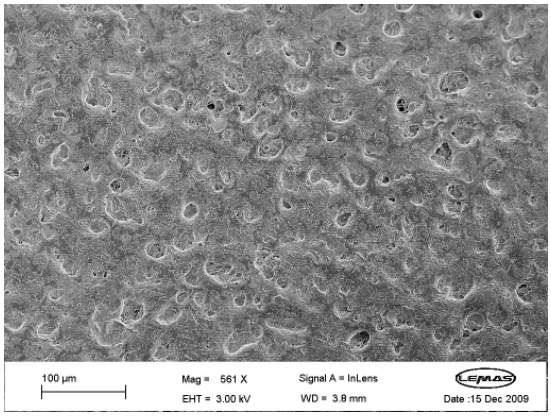

Figure 4.18fi: Tech 100 after an hour

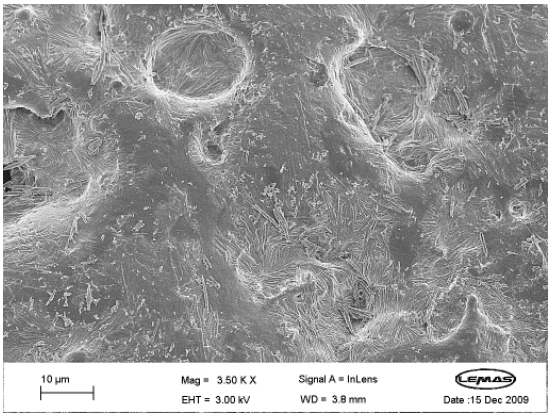

Figure 4.18fii: Higher magnification of crystals on Tech 100

Figure 4.18: SEM images of samples after an hour

The polymer surfaces, MN and MSi, show very little and scattered deposition (Figure 4.17a and Figure 4.18b). Similarly for stainless steel, the surface is not as densely covered with crystals as compared to earlier tests where the surfaces were immersed right from the start after brine mixing. A closer look at the surfaces shows that they are covered by crystals ranging in size from 2µm to 10µm which is contrary to the tests carried out in the previous section where the surfaces were mostly covered with clusters of crystals that are at least 10µm. SEM images of the bulk precipitate has shown that the precipitate is mainly comprised of aragonite at least 10µm long and very few calcite; these results show that once scaling in the bulk solution is complete, very little scale from the bulk actually adheres to the surfaces.

So far it has been shown that surfaces play an important role and act as important nucleation sites from which scale can grow, and surface modification can be considered in combination with chemical or mechanical removal for inhibition of scale. The supersaturation index for a pipe flow changes along its length and if the surface is modified at the pipe length where bulk precipitation is mostly complete, use of such structured surface can help reduce scale formation.

4.3 Micro-scale adhesion between surfaces and an aragonite crystal plate

In the previous section, it is conclusive that pre-formed scale did not seem to be a major factor – if there was a strong interaction between the crystals and the substrate it might be expected that there should be a link between adhesion and scale hence the aim of this section is to establish whether this link exists.

A study was carried out to determine if adhesion tests (conducted in a wet environment) can provide a reasonable measure of the tendency for scale deposition. Adhesion tests were designed for quantitative determination of calcium carbonate crystal adhesion to different substrate materials in a wet environment.

Adhesion tests were carried out on polished and rough surfaces of an aragonite crystal plate for which the surface roughness for each side is shown in Table 4.2. The rough side had approximately a 30 times higher surface roughness than the polished side.

Table 4.2: Surface roughness of aragonite crystal plate

Substrate	Surface Roughness (nm)
Polished aragonite surface	*18.7*
Polymer MSi	11.26
Polymer MF	7.68
Polymer MS	10.21
Polymer MN	8.63
Polymer MD	12.65
Stainless steel	120
DLC	144.45
Polymer LS	300
Rough aragonite surface	*565*
Tech 23	612.2
Tech 100	1508.9

Polymer MF has the lowest surface roughness i.e. it is the smoothest among the substrates used in the study; the rough aragonite surface was the third roughest with the coatings Tech 23 and Tech 100 being the roughest.

To obtain adhesion values, three consecutive adhesion tests were carried out on each surface and three surfaces of each substrate were tested. The flat crystal plate was 10mm by 10mm, similarly the test substrate was 10mm by 10mm in size. SEM images of the crystal plate are presented in Figure 4.19

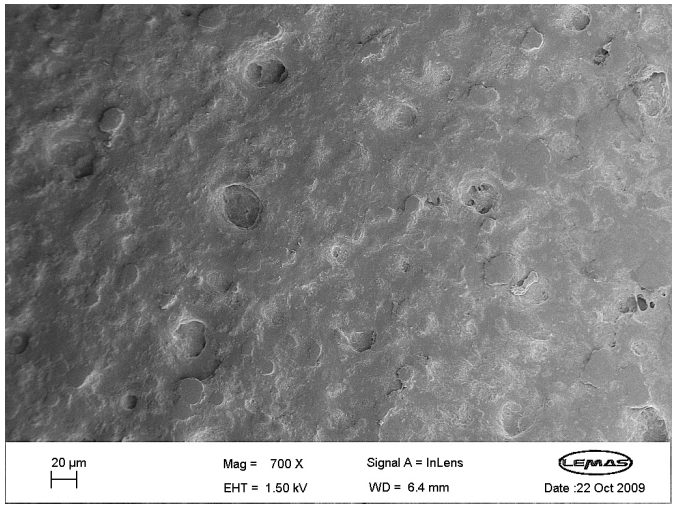

Figure 4.19a: Polished aragonite surface

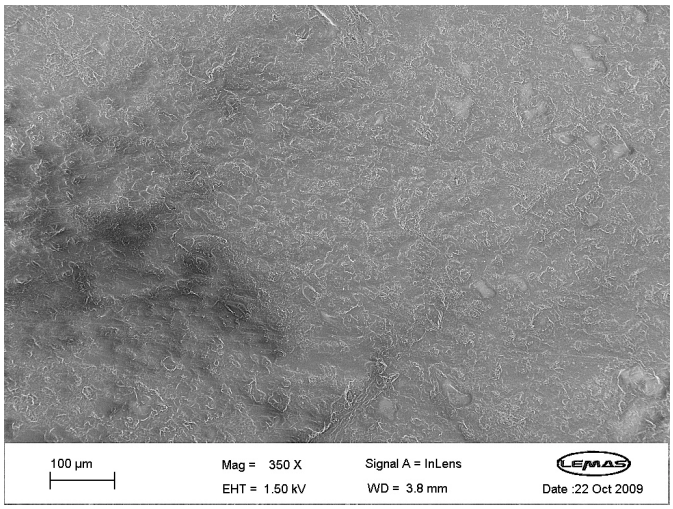

Figure 4.19b: Rough aragonite surface

Figure 4.19: SEM images of polished and rough aragonite crystal surface

The polished aragonite surface seems to have wide roughly circular pits along with smaller bumps as opposed to the rough aragonite surface which just has an irregularly roughened surface with no apparent pits and bumps. Adhesion phenomenon strongly depends on interfacial interactions thus the presence of interfacial defects due to surface geometries can affect wetting and adhesion [155].

Figure 4.20 represents the typical force-distance curves obtained from the MUST tester for the various surfaces adhering to the polished aragonite

crystal plate. It can be seen that the adhesion forces vary for the different substrates. The slope of each curve id dependent on the spring constant within the cantilever and the elastic modulus of the crystal plate.

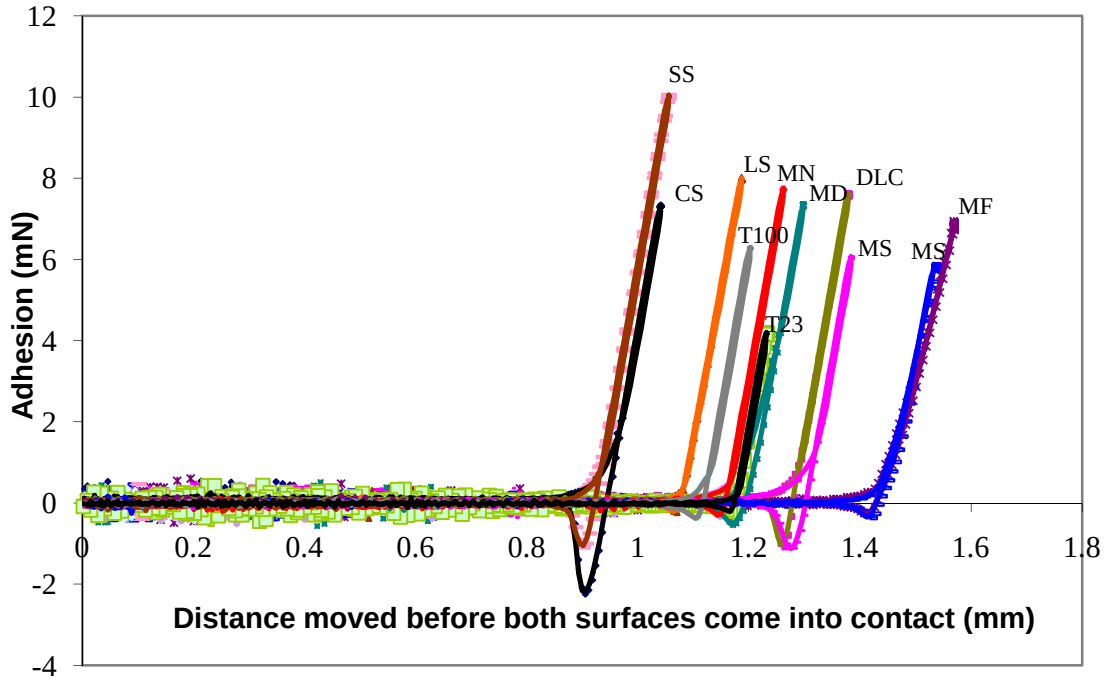

Figure 4.20: Force-distance curves obtained from MUST to obtain adhesion values

The mean adhesion values are shown in Figure 4.21 where a comparison is made between the adhesion between rough and polished crystal surfaces.

From Figure 4.21, it can be seen that generally the surfaces experience higher adhesion on the polished crystal surface except for the carbon steel, Tech 23 and Tech 100. The aim of the adhesion test is to assess whether it can be used to measure scaling tendency; if a surface is found to display high adhesion to the crystal plate, it would accordingly be expected to display high mass gain when exposed to scaling conditions in the rotating cylinder test. Nevertheless, the results so far seem to show that the adhesion test is not a feasible tool to assess scaling tendency, this can be seen in Figure 4.23. For the DLC coating and polymer MS, they had very low mass gain although they

had high adhesion values to the crystal plate. There is no obvious correlation within the polymers themselves too.

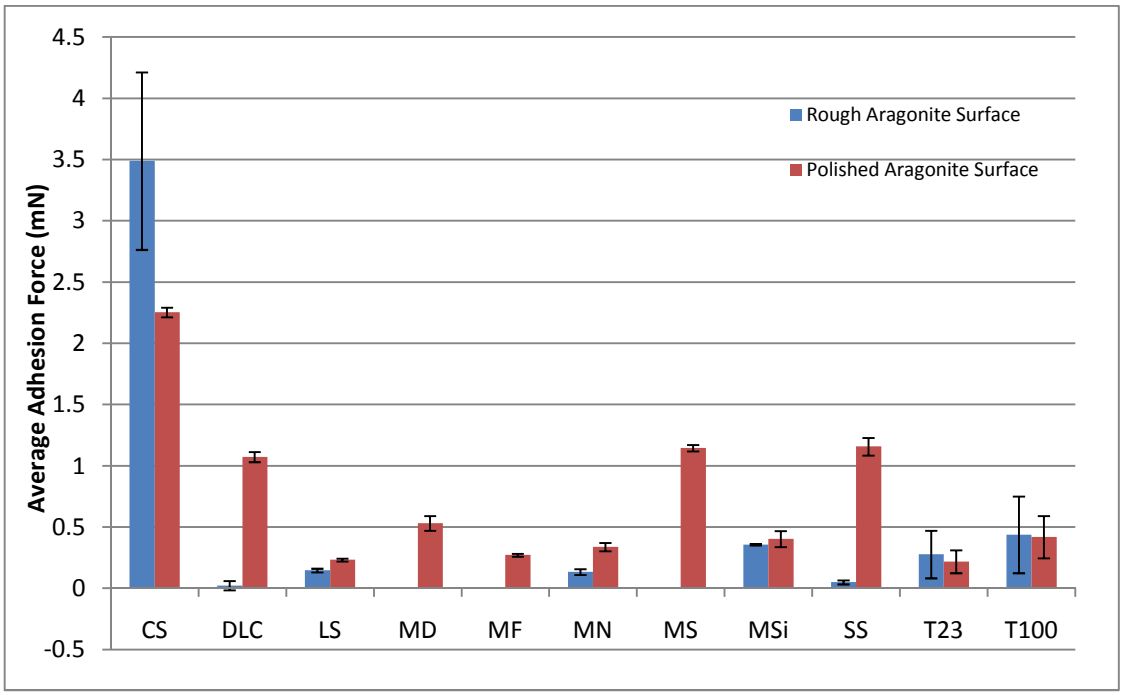

Figure 4.21: Average adhesion results for various surfaces

The water contact angle gives an estimate of the surface energy of the substrate. Superhydrophobic surfaces are often associated with low surface energy characterized by low adhesion and friction values. Hence, it would be expected here that higher water contact angles results in lower adhesion values. However, from Figure 4.22, the correlation observed is opposite to the general thinking. There is no discernable relationship for Figure 4.24and Figure 4.25 where a link between adhesion and surface roughness is not identified. Polymers having similar water contact angle values have varying adhesion values, likewise for the coatings where the Tech 23 coating had a lower adhesion although it was more hydrophobic than the Tech 100 coating.

Finally, higher adhesion would be expected for smoother surfaces as there is larger contact area between both substrates. Even though the Tech 100 coating was the roughest, it did not exhibit the lowest adhesion. The case for

the polymers is further represented in Figure 4.25. Polymer LS was the roughest among the polymers and had the lowest adhesion while the reference stainless steel substrate was the roughest among them and had the highest adhesion value. The rest of the polymers have varying adhesion values but have very similar surface roughness.

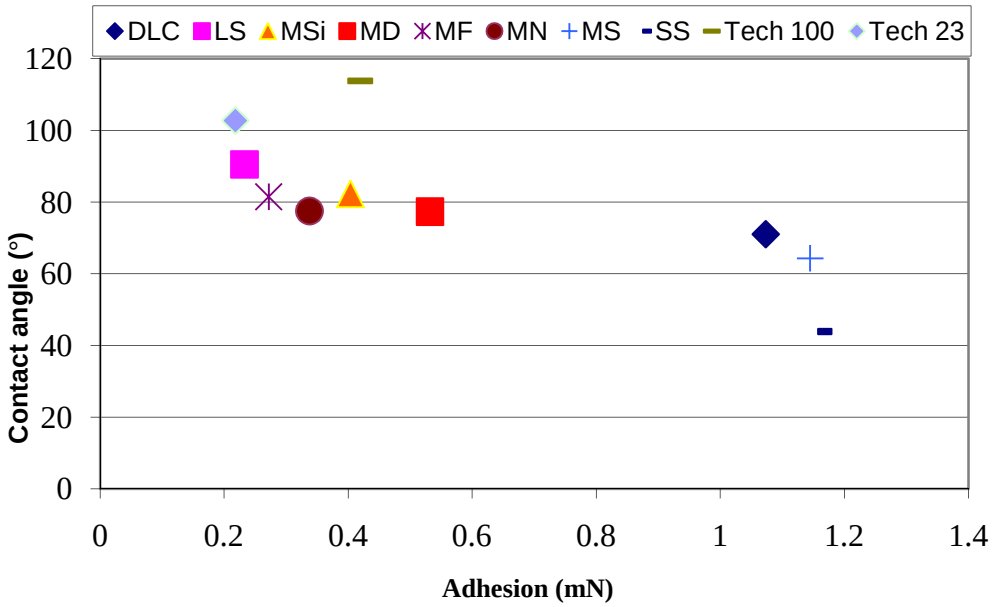

Figure 4.22: Adhesion (mN) vs. Water contact angle (°)

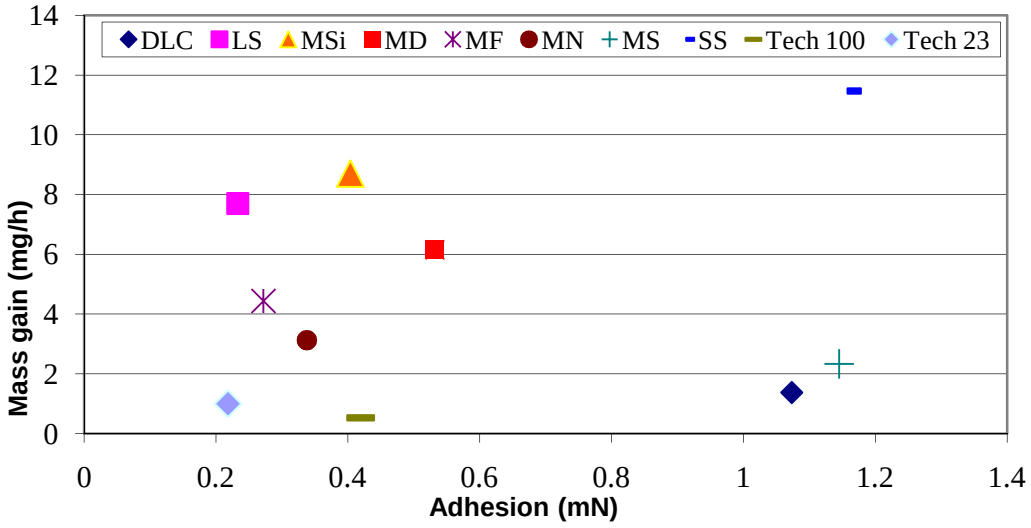

Figure 4.23: Adhesion (mN) vs. Mass gain (mg)

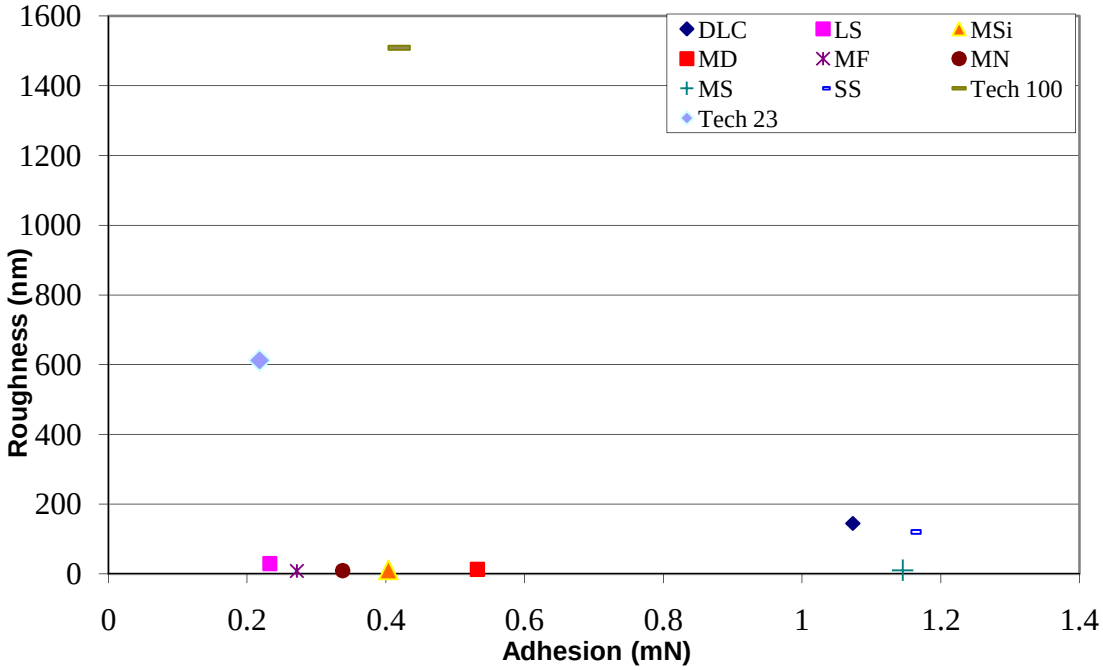

Figure 4.24: Adhesion (mN) vs. Surface Roughness (nm)

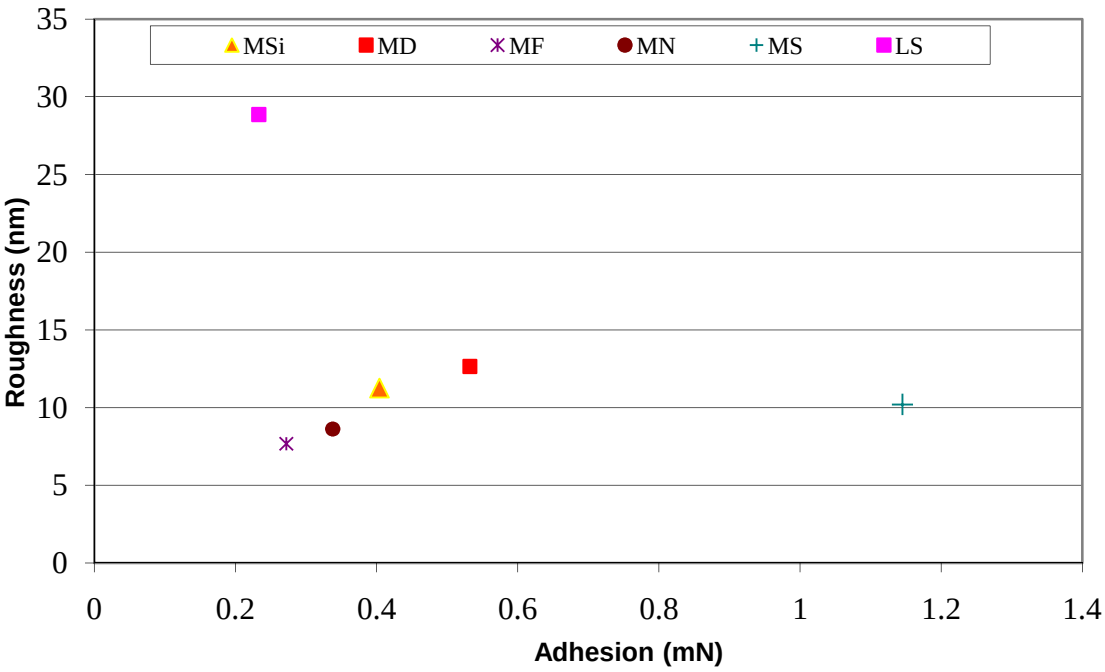

Figure 4.25: Adhesion (mN) vs. Surface Roughness (nm): Case study for polymers only.

4.4 Concluding remarks

The deposition tests carried out with the rotating cylinder electrode apparatus provide insight into the growth and deposition mechanism of calcium carbonate onto various substrates:

- The induction period is usually less than a minute in the bulk solution and nucleation is almost instantaneous for all the tests.

- The crystals mainly exhibit planar crystal faces and edges that are characteristic of crystalline calcite and the needle-like crystals are usually polycrystalline. Crystals that are mis-shapen or have irregular morphologies are most likely vaterite.

- The coatings (DLC, Tech 23 and Tech 100) have the least tendency to scale followed by polymers and stainless steel.

- The polymers which have the same surface topography have a range of performance which shows that surface chemistry also plays a role in affecting scaling tendency.

- Deposition tests carried out at earlier time intervals show the presence of vaterite on some surfaces which eventually transforms into the more stable calcite or aragonite.

- Almost all substrates have aragonite as the dominant crystal phase except for the coatings Tech 23 and Tech 100 which show mainly calcite growing on them.

- The crystals on the coated surfaces Tech 23 and Tech 100 have a tendency to grow around pores instead of inside the pores, and if they do, there is very little and seem to grow from isolated nucleation spots.

- The needle-like aragonite crystals on DLC have a lower aspect ratio i.e. shorter and rounder compared to the higher aspect ratio ones, i.e. longer and intertwined, on other surfaces.

- All the crystals formed are a lot larger than the surface asperities where crystals sit on top of them.

- Surface topography and arrangement (hexagonal or regular) affects deposition rate.

- The deposition tests can be translated into scaling rates (cm/year) which are useful in indicating the feasibility of a certain surface or material.

- Once bulk precipitation has occurred in the bulk solution it is found that very few crystals actually settled from the bulk and adhere to the surfaces even when the supersaturation index (SI) remained greater than 0.

- The crystals that grow or settle on the surfaces are a lot smaller than the crystals on the surfaces for the case when the surfaces were immediately immersed after brine mixing.

- Micro-adhesion tests between the various substrates and the rough and polished aragonite crystal plate were not an effective measure of scaling tendency.

The next chapter focuses on the effects of hydrodynamic forces on calcium carbonate adhesion.

Chapter 5
Hydrodynamic effects on surface adhesion

Previous studies were carried out at an hour and time intervals before an hour at rotational speeds of 1800rpm. As mentioned earlier, the rotating cylinder electrode (RCE) was selected as it has controlled hydrodynamic conditions; equations for mass transfer and wall shear stress are well defined. In addition, a fully developed wall shear stress is uniform over the entire surface of the cylinder under test. Therefore, exposing the test substrates to various speeds ranging from laminar to turbulent flow allows us to assess the flow effects on deposition covering shear stresses and Reynolds numbers similar to that in pipe flows. Table 5.1 lists the velocity/rotation rate relationships for a typical RCE operating in pure water. For example, if water is flowing through a smooth 8-inch pipe at 0.3m/s, an RCE should be operated at about 155rpm to match the conditions in the pipe.

Table 5.1: The velocity/rotation rate relationships for a typical RCE operating in pure water.

Pipe velocity	Some typical pipe sizes (inches)					
(m/s)	2	4	6	8	10	12
0.03	*11*	*10*	*9*	*9*	*8*	*8*
0.09	*44*	*39*	*36*	*34*	*33*	*32*
0.15	*83*	*74*	*68*	*65*	*63*	*61*
0.21	*126*	*112*	*104*	*99*	*95*	*92*
0.3	*197*	*175*	*163*	*155*	*149*	*144*

The interaction of the solid surface with the violent, rapidly fluctuating nature of turbulent flow in the viscous region and diffusion boundary layer is the primary reason that mass transfer and wall shear stress are the fundamental hydrodynamic factors that define the effect of flow rate of scaling.

In this study, deposition tests were carried out for an hour at different rotational speeds – 10rpm, 900rpm and 1800rpm. The flow is laminar at 10rpm and turbulent for the other speeds. The hydrodynamic parameters at these speeds are shown in Table 5.2.

5.1 Calcium carbonate deposition at various rotational speeds

The polymers MN and MSi along with the various coatings (DLC, Tech 23 and Tech 100) were subjected to various rotational speeds with a stainless steel surface as a reference. Polymer MN was chosen because it had hierarchical surface roughness and the lowest scaling tendency while polymer MSi was the polymer with the highest scaling tendency. In addition, it would be useful to look at industrially available commercial coatings such as DLC, Tech 23 and Tech 100. The results for the tests are presented in Figure 5.1.

Table 5.2: Hydrodynamic parameters at various rotational speeds

Rotation speed (rpm)	**10**	**900**	**1800**
Viscous sublayer (μm)	6536	103.5	59.7
Diffusion layer (μm)	~65.36	~1.04	~0.60
Reynolds number	64	5800	11600
Wall shear stress (Pa)	0.000922	1.936	6.3

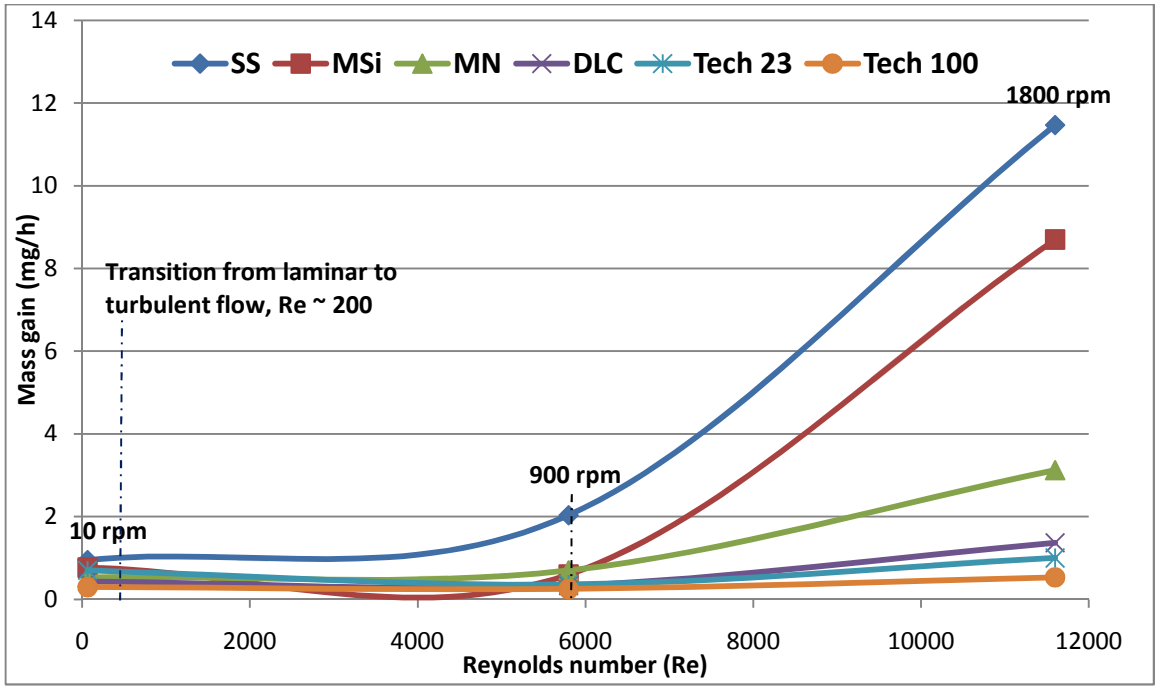

Figure 5.1: Average mass gain at various rotational speeds

It should be noted that the transition from laminar to turbulent flow is around 30rpm. There is no linear increase in mass gain as a function of Re for stainless steel and the polymers – a 8-times increase for polymer MSi, 3-times increase for polymer MN and almost a 12 times increase for stainless steel. The hydrodynamic effects on the scaling tendency for the coatings seem to be secondary for the coatings compared to the stainless steel and the polymers. A closer look at the variation in mass gain for the coatings is amplified in Figure 5.2.

From Figure 5.2, the scaling tendency was reduced when the speed was increased from 10rpm to 900rpm. This may be due to the increase in shear forces which removed crystals. This shear force removal effect is lost when the speed increased to 1800rpm. This will be further looked into in the discussion chapter.

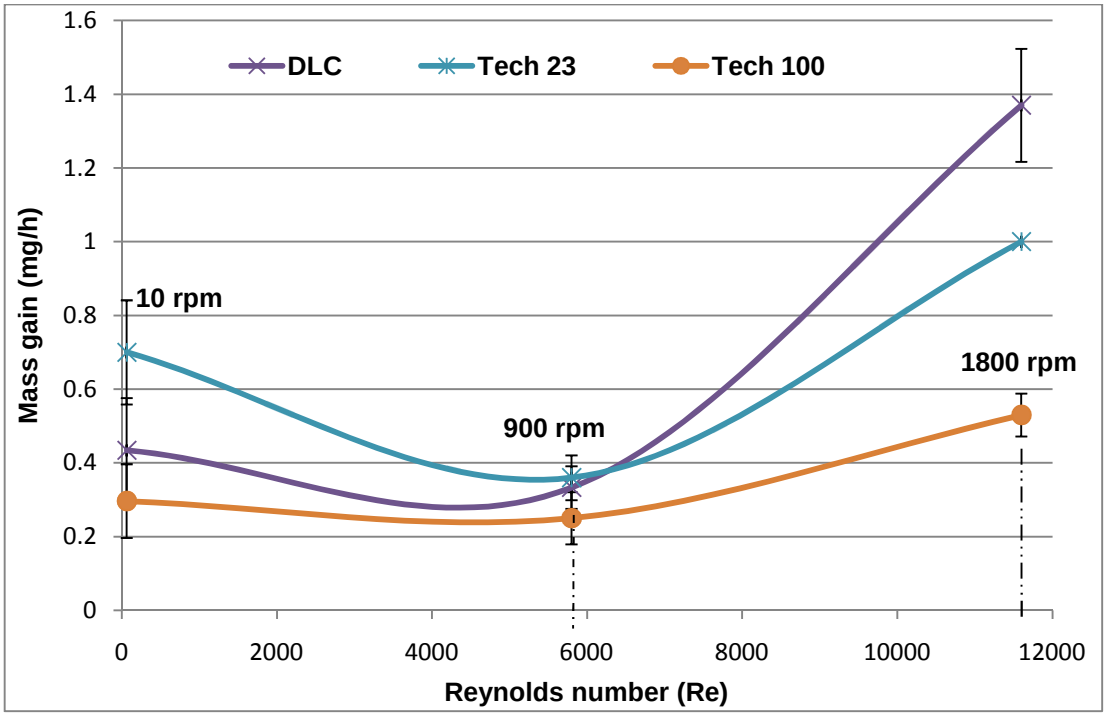

Figure 5.2: Variation in scaling tendency at various rotational speeds for coatings

Typical SEM images for the surfaces ranging from laminar flow (10rpm) to turbulent flow (1800rpm) carried out at 80°C are shown in Figure 5.3 to Figure 5.5. It is evident for most of the substrates with the exception of the coatings Tech 100 (Figure 5.3b) and Tech 23 (Figure 5.4a) that needle-like crystals characteristic of aragonite are the dominant polymorph. Otherwise, the proportion of calcite in the deposits on the coatings Tech 100 and 23 is considerably higher compared with the rest of the substrates. In addition, increasing the fluid velocity does not seem to affect the initial deposition pattern, although the deposition rate tends to increase with higher fluid velocity. While the needle-like crystals on the DLC surfaces (Figure 5.3a) tend to be limited to up to 10µm in length, the ones on stainless steel and the polymers tend to grow longer than 10µm and have a tendency to grow laterally and merge to form rather coherent clusters. The higher magnification images provided would offer a more distinct morphology of the crystals (Figure 5.6 to Figure 5.8) where it is clearly shown that fluid velocity does not have a marked effect on the dimensions of the crystals too.

The aragonite agglomerates tend to grow more rapidly than the calcite crystals which are usually found only next to the substrate as small 2µm grains; some examples can be seen in Figure 5.7ei and Figure 5.8eii. Furthermore, it is noted that these agglomerates eventually grow in a dendritic manner developing in the direction roughly perpendicular to the substrate (Figure 5.4biii, Figure 5.5aiii, biii).

Generally, the SEM micrographs of the planar view of these deposits give the impression that the crystals are irregularly laid on the deposit layer and several crystals protrude outward from the base layer especially for stainless steel and polymer MSi. Further observation with the higher magnification images seem to show that the initially randomly formed crystals grow in all directions until adjacent crystals contact each other (Figure 5.6b, Figure 5.7f, Figure 5.8f). Whereas the cohesiveness of the deposits on the coatings (DLC, Tech 23 and 100) seems inferior to that of the deposits formed on the polymers and stainless steel reference surface. The needle-like crystals deposited on the substrates were usually polycrystalline too.

At all rotational speeds, there is still evidence of visible surface except for stainless steel and polymer MSi at 1800rpm. Evidence of crystals being flipped over by shear forces can also be seen in Figure 5.10 where the bottom face of crystals is imprinted with the shape of the nanostructured polymer.

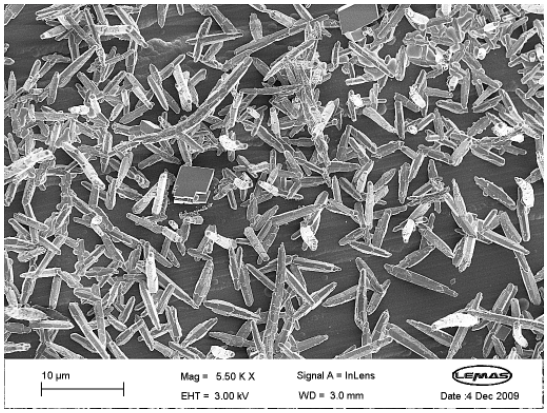

Figure 5.3ai: DLC at 10rpm

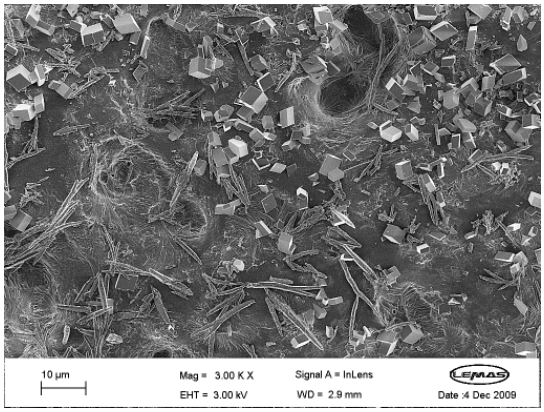

Figure 5.3bi: Tech 100 at 10rpm

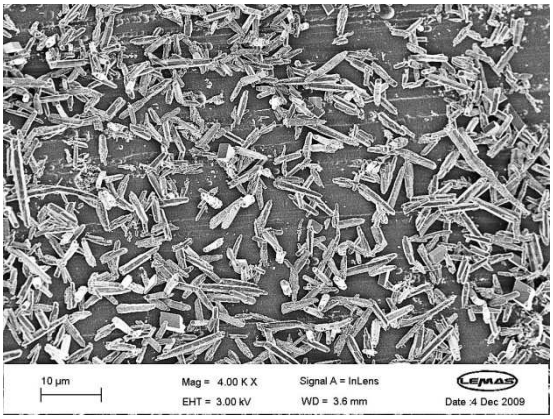

Figure 5.3aii: DLC at 900rpm

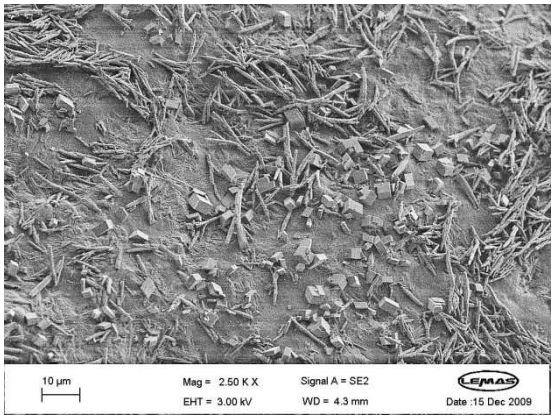

Figure 5.3bii: Tech 100 at 900rpm

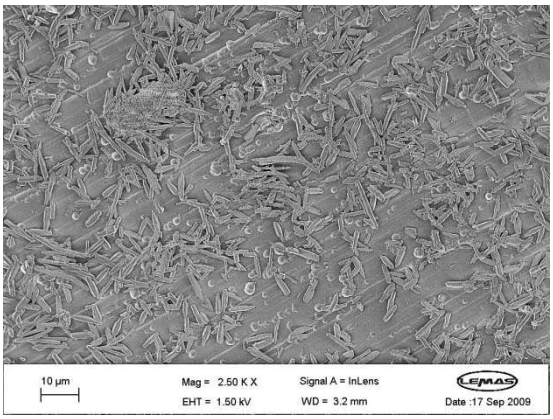

Figure 5.3aiii: DLC at 1800rpm

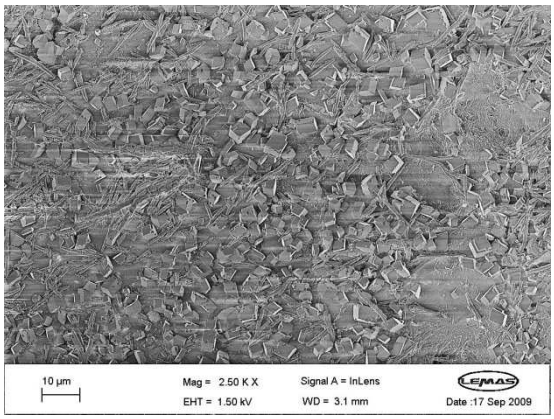

Figure 5.3biii: Tech 100 at 1800rpm

Figure 5.3: SEM images of the coatings DLC and Tech 100 at various rotational speeds ranging from 10 to 1800rpm.

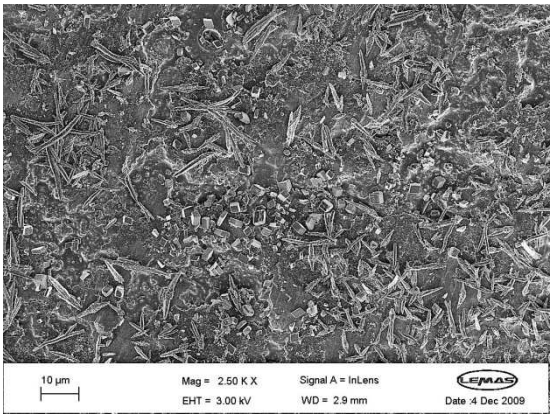

Figure 5.4ai: Tech 23 at 10rpm

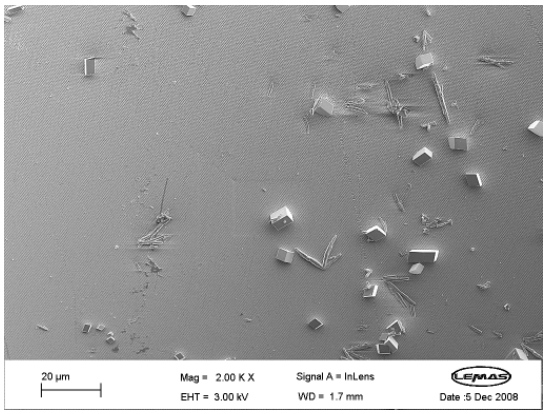

Figure 5.4bi: Polymer MN at 10rpm

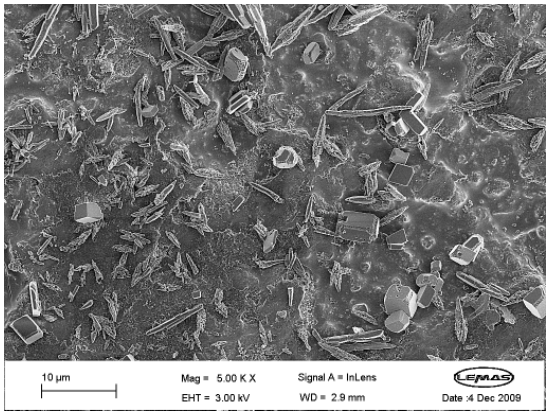

Figure 5.4aii: Tech 23 at 900rpm

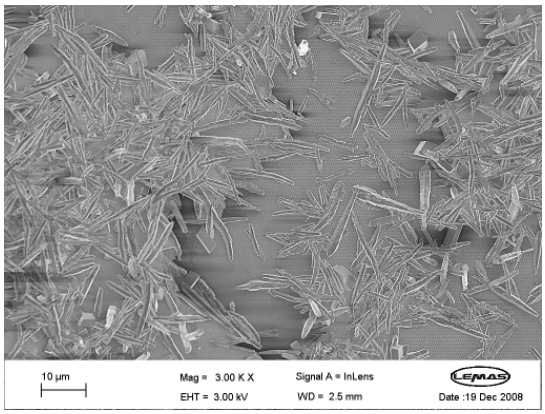

Figure 5.4bii: Polymer MN at 900rpm

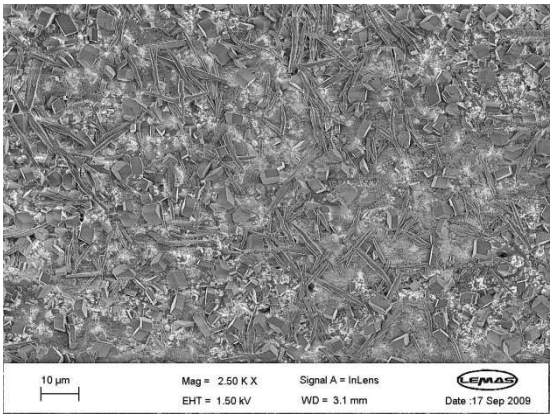

Figure 5.4aiii: Tech 23 at 1800 rpm

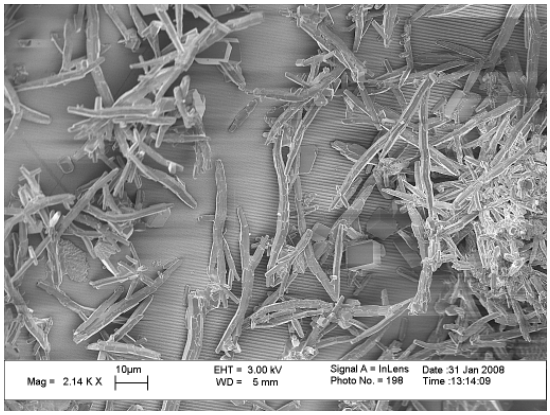

Figure 5.4biii: Polymer MN at 1800 rpm

Figure 5.4: SEM images of Tech 23 coating and polymer MN at various rotational speeds ranging from 10 to 1800rpm.

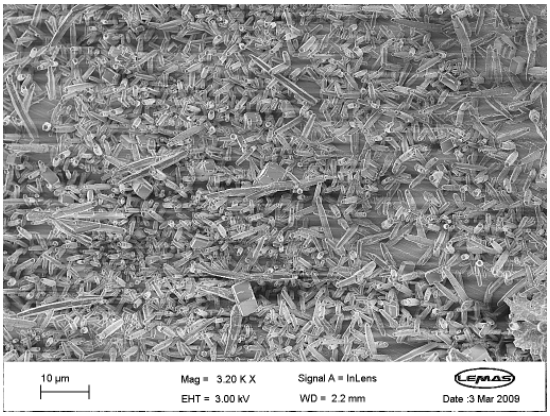

Figure 5.5ai: Stainless steel at 10rpm

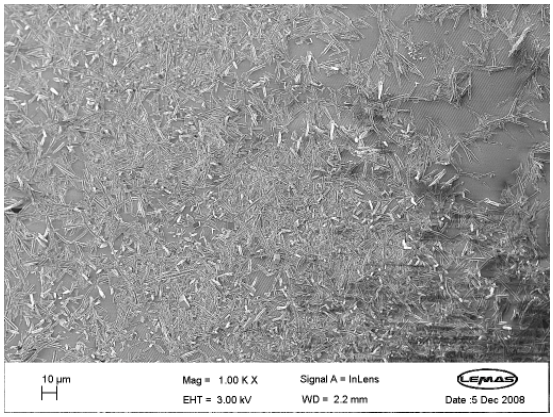

Figure 5.5bi: Polymer MSi 10rpm

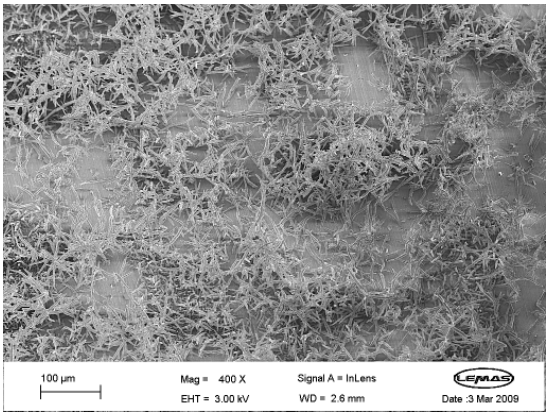

Figure 5.5aii: Stainless steel at 900rpm

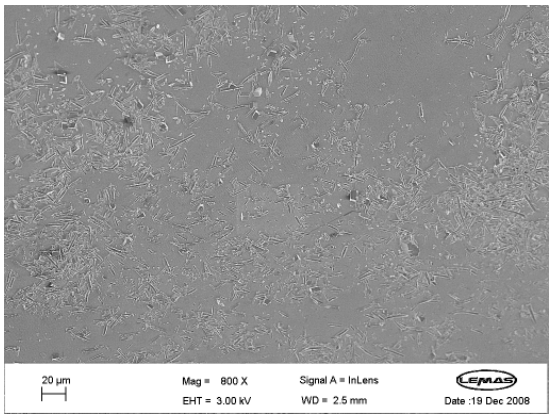

Figure 5.5bii: Polymer MSi at 900rpm

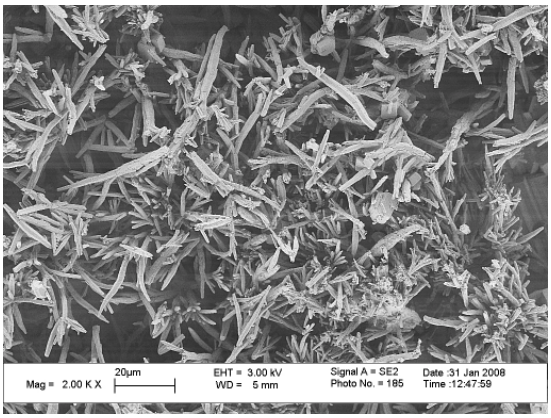

Figure 5.5aiii: Stainless steel at 1800rpm

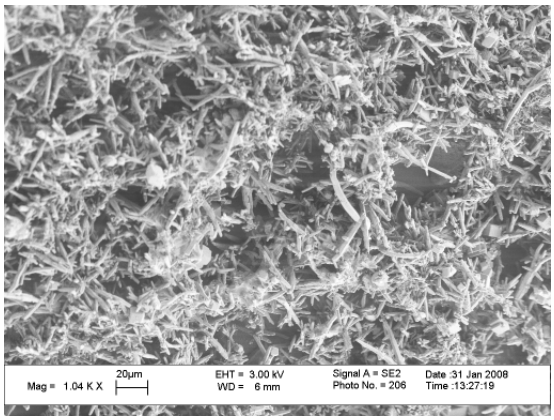

Figure 5.5biii: Polymer MSi at 1800rpm

Figure 5.5: SEM images of stainless steel and polymer MSi at various rotational speeds ranging from 10 to 1800rpm.

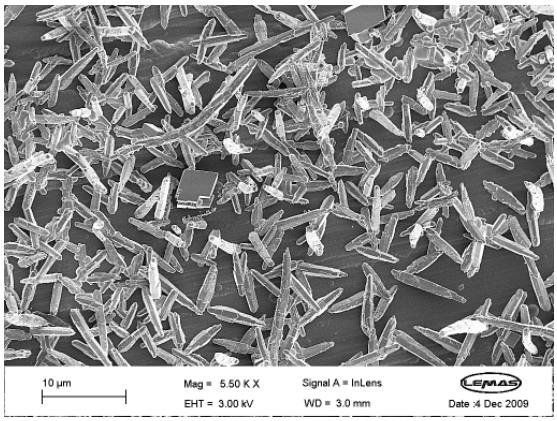

Figure 5.6a: Higher magnification of crystals on DLC surface at 10rpm

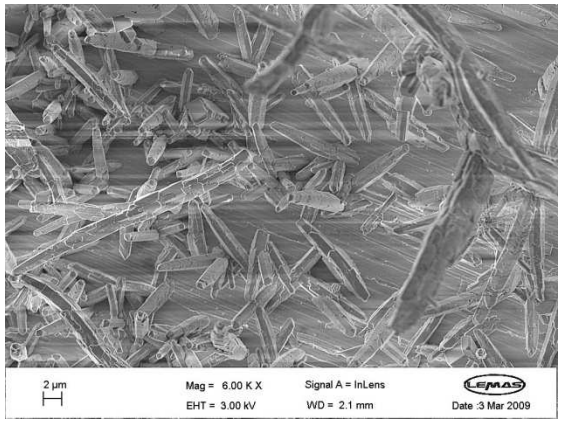

Figure 5.6b: Higher magnification of crystals on stainless steel surface at 10rpm

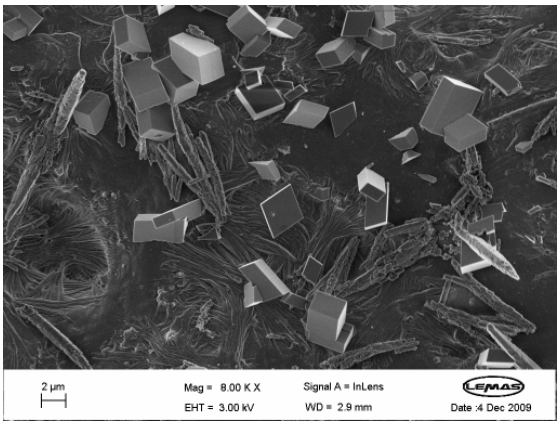

Figure 5.6c: Higher magnification of crystals on Tech 100 at 10rpm

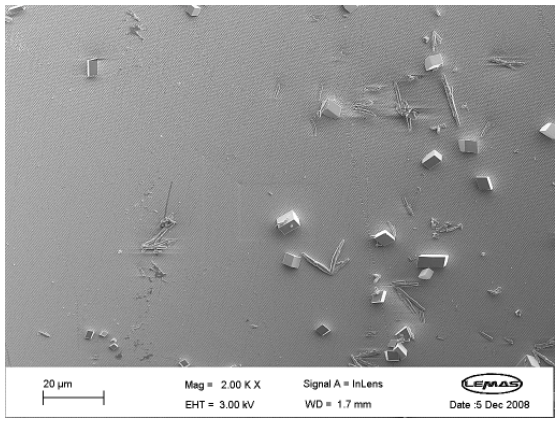

Figure 5.6d: Higher magnification of crystals on polymer MN at 10rpm

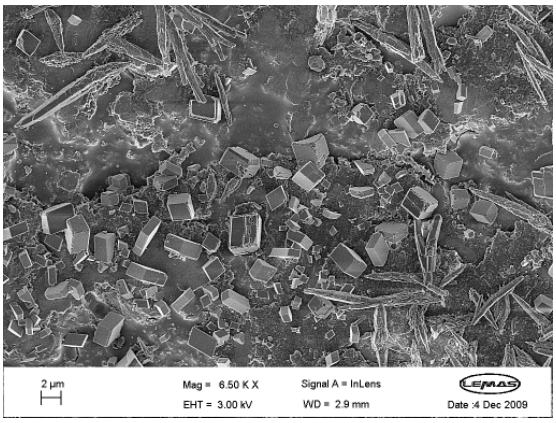

Figure 5.6e: Higher magnification of crystals on Tech 23 at 10rpm

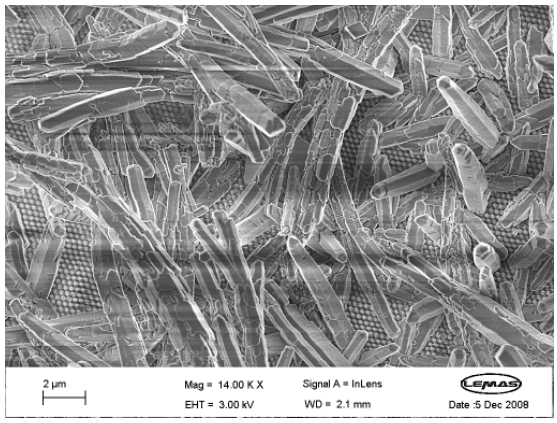

Figure 5.6f: Higher magnification of crystals on polymer MSi at 10rpm

Figure 5.6: Higher magnification SEM images of surfaces at 10rpm

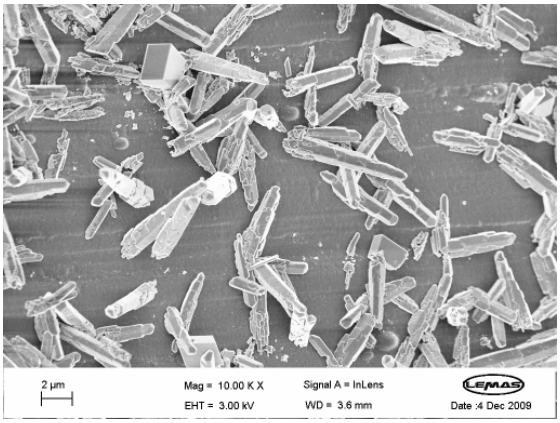

Figure 5.7a: Higher magnification of crystals on DLC at 900rpm

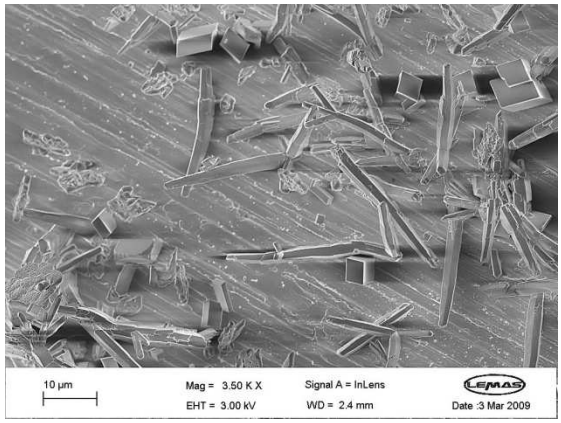

Figure 5.7b: Higher magnification of crystals on stainless steel at 900rpm

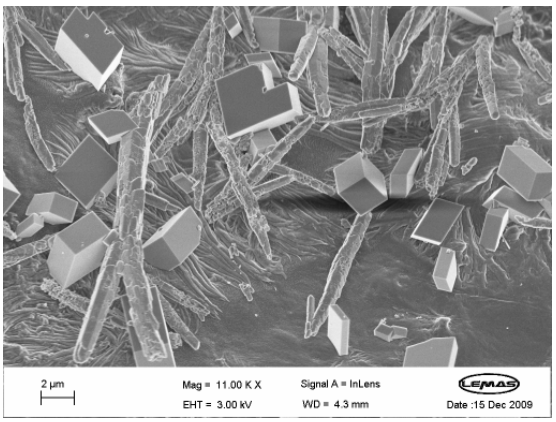

Figure 5.7c: Higher magnification of crystals on Tech 100 coating at 900rpm

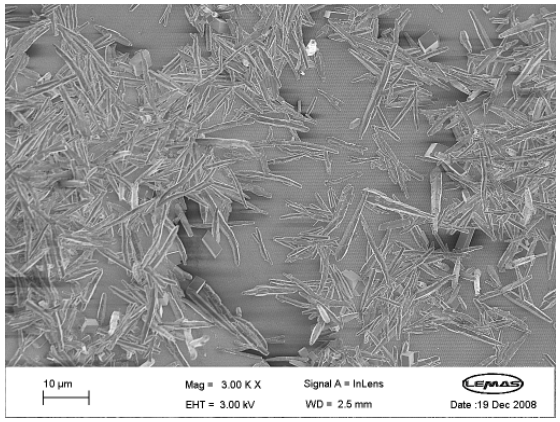

Figure 5.7d: Higher magnification of crystals on polymer MN at 900rpm

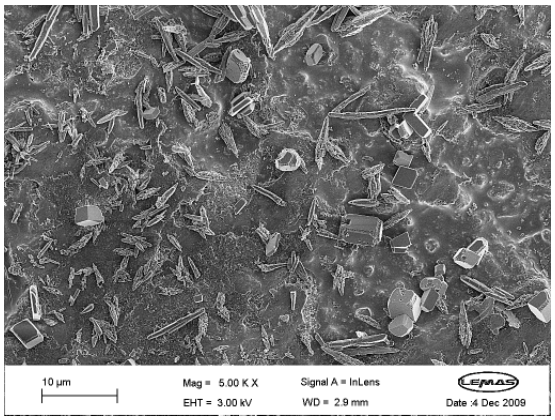

Figure 5.7e: Higher magnification of crystals on Tech 23 at 900rpm

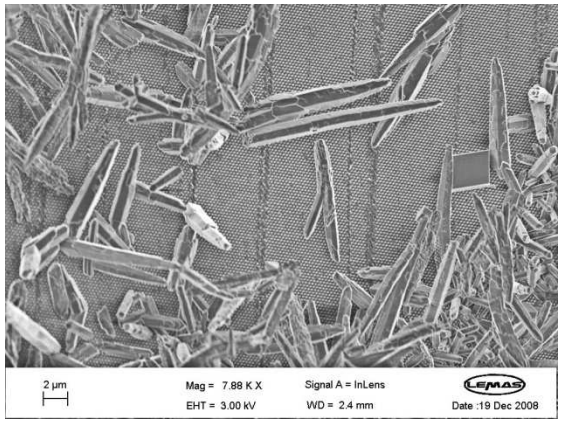

Figure 5.7f: Higher magnification of crystals on polymer MSi at 900rpm

Figure 5.7: Higher magnification SEM images of surfaces at 900rpm

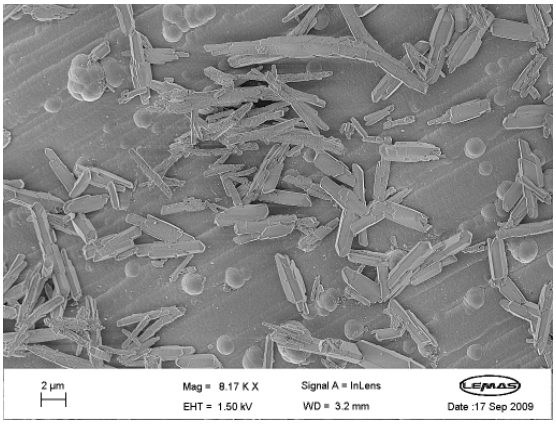

Figure 5.8a: Higher magnification of crystals on DLC at 1800rpm

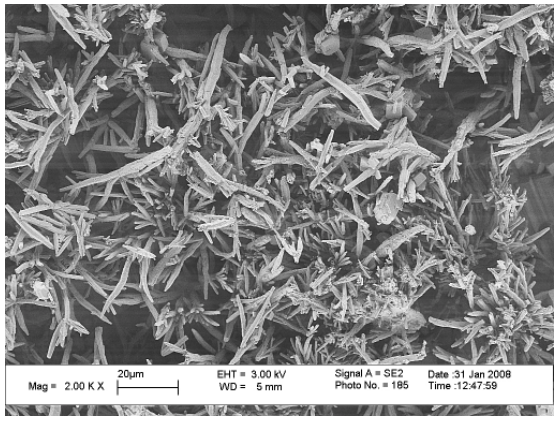

Figure 5.8b: Higher magnification of crystals on stainless steel at 1800rpm

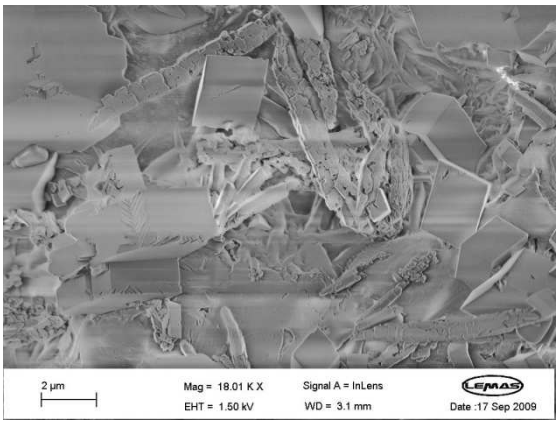

Figure 5.8c: Higher magnification of crystals on Tech 100 at 1800rpm

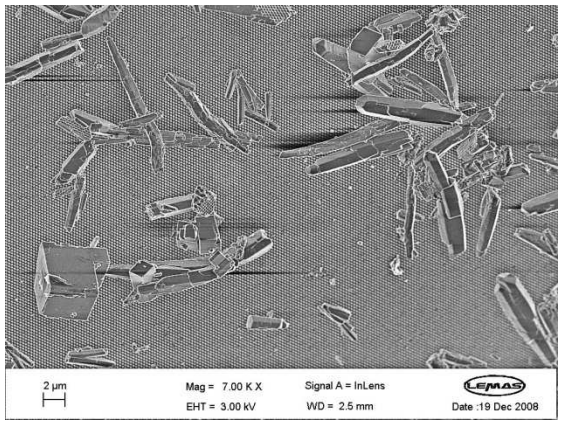

Figure 5.8d: Higher magnification of crystals on polymer MN at 1800rpm

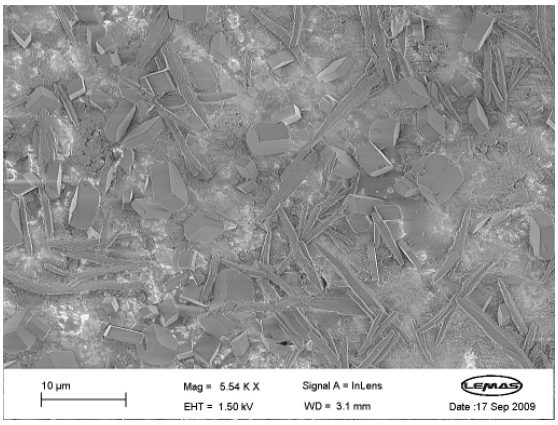

Figure 5.8e: Higher magnification of crystals on Tech 23 at 1800rpm

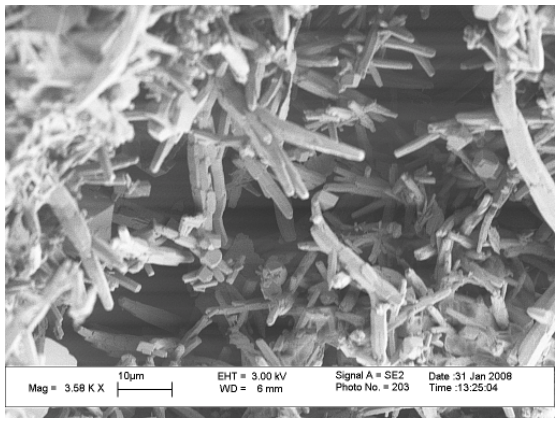

Figure 5.8f: Higher magnification of crystals on polymer MSi at 1800rpm

Figure 5.8: Higher magnification SEM images of surfaces at 1800rpm

When micrometer-sized particles approach a surface to within a fraction of their diameter, physicochemical interactions take over since they are usually much larger than Brownian or other forces. If such interactions are attractive, particles quickly move toward the minimum of the interaction potential. The competition between hydrodynamic drag and adhesive forces determines whether this leads to attachment, which in turn are affected by the smoothness and homogeneity of the interacting surfaces [270]. To remove a particle from the surface, the total external moment must be at least equal to the resistance moment due to adhesion force. The particle will roll from its equilibrium position when the critical moment is exceeded [271].

For stainless steel and the polymer surfaces MN and MSi, the increase in shear stress from rotation speeds of 900rpm to 1800rpm did not reduce the scaling tendency which indicates that calcium carbonate adhesion was more tenacious on these surfaces compared to the coatings of DLC, Tech 23 and Tech 100. On the other hand, shear stress did not have a pronounced effect on the scaling tendency of the coatings. It will be shown later in the discussion that the shear forces generated here are significantly smaller compared to other studies where the hydrodynamic shear forces were large enough to remove scale particles.

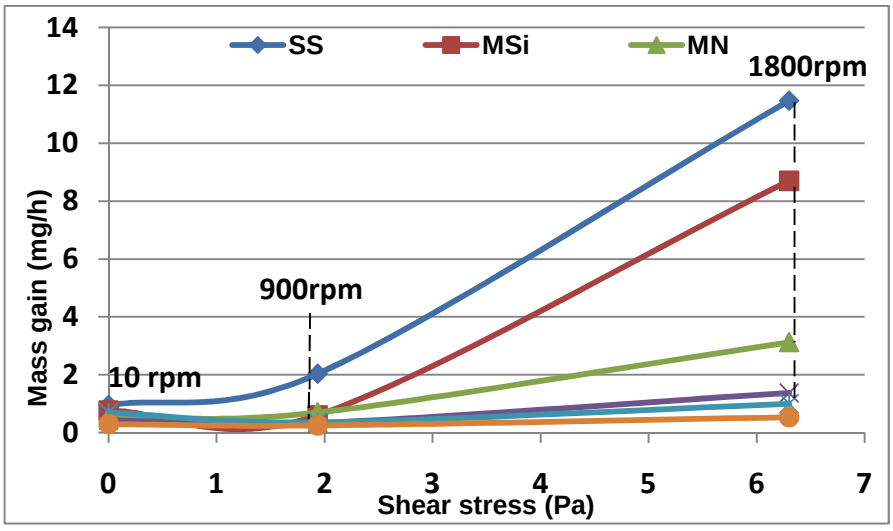

Figure 5.9: Scaling tendency as a function of hydrodynamic wall shear stress

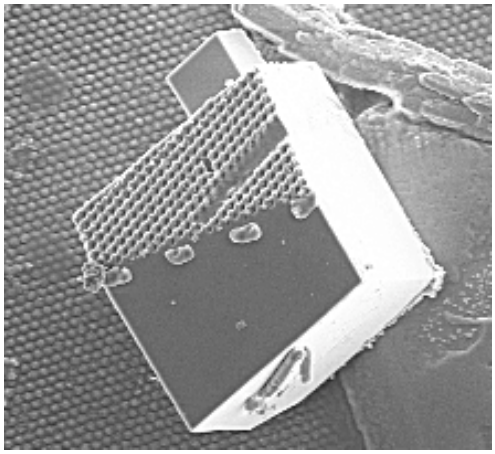

Figure 5.10a

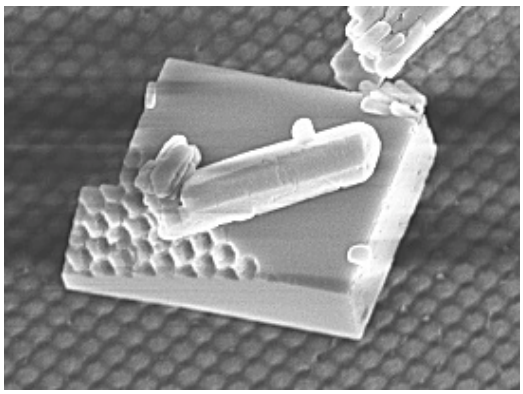

Figure 5.10b

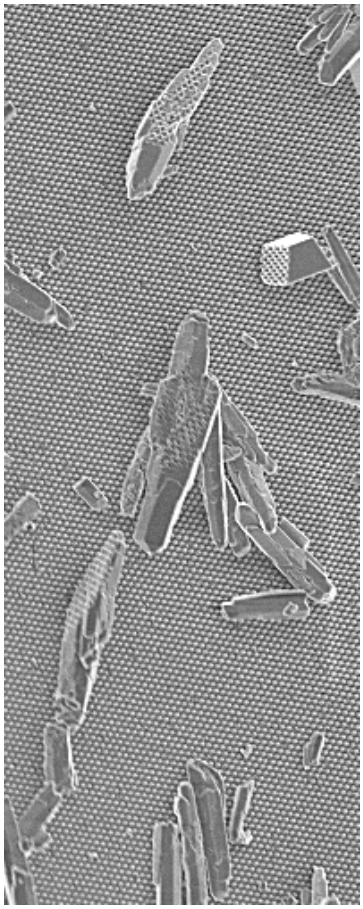

Figure 5.10c

Figure 5.10: Calcite and aragonite crystals flipped over by wall shear stress

5.2 Concluding remarks

The various findings for scale deposition tests under various hydrodynamic regimes i.e. laminar to turbulent flow are presented below.

- The increase in scaling tendency from 10rpm to 1800rpm is not linear.

- The hydrodynamic effects is secondary for the coatings (DLC, Tech 100 and Tech 23) as they are negligible when compared with the polymers and stainless steel surfaces.

- Shear force removal effect was more pronounced at 900rpm and lost when the rotational speed was increased to 1800rpm.

- Shear forces were strong enough at 900rpm to flip over some crystals.

- Visible surfaces free of scaling after an hour could be observed for all speeds except for stainless steel and polymer MSi at 1800rpm.

- At all rotational speeds, the crystals on Tech 100 and Tech 23 were mainly comprised of calcite while aragonite dominated for the remaining substrates.

Chapter 6
Discussion

The work reported in this thesis is primarily focused on understanding the mechanisms of calcium carbonate scale deposition on nano- and micro-structured surfaces along with commercially available industrial coatings with stainless steel as a reference substrate. Many aspects of scale formation processes have become clear but some aspects still require further work. Preventing or promoting deposition requires an understanding of the interactions between the crystallising solid phase and the substrate surface. Hence, this allows us to discuss the effect of a surface's physical and chemical parameters have on the deposition and growth of calcium carbonate crystals. This thesis attempts to examine the factors that make a surface susceptible to scaling. Conventionally, this has received very little attention but there has been an increase in focus in recent years. In addition, substrate effects on crystal morphology are also looked at as the nature of the substrate is clearly shown to influence the prominent polymorph in $CaCO_3$ deposition.

In this study, the adhesion of calcium carbonate to the surface is affected by the mechanism of deposition and this is assessed by whether crystals migrated from the bulk solution to settle on the surface or if crystals heterogeneously nucleated on the surface itself and subsequently grown there. The latter mechanism differs from the general concept of an anti-biofouling surface using the example of zoospores of marine green alga *Ulva* which is a predominant fouling species in marine biofilms [272]. These zoospores have whip-like whiskers called flagella that actively seek out surfaces for settlement. Once a suitable surface is detected, the spore settles and attaches to the substrate (Figure 6.1a). An anti-biofouling coating will act to prevent detection of the surface by the zoospores and prevent settlement and attachment (Figure 6.1b). Likewise, a fouling release coating can lead to easy release of the adhesive pad under moderate hydrodynamic shear stresses generated by

flowing water. The performance of such a coating is based on a few principles such as low interfacial energy with water, low intermolecular forces of interaction with biomolecules, or both.

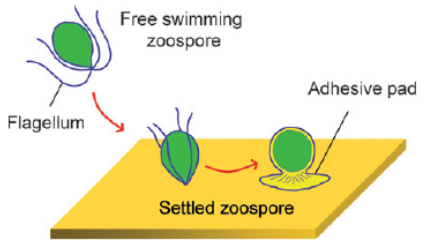

Figure 6.1a

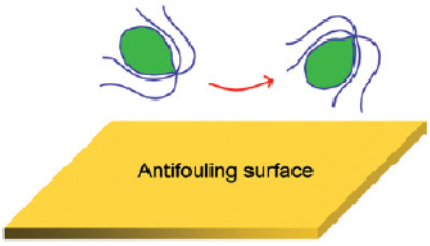

Figure 6.1b

Figure 6.1 (a) Settlement and adhesion of a zoospore of the green alga *Ulva* on a surface prone to biofouling, and (b) spore behaviour near an antifouling surface.[272]

There are three major approaches (Figure 6.2) to producing anti-biofouling surfaces [272].

- Homogeneous surfaces of hydrophobic, hydrophilic or amphiphilic character can be used. For example, hydrophilic surfaces are resistant to protein and cell settlement.
- Non-polar, low surface energy, hydrophobic coatings are inherently low adhesive that can aid the detachment of settled organisms under shear flow.
- Amphiphilic surfaces with chemical and/or textural complexity can effectively ‘confuse’ fouling organisms into avoiding settlement onto such surfaces.
- Mixed or patterned surfaces of alternating hydrophobic or hydrophilic character are also effective because of their elaborateness.
- Three dimensional surfaces are put into effect by modifying the anti-biofouling coating by control of surface topography.

Similarly, anti-crystallization surfaces can be modelled from the approaches above.

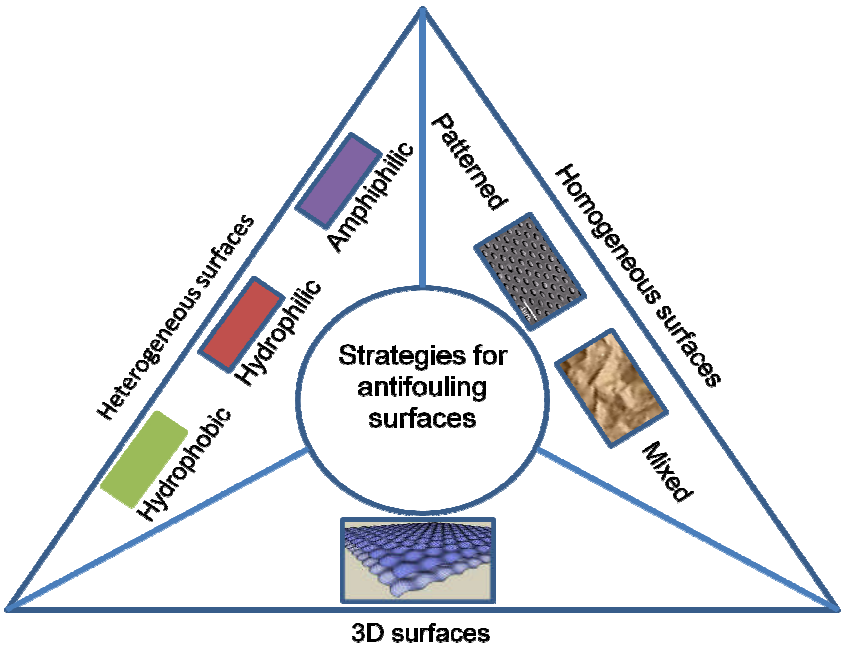

Figure 6.2: Three major approaches to producing anti-biofouling surfaces [272].

A comparative study is made here on the crystals formed in the bulk solution and on the crystals found on the test substrates. This work looks at the near surface forces that affect the adhesion of crystals to the surface and also discusses the hydrodynamic effects on the growth and hydrodynamic shear forces that may affect the scaling tendency of such surfaces.

The practical significance of these results are finally discussed by taking a look at how these results could contribute to the management of scale.

To summarize, the discussion takes the following format:

(1) Scale versus various surface parameters
(2) Effect of surface on crystallization form
(3) Adhesion versus surface deposition
(4) Hydrodynamics effect
(5) Scale management

6.1 Substrate effects on the mass of calcium carbonate deposited

Scale control at surfaces may be addressed by surface engineering options. In biofouling, there have been enormous efforts to reduce deposition of marine biological species on surfaces by some really sophisticated surface engineering systems which can release anti-fouling species at a controlled rate. In scaling, there have been few attempts at using surface engineering to control scale deposition, especially in the desalination industry. However, it is fair to say that there is potential for more widespread study and exploitation of potential systems. Despite the fact that crystal growth has been extensively studied and considerable knowledge has been accumulated on the subject, many aspects of the scale formation process on surfaces remain unclear. The aim of this part of the research is to examine the fundamentals of how the physical and chemical properties of a surface affect scaling tendency.

The polymer substrates were chosen as their surface properties mimic the functional aspects of plant surfaces [238] and moth eyes [248] that include the reduction of particle adhesion and the self-cleaning properties in the Lotus (*Nelumbo nucifera*) leaves. These surface properties are based on physio-chemical principles and can be transferred into technical “biomimetic” materials, as successfully done for the Lotus leaves and the motheye antireflective surfaces.

As seen from the 1 hour deposition test results at 1800 rpm, stainless steel has been found to have the highest scaling tendency while the polymers have a range of performance among themselves and the commercially available coatings exhibited the least scaling tendency. When the $CaCO_3$ scale deposits onto the test substrates, for example stainless steel, the first layer is formed on a metallic surface while subsequent layers grow on $CaCO_3$ crystals. It is this initial formation or deposition of scale onto the test substrates that

determines the feasibility of such surfaces for anti-scaling purposes. Depending on this initial formation layer, subsequent layers may grow to be either more compact (Figure 6.3a) or more loose and porous (Figure 6.3b) [167] which would indicate their ease of removal by hydrodynamic shear forces. This was demonstrated in another study and the results can be seen in Figure 6.3.

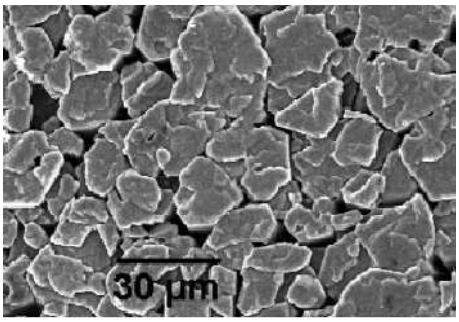

Figure 6.3a: $CaSO_4$ deposit formed on stainless steel surface

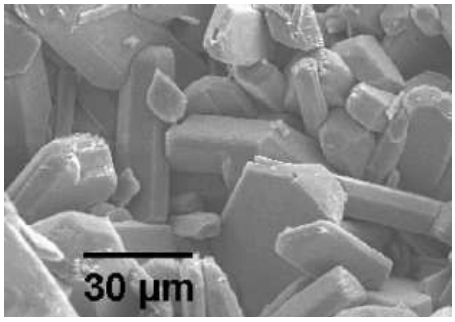

Figure 6.3b: $CaSO_4$ deposit formed on Ni-Cu-P-PTFE coated surface

Figure 6.3: The difference in compactness of $CaSO_4$ scale layer when formed on different types of substrate [167].

Generally, the surfaces of coatings (DLC, Tech 100 and Tech 23) and polymers MN and MS remained relatively clear when compared to the reference stainless steel surface. This is in effect desirable as the low scaling tendency would prolong the time it takes for scale to accumulate onto the substrate or to start forming adherent layers on top of each other.

From the water contact angle values and crystal mass gain after an hour in Figure 6.4, it can be seen that polymers MN and MS have the lowest values amongst the polymers, and can be deduced to have relatively higher surface energies. The coatings Tech 23 and Tech 100 exhibit the highest water contact angle and are seen to have the lowest surface energies. In the literature associated with fouling, whether it be organic or inorganic, there is a general appreciation that the lower the surface energy the lower the propensity for scale formation, e.g. across a range of steel, diamond-like carbon and PTFE surfaces as a general loose correlation [273].

As can be seen in the polymers' region highlighted by the green circle in Figure 6.4, there is an opposite trend of higher scaling tendency for lower surface energy surfaces. It is also clear that the two polymer surfaces that offer the best scaling resistance (polymers MN and MS) have the highest surface energy. As for the coatings (highlighted by the blue circle) and control substrate (Stainless steel (SS), DLC, Tech 23 and Tech 100 coating), there is a trend of lower scaling tendency for surfaces with lower surface energy.

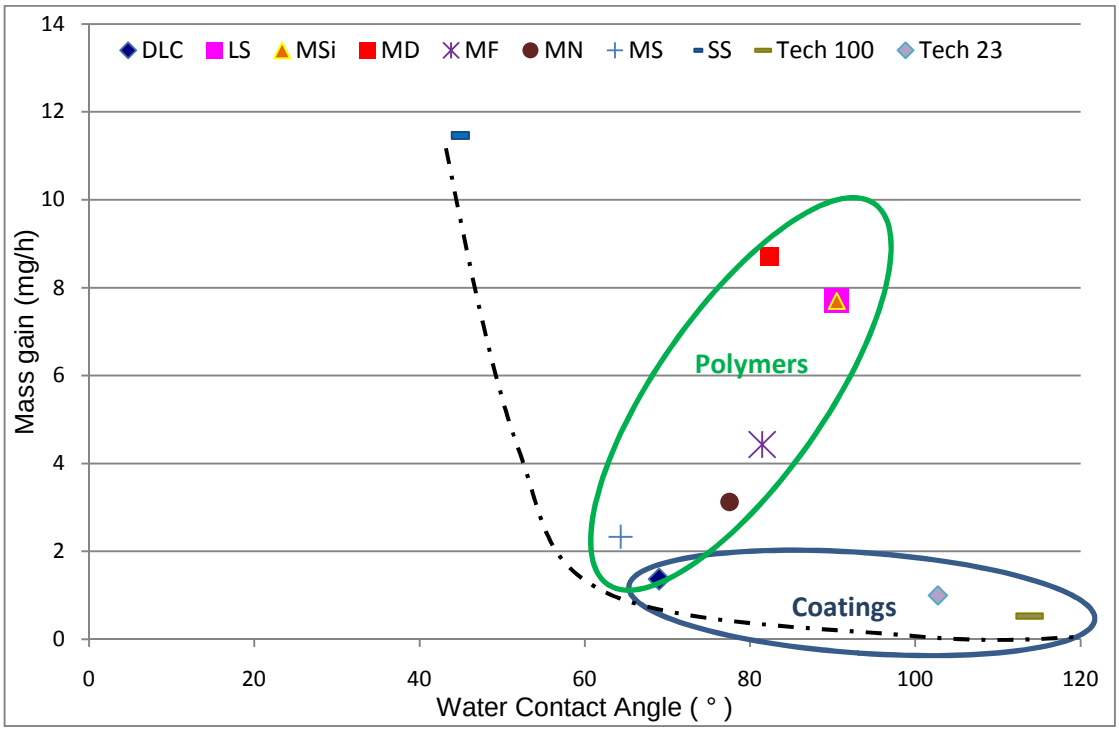

Figure 6.4: Water contact angle (°) vs. Mass gain (mg)

There are conflicting reports on the effect of surface energy of surfaces on mineral scaling tendency as mentioned in Chapter 2. One such example can be seen in Figure 6.5 where there is no obvious correlation between fouling resistance and surface energy. In similar work performed on calcium sulphate fouling, DLC was found to be the lowest fouling material despite not having the lowest surface free energy among the substrates studied [155]. In this study, micro- and nanopatterned polymers seem to exhibit the behaviour that higher surface energy will lower scaling tendency while more conventional surfaces,

such as stainless steel and coated stainless steel, follow the popular belief that lower surface energy tends to lower scaling tendency.

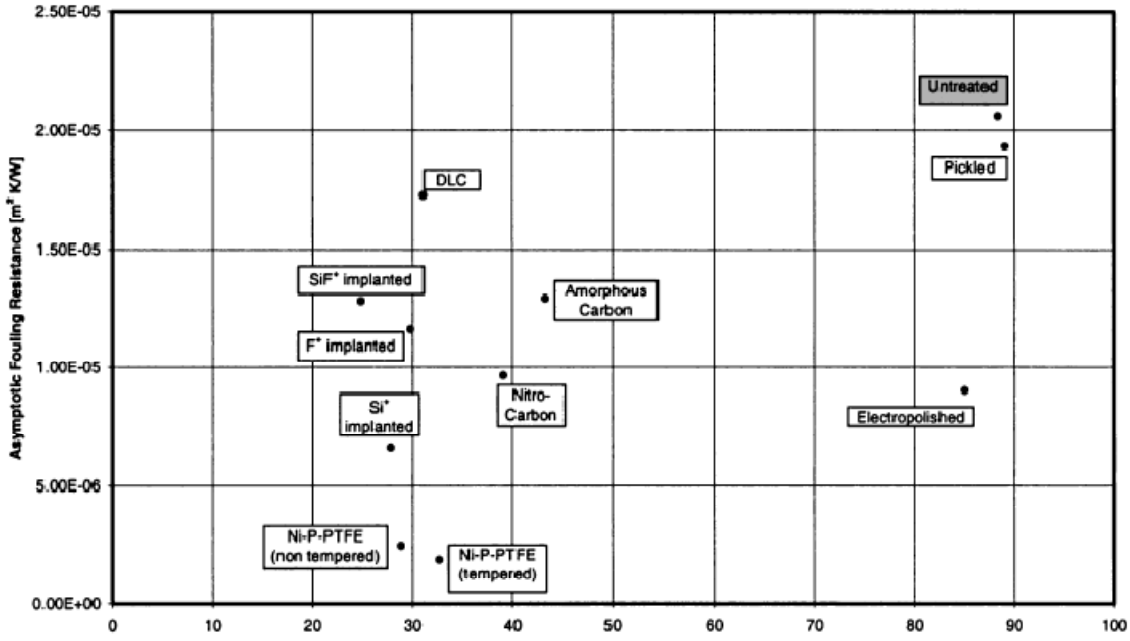

Figure 6.5: Variation of asymptotic fouling resistance with surface energy [171]

On the contrary in the field of biofouling, the role of surface energy is very distinct. For example, hydrophobic self-cleaning surfaces such as those of poly(dimethylsiloxane) (PDMS) are known to show good 'fouling release' properties, whereas the hydrophilic surfaces of polymers like poly(ethylene glycol) (PEG) that possess low values of polymer-water interfacial energy exhibit resistance to protein adsorption and cell adhesion [272]. The interfacial energy between a surface and water plays an important role in conferring antifouling characteristics to a surface.

Self-cleaning surfaces have been the focus of several contemporary and advanced technologies, ranging from coatings for ship hulls [274] and biomedical implants [275] to biosensors [276] and carriers for targeted drug delivery [277]. Thus far, these anti-fouling surfaces are based on minimizing the intermolecular forces of interactions between extracellular and the synthetic

surface such that any adhered cell can be easily removed under low shear stresses. When hydrophobicity produces a high contact angle, the surface morphology reduces the adhesion of water droplets to the surface, which slides easily across the self-cleaning surface carrying the dirt particles with them (see Figure 6.6a) [278, 279].

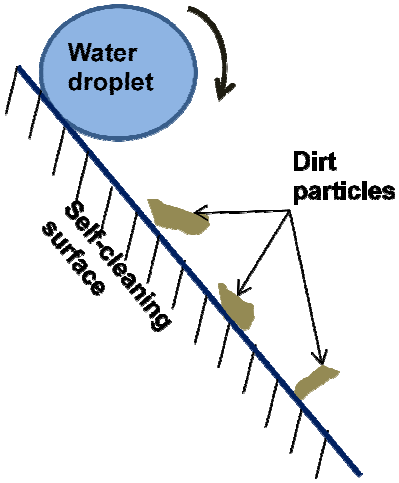

Figure 6.6a: Self-cleaning surface

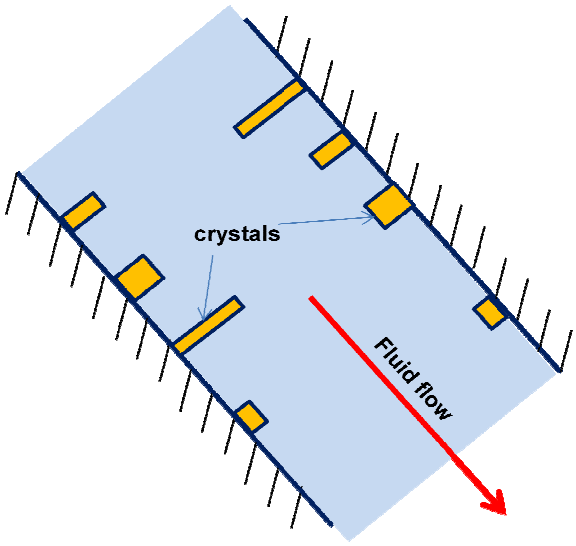

Figure 6.6b: Surface crystallization processes

Figure 6.6: Self-cleaning surface versus Surface crystallization process

In the case of a surface crystallization processes which is typical in the problem of mineral scaling and the focus of this study (refer to Figure 6.6b), the crystals are growing on the surface itself instead of attaching onto the surface which is the case for biofouling. In order for the surface crystallization to take place, nucleation and the growth of these nuclei to macroscopic dimensions will have to occur first [38, 40]. During the formation of a crystal nuclei, not only do the constituent molecules have to coagulate, resisting the urge to redissolve, but they also have to become orientated into a fixed lattice. The number of molecules in a stable crystal nucleus can vary from ten to several thousands. A stable nucleus is hardly believed to form as the result of simultaneous collisions of the required number of molecules as this would imply an extremely rare event, instead, it is more likely to result from ion-pairing and clusters will be

formed by electrostatic interactions between dissolved anions and cations. Next, the clusters will grow step by step by the addition of ions until they reach a critical size. The formation of the crystal nuclei at the surface would be facilitated by the diffusion of the reactants Ca^{2+} and HCO_3^- from the water bulk through the diffusional boundary layer towards the surface [280]. This is subsequently followed by the chemical reaction at the solution-substrate interface that leads to the formation of CO_3^{2-} and CO_2 (as described in equation (2.1)) [101].

Self-cleaning surfaces are effective as the water droplets roll down the surface and collects the dirt particles along its way (Figure 6.6a). In addition, instead of individual water droplets sitting on the surface, the surfaces are immersed in fluid for extended periods of time and any inherent advantages of the self-cleaning surfaces such as trapping of air [242], low interfacial surface energy [241] and hydrophobicity may be lost [247]. Hence, it is clear why surface energy can play an important role in self-cleaning but may not influence surface crystallization process to a great extent.

Work of adhesion (W_a) refers to the work required to separate two surfaces in contact. When a liquid (subscript l) and solid (subscript s) are placed in intimate contact, the interfacial energy can be expressed as

$$\gamma_{sl} = \gamma_s + \gamma_l - W_a. \qquad \textbf{(6.1)}$$

W_a from equation (6.1) can be obtained by considering the three components of the surface free energy

$$W_a = 2\left(\sqrt{\gamma_s^{LW}\gamma_l^{LW}} + \sqrt{\gamma_s^+\gamma_l^-} + \sqrt{\gamma_s^-\gamma_l^+}\right), \qquad \textbf{(6.2)}$$

where γ^+ is the electron-acceptor (Lewis acid) and γ^- is the electron donor (Lewis base) parameter. The general approach to calculate the surface free energy from contact angle measurements is based on a three-component approach – Lewis acid-base theory. Van Oss et al. [281] suggested solid surface free energies (γ_s^{tot}) involve both Lifshitz-van der Waals (LW) and polar acid-base (AB) interactions, namely

$$\gamma_S^{tot} = \gamma_S^{LW} + \gamma_S^{AB}. \quad \textbf{(6.3)}$$

In systems where two dissimilar materials (subscript 1 and 2) are in a third medium (subscript 3), the theoretical work of adhesion (W_{132}) is obtained by resolving the various work components of adhesion:

$$W_{132} = W_{12} + W_{33} - W_{13} - W_{23}. \quad \textbf{(6.4)}$$

The results of a study performed on a series of metal and non-metal coatings and their adhesion to calcite by Bargir et al. is shown in Figure 6.7 where they attempted to determine whether there is a link between work of adhesion and scaling rate which is a similar aim to the present investigation. Referring to Table 6.1, the Group I materials (Figure 6.7a) used in the study include stainless steel, gold and copper while Group II materials (Figure 6.7b) include carbon-based solid lubricant coatings, titanium nitride (TiN) coatings, Poly(tetrafluoroethylene) (PTFE), kettle element coating and aluminium. The probe liquids that were used for the contact angle measurement were water (W), formamide (F), ethylene glycol (E), glycerol (G) and dimethylsulfoxide (D) (Figure 6.7c).

It was found that there was no relationship between the theoretical work of adhesion and scaling rate when all materials were placed on a single plot. However, after categorizing materials under metal and non-metal substrates, a link between W_{13} (substrate-water) and W_{12} (substrate-calcite) and scaling rate became more obvious (Figure 6.7a and b). This is similar to the work carried out in the present study where a link only became apparent after polymers and coatings were circled out in Figure 6.4.

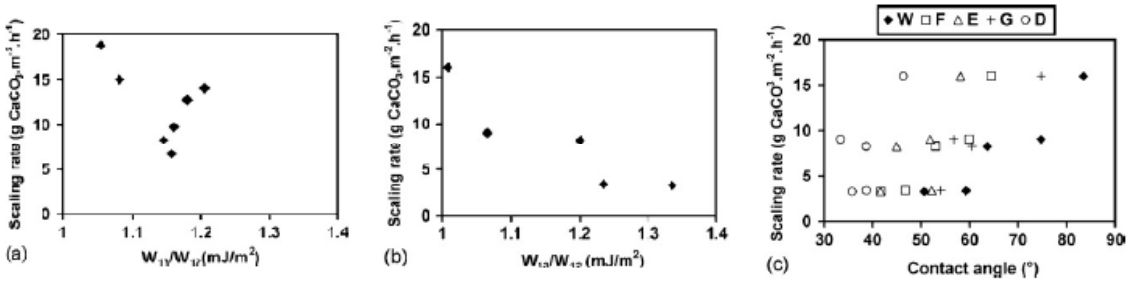

Figure 6.7a **Figure 6.7b** **Figure 6.7c**

Figure 6.7: Correlations between W_{13}/W_{12} and scaling rate using (a) metals and (b) non-metals, and (c) is the link between liquid contact angle and scaling rate [179].

The values of W_{12}, W_{13} and W_{132} (in mJ/m^2) of the materials were calculated from equation (6.2) using the data Table 6.1. Figure 6.7a shows metal substrates exhibit a narrow distribution of W_{13} and W_{12} values with no apparent correlation to scaling rate. Meanwhile, non-metals give a strong correlation between thermodynamic work of adhesion and scaling rate with water contact angles having the most influence on thermodynamic work of adhesion and scaling rate (Figure 6.7c). Their results for metal substrates were also found to be ambiguous where low W_{132} values resulted in high scaling rate and steel surfaces with similar surface roughness gave different polar contributions to their surface free energy which seem to indicate a complex interaction between the probe liquid and surface asperities. In addition, non-homogeneous surfaces can be hydrophilic or hydrophobic depending on the physical and geometrical arrangement of the microasperities. Similarly, high surface tension liquids can sit on surface asperities in the shape of tall hemispheres which in turn are capable of trapping air in between its

hemispheres. Such roughness induced effects have been reported to cause difficulties in interpreting the surface free energies of heterogeneous surfaces [282].

Table 6.1: Calculated γ^{LW}, γ^{+}, γ^{-}, γ^{AB} and γ^{total} values (in mJ/m^2) of group I/II materials and calcite, calculated from the average of four triplets BWG, BWE, BWF and BWD. Also shown are surface free energy values of materials from the literature where available) and the various triplets used in their calculation [179].

	Triplets used	γ^{LW}	γ^{+}	γ^{-}	γ^{AB}	γ^{total}
Group I						
Aluminium		36.91	0.19 ± 0.14	16.00 ± 1.64	3.29 ± 1.12	38.51 ± 0.71
Ref. [4]	BWF, BWE, BWG, BWD	36.40	0.01 ± 0.02	25.15 ± 4.68	0.39 ± 0.78	36.78 ± 0.75
Ref. [15]	BWF, BWE, BWG	37.50	0.53 ± 0.06	20.97 ± 0.35	6.67 ± 0.38	43.87 ± 0.38
Copper		40.56	0.37 ± 1.22	11.82 ± 0.77	4.06 ± 5.17	42.60 ± 0.61
Steel 2		42.13	0.38 ± 0.23	22.45 ± 5.18	5.53 ± 2.52	44.99 ± 0.70
Gold-0.3 mm		42.19	0.42 ± 0.16	18.93 ± 3.75	5.60 ± 1.51	44.94 ± 1.11
Ref. [16]	XWG, XWE, XWF*	33.5	0.17	19.3	3.01	36.5
Steel 1		40.88	0.45 ± 0.25	16.88 ± 4.31	5.30 ± 1.85	43.54 ± 0.57
Ref. [4]	BWF, BWE, BWG, BWD	40.80	0.41 ± 0.66	16.03 ± 3.51	3.65 ± 2.88	44.45 ± 2.88
Gold-0.1 mm		41.39	0.52 ± 0.23	20.56 ± 5.04	6.27 ± 0.93	44.51 ± 0.96
Steel 3		40.67	1.07 ± 1.01	10.66 ± 6.28	5.50 ± 2.36	44.00 ± 0.82
'Used' copper		43.38	3.27 ± 4.04	25.26 ± 11.24	16.98 ± 15.37	52.36 ± 3.14
Group II						
TiN		41.09	0.15 ± 0.13	21.05 ± 2.92	3.34 ± 1.68	42.76 ± 0.47
Ref. [17]	BWE, BWF, XWE, XWF*	33.20	0.04 ± 0.03	24.80 ± 0.5	1.99	34.20
Dymon-iC™		41.82	0.22 ± 0.15	35.75 ± 4.66	5.34 ± 2.29	44.54 ± 0.61
Ref. [17]	BWE, BWF, XWE, XWF*	37.40	0.12 ± 0.10	19.7 ± 0.5	3.08	38.94
'kettle coating'		34.56	0.29 ± 0.13	7.54 ± 0.58	2.89 ± 0.70	35.70 ± 0.54
Graphit-iC™		41.94	0.36 ± 0.16	25.60 ± 6.00	5.96 ± 1.79	45.00 ± 0.89
PTFE		34.96	0.70 ± 0.92	9.92 ± 2.84	4.15 ± 1.83	37.39 ± 0.38
Ref. [14]	YWG, YWE, YWF**	20.24	0.10 ± 0.17	0.13 ± 0.21	0.23 ± 0.38	20.35 ± 0.19
Adhesive						
Calcite		43.83	0.07	29.00	2.83	45.25
Ref. [18]	BWE, BWG, BWF, XWE, XWG, XWF*	40.20	1.30	54.40	16.8	48.61

This present work includes polymers as test substrates, however, not many measurements of scale accumulation on polymeric materials exposed to scaling solutions exist. Andritsos et al. [92] compared the scaling tendency on stainless steel, copper and Teflon tubes, and found surface effect to be negligible. That means that the various substrate materials tested do not seem to influence the nature of the polymorphs formed and the growth pattern. Another study [283] evaluated scaling of a range of polymers (nylon 6,6, polypropylene, polybutylene, polyphenysulfone, and Teflon) and copper tubes in a tube-in-shell heat exchanger. It was found that with the exception of nylon 6,6 calcium-rich scale accumulated on polymer tubes at rates comparable to that of copper. As for nylon 6,6, there was more scale formed which was a result

attributed to the hydrolysis of the polymer and the creation of anionic surface groups. It was also reported that $CaCO_3$ formed on polymer surfaces at a rate similar to that on metal surfaces but there was a great deal of scatter in the data which was most likely due to the nature of the flow and the high sensitivity of scaling to small variations in conditions for the supersaturation conditions used in the experiment [284].

In another report related to calcium carbonate deposition onto polymers [269] to determine the effect of water chemistry on $CaCO_3$ deposition on metal and polymer surfaces where copper and polypropylene (PP) surfaces were used, more $CaCO_3$ formed on PP surfaces as compared with copper and that nucleation was more favorable and induction time lower on PP than Cu (refer to Figure 6.9). Calcite was the dominant polymorph for deposits on copper. On PP surfaces, the deposits were a mixture of calcite, vaterite and aragonite with aragonite dominating except at low supersaturation. The observation that aragonite formed on PP and not on Cu under the same conditions is attributed to the surface chemistry of PP. Some water may have penetrated into the material and researchers have found weakened hydrogen bonding interactions between water molecules once they have diffused into PP [285]. It has also been reported that PP becomes negatively charged above pH 2 [286] and the surface would therefore attract Ca^{2+} ions. Furthermore, although trace amounts of copper ions in water are known to inhibit $CaCO_3$ formation [287], the effect of copper ions on $CaCO_3$ polymorph formation has not been investigated but may explain the preference for calcite formation on copper. In addition, surface roughness between both materials [169, 288], differences in surface chemistry and interfacial energy were thought to be responsible for the difference in nucleation and scaling behaviours of PP and Cu (Figure 6.9). The SEM images of PP and Cu tubes after being exposed to mildly supersaturated distilled water can be seen in Figure 6.8.

Similar to the above mentioned reports, different polymorphs were formed on the coatings and polymers explored here even though they were

exposed to the same test conditions. In addition, more $CaCO_3$ formed on the polymer surfaces compared to the coatings which was not expected as the polymers were expected to have lower adhesion due to their micro- and nanostructures. Aragonite was dominant on most of the polymers, reference stainless steel substrate and the coating DLC, and even so, the aragonite crystal habit seemed different from the aragonite on the polymer surfaces. On the other hand, calcite was dominant on the coatings Tech 23 and Tech 100. This will be explored further in the next section.

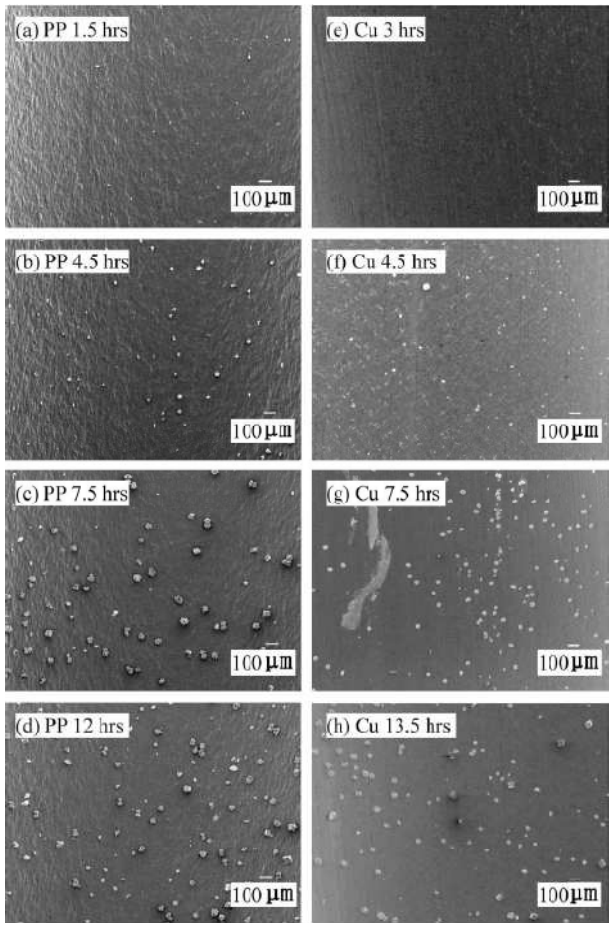

Figure 6.8: SEM images of polypropylene (PP) and Cu tubes after exposure to mildly supersaturated distilled water (S=0.8), at 50x magnfication: PP tube exposed for (a) 1.5hr, (b) 4.5hr, (c) 7.5hrs, (d) 12hrs; and Cu tube exposed for (e)3hr, (f) 4.5hr, (g) 7.5hrs and (h) 12hrs [269].

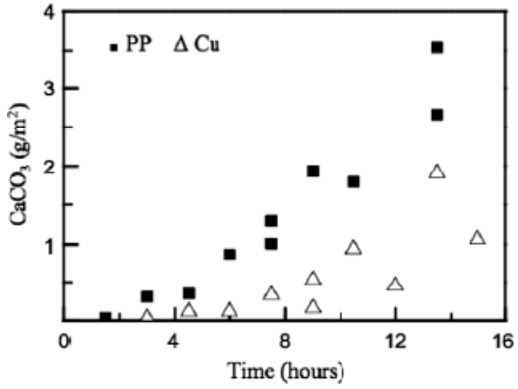

Figure 6.9: Mass of $CaCO_3$ deposited per unit area on PP and Cu [269]

6.1.1 Difference in crystal morphology: Surface roughness and surface chemistry effects

The preference of a surface for one type of polymorph over another is of fundamental interest and it is desirable to determine how these surfaces exert such an influence. It has been observed in this present work that a morphology is dominant on some surfaces and another morphology is dominant on other surfaces.

There is evidence that the nature of the substrate material influences scale nucleation. It was found that the induction time for scaling was longer on polymer surfaces that exhibited poor wetting behavior with supersaturated aqueous solutions. The surface energy of a polymer may be a factor [289]. Furthermore, surface roughness has to be taken into account for as Keysar and co-workers found lower nucleation rates on smooth substrates as compared to rough ones [138].

Furthermore in some cases, a strong dependence has been noted of the observed crystal polymorph, crystal orientation and numerical density on the type of substrate used [290-294]. Surface chemistry also affects nucleation, the concentration and the head group of the anionic surfactants intensively

influence the crystalline phase and morphology of the precipitated crystals [295]. Locally high supersaturations can also be realized when the surface selectively adsorbs species from solution. There have been studies where Ca^{2+} adsorption leads to selective formation of calcium carbonate on surfaces [290, 296]. However, it must be noted that solution temperature and pH also profoundly influenced the morphology of $CaCO_3$ [297]. Nonetheless in the study carried out here, both temperature and pH were kept constant thus the difference in crystal morphology on the substrates are attributed to substrate effects.

In the case of the coatings Tech 100 and Tech 23, there was more calcite than aragonite after an hour whilst in the earlier deposition periods of 5 and 15 minutes, there was a random mix of both aragonite and calcite. Tech 100 and Tech 23 coatings apparently actively promote the transformation to calcite. The precarious perch of the calcite rhombohedra is especially more pronounced in these coatings and the preference of each surface for a particular polymorph suggest a significant role for the surface.

On the other hand for the DLC coating, vaterite seems to be present in great numbers at the 5 minute deposition interval; subsequently for other time intervals, shorter and rounder aragonite are observed to dominate with very little calcite. The quantity of the vaterite forms decreased such that the aragonite forms dominate the calcite crystals in terms of quantity. The aragonite on the DLC surfaces also seemed to be different from the more elongated and slender aragonite seen on the polymer and stainless steel surfaces (Figure 6.11). The flow velocity may also play a role in affecting the physical characteristics of these deposits [298] where the crystals on the DLC surface may be calcite which grows lengthwise due to flow effects.

Figure 6.12d - Figure 6.12f show the various orientation of the calcite rhombohedrons perched on various corners on the test substrates used in this study, the crystals on the test polymers were not shown here as the dominant

$CaCO_3$ polymorph formed on them was aragonite. This is compared with other work [290] which demonstrated the oriented growth of calcite controlled by self-assembled monolayers (SAM) of functionalized alkanethiols supported on gold which can be seen in Figure 6.12a - Figure 6.12c. CO_2^-, SO_3^- and OH^- - terminated SAMs were found to induce highly oriented growth of calcite, each in a specific crystallographic direction. These results give further evidence that there was surface-induced nucleation processes occurring because if crystals were deposited from the bulk solution, most of them would be expected to settle on the surface in a way similar to Figure 6.12b. SEM image of the bulk precipitate filtered from the scaling solution used in this present work is shown in Figure 6.13.

The Ostwald-Lusac law of phase formation states that metastable hydrated species should be formed first and later transformed to more stable species. In addition, the presence of a metastable field in the precipitation of calcium carbonate is an experimental fact [299]. To account for the observations of two polymorphs, either two polymorphs must nucleate spontaneously or a single polymorph must undergo phase transformation to two different polymorphs. The latter scenario is believed to be more likely. Phase transformation implies that the single polymorph formed would have to be metastable with respect to at least calcite and quite probably vaterite. Thus here, the nuclei are likely to be one of the amorphous or hydrated calcium carbonate polymorphs or possibly vaterite.

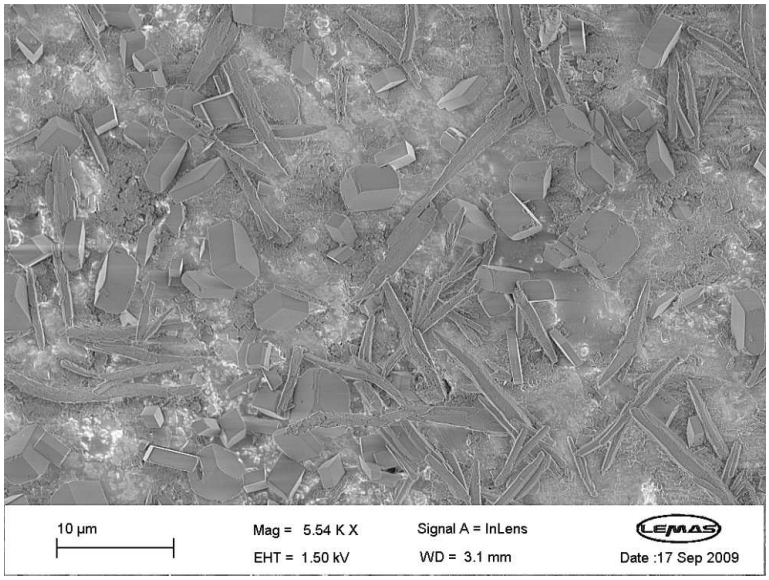

Figure 6.10a: Calcite growth on Tech 23 coating after an hour

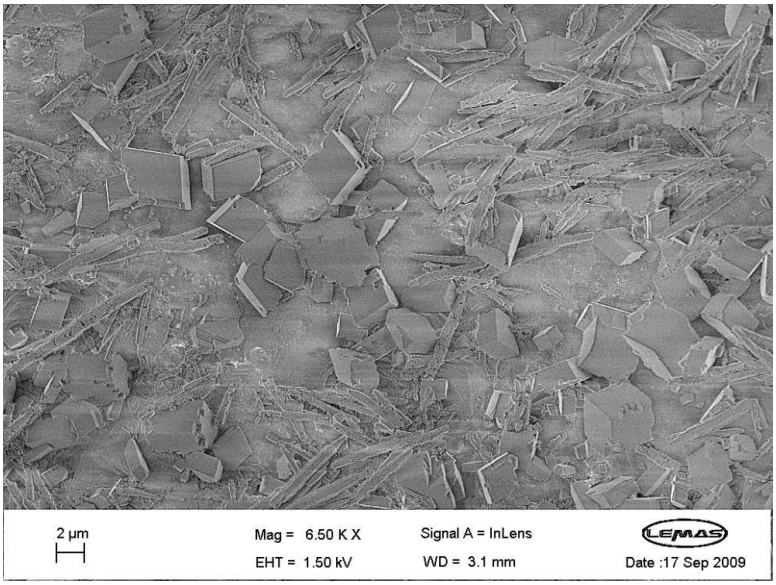

Figure 6.10b: Calcite growth on Tech 100 coating after an hour

Figure 6.10: Evidence of crystals nucleating and growing on surfaces

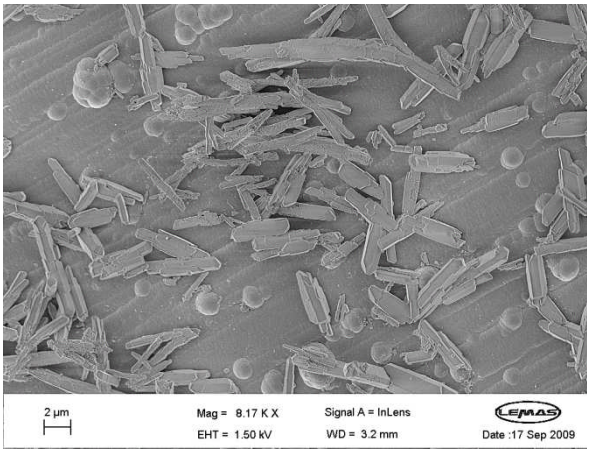

Figure 6.11a: DLC

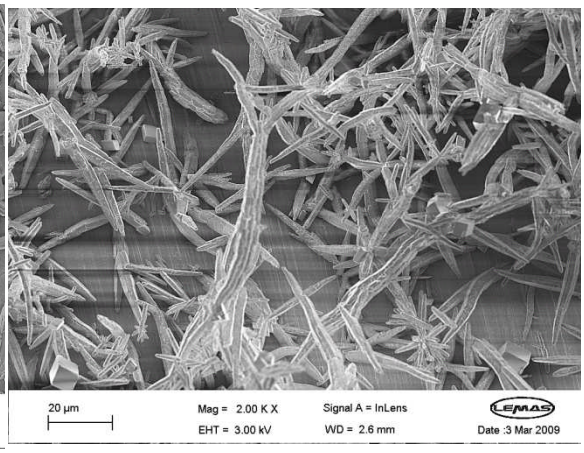

Figure 6.11b: stainless steel

Figure 6.11: Difference in shape of aragonite on DLC and stainless steel

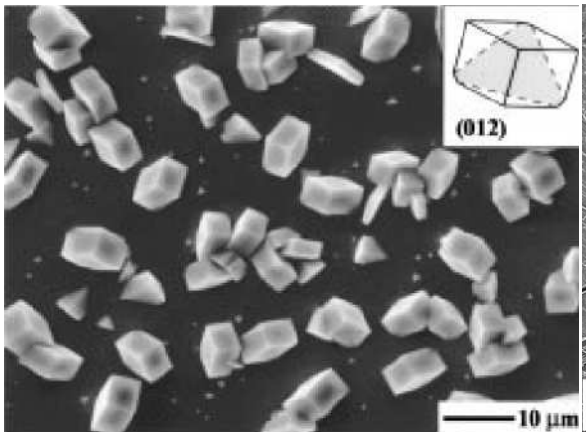

Figure 6.12a: CO_2^- terminated SAM on gold surface

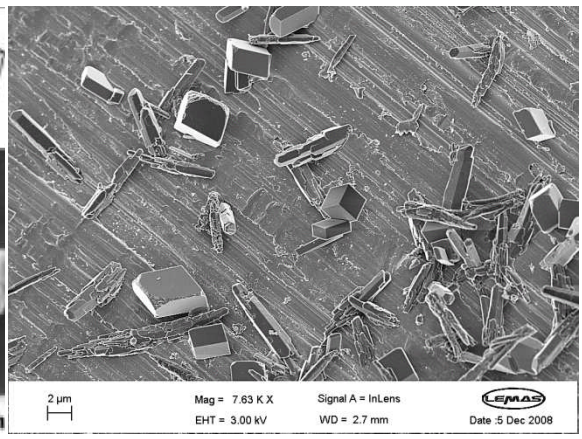

Figure 6.12d: Calcite orientation on stainless steel surface

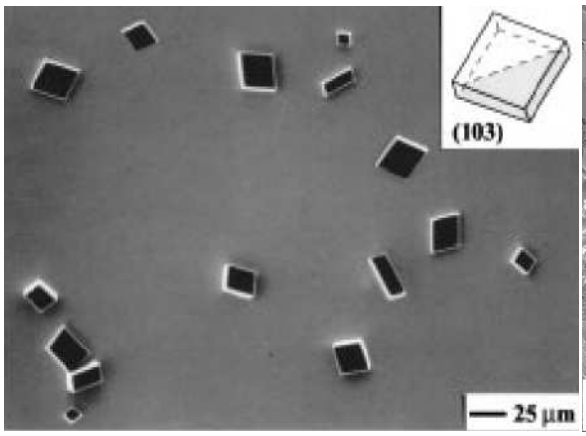

Figure 6.12b: OH terminated SAM on gold surface

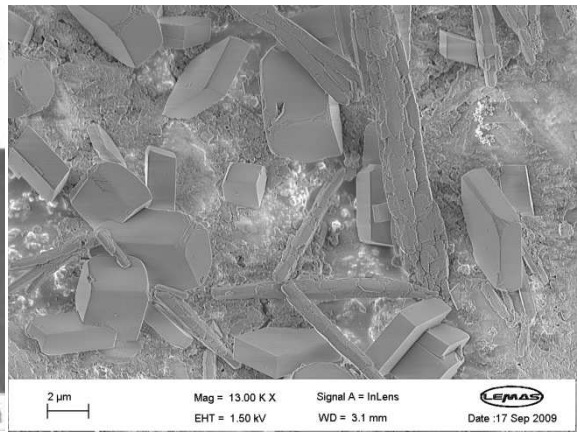

Figure 6.12e: Calcite orientation on Tech 23 coating

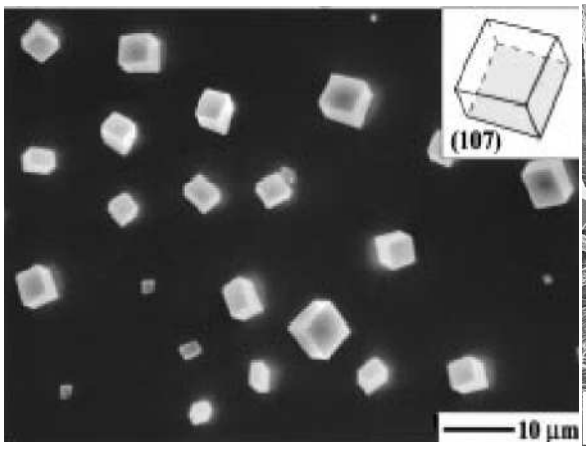

Figure 6.12c: SO_3^- terminated SAM on gold surface

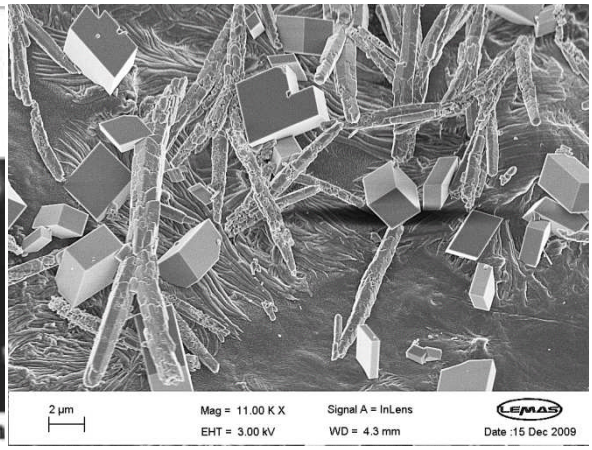

Figure 6.12f: Calcite orientation on Tech 100 coating

Figure 6.12: Scanning electron micrographs showing the face-selective nucleation of calcite crystals on the various substrates. The inserts in Figure 6.12a-c present computer generated simulations of the regular calcite rhombohedra viewed down perpendicular to the corresponding average nucleating face (shadowed).

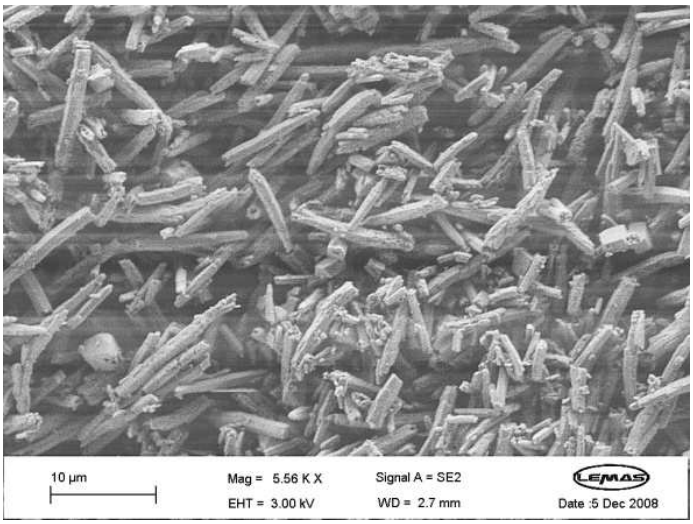

Figure 6.13: Scanning electron micrograph of the bulk precipitate

There are many experimental investigations that show less stable $CaCO_3$ modifications: amorphous calcium carbonate, as a reactive intermediate or precursor during the formation of crystalline $CaCO_3$ polymorphs with vaterite as a solid-state transition phase from the amorphous phase [300-303]. Other workers have studied aragonite to calcite transformation [304], the amorphous

calcium carbonate to vaterite or calcite transformation [303] and calcium carbonate monohydrate to calcite on sulfonated polystyrene resin [293].

The equilibrium curves for the formation reaction of polymorphs of calcium carbonate – calcite, vaterite, aragonite, ikaite, and amorphous calcium carbonate which are calculated from their equilibrium constants [61, 305, 306] are shown in Figure 6.14. The equilibrium curve for calcite is the lowest, indicating that calcite is a stable phase throughout the whole temperature range of the diagram. The driving force for nucleation of phase I ($\Delta\mu_i/k_BT$) is equal to the difference between $ln(AP)$ of the initial solution and its corresponding equilibrium curve at a given temperature.

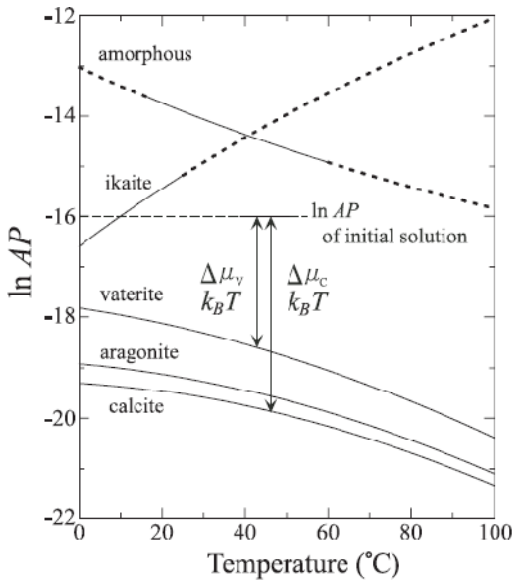

Figure 6.14: Precipitation diagram where the vertical axis is the natural logarithm of the activity product of calcium and carbonate ions, $ln(AP)$, and the horizontal axis is the temperature [307].

In the present work where the experiments were carried out at 70°C, it can be seen from Figure 6.14 that the driving force for aragonite and calcite are very close and in the presence of a substrate, the overall free energy change associated with the formation of a critical nucleus under heterogeneous conditions must be less than the corresponding free energy change associated

with homogeneous nucleation [296, 308]. Hence, the difference in crystal polymorphs or the presence of both calcite and aragonite at the same time may be explained by certain test substrates here that reduces this energy barrier for a particular polymorph while other substrates do not lower the energy barrier as much thus the promotion of another polymorph.

Initially, nucleation of the scale-forming crystals occurs and isolated tiny “islands” of solid are observed. The growth of these islands leads to the formation of a thin coherent layer, while a further increase of layer thickness is achieved by crystal growth. This is further illustrated by the aragonite crystal growth on polymer MSi as shown in Figure 6.15.

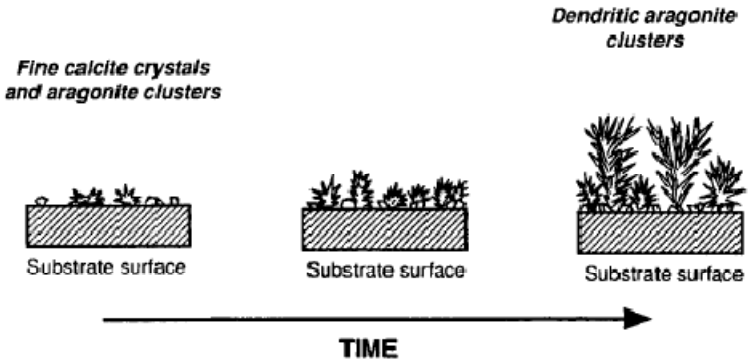

Figure 6.15a: Schematic representation of the temporal evolution dendritic aragonite deposits [92]

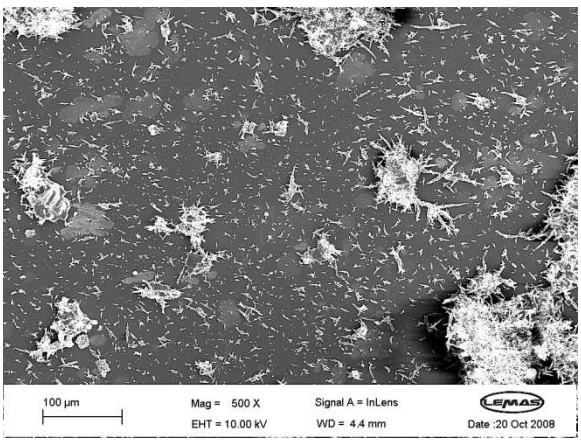

Figure 6.15b: 5 minutes at 1800rpm

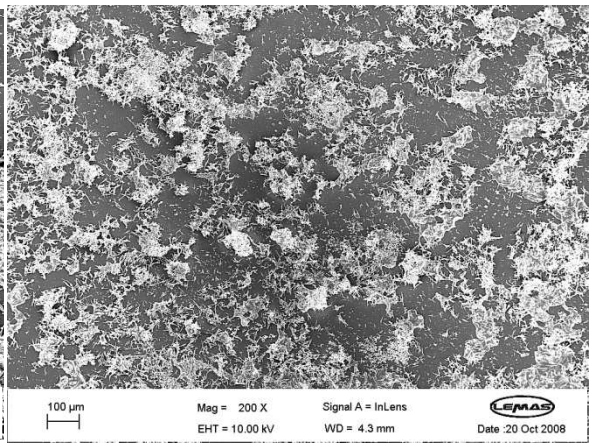

Figure 6.15c: 15 minutes at 1800rpm

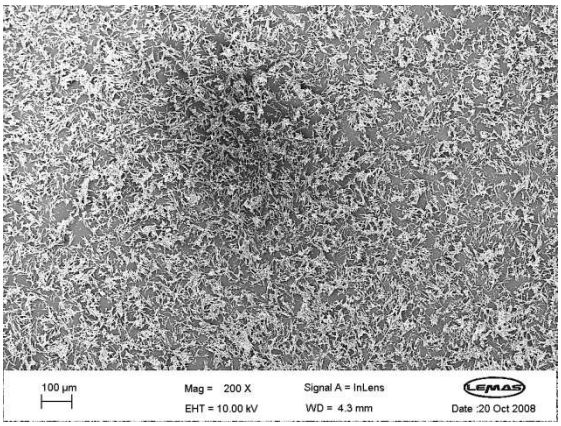

Figure 6.15d: 30 minutes at 1800rpm

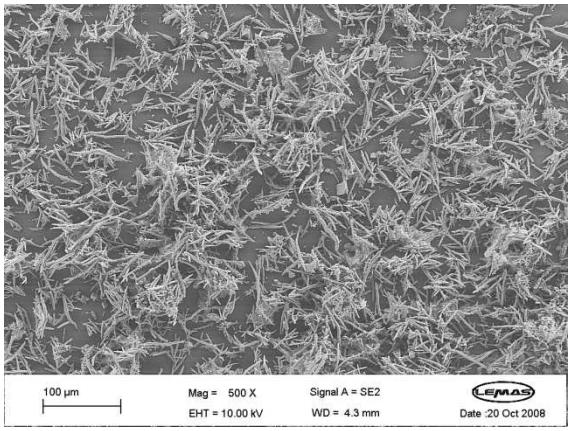

Figure 6.15e: 45 minutes at 1800rpm

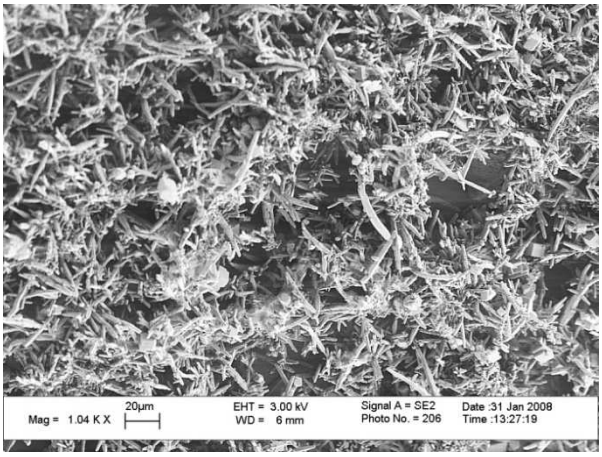

Figure 6.15f: 1 hour at 1800rpm

Figure 6.15: Predominantly aragonite crystal growth on polymer MSi from 5 minutes to an hour. Polymer substrates were immersed prior to the formation of bulk precipitate.

It can be seen from Figure 6.15 that the aragonite agglomerates in the form of clusters are outward oriented needles and these aragonite agglomerates tend to grow more rapidly than the calcite crystals when compared to other surfaces such as the coatings Tech 100 and Tech 23 which had predominately calcite crystals growing on them. The crystal aggregates obtained will be open and porous as can be seen from Figure 6.15f.

6.1.2 Physical aspects of the substrates and its effect on $CaCO_3$ deposition

Figure 6.16 displays the difference in cross sections of the surface asperities on the polymers for polymers MN, MSi, MD and LS. The scaling tendency for them is as follows: LS > MD > MSi > MN. Polymers LS and MD (both having deeper and wider structure compared to MSi and MN) have shown to be more prone to scaling compared to MN and MSi (both having the same depth and width). A difference can be seen where LS **(**Figure 6.16d) comprises of a 10 times larger structure relative to MN and MSi, it also has sharper and taller-peaks/deeper-ridges. Similarly, MD (Figure 6.16c) has a 1.4 times deeper and wider structure compared to MN and MSi.

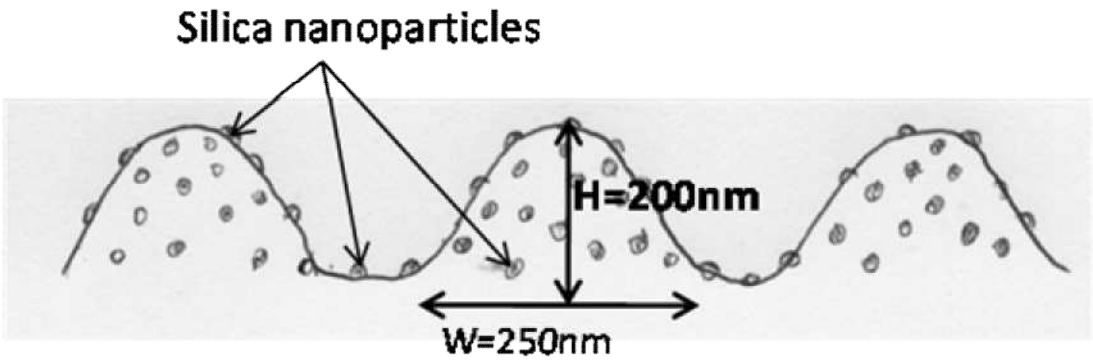

Figure 6.16a: Polymer MN - Silica nanoparticles add 'bumpiness' to surface structures.

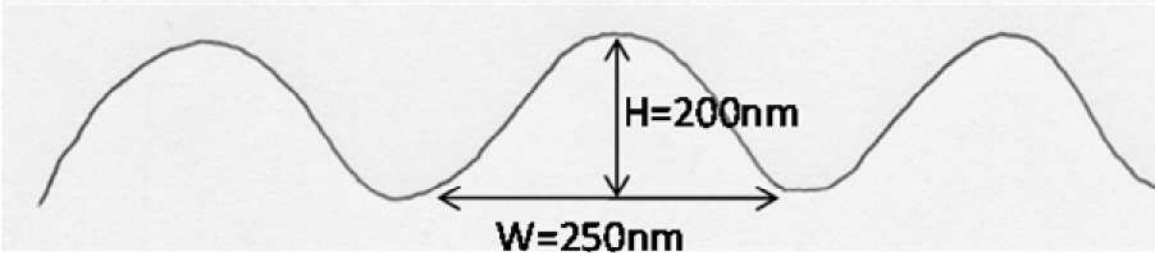

Figure 6.16b: Polymer MSi – Same physical structure as polymer MN without the silica nanoparticles i.e. smoother surface.

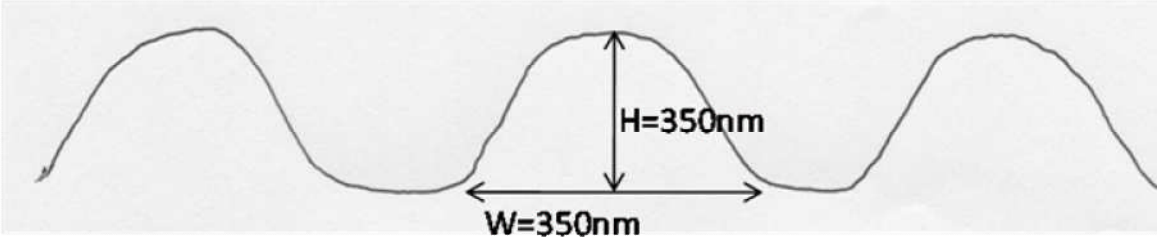

Figure 6.16c: Polymer MD – Deeper and wider structure compared to the polymers MN and MSi, also without silica nanoparticles.

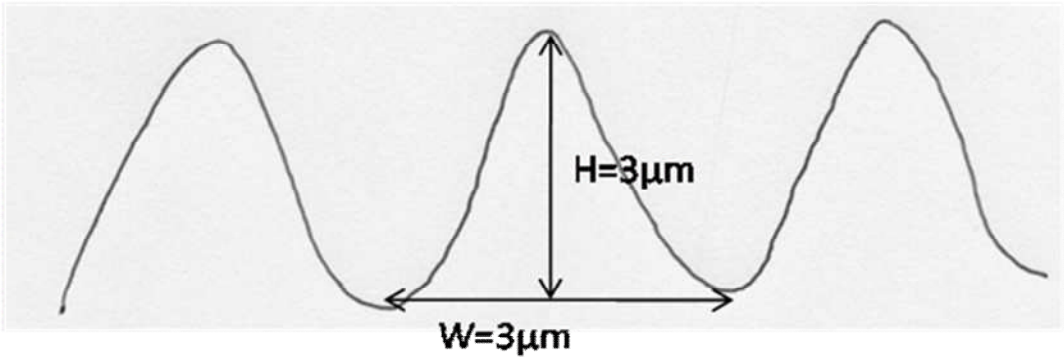

Figure 6.16d: Polymer LS – Comprises of roughly 10 times larger structure relative to the polymers MN and MSi. It also has sharper and taller peaks/deeper ridges.

Figure 6.16: Schematic diagram of the cross section of the various polymer surfaces

It can be seen for polymer MN, from Figure 6.16a, that silica nanoparticles or 'nanobumps' incorporated onto the surface asperities roughens the surface in two hierarchical levels, that results in a reduction of the contact area [142, 182, 309, 310] with the calcium carbonate crystals compared to polymer MSi (Figure 6.16b); the secondary features on the asperities can greatly enhance the surface repellence to particle adhesion [311]. In addition to the shape of these asperities, LS is arranged in a regular linear pattern (Figure 6.17a) while MD, MN and MSi are arranged hexagonally (Figure 6.17b) on the polymer surfaces.

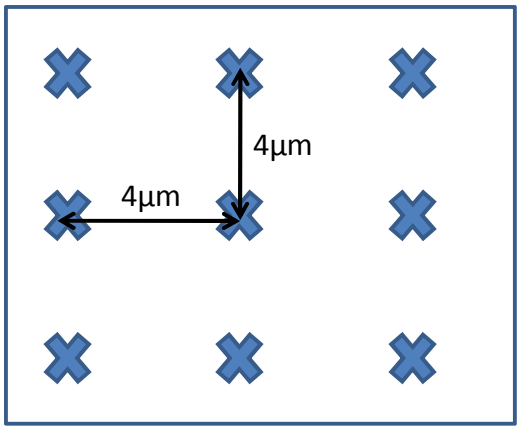

Figure 6.17a: LS is arranged in a linear and regular pattern.

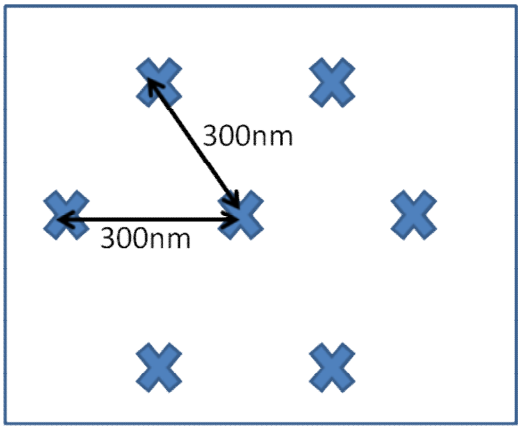

Figure 6.17b: MN, MSi and MD are arranged in a hexagonal pattern.

Figure 6.17: Geometrical arrangement of the asperities on the polymers

From this study, it can be seen that the geometrical structure of these surface asperities thus plays a role in the adhesion of crystals. A compromise between asperity spacing and other geometrical parameters such as asperity height and width spacing is necessary along with a harmonious combination of suitable materials and adequately rough geometry of surfaces can lead to a minimal adhesion of calcium carbonate scale. It can be deduced that flatter surface asperities in the form of bumps arranged in a hexagonal manner, with a range of 250-300 nm for asperity spacing and height, tend to reduce scaling tendency.

There has been a relatively extensive use of organic matrices in controlling crystal growth but very few studies have addressed the influence of surface topography on crystal growth [312-314]. This is of importance as surface roughness can considerably affect the structure of a crystallising layer [138]. Rough surfaces, constructed by the adsorption of 8 nm gold colloids on planar substrates have been used to aid the growth of calcium carbonate [315, 316]. When this is compared with the use of planar gold substrates, a higher density of crystals and a significantly higher proportion of aragonite was observed on the rough surfaces.

Using the MUST tester, it can be seen that LS surface comprises of microstructures (see Figure 6.16d) and that it has lesser adhesion between itself and the calcium carbonate crystal (aragonite) plate compared to the rest of the polymers, which is most likely due to its sharper peaks which give lower nominal contact. In addition, there is a difference in the number of contact points between the substrate and the crystal. Generally, the fewer the number of contact points, the less the adhesion force [317]. Polymer LS may have less measured adhesion but it had one of the highest mass gains after deposition tests were carried out – the sharper peaks may have acted as nucleation sites and hence promoted deposition.

On the other hand, polymer MN has round asperities which are flatter and wider so it still has low adhesion but no sharp points for crystal nucleation which leads to lower deposition. Polymer MN had less adhesion relative to MD due to its dual layer of roughness. Although polymers MN, MS, MSi and MF have similar roughness, they all exhibited a range of adhesion values and other parameters have to be considered such as surface chemistry to account for the differences.

High contact angle usually relates to higher hydrophobicity and should reduce adhesion [318]. Surface energies are associated with formation of adhesive bonds because they determine the extent to which at equilibrium, a liquid adhesive would come into contact with a solid surface [319]. However, it has to be noted that measurement of hydrophobicity involves placing a single water droplet onto the substrate while the surfaces in this study were fully immersed in a flowing solution.

From the results shown in Figure 4.22, it can be seen that Tech 100 and Tech 23 were hydrophobic with contact angles above 100° and they had low adhesion while DLC were less hydrophobic and had higher adhesion. Tech 100 is the most hydrophobic surface among the coatings and polymers and also the least fouling but it did not have the least adhesion. It is also interesting to note

that Tech 100 had the highest surface roughness (Figure 4.24) among all the substrates. Due to its roughness, the surface asperities on which crystals nucleate and grow from may protrude further out of the viscous layer which allows them to be sheared off by fluid flow.

Stainless steel on the other hand is the least hydrophobic, has the highest fouling tendency but has approximately the same amount of adhesion as polymer MS which was the second least fouling of the polymers tested. The effect of the oxide layer on the stainless steel surface may play a role in reducing adhesion [172] as carbon steel was tested against the aragonite crystal plate and it was found to have higher adhesion compared to stainless steel. On the other hand, it is widely believed that smoother surfaces discourage the fouling tendency as demonstrated by Zettler et *al*. [171] and their results of surfaces with different degrees of surface roughness and their fouling resistance is shown in Figure 6.18. In the case of electropolished plates, a smooth surface finish was achieved which resulted in less fouling. The asymptotic fouling resistance could be reduced to half that of the untreated plates.

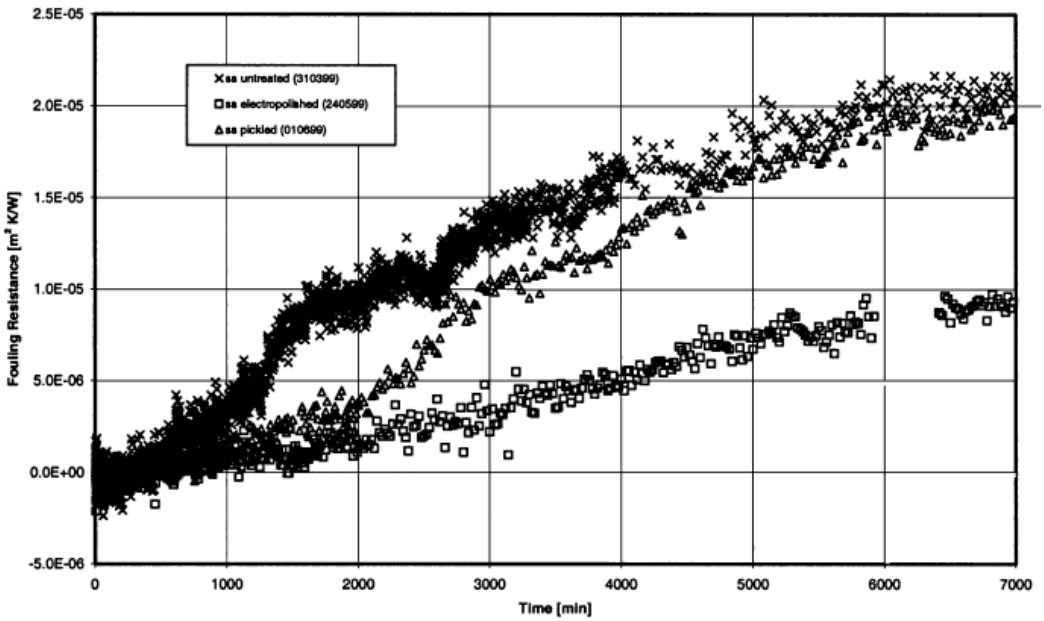

Figure 6.18: Effect of surface roughness on fouling resistance [171]

This is also linked to the general trend that the scaling tendency of surfaces increases with increasing surface roughness due to higher area of contact between surfaces, it seems to show otherwise here in this work (Figure 4.5) where rougher surfaces had less scale. A comparison is made with other work carried out on $CaCO_3$ and $CaSO_4$ in Figure 6.19. In contrast with the work of Keysar et al. [138], Herz et al. [146] and Quddus et al. [320], the surface roughness here can be considered to be in the "smooth" regime. In addition, so far the work here is also comprised of surfaces that are patterned whereas the other work does not. Furthermore, for the other studies, depending on the physical and chemical homogeneity of the surfaces, roughness-induced interactions were most likely to control the rate of scaling. In Bargir's work [179], for non-metal and metal that gave an average surface roughness (R_a) below 100nm, it was the polar contribution of the free energies that controlled calcite adhesion. Meanwhile, Förster et al. [148] found that the influence of surface macro-roughness of stainless steel on the induction time is that a minimum induction time exists which can be expected for maximum surface roughness and similar trends were observed for other surface materials but not with identical surface roughness. Hence, the link between surface roughness and its effect on scaling tendency has not been firmly established.

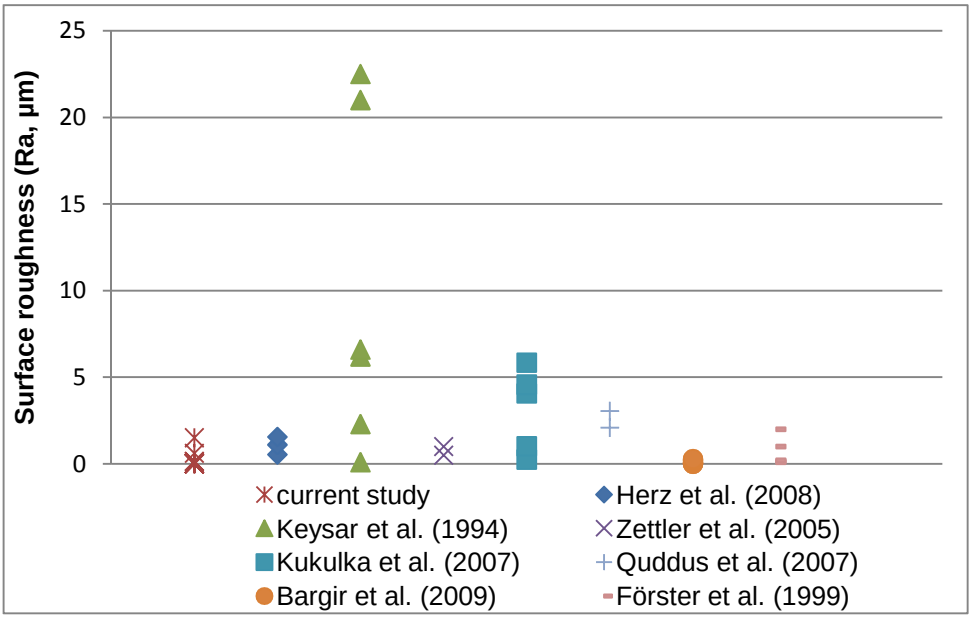

Figure 6.19: Comparison of current study with other works in $CaCO_3$ and surface roughness effect.

Table 6.2: Type of materials used here and scale deposited in comparison with other similar work repeated in literature [138, 146, 155, 171, 179, 320, 321].

	Type of materials used	Scale
Current work	• Nano- and micro-patterned polymers • DLC, Tech 23 and Tech 100 coatings • Stainless steel	$CaCO_3$
Herz et al. (2008)	• Stainless steel	$CaSO_4$
Keysar et al. (1994)	• Mild steel	$CaCO_3$
Zettler et al. (2005)	• Surface modified and untreated stainless steel (Ion beam implantation, ion sputtering, carbo-nitriding, oxidizing, Ni-P-PTFE coating)	$CaSO_4$
Kukulka et al. (2007)	• Carbon steel • Stainless steel • Aluminium	$CaCO_3$
Quddus et al. (2007)	• Aluminium	$CaSO_4$
Bargir et al. (2009)	• Stainless steel • Gold • Aluminium • Titanium nitrade • PTFE	$CaCO_3$
Förster et al. (1999)	• Mild steel • DLC • Aluminium • Copper • Perfluoroalkoxy (PFA) • Fluorinated Ethylene Propylene (FEP) • Strontium	$CaSO_4$

Figure 4.21 displays the results of the adhesion test carried out in water between a calcium carbonate crystal plate and the test substrates. Both surfaces of the crystal plate were tested, one being the rough side and the other being the polished side. It can be seen that generally the adhesion between crystal and substrate was higher on the polished side compared to the rough crystal side due to higher contact area between the surfaces.

This test was carried out in order to assess whether these adhesion tests would give a reasonable prediction of the scaling tendency for the substrates. It can be seen for stainless steel (SS) and polymer MS that they have almost the same adhesion but exhibit different gain in mass. An increase in adhesion of the test substrates leading to an increase in mass gain would be the expected result but the work here has shown that this is not a feasible approach. However, this study would be an estimate of the adhesion force expected when crystals migrate from the bulk solution to the surface.

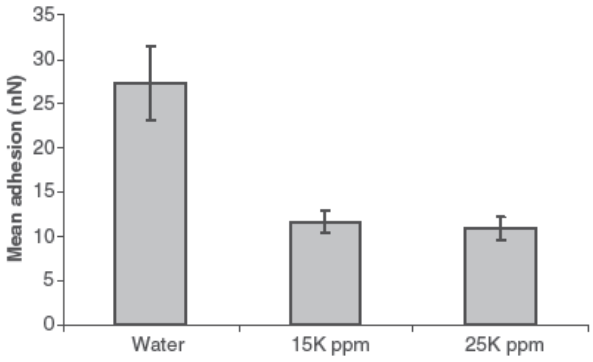

Figure 6.20a

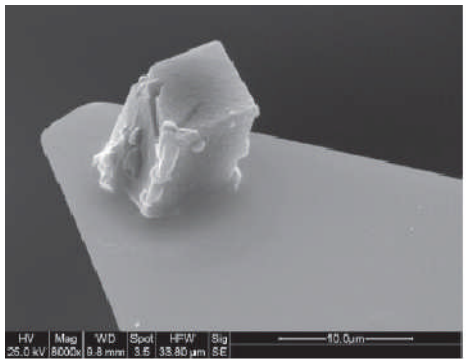

Figure 6.20b

Figure 6.20(a) Adhesion between a $CaCO_3$ crystal as AFM probe and three steel surface samples; (b) SEM image of a $CaCO_3$ crystal mounted on an AFM cantilever.

No other studies have been reported for the interaction between $CaCO_3$ and steel surface except for one. Al-Anezi et *al*. carried out adhesion measurements between a $CaCO_3$ atomic force microscopy (AFM) probe and stainless steel surface in water and synthetic sea water at concentrations of 15 and 25ppm; the mean adhesion values can be seen in Figure 6.20a [322]. They suggested that the presence of dissolved metal ions in the synthetic sea water decreased the affinity of the $CaCO_3$ crystals for the stainless steel surfaces. They found that when the adhesion between $CaCO_3$ and stainless steel surfaces of different roughness was measured, the roughest surface had a lower adhesion than the two less rough surfaces which is similar to what has been formed in the present work. This can be attributed to greater roughness

tending to give smaller contact areas, however, for particles of a size comparable to the length scale of the roughness asperities on the surface, contact area can actually be increased than if against a smoother surface.

Hence, adhesion between crystals and substrate depends on how the crystals came to be on the surface and this is looked at next.

6.2 Mechanistic model for crystal deposition on patterned polymers and other test substrates

In a supersaturated solution, particles may form directly on a surface via true surface heterogeneous nucleation or, alternatively, particles formed by spontaneous or homogeneous nucleation may physisorb on the surface [292]. Significantly less information exists for the mechanism of scale formation on a solid surface [229]. Until now, scale formation is the result of unavoidable primary nucleation on a surface thus this makes the chemistry and geometry of metal surfaces an important concern. Active chemical sites as well as the crystal geometry of a metal are important in primary nucleation [323].

In the case of inorganic fouling, two important mechanisms are recognized, among others, i.e. crystallization (Figure 6.21) and particle deposition (Figure 6.22). The former can be attributed to ionic and/or molecular species precipitating right onto the surface. Particulate matter that are present in the bulk solution is responsible for the latter [324]. Figure 6.22 illustrated a particle deposition process which can be described in a two-step process: (1) particles are transported from the bulk of the solution to the walls, according to hydrodynamics, and (2) particles adhere, according to the chemical interactions between the particle and the wall (DLVO theory) [286, 325]. The DLVO theory describes the chemical interactions where the force of adhesion is the sum of the electrostatic forces and the Van der Waals forces. The electrostatic forces are dominant during the deposition phase and this is where the relative charge

of the surfaces becomes the determinant parameter indicating whether the interaction is repulsive or attractive. Isoelectric points (IEP) of the particles and of the substrate will show the pH range where adhesion could occur, but hydrodynamics force must be considered because a strong drag force not only removes deposited particles, but also can promote the deposition by increasing the collision frequency and the kinetic energy of the particles. The effects of hydrodynamics on $CaCO_3$ deposition is examined later in this section. IEP can be measured by methods different for particles (zetameters) and for massive substrates (contact angles, streaming potential, etc).

Evidence from the present work suggests that anti-scaling and anti-fouling are not the same. The deposit layer formed by crystallization on the surface has a different structure than that formed by particulate fouling [91]. The former being more tenacious in adhesion compared to the latter form of fouling which would be expected to be more loosely adhered.

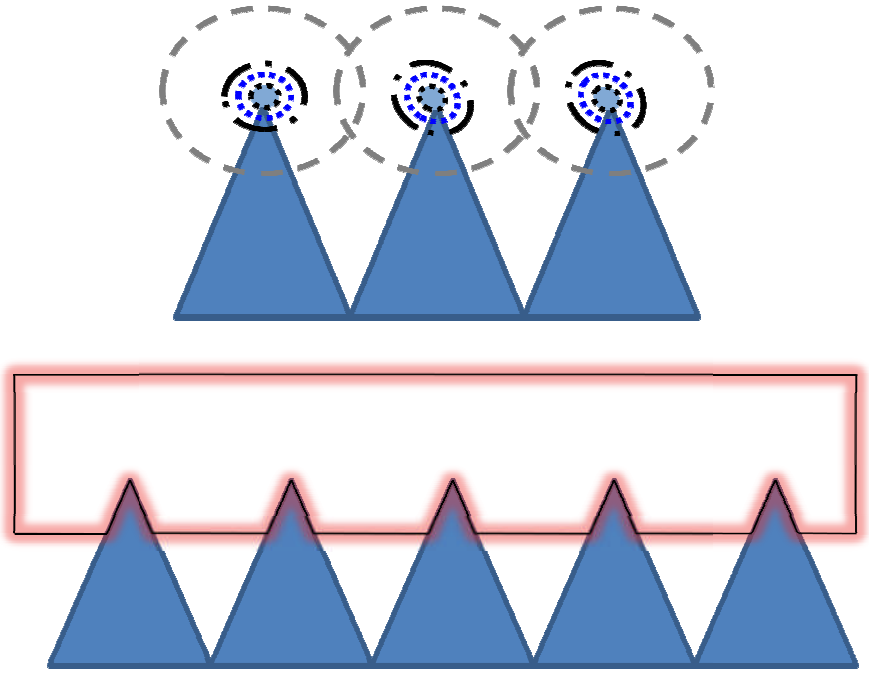

Figure 6.21: Crystals nucleate and grow from surface asperities

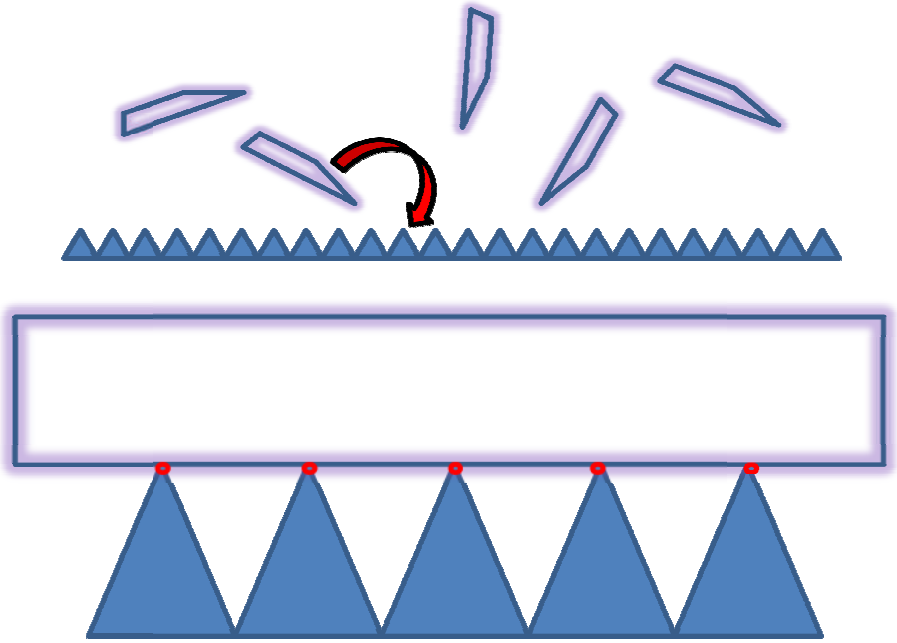

Figure 6.22: Illustration of how crystals migrate from bulk solution and settle onto surface

From Figure 6.21 and Figure 6.22, it can be deduced that a difference in adhesion between crystal and substrate in both scenarios is expected due to a larger surface area (highlighted by the red lines) in contact at the interface especially when crystals crystallized and grew from the surface itself. The adhesion at the crystal-substrate interface would be higher in Figure 6.21.

The nature of nucleation may determine the structural energy between the test substrates and the calcium carbonate scale and consequently give an idea about the basic structure of the scale formed. If nucleation proceeds in a heterogeneous manner, a strong interaction between the nucleating phase and the substrate is expected. In this case, the adherence of calcium carbonate to the substrates will be strong, and the structure of the scale formed should be compact and tough. Conversely, if the substrates did not have an effect on nucleation, nucleation will occur randomly in the bulk solution and greatly reduce the adherence at the crystal and substrate interface [308].

Evidence that the crystals have grown from the surface instead of depositing from the bulk solution can be seen when crystals are flipped over by hydrodynamic shear stress. From Figure 6.24, the patterned polymer structure is replicated in the nucleating crystal face, with a motif of close-packed hexagonal cavities patterning the faces of calcite and aragonite. Accordingly, this is an example of crystals in confinement whereby the morphology of crystals in a constrained volume is modified through interaction with the structured environment itself. Conclusive evidence in many studies [326-328] has demonstrated that single crystals with complex morphologies can be produced in the absence of complicated biological pathways; morphology of single crystals can be determined by the form of the environment in which they crystallize, an example is presented in Figure 6.23. Likewise, the present work (Figure 6.24) results in crystals that show one side which have clearly been templated by the polymer surfaces, and the other side having regular planar surfaces where the crystal had grown into the bulk solution; this is similar to Figure 6.23 where calcite was templated by the sea urchin membrane in which it formed.

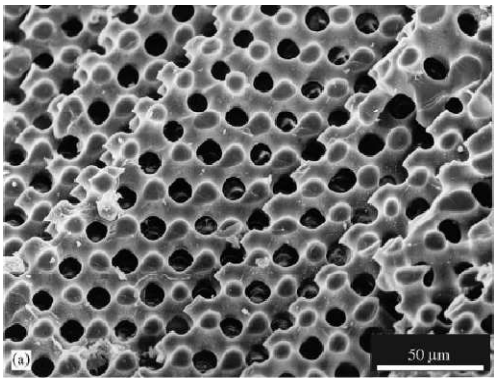

Figure 6.23a: Cross-section through a sea urchin skeletal plate showing the bicontinuous structure and pores of diameter 10-15µm [326].

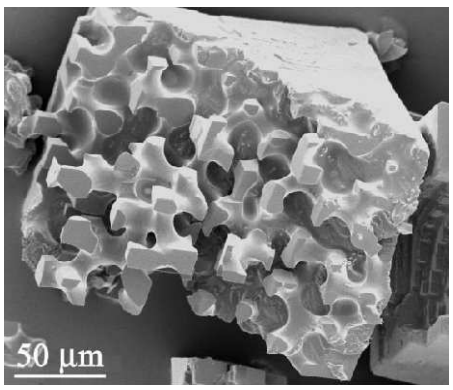

Figure 6.23b: A template single crystal of calcite precipitated within the polymer membrane [259].

Figure 6.23: (a) Calcium carbonate was precipitated within a polymer mould from sea urchin skeletal plates, (b) The curved surfaces of the calcite crystal arise when the crystal impinges on the polymer mould during growth, while the planar surfaces represent the growth front of the crystal which is not in contact with the polymer.

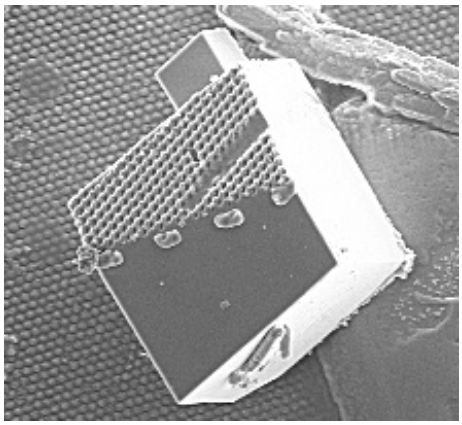

Figure 6.24a

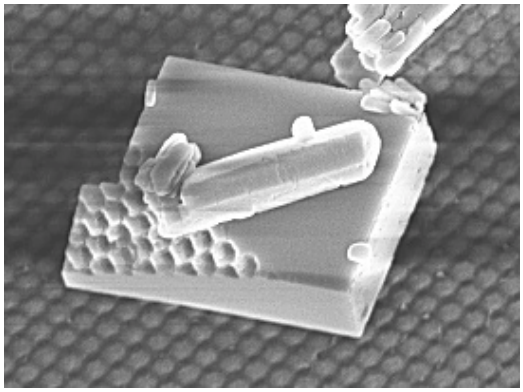

Figure 6.24b

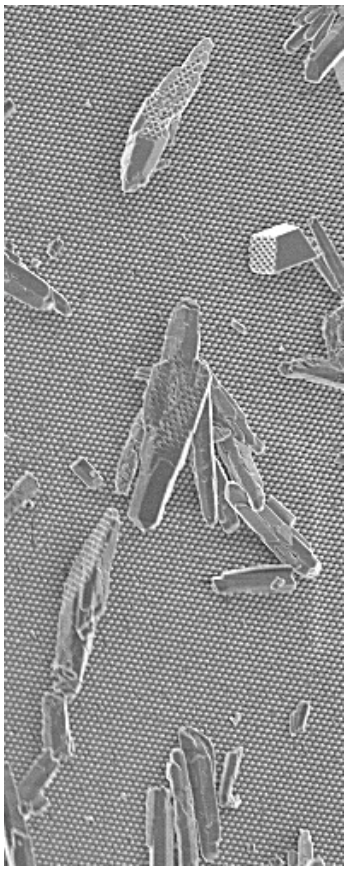

Figure 6.24c

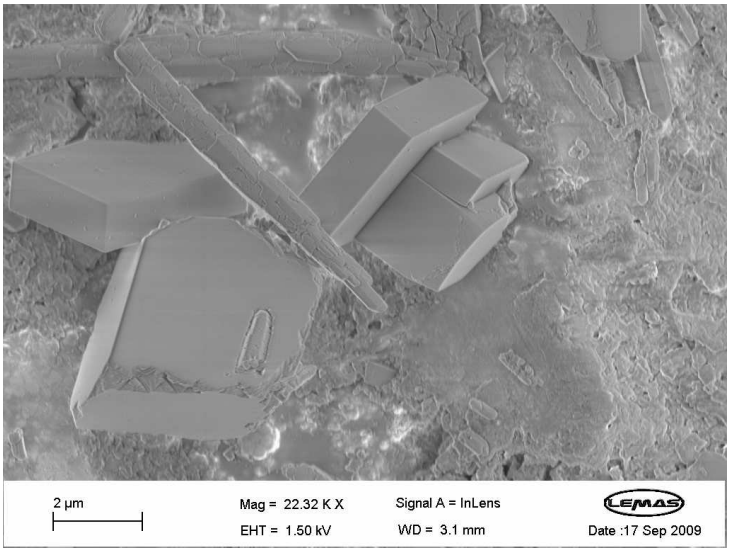

Figure 6.24d

Figure 6.24: (a,b) Calcite, (c) aragonite crystals on polymer surfaces flipped over by wall shear stress, (d) Imprint of coating surface can be seen on calcite crystal.

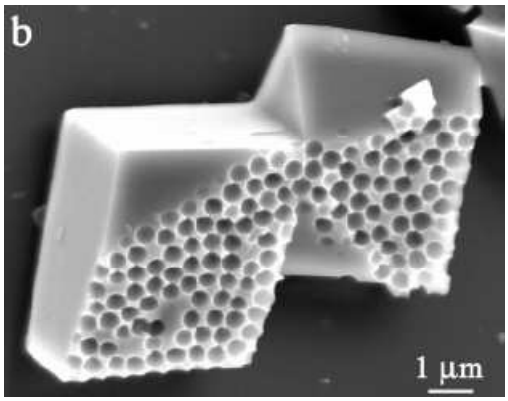

Figure 6.25a

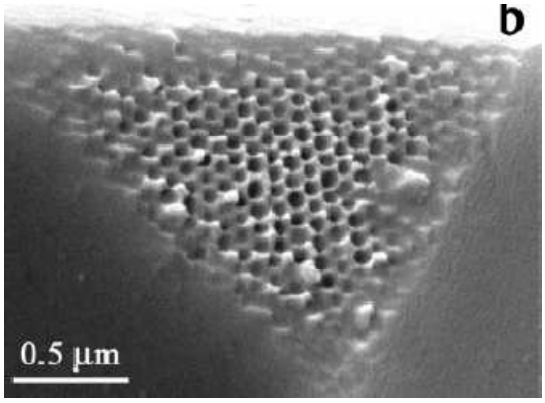

Figure 6.25b

Figure 6.25: Calcite crystals grown on 0.5µm colloidal polystyrene monolayer after dissolution of the polystyrene spheres, showing the crystal face growing in contact with the monolayer [329]

In another study where substrates of close-packed monolayers of either polystyrene or silica spheres were used to support the growth of calcium carbonate to investigate the role of surface topography and chemistry in controlling the crystal morphology, it was found that the pattern of features produced on the crystal face (Figure 6.25) perfectly replicated the topography of the substrate when the flow of ions to the growing crystal was not restricted [329]. This again supports the finding that the crystals were nucleating and growing from the test substrates here in the present work. Likewise in the previous section, the observation that the calcite crystals were perched on a corner especially on coatings Tech 23 and Tech 100 further points out that it was a surface-induced nucleation. In addition, the substrates were vertically aligned in the rotating cylinder electrode experimental setup therefore reducing the influence for sedimentation and heterogeneous nucleation would be a reasonable explanation.

Precipitates or crystals formed in one part of a system and carried to another part are less adherent than those crystals formed on site, and that impingement of solids has little effect on scale deposition [323]. Another test carried out here was to immerse the samples after the formation of bulk precipitate to determine whether crystals were growing from the surface or

settling from the bulk. A comparison between substrates immersed before and after bulk precipitation has occurred can be seen in Figure 6.26.

There seems to be a general trend where the population and size of the adhered crystals decreased when the substrates were inserted 15 minutes after bulk precipitation as seen from Figure 6.26. This observation shows that the main process of adhesion is the direct growth of the crystals on the surface and that the indirect adhesion or particulate deposition from the crystals precipitated in the solution is much less important. Hence, once bulk precipitation is completed, very little scale from the bulk solution adheres to the surface.

Immersion of samples for an hour after 15 minutes of bulk precipitation

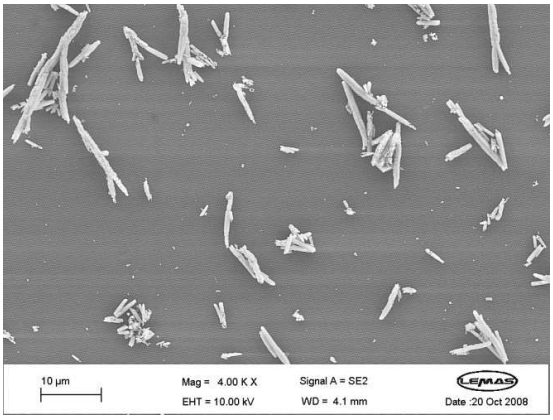

Figure 6.26a: Polymer MN

Immersion of samples prior to the formation of bulk precipitate

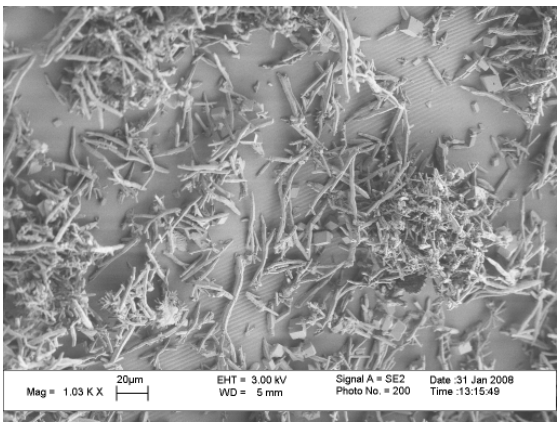

Figure 6.26b: Polymer MN

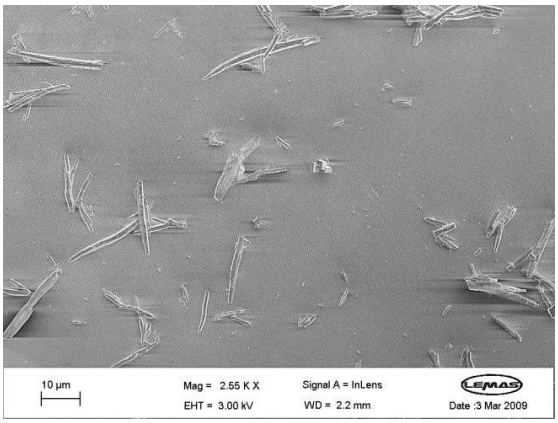

Figure 6.26c: Polymer MSi

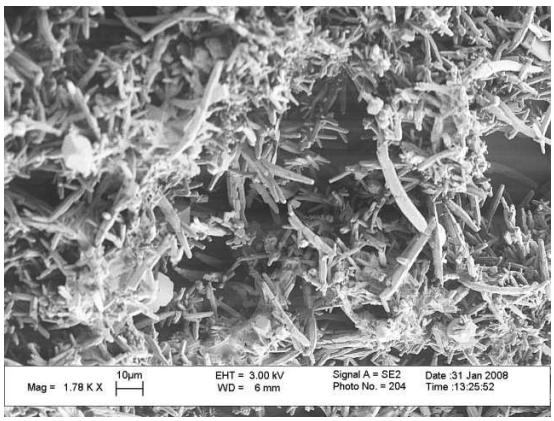

Figure 6.26d: Polymer MSi

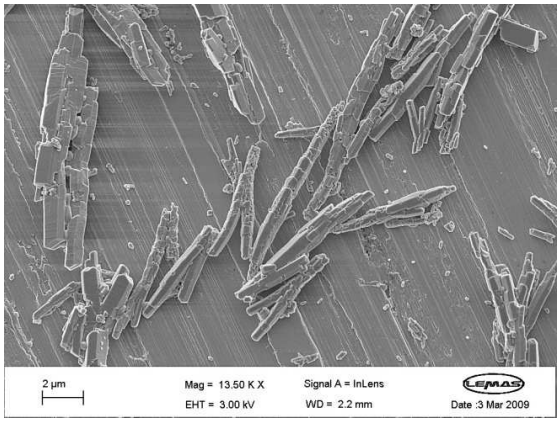

Figure 6.26e: Stainless steel

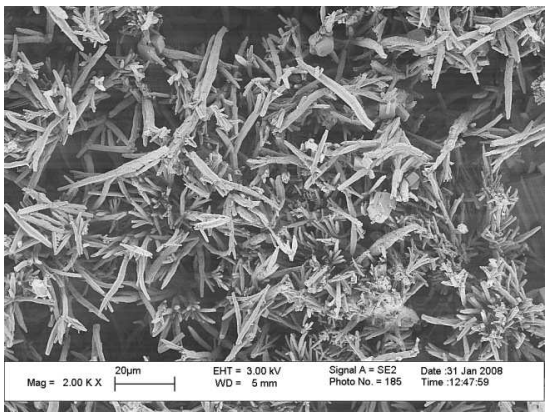

Figure 6.26f: Stainless steel

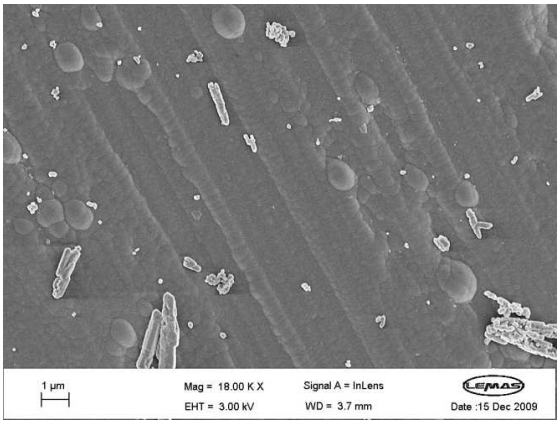

Figure 6.26g: DLC

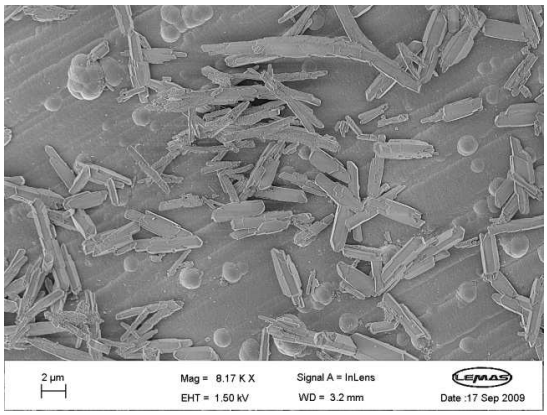

Figure 6.26h: DLC

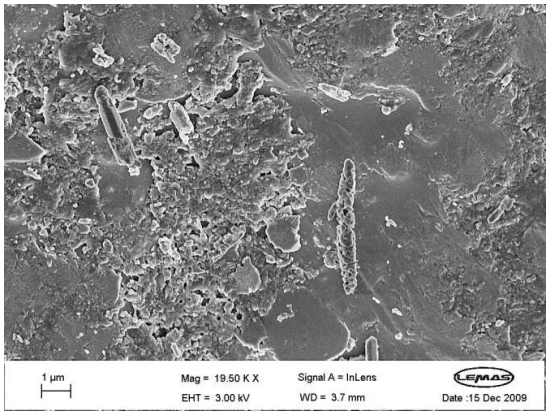

Figure 6.26i: Tech 23

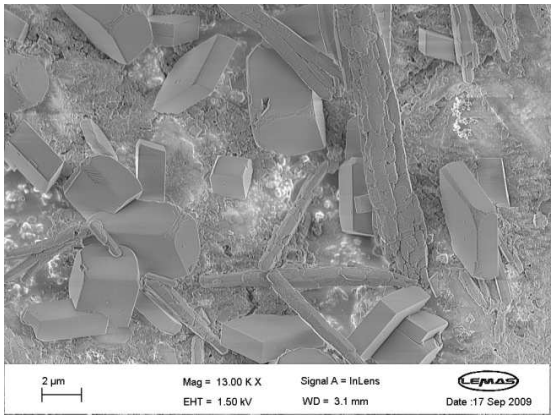

Figure 6.26j: Tech 23

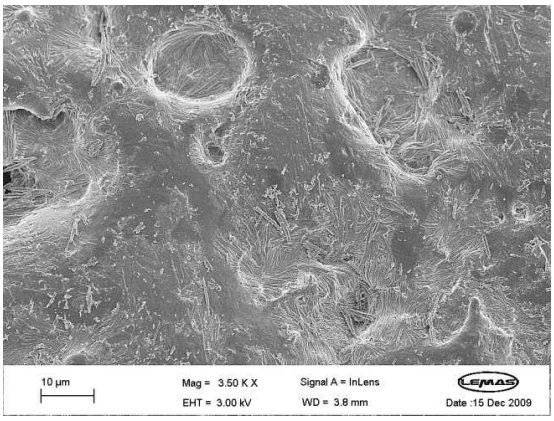

Figure 6.26k: Tech 100

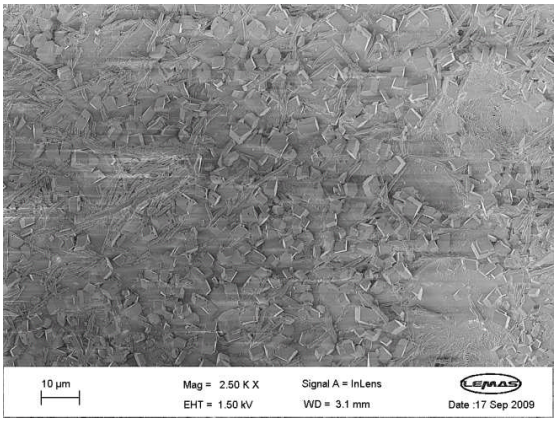

Figure 6.26l: Tech 100

Figure 6.26: Comparison of crystal numerical density between 1 hour immersion of samples right from the beginning and 15 minutes after bulk precipitation had occurred

The above finding was also reported in similar study of the adhesion mechanism of $CaCO_3$ using a combined bulk chemistry/quartz crystal microbalance (QCM) technique [229]. When the QCM sensor has been inserted in the reaction solution prior to the formation of the precipitate, orthorhombic calcite was nucleated and grown on the surface of the sensor after an induction period of several minutes of induction period. These processes synchronized to the precipitation processes in the bulk solution i.e., transformation of amorphous $CaCO_3$ (ACC) to crystalline $CaCO_3$ (calcite and vaterite) and the transformation of vaterite to calcite. When the QCM sensor was inserted in the suspension after the complete transformation of ACC, a thin disc of leaf-like vaterite was grown on the surface, whereas the vaterite of the precipitate in solution was spherical. In addition to these direct adhesions or direct growth from the surface itself, the indirect adhesion of the crystalline $CaCO_3$ already precipitated in the solution was observed, although the contribution of this adhesion to the scaling is very small.

In the case where the $CaCO_3$ crystals adheres to the surface in a liquid media, the adhesion force will include van der Waals forces and electrostatic forces. Van der Waals forces are always present, the electrostatic forces that arise from double-layer interactions occur mainly in aqueous media due to the

high electric constant of water. While, in aqueous solutions with high contents of salt such as in this present work, these interactions are screened and electrostatic forces becomes negligible [330].

6.2.1 Hydrodynamic effects

The effect of velocity on scale-growth was investigated over the range of Reynolds number (~60-12000) from laminar to turbulent flow. It is widely believed that temperature and flow velocity have a marked effect on the deposition rate and an increase in both parameters results in higher deposition rate. Similarly, it is also observed that almost all parameters investigated influence the morphology and the crystal habit of the deposits. In addition, an increase of fluid velocity tends to make the deposits somewhat more compact, resulting in an increase of the bulk density [92, 298]. Since these deposit characteristics essentially determine important properties of the deposits, such as thermal conductivity, compactness (see Figure 6.27) and propensity for removal, it would be useful to investigate the morphological features of $CaCO_3$ deposits, formed under well-controlled conditions. SEM images of scale at different rotational velocities was presented in Figures 5.3-5.5. The effect of fluid velocity on scale on the test substrates was not apparent on the morphology in this study and the mass gained from scaling increased non-linearly with an increase in higher velocity.

As seen from the results for the scaling tendency as a function of Reynolds number (Figure 5.1), the effect of hydrodynamics on the coatings DLC, Tech 23 and Tech 100 can be considered to be secondary when compared with the polymers and the reference stainless steel surface. The coatings and polymer MN had a less pronounced increase with increasing turbulence with respect to stainless steel and polymer MSi. At 10 and 900rpm, all surfaces except for stainless steel had similar deposition. The mass transfer boundary layer is thicker compared to a thinner boundary layer when the fluid velocity is increased. In addition, if particulate fouling dominates, the deposition

rate should decrease with increasing velocity which is not the case here as $CaCO_3$ is not fragile enough to be easily removed. Most likely, the peculiar structure of polymer MN which had 'nanobumps' illustrated earlier in Figure 6.16a allowed fewer contact points relative to polymer MSi and this contributes to less adhesion between crystal-substrate interface thus allowing hydrodynamic forces to shear some loosely adhered crystals off the surface.

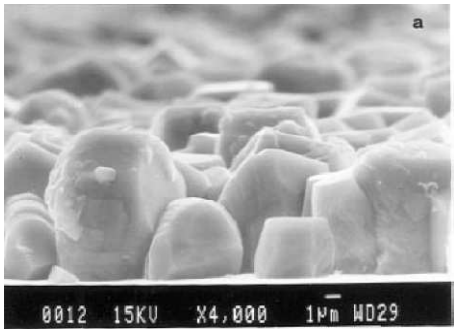

Figure 6.27a: Side view of calcite deposits

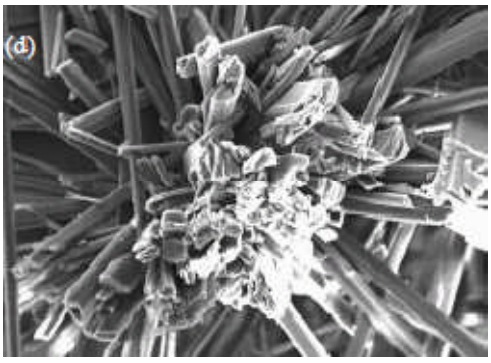

Figure 6.27b: $CaSO_4$ crystals with perpendicular growth

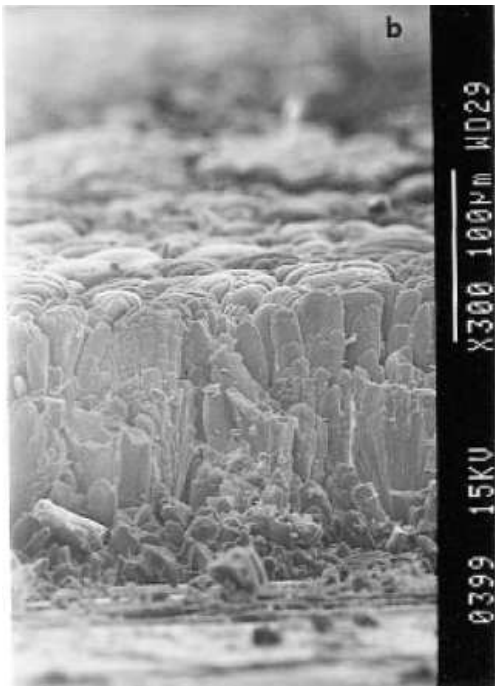

Figure 6.27c: Side view of calcite deposits

Figure 6.27: General morphology of calcite [92] and $CaSO_4$ prismatic needles/rods [95]. The needle-like crystals tend to be more porous and loose than compacted calcite crystals.

It is difficult to ascertain the effect of fluid flow on kinetics of precipitation and the exact location where the foulant forms, i.e. bulk, boundary layer or right at the surface. The thickness of the boundary layer changes with flow rates and this may quantify how the controlling step of the deposition process alternates from diffusion controlled to surface reaction controlled as the velocity of flow

increase [91]. If there are crystals forming in the bulk or in the boundary layer, deposition will be by means of particulate fouling. Crystals in the bulk would have to gain sufficient momentum in order to break into the viscous sublayer where they will lose momentum and slow down and may be entrained in this sublayer where they may eventually adhere onto the surface. Meanwhile, crystallization fouling involves the precipitation of soluble species directly on the surface. This occurs either by molecular diffusion within this laminar sublayer film or by chemical reaction at the surface, or by both mechanisms. The aragonite crystals precipitated here in the present work are usually of a minimum of 10μm in length and they agglomerate and extend upwards from the surface, while the calcite crystals are usually cubic and of 2μm in cubic length. In almost all cases, the crystals are all in the viscous sublayer unless there are thick layers of aragonite which occurs in the cases of the reference stainless steel, polymers MSi and LS.

On the other hand, other investigations have found that the scale growth rate as a function of Reynolds number gave a straight line represented and the process is diffusion-controlled. Their results can be seen in Figure 6.28 and Figure 6.29. A plot (Figure 6.28) of $CaCO_3$ scale-growth rate on heat transfer surfaces as a function of Reynolds number power 0.68 gave a straight line which suggested that diffusional mechanisms are dominant. In other words, the scale growth was controlled by the rate of forward diffusion of Ca^{2+} and HCO_3^- ions toward the scale-water interface. The difference between other studies and the present work is the substantial difference in temperatures between the surface and the bulk water to obtain the graph of Figure 6.28 because they were conducted on heat transfer surfaces thus the prime driving force is the local supersaturation at the heated surface.

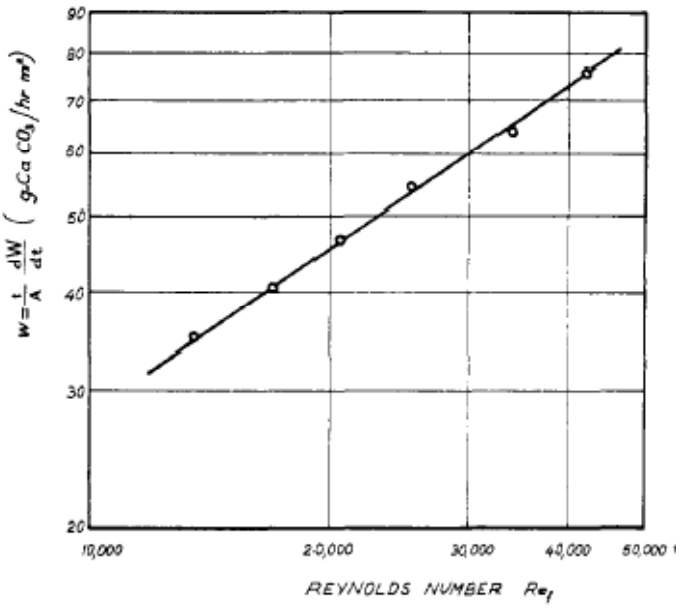

Figure 6.28: Effect of Reynolds number on the rate of growth [101]

Meanwhile, Figure 6.29a displays a nearly linear relationship of deposited PbS (which is also an inverse solubility salt like $CaCO_3$) to the flow rate. This is consistent in the case of diffusion-controlled transfer to the pipe wall of ionic species or of colloidal particles. Likewise, Figure 6.29b shows a similar pattern for calcium sulphate scaling on polished and prescaled samples.

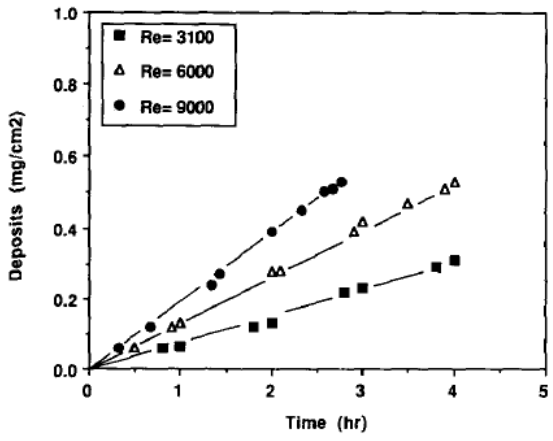

Figure 6.29a

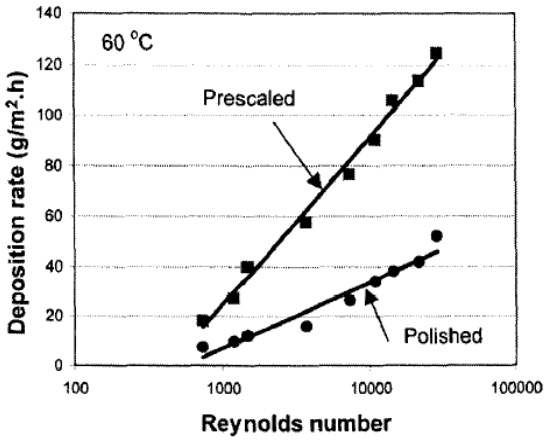

Figure 6.29b

Figure 6.29: (a) Deposition rate of PbS [324] and (b) calcium sulphate as a function of Reynolds number [102].

In contrast with the work here, there was no indication of a linear relationship between scale mass gain with Reynolds number in the range of 60-12000 rpm, this can be seen in Figure 6.30. The mass gain does increase with increase in Reynolds number like in other studies, such as in Figure 6.29, but the results obtained here indicate that the mechanism is more complex than just diffusion-controlled.

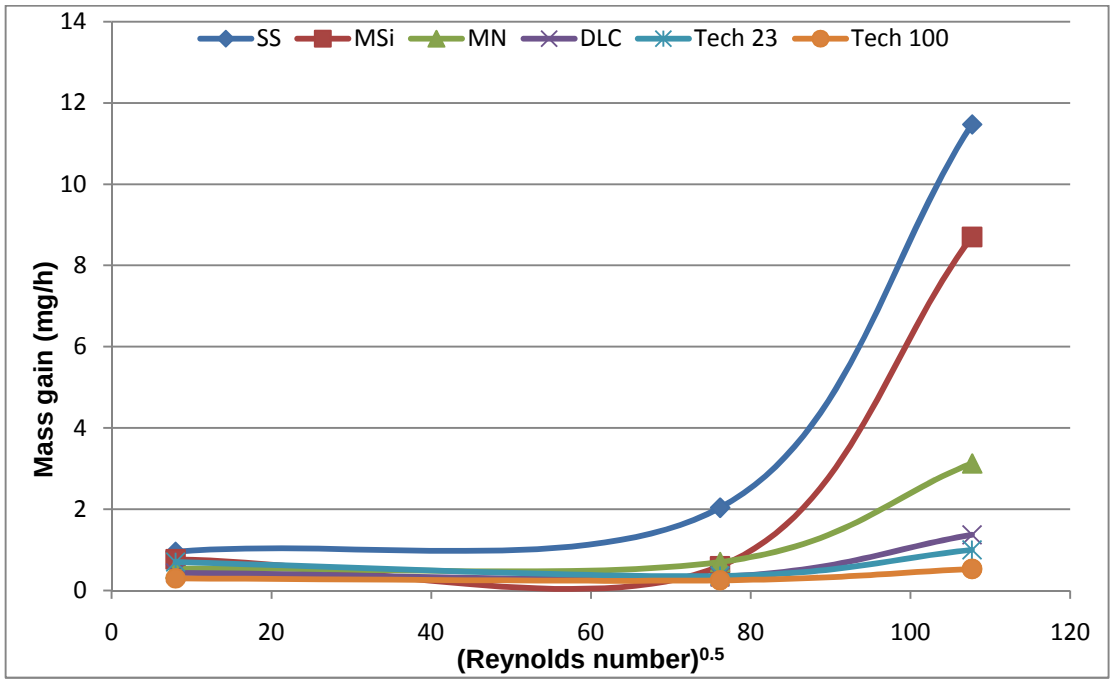

Figure 6.30: Mass gain as a function of (Reynolds number)$^{0.5}$. Linear relationship would indicate that the process of $CaCO_3$ precipitation on the surface is diffusion-controlled.

The influence of mass transport of reacting species is significant when the solution is stagnant or flows in the laminar regime. However, if the flow turns turbulent, molecular diffusion will be enhanced by turbulent eddies, such that under otherwise unchanged conditions, the rates of precipitation can increase by up to several orders of magnitude [280].

Comparison between the work reported here and others in literature are given in Figure 6.31 and Figure 6.32. From Figure 6.31, the work here is limited to the Re numbers of 0-11600 while the Quddus et al. (2009) study was extended further up to 44000. On the other hand, Hasson's study spanned

14000 to 42500. These studies were all concerning $CaCO_3$ and on the various surfaces shown in Table 6.3. Meanwhile, this study fills in the behaviour of various substrates in the lower Re range in contrast with the others that were conducted at higher Re numbers and displayed a considerably linear relationship with $CaCO_3$ scaling tendency. In the lower Re range, it has been shown that the mechanism of crystallization is more complex than just being diffusion-controlled as there is no linear relationship, as shown in Figure 6.30. The results by Quddus et al. (2007) are those obtained from $CaSO_4$ scale for surfaces with two surface roughness – 2.1 and 3µm. Again, they found that the process is diffusion-controlled because of the linear correlation. It is also useful to note that all the other studies were conducted with a solution of constant composition, which is not the case in the present work.

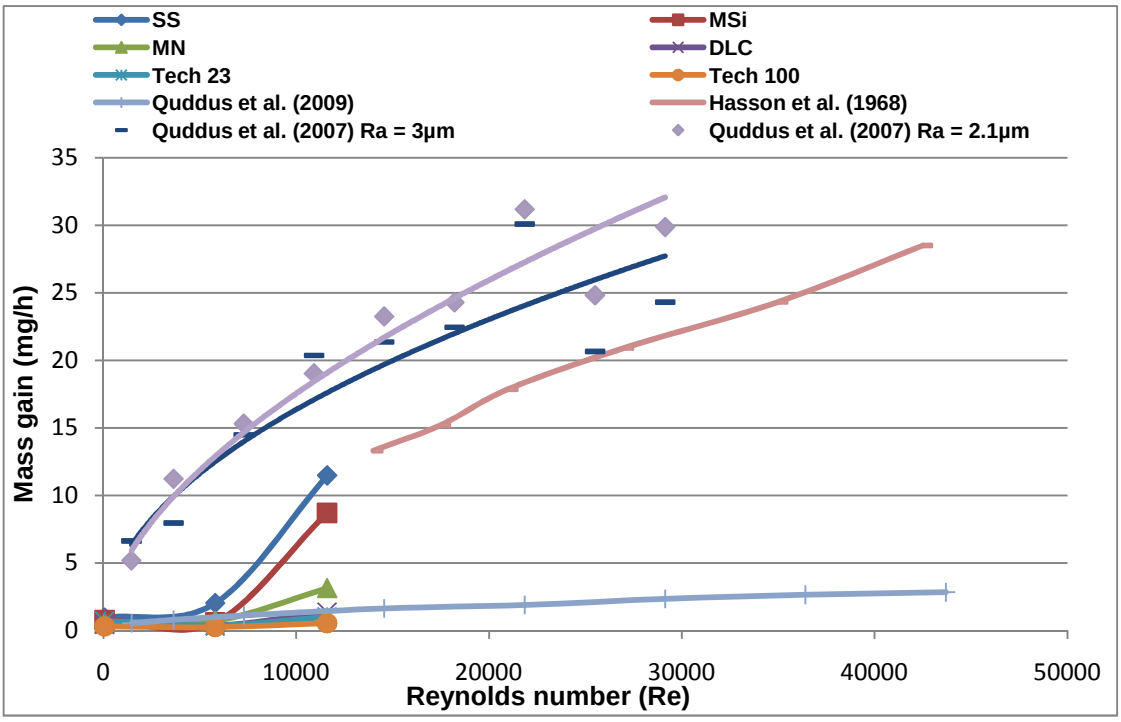

Figure 6.31: Comparison between current work and others of which the types of surface material and scale are detailed in Table 6.3 [95, 101, 320].

Table 6.3: Comparison between current work and others on type of surface material, scale and operating parameters

	Type of surface material	Type of scale and operating parameters
Current work	• Nano- and micro-patterned polymers • DLC, Tech 23 and Tech 100 coatings • Stainless steel	$CaCO_3$, conc.=0.001mole/L, temp.=70°C, effective time = 1h
Quddus et al. (2009)	• Stainless steel	$CaCO_3$ conc.=0.0008mole/L, temp.=60°C, effective time = 4h50min
Hasson et al. (1968)	• Copper	$CaCO_3$ conc.=0.0062mole/L, surface temp.=75-76.5°C, bulk temp.=45°C, effective time=16-60h
Quddus et al. (2007)	• Aluminium (At 2 surface roughness, Ra=3 and 2.1μm)	$CaSO_4$ conc.=0.03mole/L, temp.=60°C, effective time=6h

From Figure 5.9, it can be seen that an increase in hydrodynamic wall shear stress does not lead to any decrease in scaling which points out that the scale is either very tenacious and adherent or a larger shear force at the wall is required to remove crystals. In the case where particulate fouling was dominant, a decrease in scaling tendency would be expected for an increase in turbulence and flow rate which would in turn induce larger shear stresses that would generate sufficient lift forces to cause the crystals to be unstuck from the wall. The mechanism for particulate removal is illustrated in Figure 6.33.

In comparison with another study on the influence of hydrodynamic wall shear stresses, the shear stresses the surfaces experience here is in the range

0.0009-6.3Pa and was found to be insufficient to remove any noticeable amount of scale. In this study where $CaCO_3$ crystallization occurs, a tenacious layer forms in most cases and the removal rate is found to be insignificant. The effect of velocity on removal depends primarily on the wall shear stress and the mechanical strength of the scale layer. The study undertaken by Royer et al. (2010) (Figure 6.32) is in the range of 0.38-82.5Pa where it reflects the critical shear stresses required to remove significant amounts of $CaCO_3$ scale which is considerably higher than the shear stresses that were generated in the present work. They found that a shear stress of 82.5Pa was required to remove scale from untreated stainless steel surfaces, 54.3Pa for DLC coated surface, 29.1Pa for Polytetrafluoroethylene (PTFE) surfaces and 0.38Pa for Polypropylene (PP) surfaces.

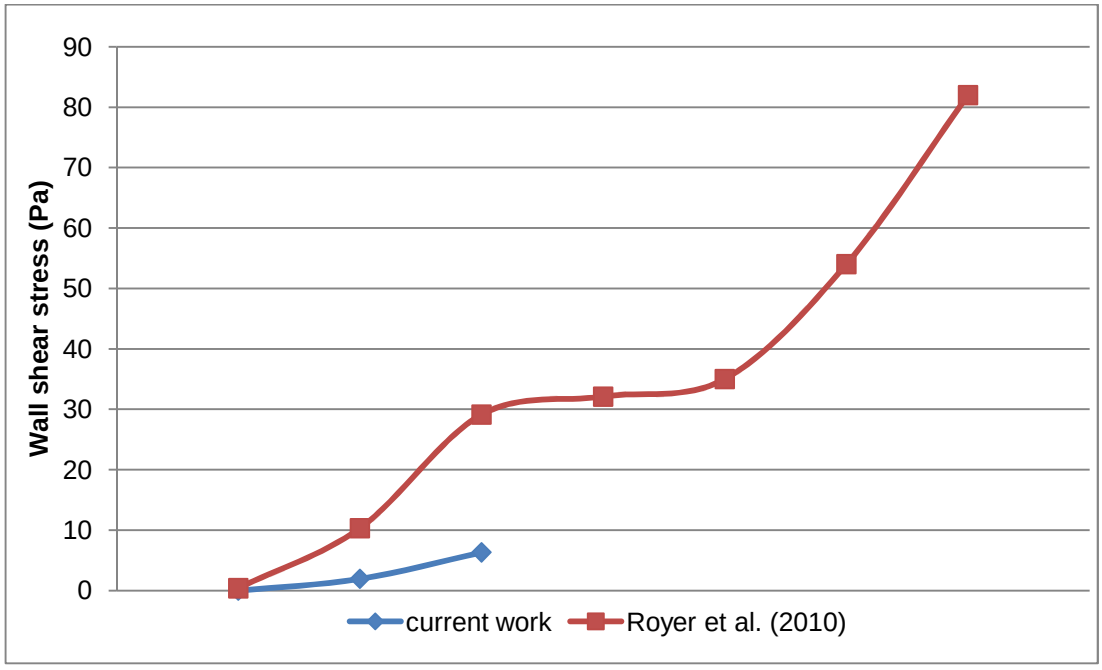

Figure 6.32: Comparison between the hydrodynamic wall shear stress applied in this work in contrast to the study of Royer et al. [331].

As mentioned earlier, there is a viscous sublayer near the wall for turbulent flow in a pipe. Where the crystal is fully submerged in the viscous sublayer, the velocity profile is linear and may be written as

$$u^+ = y^+. \qquad (6.5)$$

Figure 6.33 illustrates a particle depositing on a surface which is assumed to have a micro-roughness of height, *h*, and spacing, *s*. Two different cases of the particle-deposit ineteraction are shown. In case 1 (Figure 6.33a), the particle separation distance H is rather large compared with that in case 2 (Figure 6.33b). In the figure, F_L is the hydraulic lift force and F_i the interaction force which is obtained by adding the electrical double layer force and the van der Waals force. Hence, the net adhesive force acting on the particle may be expressed as

$$F_{net} = F_i - F_L. \qquad \textbf{6.6)}$$

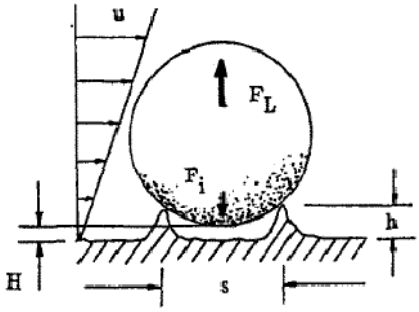

Figure 6.33a: Case 1

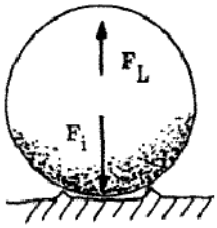

Figure 6.33b: Case 2

Figure 6.33: Forces acting on a particle at a wall [332]

If F_i is smaller than F_L the particle may roll over the wall, and eventually adhere at a place where F_i is larger than F_L or even washed away into the bulk solution.

In this study, the calcium carbonate that grew or adhered onto the test substrates are indifferent to the current wall shear stresses thus larger shear stresses or high pressure removal would be required to dislodge the crystals from the walls.

6.3 Management of scale

6.3.1 Scaling rate

Studies of surface scaling are significant because scaling issues are normally associated with deposition of scale onto tubular or equipment surfaces. Moreover, scale kinetic and inhibition data from bulk precipitation is usually not always directly transferable to surface processes [262, 266]. One method to manage scale is to have an estimation of the scaling rate derived from studies of surface growth and have a range to determine whether the rate is acceptable or unacceptable. This would aid in the management of scale build-up especially on the surfaces of critical equipment such as electrical submersible pumps (ESPs), safety control valves and gas-lift mandrels. For example, an oil well in the North Sea was found to precipitate calcium carbonate scale (91.6% $CaCO_3$) in a 6 inch tubing at a rate such that 2.5cm were precipitated downstream of the coke in one year of production; this corresponds to a calcite growth rate of around 7.9 x 10^{-10}m/s or 0.56mm/year. The time when the 6 inch tubing would be completely blocked was also calculated to be approximately 3 years [46].

6.3.2 Anti-fouling vs. Anti-scaling

Scaling problems have generally been associated with deposition of precipitate from the bulk solution that adheres onto equipment surfaces, however, this study has shown that crystals crystallizing and growing on the surface itself is an equivalently important mechanism of formation. Most biomimetic surfaces with the lotus effect or self-cleaning surfaces concentrate on preventing particles from attaching onto them thus they would not serve as effective anti-scaling surfaces especially where crystallisation on surfaces dominates.

In this study, there are polymers that have lower scaling tendency compared to stainless steel and they possess dual-roughness on the surface on top of being arranged in hexagonal lattices. The amorphous carbon coating (DLC) along with the ceramic coating (Tech 23) and polycrystalline coating (Tech 100) exhibited the least scaling tendency among all the test substrates. Thus, combining the surface features of the coatings and polymers would effectively serve as an effective anti-scaling surface that would perform well in an environment where surface crystallization and particulate deposition dominates. For example, having an amorphous carbon film on stainless steel that is nanopatterned could be a possibility. The issue would be to optimize the nanopatterns where the effects of pillar radius, aspect ratio and shape of the asperity are all taken into account. Until now, there are studies that look into the adhesion of bioinspired micropatterned surfaces and their findings could effectively serve as a platform [333, 334].

Chapter 7
Conclusions

7.1 Introduction

In this thesis, several surface-specific aspects of calcium carbonate scale formation are studied to develop a fundamental insight into the mechanism of calcium carbonate surface precipitation and deposition. This study has mainly focused on the following aspects:

(1) Substrate effect on surface adhesion of calcium carbonate scale
(2) Hydrodynamic effects on surface adhesion
(3) Mechanism of scale formation on surfaces: surface growth vs. surface deposition
(4) Difference between anti-fouling and anti-scaling surfaces

The conclusions for each aspect is summarized below and some future work are recommended.

7.2 Substrate effect on surface adhesion of calcium carbonate scale

Studies of bulk precipitation processes have always been the main focus despite scaling problems always arising from the growth of scale onto tubular or equipment surfaces, whereas the work here focuses on studies of surface scaling. The findings thus far have demonstrated that scale deposition and precipitation are two different processes.

7.2.1 Feasibility of surface coatings to resist scale

It is of importance to understand the effect surface roughness, surface energy and surface chemistry has on scale formation at the surface level in order to solve the problem of adhesion of crystals onto equipment surfaces. This can aid in the design of surfaces or coatings that are inherently less prone to scaling. Here it has been shown that surface coatings such as Tech 100, Tech 23 and DLC offer excellent potential for controlling calcium carbonate formation and has a profound effect on the initial stages of scale formation. In addition, there seems to be a substrate effect on the morphology of the crystals formed, and depending on this initial growth, the subsequent layers can be either more porous or more compact which would dictate their ease of removal.

Coatings have also deterred the formation of scale in the heat exchanger tubes of geothermal plants where the field conditions are relatively similar to the oil fields – corrosion, oxidation, abrasion and high temperature and pressure. Nevertheless, it is important to keep in mind that the surface coating will lose its beneficial effects once an initial layer of scale forms onto the coating surfaces.

7.2.2 Surface roughness, chemistry and topography

On the other hand, the micro- and nanostructured polymers had a wide range of performance in reducing scale. It has been shown that surface topography in terms of surface asperity shapes and roughness affects the tendency of a surface to scale. Asperity shapes that come in the form of sharp peaks and deep and wide ridges and arranged in a regular fashion are prone to act as nucleation sites and hence promote lower induction times and higher scaling tendency. Surfaces with patterns designed to be self-cleaning and anti-reflective with flatter and smaller spacings in between the asperities and hexagonally arranged had a wide range of performance when exposed to scaling; this can be attributed to the surface chemistry that differs from surface

to surface. Only the surface with extra nanobumps to render it with hierarchical roughness proved to be effective in reducing scale.

The structured surface of the polymers allows an example of crystals growing in confinement to be seen whereby the morphology of crystals in a constrained volume is modified through interaction with the structured environment itself. The $CaCO_3$ crystals growing on the surface show one side which have clearly been template by the polymer surfaces, and the other sides having regular planar surfaces where the crystals had grown into the bulk solution.

Surface chemistry effects were also exhibited when the coatings exhibited higher resistance to scaling with higher roughness and vice versa. Surface bonds or groups can also explain the phenomenon where certain calcium carbonate polymorph were preferred or dominant on certain surfaces. Nevertheless, more work is required in determining the role of surface chemistry and material in the type of polymorphs that grows on the surface.

Surface roughness effects were found to be secondary for the case of the polymers as they had similar and comparable roughness but displayed a huge range of performance. On the other hand, when compared with other work, the surface roughness of all the surfaces studied here can be considered to be in the “smooth” regime. Hence, this may explain the finding here where the scaling tendency of surfaces decreases with increasing surface roughness, which is opposite to the general thinking.

7.2.3 Surface energy and adhesion

Surface energy that was measured with water contact measurements did not prove to be feasible to predict the scaling tendency of a surface as there were different observations made for surface coatings and textured polymers. The surface coatings followed the popular belief that the lower the surface energy, the lower the scaling tendency. This was not the case for the textured polymers where the more hydrophilic (thus higher surface energy) the surface was, the better it was in resisting scale.

The MUST tester was applied for the first time to quantify the adhesion under water between a calcium carbonate plate and the test substrates and was also not found feasible as a tool to predict the scaling tendency of a surface. This was because polymer surfaces that performed the best in reducing scale did not display lower measured adhesion. Similarly for coatings, DLC coating gave a higher measured adhesion close to stainless steel although it was one of the best substrates that lowered scaling tendency. This test, however, would be an estimate of the adhesion force expected when crystals migrate from the bulk solution and adheres to the surface. A higher adhesion force would be expected especially where crystals grow from the surface and a higher contact area between crystal and surface increases.

7.3 Hydrodynamic effects on scale formation

The influence of mass transport of reacting species is significant when the solution is stagnant or flows in the laminar regime. However, once the flow turns turbulent, molecular diffusion will be enhanced by turbulent eddies, such that the precipitation rates can increase by up to several orders of magnitude. The results show an increase in scale with increase in turbulence and that the growth mechanism is more complex than the diffusion-controlled growth which

have been shown in other studies which mostly involved heat exchanging surfaces with a temperature difference between bulk solution and surface which is not the case in this thesis. In addition, there was no pronounced change to calcium carbonate crystal morphology with changes to the flow regime.

It has been shown that calcium carbonate scale is tenacious and does not get removed even with higher wall shear forces. The wall shear stresses experienced here – 0.001 to 6.3Pa, are lower when compared with another work where a shear stress as high as 82.5Pa was required to remove scale off the surface. Furthermore, the work here is limited to a lower range of Re (60-11600), while others have relatively higher ranges of Re such as 14000-42500.

7.4 Scale on surfaces: Deposition or crystallization?

Till now, the scaling problem is believed to arise from crystals migrating from the bulk to be deposited on the surface where they adhere onto and form cohesive layers. The work here has shown evidence that the surfaces are acting as nucleation sites for crystals to heterogeneously grow from and is also a demonstration of crystals growing in confinement. This can be seen from the replicated textured polymer motif found on the underside of crystals and from the immersion of substrates after the bulk precipitation has occurred. This would not only explain the poor performance of the self-cleaning polymers used in this work but also knowing that crystals are actually crystallizing from the surface would aid us in designing a surface that is anti-crystallization and anti-sticking would only be an added benefit if the scaling mechanism was a synergy of both. In addition, it can be seen that bulk precipitation and surface deposition are two different processes with each having their own nucleation and growth mechanism.

A general trend where the population and size of the crystals on the surfaces decreases was observed when the substrates were immersed after bulk precipitation was complete. This shows that the main process of adhesion is the direct growth of the crystals on the surface and the indirect adhesion or particulate deposition from the bulk is much less important. Hence, once bulk precipitation has been completed, very little scale from the bulk solution actually adheres to the surface.

Furthermore, this work also suggests that biofouling is a different mechanism to inorganic scaling as the former refers to organisms adhering onto the surface while the latter involves minerals growing outwards from a surface.

Until now, there has not been any standardized scaling rates that can be used to diagnose, predict and acted upon. The work here has shown that preliminary scaling rates can be obtained with the physical structure of the initial layer of calcareous deposits.

Although this work has enabled several aspects of scale formation to be investigated, however, to completely understand the mechanism of scale formation and inhibition is still a challenge.

Last but not least, with the increased awareness of protecting the environment from the harmful effects of chemical inhibitors, designing surfaces that can inherently prevent or reduce scaling would be a promising way forward.

7.5 Future work

The significant role of the interactions between a surface and scale crystals has been revealed in the present work. It is shown that the physical and chemical modification of a surface's properties could be an efficient strategy to delay or even inhibit scale formation even though the design of anti-scaling surfaces remains a major challenge. Recommendations for future work relating to calcium carbonate scale formation, inhibition and prediction are given below.

7.5.1 Use of inhibitors

In addition to considering anti-scaling surfaces as a potential way forward in delaying or preventing scale formation, the use of chemical treatment of these modified surfaces could be an effective and environmental friendly (if combined with green chemicals) method to inhibit scale. Microscopic and XRD analysis are great tools with which to study the changes of morphology and disposition of the crystals.

7.5.2 Designing anti-scaling surfaces

In order to further understand the mechanisms of the effect of modified surfaces on scale nucleation and growth, surfaces of various topographies with controlled chemistry and vice versa can be investigated. A closer step to surfaces that are inherently non-scaling can only be taken when a clearer role of the substrate itself is understood. As this work has reported, there are cases where a certain morphology is preferred on one surface and not the other, this would most likely be attributed to surface chemistry and studying the chemical bonds would add to the understanding of scale formation on surfaces.

In terms of surface topography, several factors can be studied - the effects of pillar radius, aspect ratio and the contact shape. There are several adhesion of biological systems such as flies, beetles, spiders and gecko, where the system can be adapted to functionalize a surface. In addition, the defined surface can then be coupled with a suitable surface chemistry and tested for scaling tendency.

7.5.3 Prediction of scale growth rate

The above mentioned recommendations would form an excellent precursor to developing a kinetic model to account for the more realistic conditions experienced in the field. It is important to know where, when and how much scale will be deposited during oil (and water) production. Hence, the model would be useful in predicting scale formation which would allow a more adapted treatment to be formulated.

7.5.4 Deposition tests conducted at higher rotation rates

In order to generate higher hydrodynamic wall shear stresses, a more turbulent regime is required. This would not only allow the critical shear stress required to remove $CaCO_3$ scale to be measured, but also the efficiency of the pipe material to be tested. It would be useful to investigate materials and their inherent properties that allow the easy removal of scale at a lower Reynolds number.

References

1. Hyne, N.J., *Nontechnical guide to petroleum geology, exploration, drilling and production*. 2001, Tulsa, Oklahoma: PennWell Publishing Company.
2. Civan, F., *Chapter 14: Formation damage by organic deposition*, in *Reservoir Formation Damage*. 2007, Gulf Professional Publishing: Oxford, UK.
3. Amaefule, J.O., et al. *Advances in formation damage assessment and control strategies*. in *39th Annual Technical Meeting of Petroleum Society of CIM and Canadian Gas Processors Association*. 1988. Calgary, Alberta.
4. Crabtree, M., et al., *Fighting scale - Removal and prevention*, in *Oilfield Review*. 1999, Schlumberger. p. 30-45.
5. Bader, M.S.H., *Sulfate scale problems in oil fields water injection operations.* Desalination, 2006. **201**: p. 100-105.
6. Moghadasi, J., et al., *Model study on the kinetics of oil field formation damage due to salt precipitation from injection.* Journal of Petroleum Science and Technology, 2004. **43**: p. 201-217.
7. Civan, F., *Reservoir formation damage: fundamentals, modeling, assessment, and mitigation*. 2007: Gulf Professional Publishing. 323.
8. Krumine, P.H., E.H. Mayer, and G.E. Brock, *Scale formation during alkaline flooding.* Journal of Petroleum Technology, 1985. **Aug.**: p. 1466-1474.
9. Nancollas, G.H. and J.R. Campbell, *The crystallisation and dissolution of strontium sulfate in aqueous solution.* Journal of Physical Chemistry, 1969. **23**(6): p. 1735-1740.
10. Nancollas, G.H. and S.T. Liu, *Crystal growth and dissolution of barium sulfate.* Society of Petroleum Engineers Journal, 1975(509-516).
11. Vetter, O.J., *Oilfield scale - can we handle it?* Journal of Petroleum Technology, 1972. **Dec**(1402-1408).
12. Moghadasi, J., et al. *Scale formation in Iranian oil reservoir and production equipment during water injection*. in *5th International Oilfied Scale Symposium and Exhibition*. 2003. Aberdeen, UK.
13. Zhang, Y. and R. Dawe, *The kinetics of calcite precipitation from a high salinity water.* Applied Geochemistry, 1998. **13**: p. 177-184.
14. Epstein, N., *Thinking about heat transfer fouling: A 5 x 5 matrix.* Heat Transfer Engineering, 1981. **4**(1): p. 43-56.
15. Sheikholeslami, R., *Composite fouling - inorganic and biological: A review.* Environmental Progress, 1999. **18**(2): p. 113-122.
16. Bowen, B. and N. Epstein, *Fine particle deposition in smooth parallel-plate channels.* Journal of Colloid and Interface Science, 1979. **16**: p. 81-97.
17. Sjollema, J. and H.J. Busscher, *Deposition of polystyrene latex particles toward polymethylmethacrylate in a parallel plate flow cell.* Journal of Colloid and Interface Science, 1988. **132**(2): p. 382-394.
18. Frenier, W.W. and M. Ziauddin, eds. *Formation, Removal, and Inhibition of Inorganic Scale in the Oilfield Environment*. ed. N.A. Wolf and R.L. Hartman. 2008, Society of Petroleum Engineers: Richardson, USA.

19. Pérez, M., et al., *Cupric tannate: A low copper content antifouling pigment.* Progress in Organic Coatings, 2006. **55**(4): p. 311-315.
20. Yebra, D.M. and S. Kiil, *Antifouling technology - past, present and future steps towards efficient and environmentally friendly antifouling coatings.* Progress in Organic Coatings, 2004. **50**(2): p. 75-104.
21. van Loosdrecht, M.C.M., et al., *Bacterial adhesion: A physicochemical approach.* Microbial Ecology, 1989. **17**(1): p. 1-15.
22. Bott, T.R., *Fouling of heat exchangers*. 1995: Oxford: Elsevier.
23. Sadr Ghayeni, S.B., et al., *Adhesion of waster water bacteria to reverse osmosis membranes.* Journal of Membrane Science, 1998. **138**(1): p. 29-42.
24. Turakhia, M. and W.G. Characklis, *An observation of microbial cell accumulation in a finned tube.* Canadian Journal of Chemical Engineering, 1983. **61**: p. 873-875.
25. Balz, M., et al., *Controlled crystallization of $CaCO_3$ on hyperbranced polyglycerol adsorbed to self-assembled monolayers.* Langmuir, 2005. **21**: p. 3987-3991.
26. Chave, K.E., *Physics and chemistry of biomeralization.* Annual Review of Earth and Planetary Sciences, 1984. **12**: p. 293-305.
27. Feng, Q.L., et al., *Polymorph and morphology of calcium carbonate crystals induced by proteins extracted from mollusk shell.* Journal of Crystal Growth, 2000. **216**(1-4): p. 459-465.
28. Aizenberg, J., *A bio-inspired approach to controlled crystallization at the nanoscale.* Bell Labs Technical Journal, 2005. **10**(3): p. 129-141.
29. Levi, Y., et al., *Control Over Aragonite Crystal Nucleation and Growth: An In Vitro Study of Biomineralization.* Chemistry - A European Journal, 1998. **4**(3): p. 389-396.
30. Lippmann, F., *Sedimentary Carbonate Minerals*. 1973, Berlin: Springer.
31. Falini, G., M. Gazzano, and A. Ripamonti, *Crystallization of calcium carbonate in presence of magnesium and polyelectrolytes.* Journal of Crystal Growth, 1994. **137**(3-4): p. 577-584.
32. Han, Y.-J. and J. Aizenberg, *Effect of Magnesium Ions on Oriented Growth of Calcite on Carboxylic Acid Functionalized Self-Assembled Monolayer.* Journal of the American Chemical Society, 2003. **125**(14): p. 4032-4033.
33. Manoli, F. and E. Dalas, *Spontaneous precipitation of calcium carbonate in the presence of ethanol, isopropanol and diethylene glycol.* Journal of Crystal Growth, 2000. **218**: p. 359-364.
34. Naka, K. and Y. Chujo, *Control of crystal nucleation and growth of calcium carbonate by synthetic substrates.* Chemistry of Materials, 2001. **13**: p. 3245-3259.
35. Falini, G., et al., *Control of aragonite or calcite polymorphism by mollusk shell macromolecules.* Science, 1996. **271**(5245): p. 67-69.
36. Litvin, A.L., et al., *Template-directed synthesis of aragonite under supramolecular hydrogen-bonded langmuir monolayers.* Advanced Materials, 1997. **9**(2): p. 124-127.
37. Bansal, B., X.D. Chen, and H. Müller-Steinhagen, *Analysis of 'classical' deposition rate law for crystallisation fouling.* Chemical Engineering and Processing, 2008. **47**: p. 1201-1210.
38. Mullin, J.W., ed. *Crystallization*. 4th ed. 2004, Elsevier Butterworth-Heinemann: Oxford.

39. Chen, T., A. Neville, and M. Yuan, *Calcium carbonate scale formation - assessing the initial stages of precipitation and deposition.* Journal of Petroleum Science and Technology, 2005. **46**: p. 185-194.
40. Nancollas, G.H., *The growth of crystals in solution.* Advances in Colloid and Interface Science, 1979. **10**: p. 215-252.
41. Koutsoukos, P.G., A.N. Kofina, and D.G. Kanellopoulou, *Solubility of salts in water: Key issue for crystal growth and dissolution processes.* Pure and Applied Chemisty, 2007. **79**(5): p. 825-850.
42. Söhnel, O. and J.W. Mullin, *Interpretation of crystallization induction periods.* Journal of Colloid and Interface Science, 1988. **123**(1): p. 43-50.
43. Lundager Madsen, H.E., *Theory of long induction periods.* Journal of Crystal Growth, 1987. **80**(2): p. 371-377.
44. Kim, W.T. and Y.I. Cho, *Experimental study of the crystal growth behavior of $CaCO_3$ fouling using a microscope.* Experimental Heat Transfer, 2000. **13**: p. 153-161.
45. Myerson, A.S., *Handbook of Industrial Crystallization*. 2001, Butterworth-Heinemann.
46. Dawe, R.A. and Y. Zhang, *Kinetics of calcium carbonate scaling using observations from glass micromodels.* Journal of Petroleum Science and Technology, 1997. **18**: p. 179-187.
47. Gabrielli, C., et al., *Study of calcium carbonate scales by electrochemical impedance spectroscopy.* Electrochimica Acta, 1997. **42**(8): p. 1207-1218.
48. Gabrielli, C., et al., *Estimation rate of the thermal calcareous scaling by the electrochemical impedance technique.* Journal of Electroanalytical Chemistry, 1996. **412**: p. 189.
49. Morizot, A., A. Neville, and T. Hodgkiess, *Studies of the deposition of $CaCO_3$ on a stainless steel surface by a novel electrochemical technique.* Journal of Crystal Growth, 1999. **198-199**: p. 738-743.
50. Neville, A. and A. Morizot, *A combined bulk chemistry/electrochemical approach to study the precipitation, deposition and inhibition of $CaCO_3$.* Chemical Engineering Science, 2000. **55**(20): p. 4737-4743.
51. Gabrielli, C., M. Keddam, and H. Perrot, *Characterization of the efficiency of antiscale treatments of water. Part 1: Chemical processes.* Journal of Applied Electrochemistry, 1996. **26**: p. 1125-1132.
52. Gabrielli, C., et al., *Quartz crystal microbalance investigation of electrochemical calcium carbonate scaling.* Journal of The Electrochemical Society, 1998. **145**: p. 2386-2396.
53. Devos, O., C. Gabrielli, and B. Tribollet, *Nucleation-growth process of scale electrodeposition - Influence of the mass transport.* Electrochimica Acta, 2006. **52**: p. 285-291.
54. Yang, Q., et al., *Investigation of caclium carbonate scaling inhibition and scale morphology by AFM.* Journal of Colloid and Interface Science, 2001. **240**: p. 608-621.
55. Gabrielli, C., et al., *Nucleation and growth of calcium carbonate by an electrochemical scaling process.* Journal of Crystal Growth, 1999. **200**: p. 236-250.
56. Söhnel, O. and J.W. Mullin, *Precipitation of calcium carbonate.* Journal of Crystal Growth, 1982. **60**: p. 239.

57. Wray, J.L. and F. Daniels, *Precipitation of calcite and aragonite.* Journal of the American Chemical Society, 1957. **79**(9): p. 2031-2034.
58. Peters, R.W. and T.-K. Chang, *The effect of Pb(II) as a trace impurity on the crystallization kinetics of CaCO3 precipitation.* AIChE Symposium Series, 1987. **83**(253): p. 62.
59. Vdović, N. and D. Kralj, *Electrokinetic properties of spontaneously precipitated calcium carbonate polymorphs: the influence of organic substances.* Colloids and Surfaces A: Physicochemical and Engineering Aspects, 2000. **161**: p. 499-505.
60. Alahmad, M., *Factors affecting scale formation in sea water environments - An experimental approach.* Chemical Engineering and Technology, 2008. **31**(1): p. 149-156.
61. Plummer, L.N. and E. Busenberg, *The solubilities of calcite, aragonite, and vaterite in CO_2-H_2O solutions between 0 and 90°C and an evaluation of the aqueous model for the system $CaCO_3$-CO_2-H_2O.* Geochimica et Cosmochimica Acta, 1982. **46**: p. 1011-1040.
62. Gómez-Morales, J., J. Torrent-Burgués, and R. Rodríguez-Clemente, *Nucleation of calcium carbonate at different initial pH conditions.* Journal of Crystal Growth, 1996. **169**: p. 331-338.
63. Reddy, M.M., L.N. Plummer, and E. Busenberg, *Crystal growth of calcite from calcium bicarbonate solutions at constant P (sub cod) 2 and 25 degrees C; a test of a calcite dissolution model.* Geochimica et Cosmochimica Acta, 1981. **45**(8): p. 1281-1289.
64. Verdoes, D., D. Kashchiev, and G.M. van Rosmalen, *Determination of nucleation and growth rates from induction times in seeded and unseeded precipitation of calcium carbonate.* Journal of Crystal Growth, 1992. **118**(3-4): p. 401-413.
65. van der Leeden, M.C., et al., *Advances in Industrial Crystallization*, ed. J. Garside, R.J. Davey, and A.G. Jones. 1991, London: Butterworth-Heinemann.
66. Kralj, D. and N. Vdović, *The influence of some naturally occurring minerals on the precipitation of calcium carbonate polymorphs.* Water Research, 2000. **34**(1): p. 179-184.
67. Cheng, B., et al., *Preparation of monodispersed cubic calcium carbonate particles via precipitation reaction.* Materials Letters, 2004. **58**: p. 15651570.
68. Devos, O., et al., *Nucleation-growth process of scale electrodeposition.* Journal of The Electrochemical Society, 2003. **150**(7): p. C494-C501.
69. Gal, J.-Y., Y. Fovet, and N. Gache, *Mechanisms of scale formation and carbon dioxide partial pressure influence. Part II. Application in the study of mineral waters of reference.* Water Research, 2002. **36**: p. 764-773.
70. Parlaktuna, M. and E. Okandan, *The use of chemical inhibitors for prevention of calcium carbonate scaling.* Geothermics, 1989. **18**: p. 241-248.
71. Davis, K.J., P.M. Dove, and J.J. De Yoreo, *The role of Mg^{2+} as an impurity in calcite growth.* Science, 2000. **290**(5494): p. 1134-1137.
72. van der Leeden, M.C. and G.M. van Rosmalen, *Aspects of additives in precipitation processes: Performance of polycarboxylates in gypsum growth prevention.* Desalination, 1987. **66**: p. 185-200.

73. Prieto, M., et al., *Metastability in diffusing-reacting systems.* Journal of Crystal Growth, 1994. **142**: p. 225-235.
74. Roques, H. and A. Girou, *Kinetics of the formation conditions of carbonate tartars.* Water Research, 1974. **8**(11): p. 907-920.
75. Katz, A., *The interaction of magnesium with calcite during crystal growth at 25–90°C and one atmosphere.* Geochimica et Cosmochimica Acta, 1973. **37**: p. 1563.
76. Kamiya, K., S. Sakka, and K. Terada, *Aragonite formation through precipitation of calcium carbonate monohydrate.* Materials Research Bulletin, 1977. **12**: p. 1095-1102.
77. Moller, P. and G. Rajagopalan, *Changes of excess free energies in the crystal growth processes of calcite and aragonite due to the presence of Mg^{2+} ions in solution.* Zeitschrift fur Physikalische Chemie. Neue Folge, 1976. **99**: p. 187-198.
78. Kitano, Y. and D.H. Wood, *The influence of organic material on the polymorphic crystallization of calcium carbonate.* Geochimica et Cosmochimica Acta, 1965. **29**: p. 29.
79. Sabbides, T.G. and K. P.G., *The crystallization of calcium carbonate in artificial seawater; role of the substrate.* Journal of Crystal Growth, 1993. **133**: p. 13-22.
80. Kralj, D., et al., *Effect of inorganic anions on the morphology and structure of magnesium calcite.* Chemistry - A European Journal, 2004. **10**: p. 1647-1656.
81. Tao, C., *New insights into the mechanisms of calcium carbonate mineral scale formation and inhibition*, in *School of Engineering and Physical Sciences*. 2005, Heriot-Watt University: Edinburgh. p. 239.
82. Titiloye, J.O., S.C. Parker, and S. Mann, *Atomistic simulation of calcite surfaces and the influence of growth additives on their morphology.* Journal of Crystal Growth, 1993. **131**: p. 533-545.
83. Tracy, S.L., C.J.P. François, and H.M. Jennings, *The growth of calcite spherulites from solution: I. Experimental design techniques.* Journal of Crystal Growth, 1998. **193**: p. 374-381.
84. Telkes, M., *Nucleation of supersaturated inorganic salt solutions.* Industrial and Engineering chemistry, 1952. **44**(6): p. 1308-1310.
85. Hasson, D. and J. Zahavi, *Mechanism of calcium sulfate scale deposition on heat transfer surfaces.* Industrial and Engineering Chemistry Fundamentals, 1970. **9**(1): p. 1-10.
86. Andritsos, N. and A.J. Karabelas, *Calcium carbonate scaling in a plate heat exchanger in the presence of particles.* International Journal of Heat and Mass Transfer, 2003. **46**: p. 4613-4627.
87. Bansal, B., X.D. Chen, and H. Müller-Steinhagen, *Use of non-crystallising particles to mitigate crystallisation fouling.* International Communications in Heat and Mass Transfer, 2003. **30**(5): p. 695-706.
88. Won, T.K. and I.C. Young, *A Study of the Scale Formation Around Air Bubble Attached on a Heat-transfer Surface.* International Communications in Heat and Mass Transfer, 2002. **29**: p. 1-14.
89. Najibi, S.H., H. Müller-Steinhagen, and M. Jamialahmadi, *Calcium sulphate scale formation during subcooled flow boiling.* Chemical Engineering Science, 1997. **52**(8): p. 1265-1284.

90. Efird, K.D., *Flow accelerated corrosion testing basics*, in *Corrosion NACExpo 2006 61st Annual Conference & Exposition*. 2006: San Diego Ca.
91. Walker, P. and R. Sheikholeslami, *Assessment of the effect of velocity and residence time in $CaSO_4$ precipitating flow reaction.* Chemical Engineering Science, 2003. **58**: p. 3807-3816.
92. Andritsos, N., A.J. Karabelas, and P.G. Koutsoukos, *Morphology and structure of $CaCO_3$ scale layers formed under isothermal flow conditions.* Langmuir, 1997. **13**(13): p. 2873-2879.
93. Soltani, M. and G. Ahmadi, *On particle adhesion and removal mechanisms in turbulent flows.* Journal of Adhesion Science and Technology, 1994. **8**(7): p. 763-785.
94. Yang, Q., et al., *Investigation of induction period and morphology of $CaCO_3$ fouling on heated surface.* Chemical Engineering Science, 2002. **57**: p. 921-931.
95. Quddus, A. and L.M. Al-Hadhrami, *Hydrodynamically deposited $CaCO_3$ and $CaSO_4$ scales.* Desalination, 2009. **246**: p. 526-533.
96. Najibi, S.H., H. Müller-Steinhagen, and M. Jamialahmadi, *Calcium carbonate scale formation during subcooled flow boiling.* Journal of Heat Transfer, 1997. **119**: p. 767-775.
97. Hatch, G.B., *Evaluation of scaling tendencies.* Material Protection and Performance, 1973: p. 49-55.
98. Helalizadeh, A., H. Muller-Steinhagen, and M. Jamialahmadi, *Mixed salt crystallisation fouling.* Chemical Engineering and Processing, 1999. **39**(1): p. 29-43.
99. Geddert, T., et al., *Extending the induction period of crystallization fouling through surface coating.* Heat Transfer Engineering, 2009. **30**(10-11): p. 868-875.
100. Levich, V.G., *Physicochemical Hydrodynamics*. 1962, Englewood Cliffs, NJ: Prentice-Hall.
101. Hasson, D., et al., *Mechanism of calcium carbonate scale deposition on heat-transfer surfaces.* Industrial and Engineering Chemistry, 1968. **7**(1): p. 59-65.
102. Quddus, A., *Effect of hydrodynamics on the deposition of the $CaSO_4$ scale on stainless steel.* Desalination, 2002. **142**: p. 57-63.
103. Kralj, D., L. Brečević, and J. Kontrec, *Vaterite growth and dissolution in aqueous solution III. Kinetics of transformation.* Journal of Crystal Growth, 1997. **177**: p. 248-257.
104. Meldrum, F.C., *Calcium carbonate in biomineralisation and biomimetic chemistry.* International Materials Reviews, 2003. **48**(3): p. 187-224.
105. Park, W.K., et al., *Effects of magnesium chloride and organic additives on the synthesis of aragonite precipitated calcium carbonate.* Journal of Crystal Growth, 2008. **31**: p. 2593-2601.
106. Gal, J.-Y., Y. Fovet, and N. Gache, *Mechanisms of scale formation and carbon dioxide partial pressure influence. Part I. Elaboration of an experimental method and a scaling model.* Water Research, 2002. **36**: p. 755-763.
107. Spanos, N. and P.G. Koutsoukos, *Kinetics of precipitation of calcium carbonate in alkaline pH at constant supersaturation. Spontaneous and*

seeded growth. Journal of Physical Chemistry B, 1998. **102**: p. 6679-6684.
108. Xyla, A.G., J. Mikroyannidis, and P.G. Koutsoukos, *The inhibition of calcium carbonate precipitation in aqueous media by organophosphorus compounds.* Journal of Colloid and Interface Science, 1992. **153**(2): p. 537-551.
109. Wada, N., K. Yamashita, and T. Umegaki, *Effects of divalent cations upon nucleation, growth and transformation of calcium carbonate polymorphs under conditions of double diffusion.* Journal of Crystal Growth, 1995. **148**(3): p. 297-304.
110. Chakraborty, D., et al., *Steady-state transitions and polymorph transformations in continuous precipitation of calcium carbonate.* Industrial and Engineering Chemistry Research, 1994. **33**(9): p. 2187-2197.
111. Ogino, T., T. Suzuki, and K. Sawada, *The rate and mechanism of polymorphic transformation of calcium carbonate in water.* Journal of Crystal Growth, 1990. **100**: p. 159-167.
112. Bischoff, J.L., *Catalysis, inhibition, and the calcite-aragonite problem; [Part] 2, The vaterite-aragonite transformation.* American Journal of Science, 1968. **266**: p. 80-90.
113. Kralj, D., L. Brečević, and A.E. Nielsen, *Vaterite growth and dissolution in aqueous solution I. Kinetics of crystal growth.* Journal of Crystal Growth, 1990. **104**: p. 793-800.
114. Rankama, K. and T.G. Sahama, *Geochemistry.* Geochemistry, 1950: p. 912.
115. Hostomsky, J. and A.G. Jones, *Calcium carbonate crystallization, agglomeration and form during continuous precipitation from solution.* Journal of Physics D (Applied Physics), 1991. **24**(2): p. 165-170.
116. Tai, C.Y., P.-C. Chen, and S.M. Shih, *Size-dependent growth and contact nucleation of calcite crystals.* AIChE Journal, 1993. **39**: p. 1472.
117. Klein, C., *Manual of Mineralogy*. 1985, John Wiley: New York.
118. Johnson, A., D. Eslinger, and H. Larsen. *An abrasive jetting removal system*. in *SPE/IcoTA Coiled Tubing Roundtable*. 1998. Houston, Texas, USA.
119. Martel, A.E. and M. Calvin, *Chemistry of Metal Chelate Compounds*. 1952, New York: Prentice-Hall.
120. Frenier, W.W., et al. *Use of highly acid-soluble chelating agents in well stimulation services*. in *SPE Annual Technical Conference and Exhibition*. 2000. Dallas: SPE.
121. Freedman, A.J. (1983) *Cooling Water Technology in the Eighties*. Corrosion, NACE conference **273**.
122. Davis, R.V., et al., *The use of modern methods in the development of calcium carbonate inhibitors for cooling water systems.* Mineral Scale Formation and Inhibition, 1995.
123. Schwamborn, M., *Chemical synthesis of polyaspartates: a biodegradable alternative to currently used polycarboxylate homo- and copolymers.* Polymer Degradation and Stability, 1998. **59**: p. 39-45.
124. Nancollas, G.H., T.F. Kazmierczak, and E. Schuttringer, *A controlled composition study of calcium carbonate growth: The influence of scale inhibitors.* Corrosion-NACE, 1981. **37**(2): p. 76-81.

125. Quraishi, M.A., I.H. Farooqi, and P.A. Saini, *Natural compounds as corrosion inhibitors for highly cycled systems*, in *Paper 95 presented at NACE International Corrosion*. 1999: Houston.
126. Sikes, C.S., et al., *Polyamino acids as antiscalants, corrosion inhibitors and dispersants: Atomic force microscopy and mechanism of action*, in *Paper 465 NACE International Corrosion*. 1993: Houston.
127. Gill, J.S. *Development of scale inhibitors*. in *Paper 229 presented at NACE International Corrosion*. 1996. Houston.
128. Tantayakom, V., *Scale inhibition study by turbidity measurement.* Journal of Colloid and Interface Science, 2005. **287**(1): p. 57-65.
129. Pina, C.M., et al., *An atomic force microscopy and molecular simulations study of the inhibition of barite growth by phosphonates.* Surface Science, 2004. **553**(1-3): p. 61-74.
130. Estievenart, C., et al., *Mechanisms of scale and corrosion inhibition by polyaspartate.* Corrosion, 2004. **Paper no 04536**.
131. Graham, G.M., L.S. Boak, and K. Sorbie. *The influence of formation calcium and magnesium on the effectiveness of generically different barium sulphate oilfied scale inhibitors*. in *International symposium on Oilfield Chemistry*. 1997. Houston, USA.
132. Yu, J., et al., *Effects of PAA additive and temperature on morphology of calcium carbonate particles.* Journal of Solid State Chemistry, 2004. **177**(3): p. 681.
133. van der Leeden, M.C. and G.M. van Rosmalen, *Adsorption behavior of polyelectrolytes on barium sulfate crystals.* Journal of Colloid and Interface Science, 1995. **171**(1): p. 142-149.
134. Reddy, M.M. and G.H. Nancollas, *Calcite crystal growth inhibition by phosphonates.* Desalination, 1973. **12**(1): p. 61.
135. Davis, K.P., et al. *Novel scale inhibitor polymers with enhanced adsorption properties*. in *SPE 80381 presented at SPE International Symposium on Oilfield Scale*. 2003. Aberdeen.
136. Davis, R.A. and J.E. MchElhiney, *The advancement of sulfate removal from seawater in offshore waterflood operations*, in *Paper 314 presented at NACE International Corrosion*. 2002: Houston.
137. Kukulka, D.J., *An evaluation of heat transfer surface materials used in fouling applications.* Heat Transfer Engineering, 2005. **26**(5): p. 42-46.
138. Keysar, S., et al., *Effect of surface roughness on morphology of calcite crystallization on mild steel.* Journal of Colloid and Interface Science, 1994. **162**: p. 311-319.
139. Epstein, N., ed. *Fouling of augmented surfaces - conceptually*. Fouling of Heat Exchangers, ed. J. Taborek, G.F. Hewitt, and N. Afgan. 1983, Hemisphere.
140. Sheng, Y.-J., S. Jiang, and H.-K. Tsao, *Effects of Geometrical Characteristics of Surface Roughness on Droplet Wetting.* The Journal of Chemical Physics, 2007. **127**: p. 234704.
141. Callies, M., et al., *Microfabricated textured surfaces for super-hydrophobicity investigations.* Microelectronics engineering, 2005. **78-79**: p. 100-105.
142. Nosonovsky, M. and B. Bhushan, *Multiscale friction mechanisms and hierarchical surfaces in nano- an bio-tribology.* Materials Science and Engineering R, 2007. **58**: p. 162-193.

143. Bhushan, B., Y.C. Jung, and K. Koch, *Micro-, nano- and hierarchical structures for superhydrophobicity, self-cleaning and low adhesion.* Philosophical Transactions of The Royal Society A, 2009. **367**: p. 1631-1672.
144. Volmer, M., *Kinetik der Phasenbildung*. 1939, Steinkopf: Leipzig.
145. Fedot'ev, N.P., *Electropolishing, Anodizing and Electrolytic Pickling of Metals*. 1959, Teddington, U.K.: trans. by A. Behr, Robert Draper Ltd.
146. Herz, A., M.R. Malayeri, and H. Müller-Steinhagen, *Fouling of roughened stainless steel surfaces during convective heat transfer to aqueous solutions.* Energy Conversion and Management, 2008. **49**: p. 3381-3386.
147. Adamson, A.W. and A.P. Gast, *Physical Chemistry of Surfaces*. 1997, New York: Wiley.
148. Förster, M. and M. Bohnet, *Influence of the transport properties of the crystal/heat transfer surface interfacial on fouling behavior.* Chemical Engineering and Technology, 2003. **26**: p. 1055-1060.
149. Krupp, H., *Particle adhesion theory and experiment.* Advances in Colloid and Interface Science, 1967. **1**(2): p. 111-239.
150. Tabor, D., *Surface forces and surface interactions.* Journal of Colloid and Interface Sciences, 1977. **58**(1): p. 2-13.
151. Briscoe, B.J. and S.S. Panesar, *Effect of surface topography on the adhesion of poly(urethane) - metal contacts.* Journal of Physics D (Applied Physics), 1992. **25**(1A): p. A20-A27.
152. Oliveira, R., *Understanding adhesion: A means for preventing fouling.* Experimental Thermal and Fluid Science, 1997. **14**: p. 316-322.
153. Katainen, J., et al., *Adhesion as an interplay between particle size and surface roughness.* Journal of Colloid and Interface Science, 2006. **304**(2): p. 524-529.
154. Yang, Q., D.Q. Xu, and Z. Shen, *A theoretical analysis and experimental study of the induction period of calcium carbonate scaling.* Journal of Chemical Industry and Engineering (China), 1994. **45**: p. 199-205.
155. Förster, M. and W. Augustin, *Influence of the adhesion force crystal/heat exchanger surface on fouling mitigation.* Journal of Chemical Engineering and Processing, 1999. **38**: p. 449-461.
156. Müller-Steinhagen, H. and Q. Zhao, *Investigation of low fouling surface alloys made by ion implantation technology.* Chemical Engineering Science, 1997. **52**(19): p. 3321-3332.
157. Rankin, R.H. and W.L. Adamson, *Scale formation as related to evaporator surface conditions.* Desalination, 1973. **13**: p. 63.
158. Bornhorst, A., H. Muller-Steinhagen, and Q. Zhao, *Reduction of scale formation under pool boiling conditions by ion implantation and magnetron sputtering on heat transfer surfaces.* Heat Transfer Engineering, 1999. **20**(2): p. 6-14.
159. Yang, Q., J. Ding, and Z. Shen, *Investigation on fouling behaviors of low-energy surface and fouling fractral characteristics.* Chemical Engineering Science, 2000. **55**: p. 797-805.
160. Yang, Q., J. Ding, and Z. Shen, *Investigation of calcium carbonate scaling on ELP surface.* Journal of Chemical Engineering of Japan, 2000b. **33**: p. 591-596.

161. Zhao, Q. and X. Wang, *Heat transfer surfaces coated with fluorinated diamond-like carbon films to minimize scale formation.* Surface & Coatings Technology, 2004. **192**: p. 77-80.
162. Nejim, A., et al., *Ion implantation of stainless steel heater alloys for anti-fouling applications.* International Conference on Ion Implantation Technology. Proceedings (Cat. No. 98EX144), 1998. **2**: p. 869-872.
163. Hadley, J.S. and L.E. Harland, *Electroless nickel/PTFE composite coatings.* Metal Finishing, 1987. **85**: p. 51-53.
164. Nishira, M. and O. Takano, *Friction and wear characteristics of electroless Ni-P-PTFE composite coatings.* Plating and Surface Finishing, 1994. **81**: p. 48-50.
165. Paul, S., *Surface Coatings - Science & Technology, 2nd ed*. 1996, Chichester, U.K.: John Wiley & Songs.
166. Zhao, Q. and Y. Liu, *Investigation of graded Ni-Cu-PTFE composite coatings with antiscaling properties.* Applied Surface Science, 2004. **229**: p. 56-62.
167. Zhao, Q., et al., *Effect of surface free energy on the adhesion of biofouling and crystalline fouling.* Chemical Engineering Science, 2005. **60**(17): p. 4858-4865.
168. Tulsi, S.S., *Composite PTFE-Nickel coatings for low friction applications.* Finishings, 1983. **November**: p. 14-18.
169. Bohnet, M., *Influence of the transport properties of the crystal/heat transfer surface interfacial on fouling behavior.* Chemical Engineering and Technology, 2003. **26**(10): p. 1055-1060.
170. Förster, M. and M. Bohnet, *Modification of molecular interactions at the interface crystal/heat transfer surface to minimize heat exchanger fouling.* International Journal of Theoretical Science, 2000. **39**: p. 697-708.
171. Zettler, H.U., et al., *Influence of surface properties and characteristics on fouling in plate heat exchangers.* Heat Transfer Engineering, 2005. **26**(2): p. 3-17.
172. Premathilaka, S., et al., *A study on the effects of surface chemistry on the initial deposition mechanisms of dairy fouling.* Food and Bioproducts Processing, 2006. **84**(4): p. 265-273.
173. Okada, M., et al., *Interfacial interactions between calcined hydroxyapatite nanocrystals and substrates.* Langmuir, 2009. **25**(11): p. 6300-6306.
174. Allen, K.W., *"At Forty Cometh Understanding" A Review of Some Basics of Adhesion Over the Past Four Decades.* International Journal of Adhesion & Adhesives, 2002. **23**: p. 87-93.
175. Gerberick, W.W. and M.J. Cordill, *Physics of Adhesion.* Reports on Progress in Physics, 2006. **69**: p. 2157-2203.
176. Pashley, M.D., J.B. Pethica, and D. Tabor, *Adhesion and micromechanical properties of metal surfaces.* Wear, 1984. **100**: p. 7-31.
177. Kallay, N., et al., *Particle adhesion and removal in model systems.* Journal of Colloid and Interface Science, 1986. **114**(2): p. 357-362.
178. Collins, I.R., *A new model for mineral scale adhesion.* Society of Petroleum Engineers Journal, 2002. **SPE 74655**.
179. Bargir, S., et al., *The use of contact angle measurements to estimate the adhesion propensity of calcium carbonate to solid substrates in water.* Applied Surface Science, 2009. **255**: p. 4873-4879.

180. Zou, M., et al., *Ni Nanodot-Patterned Surfaces for Adhesion and Friction Reduction.* Tribology Letters, 2006. **24**: p. 137-142.
181. Bhushan, B., K. Koch, and Y.C. Jung, *Nanostructures for superhydrophobicity and low adhesion.* Soft Matter, 2008. **4**: p. 1799-1804.
182. Nosonovsky, M. and B. Bhushan, *Roughness induced superhydrophobicity: A way to design non adhesive surfaces.* Journal of Physics: Condensed Matter, 2008. **20**: p. 225009.
183. Li, Q. and M. Elimelech, *Organic fouilng and chemical cleaning of nanofiltration membranes: Measurement and mechanisms.* Environmental Science and Technology, 2004. **38**: p. 4683-4693.
184. Fuller, K.N.G. and D. Tabor, *The effect of surface roughness on the adhesion of elastic solids.* Proceedings of the Royal Society of London, Series A, 1975. **345**(1642): p. 327-342.
185. Zou, M., L. Cai, and H. Wang, *Adhesion and Friction Studies of a Nano-textured Surface Produced by Spin Coating of Colloidal Silica Nanoparticle Solution.* Tribology Letters, 2006. **21**: p. 25-30.
186. Gjerde, K., et al., *Carbon nanotube forests a non-stick workbench for nanomanipulation.* Nanotechnology, 2006. **17**: p. 4917-4922.
187. Pronk, P., C.A. Infante Ferreira, and G.J. Witkamp, *Prevention of fouling and scaling in stationary and circulating liquid–solid fluidized bed heat exchangers: Particle impact measurements and analysis.* International Journal of Heat and Mass Transfer, 2009. **52**: p. 3857-3868.
188. Kubiak, J.A. and G. Urquiza-Beltráz, *Simulation of the effect of scale deposition on a geothermal turbine.* Geothermics, 2002. **31**: p. 545-562.
189. Dalas, E. and P.G. Koutsoukos, *Calcium carbonate scale formation on heated metal surfaces.* Geothermics, 1989. **18**(1/2): p. 83-88.
190. Elimelech, M., et al., *Role of membrane surface morphology in colloidal fouling of cellulose acetate and composite aromatic polyamide reverse osmosis membranes.* Journal of Membrane Science, 1997. **127**: p. 101-109.
191. Jucker, C. and M. Clark, *Adsorption of aquatic humic substances on hydrophobic ultrafiltration membranes.* Journal of Membrane Science, 1994. **97**: p. 35-52.
192. Yuan, W. and A.L. Zydney, *Effects of solution environment on humic acid fouling during microfiltration.* Desalination, 1997. **122**: p. 63-76.
193. Cowling, M.J., et al., *An alternative approach to antifouling based on analogues of natural processes.* The Science of the Total Environment, 2000. **258**: p. 129-137.
194. Cheng, Y.H., et al., *Effect of the microstructure on the properties of Ni-P deposits on heat transfer surface.* Surface & Coatings Technology, 2009. **203**: p. 1559-1564.
195. Zhao, Q., et al., *Graded Ni-P-PTFE coatings and their potential applications.* Surface & Coatings Technology, 2002. **155**: p. 279.
196. Sugama, T. and K. Gawlik, *Anti-slica fouling coatings in geothermal environments.* Materials Letters, 2002. **57**: p. 666-673.
197. Sugama, T. and D. Elling, *Poly(phenylenesulfide)-based coatings for carbon steel heat exchanger tubes in geothermal environment.* Journal of Materials Science, 2002. **37**: p. 4871-4880.

198. Mrksich, M. and G. Whitesides, *Using self-assembled monolayers to understand the interactions of man-made surfaces with proteins and cell.* Annual Review of Biophysics and Biomolecular Structure, 1996. **25**: p. 55-78.
199. Wiencek, K. and M. Fletcher, *Bacterial adhesion to hydroxy- and methyl-terminated alkanethiol self-assembled monolayers.* The Journal of Bacteriology, 1995. **177**: p. 1959-1966.
200. Ista, L., et al., *Attachment of bacteria to model solid surfaces: oligo (ethylene glycol) surfaces inhibit bacterial attachment.* FEMS Microbiology Letters, 1996. **142**.
201. Wahl, M., *Marine epibiosis: I. Fouling and Antifouling: some basic aspects.* Marine Ecology Progress Series, 1989. **58**: p. 175-189.
202. Finlay, J.A., et al., *The influence of surface wettability on the adhesion strength of settled spores of the green alga Enteromorpha and the Diatom Amphora.* Integrative and Comparative Biology, 2002. **42**(6): p. 1116-1122.
203. Hoipkemeier-Wilson, L., et al., *Antifouling potential of lubricious, micro-engineered, PDMS elaastomers against zoospores of the green fouling alga Ulva(Enteromorpha).* Biofouling, 2004. **20**.
204. Carman, M., et al., *Engineered antifouling microtopographies - correlating wettability with cell attachment.* Biofouling, 2006. **22**.
205. Jelvestam, M., et al., *Biomimetic materials with tailored surface micro-architecture for prevention of marine biofouling.* Surface and Interface Analysis, 2003. **35**: p. 168-173.
206. Scardino, A., E. Harvey, and R.D. NYS, *Testing attachment point theory: diatom attachment on microtextured polyimide biomimics.* Biofouling, 2006. **22**: p. 55-60.
207. Brady, R. and I. Singer, *Mechanical factors favoring release from fouling release coatings.* Biofouling, 2002. **15**: p. 73-81.
208. Gan, D., A. Mueller, and K. Wooley, *Amphiphilic and hydrophobic surface patterns generated from hyperbranched fluoropolymer/linear polymer polymer networks: minimally adhesive coatings via the crosslinking of hyperbranced fluoropolymers.* Journal of Polymer Science Part A: Polymer Chemistry, 2003. **41**: p. 3531-3540.
209. Gudipati, C., et al., *Hyperbranched fluoropolymer and linear poly(ethylene glycol) based amphilphilic crosslinked networks as efficient antifoulign coatings: an insight into the surface compositions, topographies, and morphologies.* Journal of Polymer Science Part A: Polymer Chemistry, 2004. **42**: p. 6193-6208.
210. Callow, J. and M. Callow, *The Ulva spore adhesive system*. 2006, Berlin heidelberg: Springer-Verlag.
211. Chiovetti, A., T. Dugdale, and R. Wetherbee, *Diatom adhesives: molecular and mechanical properties*. 2006, Berlin Heidelberg: Springer-Verlag.
212. Holland, R., et al., *Adhesion and motility of fouling diatoms on a silicone slastomer.* Biofouling, 2004. **20**: p. 323-329.
213. Chaudhury, M., et al., *The influence of elastic modulus and thickness on the soft fouling alga Ulva linza (Enteromorpha linza) from polydimethyl siloxane (PDMS) networks.* Biofouling, 2005. **21**: p. 41-48.

214. Anderson, C., et al., *The development of foul-release coatings for seagoing vessels.* Journal of Marine Design Operations, 2003. **84**: p. 11-23.
215. Rosmaninho, R., et al., *Calcium phosphate fouling on TiN-coated stainless steel surfaces: Role of ions and particles.* Chemical Engineering Science, 2007. **62**: p. 3821-3831.
216. Meier-Haack, J., S. Derenko, and J. Seng, *Fouling reduction by graft-modification with hydrophilic polymers.* Desalination, 2006. **199**: p. 509-511.
217. Yu, H.-Y., et al., *Surface modification of polypropylene microporous membrane to improve is antifouling property in MBR: CO_2 plasma treatment.* Journal of Membrane Science, 2005. **254**: p. 219-227.
218. Yu, H. and R. Sheikholeslami, *Effect of thermohydraulic conditions on fouling of calcium oxalate and silica.* Materials, interfaces, and electrochemical phenomena, 2005. **51**: p. 641-648.
219. Bae, T.-H. and T.-M. Tak, *Interpretation of fouling characteristics of ultrafiltration membranes during the filtration of membrane bioreactor mixed liquor.* Journal of Membrane Science, 2005. **264**: p. 151-160.
220. Bae, T.-H., I.-C. Kim, and T.-M. Tak, *Preparation and characterization of fouling-resistant TiO_2 self-assembled nanocomposite membranes.* Journal of Membrane Science, 2006. **275**: p. 1-5.
221. Zhang, Y., et al. *Study on retarding membrane fouling by ferric salts dosing in membrane bioreactors*. in *Proceedings of the Water Environment-Membrane Technology Conference*. 2004. Seoul, Korea.
222. Loh, S., et al., *Interplay among membrane properties, protein properties and operating conditions on protein fouling during normal-flow microfiltration.* Journal of Membrane Science, 2009. **332**: p. 93-103.
223. Hatakeyama, E., et al., *New protein-resistant coatings for water filtration membranes based on quaternary ammonium and phosphonium polymers.* Journal of Membrane Science, 2009. **330**: p. 104-116.
224. Chae, K., et al., *Anti-fouling epoxy coatings for optical biosensor application based on phosphorychloine.* Sensors and Actuators B: Chemical, 2007. **124**: p. 153-160.
225. Johnson, R., *Specifying plastic lined pipe.* Chemical Engineering, 1982. **89**: p. 119-125.
226. Frost, S., et al., *Service experience with glass reinforced epoxy pipelines and the way forward.* European Federation of Corrosion Publication, 1999. **26**(441-452).
227. Muckle, D., *Shape memory polyethylenes for pipe repairs.* Mat. World, 2000. **8**: p. 20-21.
228. Collie, G. and I. Black, *State-of-the-art production processes for convoluted, corrosion-resistant, high-pressure oilfield pipework.* Journal of Process Mechanical Engineering, 2005. **219**(Part E): p. 345-355.
229. Abdel-Aal, N., K. Satoh, and K. Sawada, *Study of the adhesion mechanism of $CaCO_3$ using a combined bulk chemistry/QCM technique.* Journal of Crystal Growth, 2002. **245**: p. 87-100.
230. Jaouhair, R., et al., *Influence of water composition and substrate on electrochemical scaling.* Journal of The Electrochemical Society, 2000. **147**(6): p. 2151-2161.

231. Euvrard, M., et al., *Kinetic study of the electrocrystallization of calcium carbonate on metallic substrates.* Journal of Crystal Growth, 2006. **291**: p. 428-435.
232. Gabrielli, C., et al., *An electrochemical method for testing the scaling susceptibility of insulating materials.* Journal of The Electrochemical Society, 2001. **148**(12): p. B517-B521.
233. Jung, Y.C. and B. Bhushan, *Contact angle, adhesion and friction properties of micro- and nanopatterned polymers for superhydrophobicity.* Nanotechnology, 2006. **17**: p. 4970-4980.
234. Ochoa, N.A., M. Masuelli, and J. Marchese, *Devlopment of charged ion exchange resin-polymer ultrafiltration membranes to reduce organic fouling.* Journal of Membrane Science, 2005. **278**: p. 457-463.
235. Jeffrey, L.D. and B.M. Phillip, *Bioinspired antifouling polymers.* Materials Today, 2005. **September**: p. 38-46.
236. Hanein, Y., et al., *Micromachining of non-fouling coatings for bio-MEMS applications.* Sensors and Actuators B: Chemical, 2001. **81**(1): p. 49-54.
237. Brétagnol, F., et al., *Fouling and non-fouling surfaces produced by plasma polymerization of ethylene oxide monomer.* Acta Biomaterialia, 2006. **2**(2): p. 165-172.
238. Koch, K., B. Bhushan, and W. Barthlott, *Diversity of structure, morphology and wetting of plant surfaces.* Soft Matter, 2008. **4**: p. 1943-1963.
239. Nun, E., M. Oles, and B. Schleich, *Lotus-effect - Surfaces.* Macromolecular Symposium, 2002. **187**: p. 677-682.
240. Koch, K., et al., *Fabrication of artificial Lotus leaves and significance of hierarchical structure for superhydrophobicity and low adhesion.* Soft Matter, 2009. **5**: p. 1386-1393.
241. Yamashita, H., et al., *Coating of TiO2 photocatalysts on super-hydrophobic porous teflon membrane by an ion assisted deposition method and their self-cleaning performance.* Nuclear Instruments and Methods in Physics Research Section B: Beam Interactions with Materials and Atoms, 2003. **206**: p. 898-901.
242. Neinhuis, C. and W. Barthlott, *Seasonal changes of leaf surface contamination in beech, oak, and ginkgo in relation to leaf micromorphology and wettability.* New Phytologist, 1997. **138**(1): p. 91-98.
243. Packham, D.E., *Surface energy, surface topography and adhesion.* International Journal of Adhesion & Adhesives, 2003. **23**: p. 437-448.
244. Zhang, H., R. Lamb, and J. Lewis, *Engineering nanoscale roughness on hydrophobic surface - preliminary assessment of fouling behaviour.* Science and Technology of Advanced Materials, 2005. **6**(3-4): p. 236-239.
245. Otten, A. and S. Herminghaus, *How plants keep dry: A physicist's point of view.* Langmuir, 2004. **20**: p. 2405-2408.
246. Nosonovsky, M. and B. Bhushan, *Roughness optimization for biomimetic superhydrophobic surfaces.* Microsystem Technologies, 2005. **11**: p. 535-549.
247. Cheng, Y.-T. and D.E. Rodak, *Is the lotus leaf superhydrophobic?* Applied Physics Letters, 2005. **86**: p. 144101.

248. Nosonovsky, M. and B. Bhushan, *Multiscale effects and capillary interactions in functional biomimetic surfaces for energy conversion and green engineering.* Philosophical Transactions of The Royal Society A, 2009. **367**: p. 1511-1539.
249. Abbott, S.J. and P.H. Gaskell, *Mass production of bio-inspired structured surfaces.* Proceedings of the Institution of Mechanical Engineers, Part C: Journal of Mechanical Engineering Science, 2007. **221**(10): p. 1181-1191.
250. Boden, S.A. and D.M. Bagnall, *Tunable reflection minima of nanostructured antireflective surfaces.* Applied Physics Letters, 2008. **93**: p. 133108.
251. Gorb, S., *Functional surfaces in biology: mechanisms and applications*, in *Biomimetics: biologically inspired technologies*, Bar-Cohen, Editor. 2006, Taylor and Francis: Boca Raton. p. 381-397.
252. Wilson, S.J. and M.C. Hutley, *The optical properties of the 'Moth-eye' antireflective surfaces.* Journal of Modern Optics, 1982. **29**: p. 993-1009.
253. Clapham, P.B. and M.C. Hutley, *Reduction of length reflection by moth eye principle.* Nature, 1973. **244**: p. 281-282.
254. Sukharev, M. and T. Siedman, *Coherent control of light propagation via nanoparticle arrays.* Journal of Physics B: Atomic, Molecular and Optical Physics, 2007. **40**: p. S283-S298.
255. Gabe, D.R. and D.J. Robinson, *Mass transfer in a rotating cylinder cell. I. Laminar flow.* Electrochimica Acta, 1972. **17**(6): p. 1121-1127.
256. Gabe, D.R., *Rotating cylinder electrode.* Journal of Applied Electrochemistry, 1974. **4**(2): p. 91-108.
257. De Bièvre, P. and H. Günzler, *Traceability in chemical measurement*. 2005: Springer.
258. Kuldipkumar, A., G.S. Kwon, and G.G.Z. Zhang, *Determining the growth mechanism of tolazamide by induction time measurement.* Crystal Growth & Design, 2007. **7**(2): p. 234-242.
259. Park, R.J. and F.C. Meldrum, *Shape-constraint as a route to calcite single crystals with complex morphologies.* Journal of Materials Chemistry, 2004. **14**: p. 2291-2296.
260. Hu, Z., et al., *Synthesis of needle-like aragonite crystals in the presence of magnesium chloride and their application in papermaking.* Advanced Composite Materials, 2009. **18**: p. 315-326.
261. Dunn, D.J., *Effect of surface roughness on the nucleation and growth of calcium sulphate on metal surface.* Journal of Crystal Growth, 1980. **50**: p. 533-540.
262. Graham, A.L., et al., *How Minimum Inhibitor Concentration (MIC) and sub-MIC concentrations affect bulk precipitation and surface scaling rates.* Society of Petroleum Engineers Journal, 2005. **SPE 93311**.
263. Han, Y.S., et al., *Crystallization and transformation of vaterite at controlled pH.* Journal of Crystal Growth, 2006. **289**: p. 269-274.
264. Spanos, N. and P.G. Koutsoukos, *The transformation of vaterite to calcite: effect of the conditions of the solutions in contact with the mineral phase.* Journal of Crystal Growth, 1998. **191**: p. 783-790.
265. Söhnel, O. and J. Garside, *Precipitation - Basic Principles and Industrial Applications*. 1992, Oxford: Butterworth Heinenann.

266. Hasson, D., et al., *Influence of the flow system on the inhibitory action of $CaCO_3$ scale prevention additives.* Desalination, 1996. **108**: p. 67-79.
267. Zhang, Y., et al., *The kinetics of carbonate scaling-application for the prediction of downhole carbonate scaling.* Journal of Petroleum Science and Technology, 2001. **29**: p. 85-95.
268. Sullivan, P.J., T. Young, and J. Carey, *Effectiveness of polymer phosphonate blends for inhibition of $CaCO_3$ scale.* Industrial Water Treatment, 1996. **26**: p. 39-44 (November/December).
269. Wu, Z., J.H. Davidson, and L.F. Francis, *Effect of water chemistry on calcium carbonate deposition on metal and polymer surfaces.* Journal of Colloid and Interface Science, 2010. **343**: p. 176-187.
270. Yiantsios, S.G. and A.J. Karabelas, *Deposition of micron-sized particles on flat surfaces: effects of hydodynamic and physicochemical conditions on particle attachment efficiency.* Chemical Engineering Science, 2003. **58**: p. 3105-3113.
271. Soltani, M. and G. Ahmadi, *Detachment of rough particles with electrostatic attraction from surfaces in turbulent flows.* Journal of Adhesion Science and Technology, 1999. **13**(3): p. 325-355.
272. Krishnan, S., C.J. Weinman, and C.K. Ober, *Advances in polymers for anti-biofouling surfaces.* Journal of Materials Chemistry, 2008. **18**: p. 3405-3413.
273. Wang, Z., A. Neville, and A.W. Meridith, *How and why does scale stick - Can the surface be engineered to decrease scale formation and adhesion?* SPE Seventh International Symposium on Oilfied Scale 2005 85-92, 2005. **SPE 94993**.
274. Chambers, L.D., et al., *Modern approaches to marine antifouling coatings.* Surface & Coatings Technology, 2006. **201**(6): p. 3642-3652.
275. Werner, C., M.F. Maitz, and C. Sperling, *Current strategies towards hemocompatible coatings.* Journal of Materials Chemistry, 2007. **17**: p. 3376-3384.
276. Wisniewski, N. and M. Reichert, *Methods for reducing biosensor membrane biofouling.* Colloids and Surfaces B: Biointerfaces, 2000. **18**(3-4): p. 197-219.
277. Otsuka, H., Y. Nagasaki, and K. Kataoka, *PEGylated nanoparticles for biological and pharmaceutical applications.* Advanced Drug Delivery Reviews, 2003. **55**(3): p. 403-419.
278. Rios, P.F., et al., *Durable ultra-hydrophobic surfaces for self-cleaning applications.* Polymers for Advanced Technologies, 2008. **19**: p. 1684-1691.
279. Bhushan, B., Y.C. Jung, and K. Koch, *Self-cleaning efficiency of artificial superhydrophobic surfaces.* Langmuir, 2009. **25**: p. 3240-3248.
280. Liu, Z. and W. Dreybrodt, *Dissolution kinetics of calcium carbonate minerals in H_2O-CO_2 solutions in turbulent flow: The role of the diffusion boundary layer and the slow reaction $H_2O + CO_2 <> H^+ + HCO_3^-$.* Geochemica et Cosmochimica Acta, 1997. **61**(14): p. 2879-2889.
281. Van Oss, C.J., R.J. Good, and M.K. Chaudhury, *The role of van der Waals forces and hydrogen bonds in "hydrophobic interactions" between biopolymers and low energy surfaces.* Journal of Colloid and Interface Science, 1986. **111**(2): p. 378-390.

282. Škvarla, J., *Hydrophobic interaction between macroscopic and microscopic surfaces. Unification using surface thermodynamics.* Advances in Colloid and Interface Science, 2001. **91**: p. 335-390.
283. Wang, Y., J. Davidson, and L.F. Francis, *Scaling in polymer tubes and interpretation for use in solar water heating systems.* Journal of Solar Energy Engineering, 2005. **127**: p. 3-14.
284. Sanft, P. and L.F. Francis, *Calcium carbonate formation on cross-linked polyethylene (PEX) and polypropylene random copolymer (PP-r).* Journal of Solar Energy Engineering, 2006. **128**(2): p. 251-254.
285. Yi, X. and J. Pellegrino, *Diffusion measurements with fourier transform infrared attenuated total reflectance spectroscopy: Water diffusion in polypropylene.* Journal of Polymer Science: Part B: Polymer Physics, 2002. **40**: p. 980-991.
286. Lefèvre, G., et al., *A turbidimetric method to measure isoelectric points and particles deposition onto massive substrates.* Colloids and Surfaces A: Physicochemical and Engineering Aspects, 2006. **280**(1-3): p. 32-38.
287. Lédion, J., C. Braham, and F. Hui, *Anti-scaling properties of copper.* Journal of Water Supply: Research and Technology - AQUA, 2002. **51**(7): p. 389-398.
288. Linnikov, O.D., *Investigation of the inital period sulphate scale formation Part 1. Kinetics and mechanism of calcium sulphate surface nucleation at its crystallization on a heat-exchange surface.* Desalination, 1999. **122**(1): p. 1-14.
289. Roques, H. and A. Girou, *Kinetics of the formation conditons of carbonate tartars.* Water Research, 1974. **8**: p. 907-920.
290. Aizenberg, J., A.J. Black, and G.M. Whitesides, *Oriented growth of calcite controlled by self-assembled monolayers of functionalized alkanethiols supported on gold and silver.* Journal of the American Chemical Society, 1999. **121**: p. 4500-4509.
291. Mann, S., et al., *Controlled crystallization of $CaCO_3$ under steric acid monolayers.* Nature, 1988. **334**: p. 692-695.
292. Rieke, P.C., *Selection of phase and control of orientation during physisorption on surfaces on homogeneously formed calcium carbonate nuclei.* Materials Science and Engineering, 1995. **C2**: p. 181-189.
293. Dalas, E., J. Kallitsis, and P.G. Koutsoukos, *The crystallization of calcium carbonate on polymeric substrates.* Journal of Crystal Growth, 1988. **89**(2-3): p. 287-294.
294. Addadi, L., et al., *A chemical model for the cooperation of sulfates and carboxylates in calcite crystal nucleation: Relevance to biominerlization.* Proceedings of the National Academy of Sciences of the United States of America, 1987. **84**: p. 2732-2736.
295. Wei, H., et al., *On the crystallization of calcium carbonate modulated by anionic surfactants.* Journal of Crystal Growth, 2005. **279**: p. 439-446.
296. Mann, S., et al., *Crystallization at inorganic-organic interfaces: Biominerals and biomimetic synthesis.* Science, 1993. **261**: p. 1286-1292.
297. Tai, C.Y. and F.-B. Chen, *Polymorphism of $CaCO_3$ precipitated in a constant-composition environment.* AIChE Journal, 1998. **44**(8): p. 1790-1798.

298. Hasson, D., *Fouling of heat transfer equipment*, ed. E.F.C. Somerscales and J.G. Knudsen. 1981: McGrawHill.
299. Elfil, H. and H. Roques, *Role of hydrate phases of calcium carbonate on the scaling phenomenon.* Desalination, 2001. **137**(1-3): p. 177-186.
300. Gebauer, D., A. Volkel, and H. Colfen, *Stable prenucleation calcium carbonate clusters.* Science, 2008. **322**(5909): p. 1819-1822.
301. Pouget, E.M., et al., *The initial stages of template-controlled $CaCO_3$ formation revealed by cryo-TEM.* Science, 2009. **323**(5920): p. 1455-1458.
302. Neira-Carrillo, A., et al., *Influence of conducting polymers based on carboxylated polyaniline on in vitro $CaCO_3$ crystallization.* Langmuir, 2008. **24**: p. 12496-12507.
303. Ogino, T., T. Suzuki, and K. Sawada, *The formation and transformation mechanism of calcium carbonate in water.* Geochimica et Cosmochimica Acta, 1987. **51**(10): p. 2757-2767.
304. Bischoff, J.L. and W.S. Fyfe, *Catalysis, inhibition, and the calcite-aragonite problem; [Part] 1, The aragonite-calcite transformation.* American Journal of Science, 1968. **266**: p. 65-79.
305. Bischoff, J.L., J.A. Fitzpatrick, and R.J. Rosenbauer, *The solubility and stabilization of ikaite $CaCO_3.6H_2O$ from 0 to 25°C.* Journal of Geology, 1993. **101**: p. 21-33.
306. Clarkson, J.R., T.J. Price, and D.J. Adams, *Role of metastable phases in the spontaneous precipitation of calcium carbonate.* Journal of the Chemistry Society, Faraday Transactions, 1992. **88**: p. 243-249.
307. Kawano, J., et al., *Precipitation diagram of calcium carbonate polymorphs: its construction and significance.* Journal of Physics: Condensed Matter, 2009. **21**(42): p. 425102.
308. Liu, X.Y. and S.W. Lim, *Templating and supersaturation-driven anti-templating: Principles of biomineral architecture.* Journal of the American Chemical Society, 2002. **125**: p. 888-895.
309. Nosonovsky, M. and B. Bhushan, *Hierarchical roughness makes superhydrophobic states stable.* Microelectronics engineering, 2007. **84**: p. 382-386.
310. Wagner, J. and R. Furstner, *Quantitative assessment to the structural basis of water repellency in natural and technical surfaces.* Journal of Experimental Botany, 2003. **54**: p. 1295-1303.
311. Extrand, C., *Modeling of ultralyophobicity: suspension of liquid drops by a single asperity.* Langmuir, 2005. **21**: p. 10370-10374.
312. Hiremath, R. and J.A. Swift, *Directed nucleation of molecular crystals on self-assembled monolayer surfaces.* Molecular Crystals and Liquid Crystals, 2006. **456**(1): p. 95-106.
313. Heywood, B.R. and S. Mann, *Template-directed nucleation and growth of inorganic materials.* Advanced Materials, 1994. **6**(1): p. 9-20.
314. Volkmer, D., et al., *Interfacial electrostatics guiding the crystallization of $CaCO_3$ underneath monolayers of calixarenes and resorcarenes.* Journal of Materials Chemistry, 2004. **14**: p. 2249.
315. Küther, J., et al., *Rough surfaces by design: Gold colloids tethered to gold surfaces as substrates for $CaCO_3$ crystallization.* Advanced Materials, 1998. **10**: p. 401-404.

316. Küther, J., et al., *Mercaptophenol-protected gold colloids as nuclei for the crystallization of inorganic minerals: Templated crystallization on curved surfaces.* Chemistry of Materials, 1999. **11**: p. 1317.
317. Thoreson, E.J., J. Martin, and N.A. Burnham, *The role of few-asperity contacts in adhesion.* Journal of Colloid and Interface Science, 2006. **298**: p. 94-101.
318. Burton, Z. and B. Bhushan, *Hydrophobicity, adhesion and friction properties of nanopatterned polymers and scale dependence for micro- and nanoelectromechanical systems.* Nano letter, 2005. **5**: p. 1607-1613.
319. Dillard, D., A.V. Pocius, and M. Chaudhury, *Adhesion Science and Engineering Volume 2, The Mechanics of Adhesion/Surfaces, Chemistry Applications*. 2002: Elsevier.
320. Quddus, A. and L.M. Al-Hadhrami, *Influence of solution hydrodynamics on the deposition of $CaSO_4$ scale on aluminum.* Desalination, 2007.
321. Kukulka, D.J. and M. Devgun, *Fouling surface finish evaluation.* Applied Thermal Engineering, 2007. **27**: p. 1165-1172.
322. Al-Anezi, K., D.J. Johnson, and N. Hilal, *An atomic force microscopy study of calcium carbonate adhesion to desalination process equipment: effect of anti-scale agent.* Desalination, 2008. **220**: p. 359-370.
323. Cowan, J.C. and D.J. Weintritt, *Water-formed scale deposits*. 1976, Houston, Texas: Gulf Publishing Company.
324. Andritsos, N. and A.J. Karabelas, *Crystallization and deposit formation of lead sulfide from aqueous solutions I. Deposition rates.* Journal of Colloid and Interface Science, 1991. **145**(1): p. 158-169.
325. Israelachvili, J.N., *Intermolecular and Surface Forces*. 1992, London: Academic Press.
326. Yue, W., et al., *Macroporous inorganic solids from a biomineral template.* Journal of Crystal Growth, 2006. **294**: p. 69-77.
327. Loste, E., et al., *Precipitation of calcium carbonate in confinement.* Advanced Functional Materials, 2004. **14**(2): p. 1211-1220.
328. Yue, W., A.N. Kulak, and F.C. Meldrum, *Growth of single crystals in structured templates.* Journals of Materials Chemistry, 2006. **16**: p. 408-416.
329. Hetherington, N.B.J., et al., *Crystallization on surfaces of well-defined topography.* Langmuir, 2006. **22**: p. 1955-1958.
330. Serro, A.P., R. Colaço, and B. Saramago, *Adhesion forces in liquid media: Effect of surface topography and wettability.* Journal of Colloid and Interface Science, 2008. **325**: p. 573-579.
331. Royer, M., et al., *Shear induced removal of calcium carbonate scale from polypropylene and copper tubes.* Journal of Solar Energy Engineering, 2010. **132**: p. 011013-1-011013-9.
332. Kim, N.-H. and R.L. Webb, *Particulate fouling of water in tubes having a two-dimensional roughness geometry.* International Journal of Heat and Mass Transfer, 1991. **34**(11): p. 2727-2738.
333. Greiner, C., A. del Campo, and E. Arzt, *Adhesion of bioinspired micropatterned surfaces: Effects of pillar radius, aspect ratio and preload.* Langmuir, 2007. **23**: p. 3495-3502.
334. Spolenak, R., et al., *Effects of contact shape on the scaling of biological attachments.* Proceedings of the Royal Society of London, Series A, 2005. **461**: p. 305-319.